To the Graduate Council:

I am submitting herewith a thesis written by Kirtan Maheshbhai Davda entitled "Understanding the impact of divertor and main chamber ion fluxes on divertor closure in the DIII-D tokamak." I have examined the final paper copy of this thesis for form and content and recommend that it be accepted in partial fulfillment of the requirements for the degree of Doctor of Philosophy, with a major in Energy Science and Engineering.

Dr. Ezekial A. Unterberg,
Research Advisor / Major Professor

We have read this thesis
and recommend its acceptance:

Dr. David Donovan

Dr. Peter Stangeby

Dr. Morgan Shafer

Dr. Zhili Zhang

Accepted for the Council:

Carolyn R. Hodges

Vice Provost and Dean of the Graduate School

To the Graduate Council:
I am submitting herewith a thesis written by Kirtan Maheshbhai Davda entitled "Understanding the impact of divertor and main chamber ion fluxes on divertor closure in the DIII-D tokamak." I have examined the final electronic copy of this thesis for form and content and recommend that it be accepted in partial fulfillment of the requirements for the degree of Doctor of Philosophy, with a major in Energy Science and Engineering.

Dr. Ezekial A. Unterberg, Research Advisor

We have read this thesis
and recommend its acceptance:

Dr. David Donovan

Dr. Peter Stangeby

Dr. Morgan Shafer

Dr. Zhili Zhang

Accepted for the Council:

Carolyn R. Hodges

Vice Provost and Dean of the Graduate School

(Original signatures are on file with official student records.)

Understanding the impact of divertor and main chamber ion fluxes on divertor closure in the DIII-D tokamak

A Dissertation Presented for the

Doctor of Philosophy

Degree

The University of Tennessee, Knoxville

Kirtan Maheshbhai Davda

May 2024

© by Kirtan Maheshbhai Davda, 2024
All Rights Reserved.

To my parents - Aruna and Mahesh Davda

Acknowledgements

I would like to sincerely thank my advisor/mentor, Dr. Ezekiel (Zeke) Unterberg, without whose expertise, guidance, and encouragement, this thesis would not be possible. Thanks to his continuous support and help, I have grown a lot as a person and have become a better researcher. I would also like to thank Dr. Donovan and his team for their continuous feedback and support. I would like to thank Dr. Stangeby for his book, feedback and conversations because of which I have gained knowledge in this field. I would also like to thank Dr. Morgan Shafer, Dr. Jeff Herfindal, and the rest of the DIII-D team for helping me at DIII-D.

I would sincerely like to thank Dr. Lee Reidinger, Dr. Ezekiel Unterberg, along with Dr. Ted Biewer and Wanda Davis (from the Bredesen Center) for believing in me in the initial days of my PhD and accepting me as a graduate student in the Bredesen Center program.

Over the years, I have crossed paths with many colleagues from whom I have learned and have become friends. I would like to thank them for being there for me, helping me in every possible way, listening to me whine about little things, and making the journey of this PhD a tad bit easier. The names of them are as follows - in no particular order: Davis Easley, Wendy Garcia, Monica Gehrig, Yashika Ghai, Katie Butler, Andrew Irvine, Jonah Duran, Shawn Zamperini, and many others along the way.

A special mention to Dr. Shawn Zamperini, Dr. Jake Nichols, Jeremy Mateja, and Dr. David Elder for helping me with OEDGE and introducing me to the world

of computational physics. Thank you for helping me in every small possible way and being so patient.

I would also like to thank my parents, Mahesh and Aruna Davda, for their constant support and encouraging me to do the right thing. Their constant support, motivation, guidance and praise is truly incomparable. There were days when I wished I spoke to my parents more because the passion and drive in me got refueled after the phone call. Their prayers, patience and acceptance of everything means a lot to me. I would also like to thank my sister, brother-in-law, and my nephew(s) for giving me a constant source of happiness. Their support is most under-rated. I always had a friend in the form of my sister a phone call away.

I would like to thank my fiancee, future Dr. Swati Mishra. She has been a perfect partner by being my teacher, caretaker, chef, activity planner, and everything that I cannot describe in words. Her presence and support has made the PhD years more tolerable, relaxing and upbeat. She did all this while pursuing her own PhD, which is mind-boggling. I would also like to thank my in-laws, for being there for me virtually and supporting me with prayers.

Also, I would like to thank so many other friends who made me feel Knoxville was my second home and kept me from feeling homesick. I would like to thank Falgunbhai, Anupbhai, Deepkabhai, Bhavinbhai, Nileshbhai, Parth, Bhavin, Tej, Akshar and other members of the BAPS Knoxville Yuvak Mandal.

Lastly, I would like to thank Akshar-Purushottam Maharaj, Bhagwan Swaminarayan, Pramukh Swami Maharaj, and Mahant Swami Maharaj for their grace with which I could achieve such knowledge and wisdom in my life.

"Two steps forward and one step back" - Dr. Ezekial Unterberg

Abstract

The diverted tokamak redirects extreme heat and particles to targets, a plasma-facing component designed for such loads. Here, the local fluxes produce strong particle recycling and sputtering. Recycled neutrals can "leak" into the region between the core and wall, the scrape-off-layer (SOL), impacting plasma performance. Increasing divertor closure can reduce leakage by containing neutrals within the divertor. However, there exists a need to quantify divertor baffle restrictions and understand closure directly from empirical data as opposed to indirectly through modeling.

Our study introduces the Geometric Restriction Parameter (GRP) based on simplifying neutral transport to ballistic pathways. Specifically, it considers the angle subtended between the strike point and target, as well as the outboard baffling. The GRP serves as an indicator of neutral retention in attached conditions, with lower values corresponding to reduced restrictions and increased leakage. Leveraging data from 12 DIII-D discharges characterized by different divertor geometries, plasma conditions, and drift orientations, we utilize Window-Frame Analysis (WFA) and a modeling tool, OEDGE, to gain insights into neutral dynamics in the SOL.

Our analysis shows DIII-D divertor configurations can access a full range of GRP values. Furthermore, we quantitatively assess main chamber fluxes in relation to calculated divertor restriction. Our findings indicate increased neutral leakage with lower divertor restrictions and underscore the impact of drift on neutral particle transport in L-mode. An inverse correlation between structural closure and main

chamber flux magnitude shows the significance of divertor restrictions in H-mode. While our empirical values align with OEDGE modeling, it is imperative to note that the model's validity pertains solely to attached plasma conditions.

In summary, our study shows the divertor closure's impact on main chamber and divertor fluxes, emphasizing the importance of SOL opacity on closure. In L-mode favorable drift conditions, divertor recycling emerge as the dominant factor with increased restrictions and neutral compression. The WFA exhibits a decreasing flux trend as the GRP increases, contrasting with the lack of discernible trend in unfavorable drift conditions. Additionally, divertor compression estimates, influenced by varying opacity, have implications for GRP estimation, highlighting the need to consider the SOL operating regime.

Table of Contents

1 Introduction to Thesis Topic & Fusion Energy **1**

1.1 Thesis goals and outline 1

1.2 World Energy Consumption today 3

1.2.1 Current Energy Sources for electricity production 3

1.3 Introduction to Fusion Energy Concepts 5

1.3.1 Fusion triple product and gain 9

1.3.2 Types and Modes of Plasma Confinement 11

1.3.3 Tokamak Terminology 18

1.4 Overview of the DIII-D Tokamak 21

2 Tokamak divertor closure: fundamentals, measurements and modeling **24**

2.1 Tokamak Divertor and SOL physics 25

2.1.1 SOL particle transport and edge turbulence 25

2.1.2 SOL Density and temperature gradients 26

2.1.3 The Two-Point SOL Model 27

2.1.4 SOL collisionality regimes 29

2.1.5 A simple SOL 32

2.1.6 SOL Drifts 32

2.2 Physics regimes of the tokamak divertor 33

2.2.1 Relationship between divertor regimes and SOL collisionality . 36

2.2.2 Sheath Limited Regime - weakly collisional . . . 36
2.2.3 Conduction Limited / High Recycling Regime - intermediately collisional . . . 37
2.2.4 Detached Regime . . . 40
2.3 Divertor closure, leakage and design . . . 43
2.3.1 How are neutrals formed and measured? . . . 43
2.3.2 Divertor closure . . . 65
2.3.3 Divertor Leakage . . . 68
2.3.4 Effects of Divertor Design on Divertor Physics . . . 75
2.4 Edge and divertor modeling for tokamak closure . . . 84
2.4.1 SOLPS . . . 86
2.4.2 EIRENE Model . . . 89
2.4.3 Onion Skin Model (OSM) . . . 92
2.4.4 OEDGE . . . 96
2.5 DIII-D Tokamak Diagnostic Suites used to quantify ion fluxes in main chamber and divertor region . . . 99
2.5.1 Thomson Scattering . . . 99
2.5.2 Langmuir Probes . . . 100
2.5.3 The Filterscope . . . 104
2.5.4 Neutral pressure gauges . . . 105

3 Analysis framework for tokamak closure interpretation 109
3.1 Understanding the neutral pathways in the tokamak edge . . . 109
3.2 Methodology - Measurement of ion fluxes in main chamber and the divertor to interpret divertor closure . . . 114
3.2.1 Window Frame Analysis . . . 114
3.2.2 The Geometric Restriction Parameter (GRP) . . . 125
3.3 Methodology - Interpretive analysis of poloidally averaged ion fluxes in the main chamber . . . 134

3.3.1 Ratio of poloidally average flux densities at the main chamber to the divertor . . . 135
3.3.2 Critical Considerations in OEDGE Simulation Setup . . . 136

4 DIII-D Database development for closure interpretation 140

4.1 Systematic investigation of empirical and model-derived f_{wall} for one plasma discharge . . . 141
4.1.1 Empirical estimation of f_{wall} . . . 143
4.1.2 Estimation of I_{wall} . . . 145
4.1.3 Estimation of I_{div} . . . 147
4.1.4 Modeled f_{wall}: Introduction to OEDGE results . . . 149
4.1.5 Estimation of $f_{wall-oedge}$ . . . 149
4.1.6 Estimation of poloidally averaged $< f_{wall-oedge} >$ . . . 155
4.2 Summary for Shot 186703 and database of plasma discharges for comparative study between divertor design . . . 155
4.3 Results from GRP estimation for conventional and non-conventional divertor . . . 157
4.3.1 Effect of geometry on neutral particle restrictions . . . 165

5 Conclusions from DIII-D divertor closure analysis 168

5.1 Restrictions influencing main chamber and divertor recycling as measured by Filterscope . . . 168
5.2 Understanding the neutral opacity with respect to closure using OEDGE 174
5.3 Breakdown of wall and divertor fluxes in empirical and modeled procedures . . . 180
5.3.1 Estimation of main chamber and divertor fluxes using WFA showing lower main chamber fluxes with higher restrictions . . . 180
5.3.2 Estimation of main chamber and divertor fluxes using OEDGE showing higher main chamber fluxes with higher restrictions for near SOL measurements . . . 185

5.3.3 Comparing experimental results with Modeled results show deviation . . . 188
5.4 Discussions . . . 192

6 Future Work **195**

Bibliography **199**

Appendix **239**

A Comprehensive Analysis of the Filterscope Diagnostic Tool **240**
A.1 Hardware Overview . . . 240
A.2 Operating Principle . . . 244
A.3 Determining the output of the Filterscope: Line Normalized Radiance 246
A.4 Calibration Philosophy . . . 246
A.5 Introduction to Statistical Machine Learning for Estimating the Calibration coefficients . . . 251

B GRP Estimation Flow Chart **259**

C Details about running a successful OEDGE case **261**
C.1 Setting up OEDGE workspace in IRIS . . . 262
C.1.1 Configuration of the Bash profile . . . 263
C.2 Creating a grid using DG - Carre . . . 264

D Details about obtaining I_{wall} and I_{div} for all divertor configurations **278**
D.1 Global parameters compared between plasma discharges used for closure interoperability . . . 279
D.2 Diagnostic measurements in DIII-D tokamak . . . 282
D.2.1 Electron Density and Temperature Measurements . . . 282
D.2.2 Filterscope Measurements . . . 291
D.3 Divertor Plasma Solution using OEDGE . . . 291

D.3.1 LSN Shelf Configuration 291
D.3.2 LSN Floor Configuration 298
D.3.3 USN Floor Configuration 305

E DIII-D Mini proposal for an experiment 311
E.1 Purpose of the Experiment 311
E.2 Background 311
E.3 Experimental Approach 313
E.4 Resources 314
E.4.1 Diagnostic Requirements 314
E.4.2 Analysis Requirements 315
E.5 Experimental Plan 316
E.6 Analysis plan and Deliverables 316
E.7 Radiation Awareness 317

F Divertor Detachment 319

Vita 330

List of Tables

2.1 Four different types of SOL defined with respect to its temperature (T) gradient and isothermal property 31

2.2 Spectral Line Data for Hydrogen (Lyman & Balmer) 48

2.3 Comparison of DLP values in different divertor geometry with different divertor plasma conditions Casali et al. [2020] 71

4.1 Summary of calculation of f_{wall} via experiment and OEDGE model for Shot 186703 156

4.2 Details of plasma discharges in L-mode and H-mode for $B \times \nabla B$ towards the target 158

4.3 Details of plasma discharges in L-mode and H-mode for $B \times \nabla B$ away from the target 158

4.4 Summary table of calculated GRP values for conventional and non-conventional divertor geometry in DIII-D 166

4.5 Details of plasma discharges in L-mode and H-mode for $B \times \nabla B$ towards the target and away from the target 166

A.1 Description of model interpretability and model accuracy for using non-least squares estimates 257

E.1 Shot plan during the experiment day 318

List of Figures

1.1 Distribution of gross world electricity production by source 4
1.2 Energy production plotted against cross-section and temperature . . . 8
1.3 Fusion triple product in various fusion devices over the last 50 years. 10
1.4 A schematic of a tokamak device 15
1.5 Distinction between L and H mode in a plasma discharge 17
1.6 Limiter and Divertor Configuration of a Tokamak 20
1.7 A cutaway schematic of the DIII-D tokamak 22
1.8 Types of divertor targets available in DIII-D 22

2.1 A description of the Two-Point Model in a schematic way with a flat-SOL variation 28
2.2 Different SOL collisionality Regimes 31
2.3 Depiction of various drifts in poloidal and toroidal magnetic field . . . 34
2.4 Cartoon depiction of three different physics regimes in the divertor target 35
2.5 Different divertor regimes plotted in terms of collisionality 39
2.6 Depiction of neutral flux in a high recycling divertor 39
2.7 Increase in plasma density leading to loss in plasma pressure and target temperature 42
2.8 PMI process occurring in the SOL 44
2.9 Reaction rate coefficients on Hydrogen in both atomic and molecular state 44

2.10 Neutral hydrogen and deuterium density measurement with and without accounting for the influence of opacity on Lyman lines 54
2.11 Escape factor and absorption coefficients used to understand opacity . 58
2.12 Balmer line ratio as a function of electron temperature and degree of dissociation 59
2.13 Neutral ionization pattern in Vertical and Horizontal Targets 67
2.14 Flow of neutrals through SOL, divertor and core plasma 69
2.15 The DLP as a function of separatrix density in Open (LSN) and Closed (USN) DIII-D divertor geometry 71
2.16 Flattened out SOL depicting the cross-field plasma flux moving towards the divertor targets 74
2.17 Depiction of neutral flux density at the midplane and below the heatshield (green) versus neutral density in the divertor baffle in ASDEX-Upgrade 77
2.18 Divertor designs in various experimental tokamaks worldwide 78
2.19 Flux onto the divertor target with varying x-point height 81
2.20 Measured neutral pressures at the divertor in JET 81
2.21 Midplane Neutral compression presented for varying density 83
2.22 Schematic of a SOLPS-ITER workflow 88
2.23 Schematic depicting EIRENE MC Solver 90
2.24 Plasma solution depicting n_e from OEDGE 98
2.25 Cross-section of DIII-D with Thomson system laser path and view ports 101
2.26 Plot depicting the electron temperature (dashed) and density (solid) measured via Thomson Scattering 101
2.27 Current - Voltage characteristic from a Langmuir Probe 102
2.28 Line of sights for Filterscope on the DIII-D tokamak 107
2.29 Schematic of the ASDEX gauge 108
2.30 Midplane pressure measurements for plasma discharges 108

3.1 Neutral and ion pathways at the edge of the tokamak 111
3.2 Schematic representing window frame analysis 117
3.3 A schematic of the window-frame placement on the DIII-D tokamak . 118
3.4 Measurement of local particle flux density measurement in the main chamber measured using Filterscope and Pressure gauges plotted against the measurements from RCP 120
3.5 Measurement of local particle flux in the main chamber measured using Filterscope and Pressure gauges plotted against the measurements from embedded Langmuir probe at the windowpane in the divertor . 121
3.6 Schematic representation of the modified window frame analysis . . . 123
3.7 DIII-D cross-section showcasing of multiple divertor target in the machine 130
3.8 Two plasma discharges on the LSN Floor with varying strike point on the divertor target 130
3.9 Illustration depicting the geometric configuration of a divertor, highlighting the elements utilized in the derivation of the GRP 131
3.10 Plasma solution depicting n_e, windowpane and Region of Interests (ROIs) 138
3.11 Flowchart depicting scenarios for a successful OEDGE run 139

4.1 Global Parameters of Plasma discharge #186703 with $B \times \nabla B$ ion drift directed both towards the target in H mode configuration 142
4.2 n_e and T_e along with SXB and PEC values for plasma discharge #186703 144
4.3 Details regarding estimation of I_{wall} shown along with a 2D cross section layout of DIII-D tokamak for Shot 186703 146
4.4 Details regarding estimation of I_{div} for Shot 186703 148
4.5 Cross-section of DG-Carre created surface and mesh 150
4.6 2D profiles of shot 186703 showing data that is used to calculated particle flux density from n_e and velocity 150
4.7 Validation of n_e and T_e through OSM with the Thomson Scattering data 152

4.8 Validation of n_e, T_e and J_{SAT} through OSM with the Langmuir Probe data . . . 152
4.9 n_e estimation in three regions using OEDGE . . . 153
4.10 v estimation in three regions using OEDGE . . . 153
4.11 Γ_{wall} estimation in three regions using OEDGE . . . 154
4.12 average n_e and v estimation poloidally across cross-section . . . 156
4.13 Seven different divertor configurations with respective GRP . . . 159
4.14 α and θ_{max} for 58 plasma discharges in LSN Floor divertor . . . 159
4.15 Variation of the hypotenuse (length between OSP to the PFC_i value) plotted as a function of discretized wall index . . . 161
4.16 Variation of the GRP values with respect to time for conventional divertor configurations . . . 161
4.17 Variation of the GRP values with respect to time for non-conventional divertor configurations . . . 167

5.1 Particle flux measured by Filterscope D_α at the divertor and outboard midplane region . . . 170
5.2 Ratio of neutral density measured upstream and at the target (1/neutral compression) plotted as a function of neutral opacity (plasma density × minor radius) . . . 177
5.3 Ratio of neutral density measured upstream and at the target plotted as a function of neutral opacity (plasma density × minor radius) for separate divertors . . . 179
5.4 f_{wall} estimation on experimental data . . . 181
5.5 f_{wall} plotted as a function of pedestal density, outer gap, outer strike point . . . 184
5.6 $f_{wall-oedge}$, $\langle f_{wall-oedge} \rangle$ along S poloidal and modified DLP estimation using OEDGE model . . . 187
5.7 Comparison of f_{wall} between experimental and modeled findings . . . 190

6.1 Expected results from an experiment slated for future 198

A.1 A detailed schematic of the Filterscope system 242
A.2 Filterscope midplane location and hardware 243
A.3 Detailed schematic of the PMT module describing the operating principle of the Filterscope system 245
A.4 Each component that makes up the filtered spectral radiance in Filterscope 249
A.5 Fourth order polynomial fit of G_{PMT} on a single PMT of the Filterscope system 250
A.6 Estimation of gain calibration coefficients using the parametric approach 253
A.7 Alternatives to least square Estimation 257

B.1 A flowchart of GRP Estimation 260

C.1 Screen cap of DG system to grab Template 266
C.2 Screen cap of DG system to grab equilibrium 266
C.3 Screen cap of DG system to have better display option 268
C.4 Screen cap of DG system to have SOL surfaces known using the right click mouse option 269
C.5 Screen cap of DG system to have SOL surfaces known using the right click mouse option 269
C.6 Screen cap of DG system to select target surfaces 271
C.7 Screen cap of DG system to select DIII-D structure surfaces 271
C.8 Screen cap of DG system to produce grid points on the equilibrium . 272
C.9 Screen cap of DG system showing the necessity of equidistant grid points 272
C.10 Screen cap of DG system to produce grid points on the equilibrium . 273
C.11 Screen cap of DG system showing the SOL edge and PFR edge for inner and outer target 276
C.12 Screen cap of DG system showing the surface and meshes 276

D.1 Global Parameters of Plasma discharges in Fwd B_t H mode configuration 280
D.2 n_e from Thomson Scattering - $B_T \times \nabla B \downarrow$ in L mode and H mode configuration 284
D.3 T_e from Thomson Scattering - $B_T \times \nabla B \downarrow$ in L mode and H mode configuration 285
D.4 T_e from Thomson Scattering - $B_T \times \nabla B \uparrow$ in L mode and H mode configuration 286
D.5 T_e from Thomson Scattering - $B_T \times \nabla B \uparrow$ in L mode and H mode configuration 287
D.6 n_e, T_e and J_{sat} as measured by embedded Langmuir probes on the divertor target 289
D.7 n_e, T_e and J_{sat} as measured by embedded Langmuir probes on the divertor target 289
D.8 n_e, T_e and J_{sat} as measured by embedded Langmuir probes on the divertor target 290
D.9 n_e, T_e and J_{sat} as measured by embedded Langmuir probes on the divertor target 290
D.10 D_α radiance and emissivity as measured by midplane Filterscope system for LSN Shelf configuration 292
D.11 D_α radiance and emissivity as measured by midplane Filterscope system for LSN Shelf configuration 292
D.12 D_α radiance and emissivity as measured by midplane Filterscope system for USN Floor configuration 293
D.13 Electron density, velocity, and Flux density estimation at regions 1, 2 and 3 295
D.14 Electron density, velocity, and Flux density estimation at regions 1, 2 and 3 295
D.15 2D measurements of Density, Velocity, temperature and flux 296
D.16 2D measurements of Density, Velocity, temperature and flux 296

D.17 Flux density estimation at regions 1, 2 and 3 297
D.18 Electron density, velocity, and Flux density estimation at regions 1, 2 and 3 297
D.19 2D measurements of Density, Velocity, temperature and flux 299
D.20 2D measurements of Density, Velocity, temperature and flux 299
D.21 Electron density, velocity, and Flux density estimation at regions 1, 2 and 3 300
D.22 Electron density, velocity, and Flux density estimation at regions 1, 2 and 3 300
D.23 2D measurements of Density, Velocity, temperature and flux 302
D.24 2D measurements of Density, Velocity, temperature and flux 302
D.25 Electron density, velocity, and Flux density estimation at regions 1, 2 and 3 303
D.26 Electron density, velocity, and Flux density estimation at regions 1, 2 and 3 303
D.27 2D measurements of Density, Velocity, temperature and flux 304
D.28 2D measurements of Density, Velocity, temperature and flux 304
D.29 Electron density, velocity, and Flux density estimation at regions 1, 2 and 3 307
D.30 Electron density, velocity, and Flux density estimation at regions 1, 2 and 3 307
D.31 2D measurements of Density, Velocity, temperature and flux 308
D.32 2D measurements of Density, Velocity, temperature and flux 308
D.33 Electron density, velocity, and Flux density estimation at regions 1, 2 and 3 309
D.34 Electron density, velocity, and Flux density estimation at regions 1, 2 and 3 309
D.35 2D measurements of Density, Velocity, temperature and flux 310
D.36 2D measurements of Density, Velocity, temperature and flux 310

E.1 Shot plan review and the conditions being met during one plasma discharge 318

F.1 Transition to detachment with increasing plasma density at DIII-D . 323
F.2 Gradual transition to detachment in JET-ILW with time 323
F.3 Attached vs detached divertor plasmas in Alcator C-Mod 329
F.4 Degree of detachment for JET inner divertor with early onset of detachment indicated 329

Chapter 1

Introduction to Thesis Topic & Fusion Energy

1.1 Thesis goals and outline

The purpose of this thesis is to understand the impact of divertor design on neutral transport and its magnitude in the divertor and main chamber region. In this work, divertor restriction is calculated based on simplified neutral transport to ballistic pathways while considering the magnetic plasma equilibrium and the baffling , i.e., the angle subtended between the strike point and the divertor target and the physical baffling present outboard of at the target and we term it as Geometric Restriction Parameter (GRP). Here, divertor restriction is scanned to correlate the magnitude of particle flux in the main chamber and divertor target in DIII-D for L-mode and H-mode discharges.

This helps to understand the mechanism of neutral leakage (via proxy estimation of neutral flux in different regions) due to different divertor geometry and plasma configuration, potentially leading to understanding in the following tokamak divertor physics areas/topics:

- Impact of target design on the SOL neutral dynamics

- Impact of particle sourcing due to divertor design
- Effect of closure on SOL fluxes

This document introduces the following hypothesis questions to address the topics mentioned above:

- How does neutral leakage pathway correlate with divertor closure?
- Is divertor closure driven by baffling alone?

Specifically, we aim to determine if there are noticeable changes: with the extent to which neutrals reclaimed from the divertor target can exit the divertor region, called the divertor closure, with target geometry (open, closed, and vertical target); and, with favorable and unfavorable drift conditions. This range of parameters allows us to obtain data to build a data set to compute different divertor operating points.

This thesis comprises six chapters. The initial sections of Chapter 1 introduce nuclear fusion and its fundamental concepts. The terminology employed in the hypothesis questions is explicated in Chapter 1. Next, Chapter 2 conducts an extensive literature review on tokamak neutral dynamics, including its core principles, measurement techniques, and modeling foundations. Subsequently, Chapter 3 delineates the methodological approach adopted, utilizing both empirical and modeling frameworks to address the thesis's hypothesis questions. Chapter 4 presents analysis of the methodology with results. Following this, Chapter 5 delves into the physics underpinning the obtained results and draws overall conclusions. Lastly, Chapter 6 outlines future work, identifying areas that warrant further investigation to provide a more comprehensive understanding of the hypothesis questions.

1.2 World Energy Consumption today

The advent of the industrial revolution marked a profound shift in human society, transitioning it from primarily agricultural to industrialized Editors [2009]. During this period, the steam engine played a pivotal role in the establishment of cotton mills Hopley [2020], iron works, waterworks, and paper mills Editors [2009]. Operating on coal, the steam engine triggered an unprecedented surge in the demand for this fuel. Subsequent technological advancements, including the development of railroads, further fueled the escalating need for coal Rosen [2010]. Since the mid-18th century, coal has consistently ranked as the most extensively utilized fuel to meet the requirements of a growing population Group [2019]. The escalating consumption of energy, predominantly in the form of electricity IEA [2020, 2019b], continues to be a prominent trend, as illustrated in Figure 1.1 IEA [2018c, 2019b, 2018b].

1.2.1 Current Energy Sources for electricity production

Figure 1.1 describes the present-day energy sources employed for electricity generation. Subfigure 1.1(b) reveals that fossil fuels account for 63% of the total global production whereas subfigure 1.1(a) further breaks down the contribution of various energy sources, including biofuels and waste (2.4%), solar energy (2.6%), wind energy (5.3%), geothermal, tidal, and other sources (0.5%), hydro (16%), and nuclear fuels (10.3%) IEA [2019b]. Considering that coal stands out as the predominant energy source at 36.7%, it holds significant implications for climate change and global warming IEA [2019a]. The combustion of coal releases carbon dioxide, a greenhouse gas that contributes to the formation of a layer in the Earth's atmosphere, trapping heat and resulting in elevated surface temperatures, rising sea levels, and biodiversity loss blogpost [2019].

Natural gas contributes almost a quarter of the world's energy demand, making it the fastest-growing fossil fuel market IEA [2018a]. Hydro-power, the world's largest source of renewable energy production, has the capacity to produces over 1307 GW

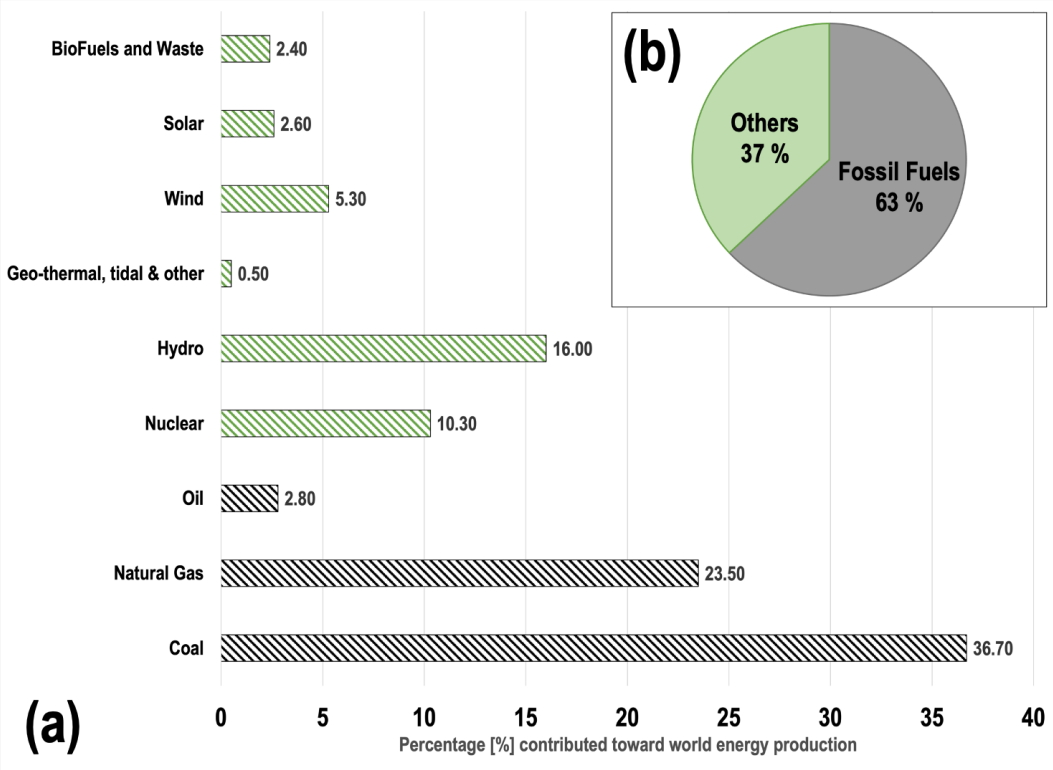


Figure 1.1: (a) Gross world electricity production by source in percentage. (b) Pie chart depicting the percentage of fossil fuels out of the total production. Image produced from IEA [2019b]

of energy, globally. This plays a critical role in decarbonizing the power system in today's world IEA [2019c]. As far as nuclear fission energy is concerned, there were 452 nuclear fission reactors worldwide, generating around 2.6 PWh of electricity in total IEA [2018e]. Since its inception, electricity produced using nuclear energy has been the largest contributor to carbon-free electricity generation IEA [2018e], and around 20% of electricity is generated in the United States is by nuclear energy EIA [2020].

There are many advantages to nuclear energy. It is competitive in operating a nuclear reactor compared to operating coal or a gas power plant in terms of fuel cost Lane [2020]. Nuclear fuel has a high energy density – for example, the energy released from six grams of uranium is equivalent to a ton of coal, 17,000 cubic feet of natural gas Sen [2019], and 149 gallons of oil. Lastly, nuclear energy is climate-friendly, i.e., there is very low pollution associated with nuclear energy. It has avoided 55 Gt of carbon dioxide emission over the past 50 years, which is nearly the same amount of carbon dioxide emitted by fossil fuels every two years IEA [2018d].

The years of fossil fuel reserves left are numbered. For example, data from 2016 suggests that global estimated coal reserves will deplete in 114 years. The estimated reserve for both natural gas and oil will last only for the next 50 years BP [2016]. Also, the other energy sources – solar, wind, batteries, etc. are still not efficient in supporting the global electricity needs. Since the effects of greenhouse gas emissions on global warming and climate change are visible and increasing – these become clear indicators that there is a need for a green, alternative, sustainable, carbon–emission-free energy source – Fusion.

1.3 Introduction to Fusion Energy Concepts

The process of fusing two or more lighter atoms to form a heavier atom is termed nuclear fusion, and the energy produced from the fusion of lighter atoms that is net-positive based on triple product (See Section 1.3.1) is called nuclear fusion energy

ANS [2018]. Fusion reactions were discovered in the 1920s and were soon applied to make the first hydrogen bomb in 1952. However, more than 50 years after the implementation of the hydrogen bomb, the controlled fusion is still in the research and developmental stage because of engineering and physics challenges faced in order to confine plasma that can be sustained for a longer duration of time Miyamoto [2005].

All the matter in the universe consists of at least 75% hydrogen, and the abundance of hydrogen leads to the formation of stars. These stars are working fusion reactors as they constantly fuse the already abundant hydrogen by utilizing the gravitational force in space Kikuchi [2011]. On Earth fusion technology holds the promise of producing energy at a rate four times greater per kilogram of fuel compared to conventional fission, commonly employed in nuclear power plants. Furthermore, its energy output potential is estimated to be nearly four million times higher than that achieved through the combustion of oil or coal.

Contemporary fusion reactor designs, currently in development, predominantly involve the fusion of deuterium and tritium, both isotopes of hydrogen possessing additional neutrons as seen in Equations 1.2, 1.1, 1.3, 1.4. Theoretically, a minute quantity of these reactants— measured in grams — has the potential to yield a terajoule of energy. To put this in perspective, such an energy yield is approximately equivalent to the energy consumption of an individual in a developed country over a period of around sixty years Barbarino [2023].

The following equations show four different ways fusion takes place using deuterium, tritium, and their byproduct Helium. Equation 1.2 shows the fusion of two deuterium atoms forming tritium along with an energetic proton with an energy of 3.03 MeV. Two deuterium atoms can also make the next heaviest element in the periodic table – Helium (but with one less neutron, i.e., Helium 3) with an energetic neutron of energy 2.45 MeV as shown in Equation 1.1. This Helium 3 reacts with a deuterium atom to create a 'stable' helium atom (i.e., with two neutrons, two protons, and two electrons: helium 4) along with an energetic proton with energy 14.67 MeV as shown in Equation 1.4. Lastly, the fusion of deuterium and tritium can also form

Helium four along with an energetic neutron with energy 14.06 MeV, as shown in Equation 1.3 Miyamoto [2005].

$$D + D \rightarrow He^3\,(0.82MeV) + n\,(2.45MeV) \tag{1.1}$$

$$D + D \rightarrow T\,(1.01MeV) + p\,(3.03MeV) \tag{1.2}$$

$$T + D \rightarrow He^4\,(3.52MeV) + n\,(14.06MeV) \tag{1.3}$$

$$D + He^3 \rightarrow He^4\,(3.67MeV) + p\,(14.67MeV) \tag{1.4}$$

Note that the energy produced in the above equations is in MeV – Mega Electron Volts. In the plasma physics community, Electron-Volt (eV) is used as the unit of energy. It is defined as the energy needed to move an electron with charge 'e' (e = 1.602×10^{-19} Coulomb) against 1 Volt of potential difference, i.e., 1 eV = 1.602 x 10^{-19} J and/or $1eV = 1.1610^4K$ which is obtained as energy, can also be expressed by using the Boltzmann constant to give eV to K. Comparing energy released in the above equations, one can say that Equations 1.3 and 1.4 produce the most energy between the four equations. However, it is the D-T reaction (equation 1.3) that is preferred to achieve fusion as it has a large cross-section (a measure of the probability of the reaction in terms of the kinetic energy between the two fusing nuclei) at a lower temperature as seen in Figure 1.2 Christian [2018]. It depicts the fusion cross sections 'σ' (y-axis) for the energy of the center of masses (CofM) of the fusion reactant species over keV of temperature (bottom x-axis). Comparing all the three common fusion reactors, it can be seen that the D – T curve achieves the highest cross-section at the lowest temperature and the input energy, and therefore future fusion reactors will most likely operate with D – T reaction ITER [2023].

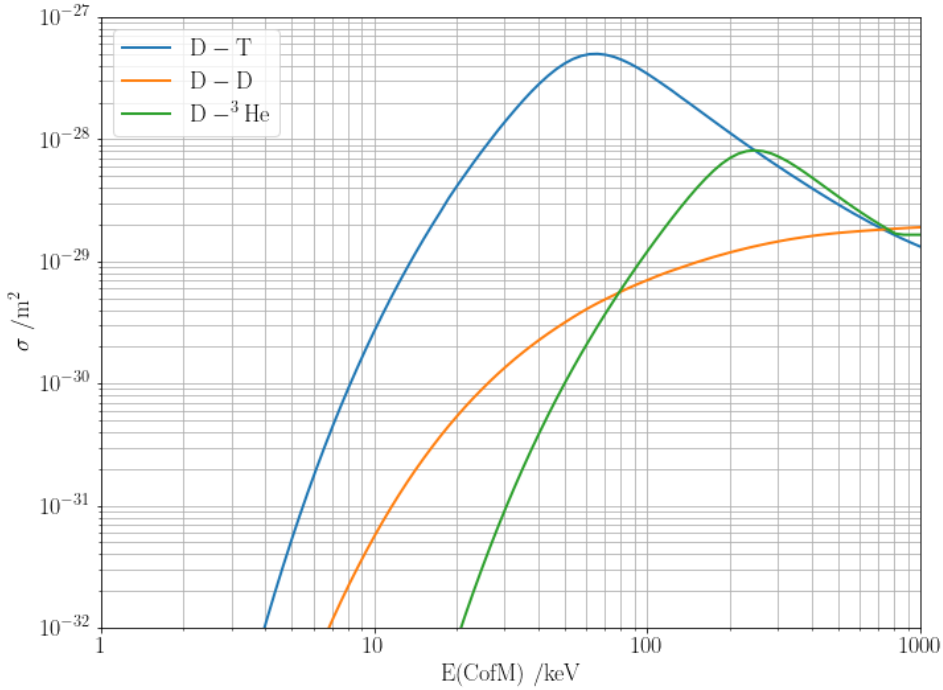


Figure 1.2: Fusion cross sections 'σ' (y-axis) plotted versus the energy of the center of masses (CofM) of the fusion reactant species over keV of temperature. Image produced from Christian [2018]

1.3.1 Fusion triple product and gain

A material changes its state from solid to liquid to gas as the temperature rises. However, when the temperature is raised even further, the atoms in the gaseous state are ionized while the charge between the electrons and ions remains the same. This state of free-flowing electrons and ions in space is called plasma Miyamoto [2005]. A fusion plasma starts by ionizing deuterium and tritium gas into plasma, where the behavior of the plasma is governed by long-range electric and magnetic fields, making it a great conductor of electricity that is 40 times better than copper Freidberg [2007].

To create nuclear fusion one must heat and confine the plasma, which produces energy that can be extracted to generate electricity. Just as coal, natural gas, and/or nuclear fission power plants work, the nuclear fusion power plant is also expected to have a net positive energy output. While there are many ways to confine plasma (see Section 1.3.2 for details), Triple product is a single metric that tells us how close we are to net-positive energy output in a fusion reactor irrespective of the confinement method by indicating the approach to thermo-dynamic nuclear fusion. It is the product of three parameters: n, T and τ_E; where 'n' represents the density of the ions in the plasma [$ions/m^3$], 'T' is the temperature of the ions [keV] and 'τ_E' is the energy confinement time [seconds] Wurzel [2019].

The value of the triple product for a D-T fusion plasma reactor should be $\geq 3 \times 10^{21}$ keVm^{-3} s with temperature ranging from 10 – 20 keV Wesson [2011]. It was Lawson who showed that the product of confinement time and ion density determined the minimum conditions for productive fusion Lawson [1957]. Hence this criterion is now famously known as the Lawson's criteria , and the Triple product is derived from the Lawson Criteria that states that the triple product combines the three critical parameters (n, T, τ_E) that are needed to make fusion possible Pitts et al. [2006].

Figure 1.3 displays various fusion experiments, showcasing experimentally derived Lawson's criteria plotted against ion temperature in keV. Additionally, the fusion experiments are presented in relation to the fusion power gain (Q_{sci}^{MCF}), representing

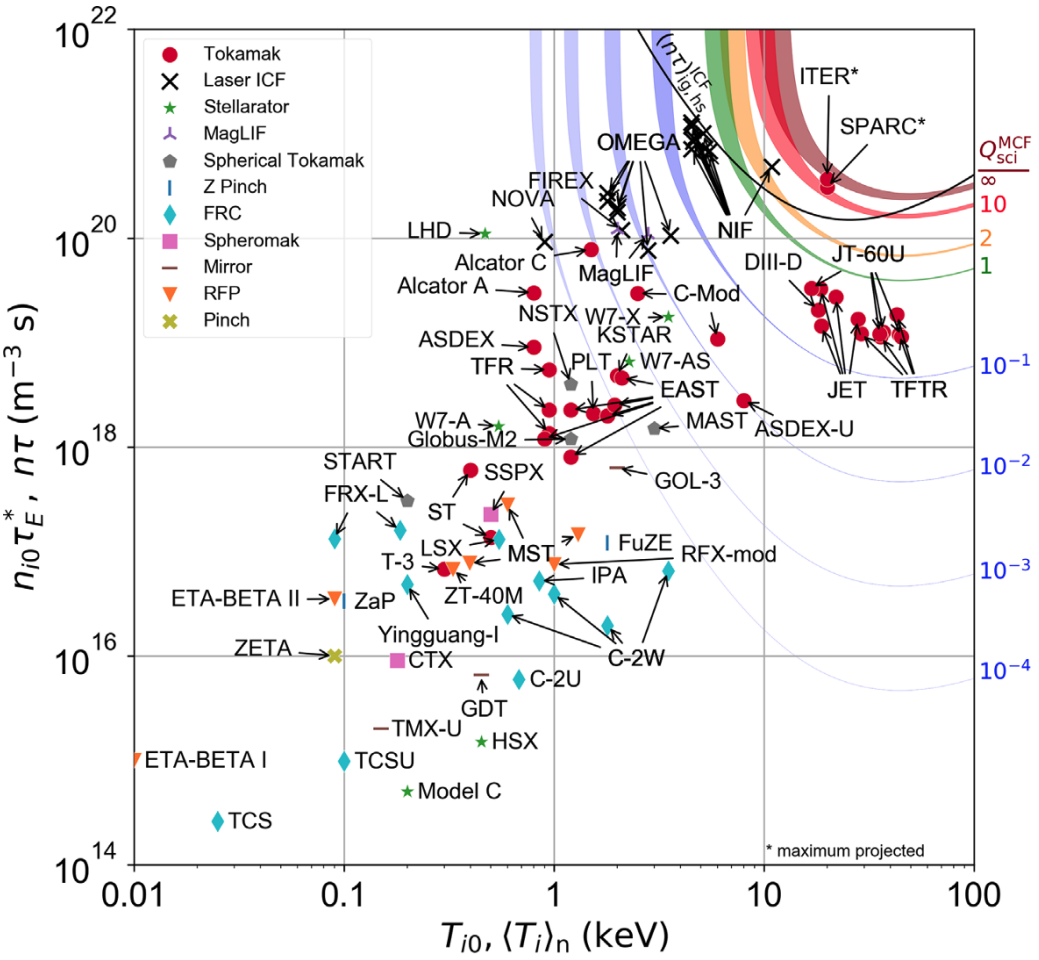


Figure 1.3: The experimentally derived Lawson parameters ($n_{i0}\tau_E^*$ for MCF and $n\tau$ for ICF) from fusion experiments are compared to T_{i0} for MCF and $\langle T_i \rangle_n$ for ICF. The colored contours in the figure represent the Lawson parameters and ion temperatures necessary to achieve specified scientific gain values (Q_{sci}^{MCF} for MCF). The black curve, identified as $(n\tau)_{ig,hs}^{ICF}$, corresponds to the Lawson parameters and ion temperatures required for achieving hot-spot ignition in ICF. Wurzel and Hsu [2022]

the ratio of fusion power output to the power required for plasma heating Wurzel and Hsu [2022].

Specifically focusing on Q_{sci}^{MCF}, the plot on the right axis depicts its variation concerning ion temperature and Lawson's criteria. Notably, several experiments exhibit $Q_{sci}^{MCF} > 10^{-4}$, and the collective objective is to attain Q_{sci}^{MCF} of at least 10. This target implies achieving ten times more output energy compared to the input energy. Figure 1.3 suggests that ITER and SPARC are anticipated to reach this benchmark. As of 2022, the National Ignition Facility (NIF) is the only facility that has achieved $Q_{sci}^{MCF} > 1$. In other magnetic confinement experiments such as JET and JT-60U, equivalent Q_{sci}^{MCF} values of 1 have been reached Pitts et al. [2006], Wurzel and Hsu [2022].

ITER aims to achieve a fusion power gain (Q) of 10 – indicative of reactor-level conditions – by 2035, generating 400 MW of energy for a few minutes with a plasma volume of 800 m^3 Aymar et al. [2002], Pitts et al. [2006], Mlynar [2007]. This signifies that the output from the ITER experiment would be ten times greater than the input power. Theoretically, in the future, a nuclear fusion-powered plant could achieve $Q_{sci}^{MCF} = \infty$ Pitts et al. [2006].

1.3.2 Types and Modes of Plasma Confinement

To achieve a nuclear fusion-powered plant, one main focus is to improve the confinement time in the triple product. There are six different ways to confine plasma: confinement by Radio Frequency (RF) fields, electrostatic fields, solid walls, gravity, inertia, and magnetic fields Dolan [1982].

Solid wall confinement can be used to confine low-temperature plasma such as glass discharges in a fluorescent tube light. A disadvantage of this configuration is that the solid surface is in direct contact with the wall and hence would overheat the wall and quench the plasma. Confinement by gravity is how the sun in our solar system sustains plasma. However, laboratory plasma is far too small to create and

sustain plasma by self-gravitational forces. RF fields and electrostatic fields can both sustain plasma that has low temperatures. RF field, however, requires an enormous amount of power to create plasma and cannot reach the desired value of Q = 10 value. The electrostatic field can create high plasma density at some localized location but cannot uniformly heat plasma throughout the system and hence is used for small-scale plasma generators Dolan [1982].

The fusion research community today focuses on two major types of plasma confinement: inertial confinement (ICF) and magnetic confinement (MCF) LLNL [2020], Dolan [2013], Wynn [2017]. ICF works on the principle of compressing and heating the hydrogen isotopes using powerful laser beams to produce fusion. There are two types of approaches to ICF: direct drive and indirect drive LLNL [2020]. Each ICF types show some promise to be used as a nuclear fusion energy source. However, it comes with many technical difficulties, such as the requirement of high density Dolan [2013], non-uniform heating, asymmetrical implosion, and uniform firing rate of all the laser at once, to name a few Wynn [2017]. A promising way to confine plasma is by magnetic fields called the Magnetic Confinement Fusion (MCF).

Magnetic Confinement of Fusion (MCF)

In MCF, a strong magnetic field binds plasma as a result of the Lorentz force. The charged particle follows a corkscrew / helical path around the magnetic field line. The motion of the charged particle can be described in two ways: circular and linear. The circular motion of the charged particle is denoted by its radius of gyration (also known as Larmor radius), $r_L = v_\perp/\omega_c$ where '$v_\perp$' is the perpendicular component of its velocity and 'ω_c' is the angular cyclotron frequency. $\omega_c = q_p B/m$ where, 'q_p' is the charge of the particle, 'B' is the magnetic field strength, and 'm' is the mass of the charged particle. The linear motion of the charged particle is characterized by its parallel velocity '$v_\parallel$' along the magnetic field line. Since the mass of an electron is much smaller than an ion, the angular cyclotron frequency of an electron will be

higher compared to that of an ion, and hence its Larmor radius will be much smaller Ongena et al. [2016].

The simplest method for plasma confinement involves the utilization of two magnets to create a 'magnetic bottle,' also known as a Helmholtz coil. In this arrangement, the concern arises that the plasma could escape from the ends of the 'bottle.' To address this issue, two stronger magnets were introduced at the ends of the 'bottle' to effectively retain the plasma inside Dean [2013]. This confinement setup, known as magnetic mirror confinement, was first developed in the 1950s at Lawrence Livermore National Laboratory by R. Post and his colleagues Post [1956]. The design of the magnetic mirror aimed to reflect the plasma towards the center of the magnetic bottle. However, some plasma particles with higher $v_{\parallel}$ and elevated energies would inevitably exit the bottle. Consequently, this approach did not gain widespread acceptance over the years, primarily due to losses at the bottle's ends and the ensuing instabilities Ongena et al. [2016].

The next logical progression in the effort to confine all plasma particles within the magnetic bottle involves connecting the ends of the bottle to create a toroidal shape Ongena et al. [2016]. Presently, there are two primary types of toroidal magnetic confinements: the stellarator and the tokamak. Wendelstein 7-X, the most successful optimized superconducting stellarator, is designed with high-iota, low shear, an optimized magnetic field geometry, and a plasma volume of 30 m^3. It aims to demonstrate the steady-state generation and confinement of fusion-relevant hydrogen and deuterium plasmas. The Wendelstein 7-X has a major radius (R) of 5.5 m, a minor radius (a) of 0.5 m, and a plasma volume of 30 m^3, as detailed in Boozer [2009], Nührenberg and Zille [1986]

Plasma densities in the stellarator range from 1 to 4.5×10^{19} m^{-3}, with central electron temperatures oscillating between 5 and 10 keV. Through hydrogen pellet injection and helium gas fueling, the stellarator achieved plasma densities of up to 1.4×10^{20} m^{-3} Craig Beidler and Wobig [1990]. It exhibits $nT_i(0)\tau_E = 6.4 \times 10^{19}$ keV s m^{-3}, a peak diamagnetic energy of 1.1 MJ, and a volume-averaged normalized

plasma pressure $\langle\beta\rangle = 1.2\%$ Klinger et al. [2016, 2019]. Despite its advantages, the stellarator faces technological and engineering challenges that have impeded its success compared to the tokamak.

The Tokamak

The tokamak is a toroidal apparatus symmetrically arranged around its axis ϕ (refer to Figure 1.4), featuring a substantial toroidal magnetic field, a minor toroidal current, and a relative plasma pressure. Figure 1.4 illustrates a typical contemporary tokamak schematic. The tokamak design includes four crucial electromagnet structures vital for plasma confinement: (1) toroidal field coils (depicted in blue) that generate the toroidal magnetic field (represented by a blue arrow); (2) inner poloidal field coils, also known as the ohmic transformer (displayed in green), which induces plasma electric current (illustrated by a green arrow) essential for ohmic heating and plasma equilibrium; (3) outer poloidal field coils (shown in gray) utilized are balance coils for the plasma pressure control. As shown they are the vertical field coils; and (4) vertical field coils (not depicted) employed to counterbalance toroidal forces. Theiler [2011], Stangeby [2000], Freidberg [2007].

The poloidal and toroidal field coils generate a helical magnetic field (shown as black lines) with each field line being nested on top of each flux surface. Safety factor, 'q', is a measure of the safety of a device in terms of magnetohydrodynamic (MHD) stability and is defined as $q(r) \approx rB_\phi/R_0B_\theta$, where 'r' is the radius of the plasma, 'R_0' is the radius of the device, 'B_ϕ' is the toroidal magnetic field, and 'B_θ' is the poloidal magnetic field. Do note; this is safety for the machine in terms of plasma stability Theiler [2011], Stangeby [2000], Freidberg [2007].

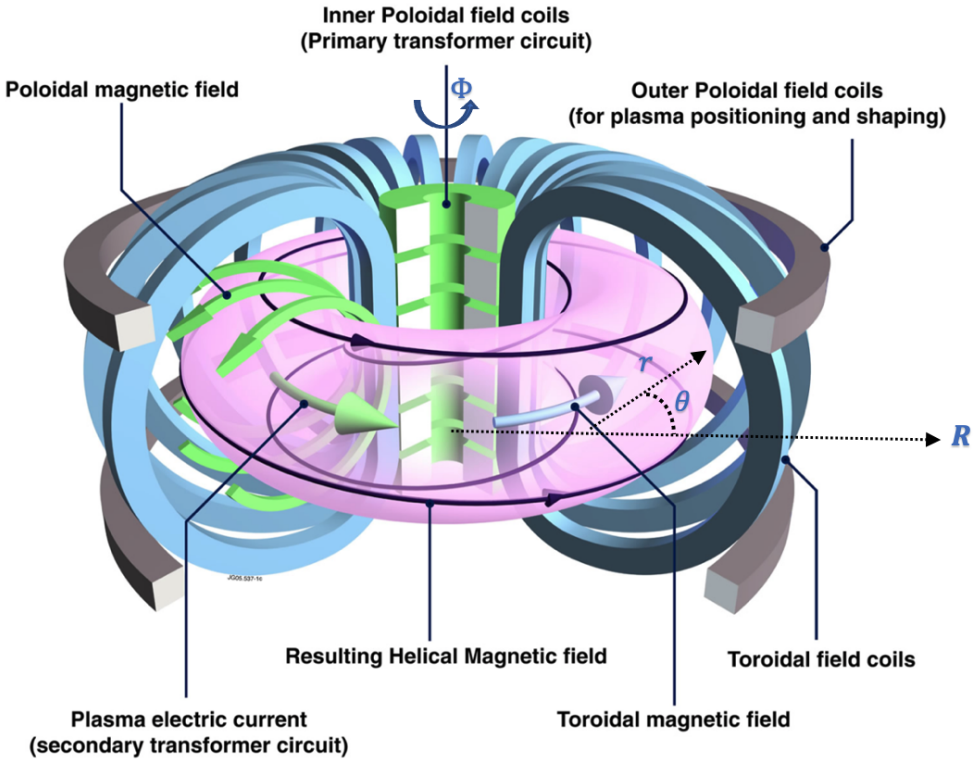


Figure 1.4: A schematic of a tokamak device showcasing the toroidal and poloidal magnetic field coils and resulting current and magnetic field

Modes of Confinement in a Tokamak

One of the main challenges for magnetic confinement is to increase the confinement time of the tokamak device and to understand and reduce the plasma transport losses. Before 1982, tokamaks operated in Low confinement mode (L – mode) where the pre-ionized gas was heated with just ohmic heating Keilhacker [1987] and/or neutral beams. However, in 1982, a high confinement mode (H–mode) was discovered in ASDEX Wagner et al. [1982], where the plasma confinement time was 2 – 3 times higher than the L-mode Keilhacker [1987]. This was later observed in other tokamak experiments such as JET and DIII-D Tanga et al. [1987].

H-mode plasmas are distinguished by the presence of an edge transport barrier (ETB) located in a narrow edge region within the last closed flux surface (separatrix). Within this ETB, ion transport is reduced to levels similar to those predicted by neoclassical transport, leading to the development of steep gradients in both temperature and density profiles. Consequently, these profiles rise sharply within the separatrix, causing a corresponding increase in the plasma core. The resulting profiles resemble those observed in L-mode (seen for input power below a specific L→H threshold) but are displaced upward by a pedestal. Figure 1.5 illustrates typical radial pressure profiles for L-mode and H-mode confinement Lang et al. [2013]. The pedestal height impacts the fusion power and gain of tokamak devices Kinsey et al. [2011]. H-mode profiles are characterized by steep gradients at the pedestal, and the height of this pedestal plays an important on the fusion power gain of plasma devices. Over the years, fusion scientist has developed theories to better understand H-mode stability. These have allowed even better than H-mode confinement (Super-H) and are promising avenues toward building a more efficient tokamak fusion reactor. This has been successfully implemented on DIII-D Solomon et al. [2014].

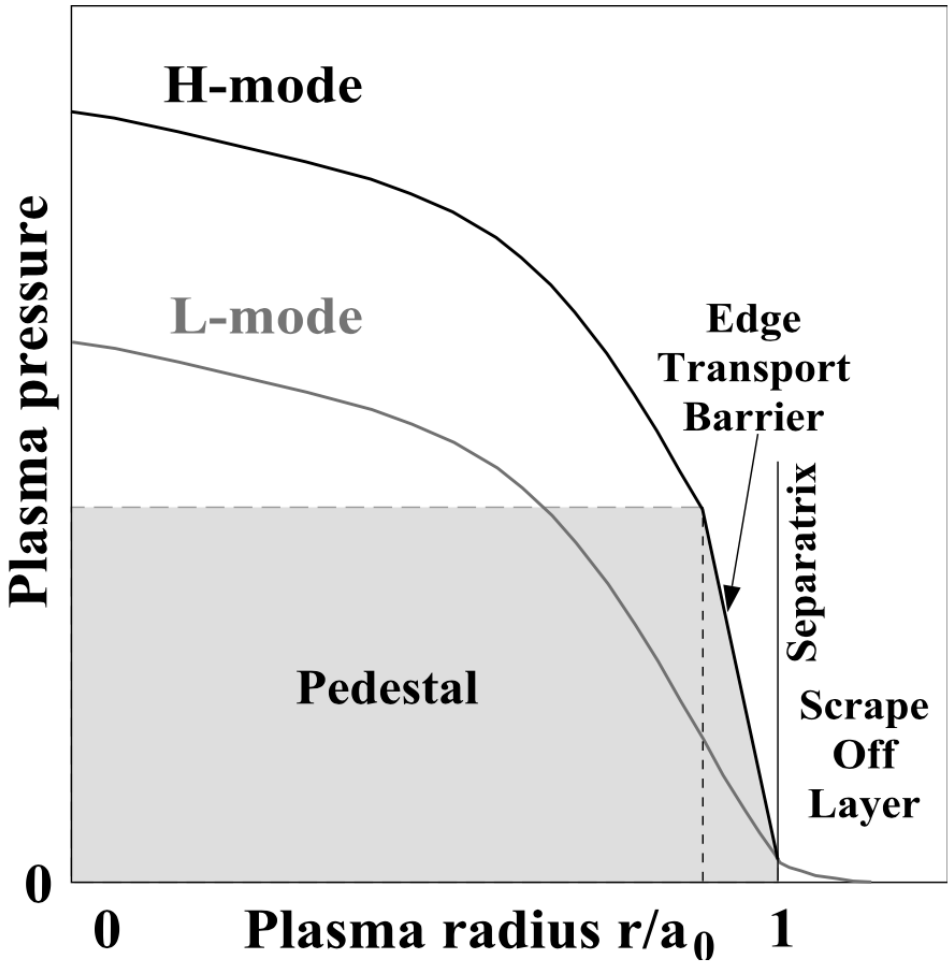


Figure 1.5: Pressure profiles typically observed during L- and H-mode phases reveal distinctive characteristics. The establishment of a transport barrier just inside the separatrix introduces a pronounced gradient at the edge leading to a pedestal. Image from Lang et al. [2013]

1.3.3 Tokamak Terminology

The tokamak is comprised of nested magnetic surfaces known as closed flux surfaces, with magnetic field lines (illustrated as black lines in Figure 1.6(a)) situated above them. The outermost closed flux surface interacts with the first wall in the vacuum vessel, resulting in elevated heat loads on the wall due to the plasma flow along the closed flux surface. To mitigate plasma-material interaction (PMI), modern tokamaks have incorporated two configurations: a limiter configuration and a divertor configuration.

Limiter versus Divertor Tokamak

In a tokamak with a limiter, a constraining/limiting object is installed within the plasma chamber, intersecting the enclosed magnetic flux surfaces as illustrated in figure 1.6(a). This object establishes the outermost closed flux surface, represented by the dashed line. Consequently, it divides the plasma volume into two distinct regions: an inner area, characterized by enclosed magnetic flux surfaces (depicted in dark grey), and the scrape-off layer (SOL, shown in light grey), featuring short open field lines terminating on the limiter surface.

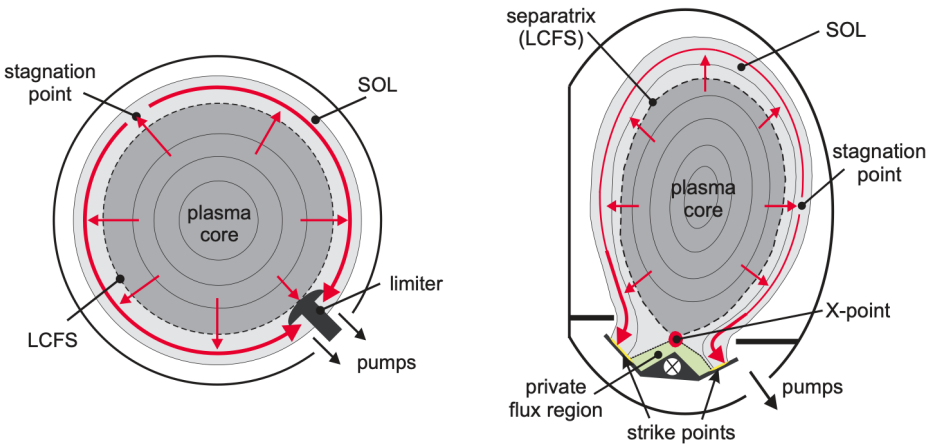
The transport mechanisms for particles and heat vary fundamentally in these two regions. Cross-field transport is the primary mode for particles and heat moving from the plasma core, traversing the Last Closed Flux Surface (LCFS) into the SOL. Within the SOL, parallel transport along open field lines takes precedence, rapidly directing particles and heat toward the limiting surfaces. This concentration of plasma-surface interaction on relatively small surfaces necessitates the ability to withstand localized, intense thermal fluxes. The sputtering of surface material by impinging plasma particles results in the contamination of the plasma by the plasma-facing material. To mitigate excessively high power flux densities on the limiter, the plasma-wetted area is increased which is achievable through appropriate shaping of the limiter. Previously, toroidal limiters were employed on fusion experiments with pumps for

effective helium ash removal. Furthermore, pump limiters facilitate improved control of plasma density. Due to the presence of a limiter, released impurities and recycled neutrals (recombined ions and electrons at the wall) may directly enter the main plasma, limiting the impurity screening capabilities. Therefore, it is advantageous to relocate the plasma-wall interaction zone as far as possible from the confined volume, aligning with the basic concept of the divertor configuration Spitzer [1958], Clever [2010].

A divertor configuration within a tokamak is established by introducing additional coils into the vacuum vessel. These coils redirect the outermost magnetic field lines away from the main plasma chamber, guiding them into a separate chamber where they intersect a material divertor target (refer to fig. 1.6(b)). Toroidal coils, carrying current in the same direction as the plasma current, create a poloidal divertor by forming a null in the net poloidal magnetic field, known as the X-point. The magnetic field lines passing through the X-point define the separatrix (represented by the dashed line), marking the last closed flux surface. Field lines within the separatrix remain confined within the plasma, confining particles on them. However, particles crossing the separatrix are carried along the field lines in the scrape-off layer (SOL) to the divertor target plates Clever [2010], Stangeby [2000].

The region struck by particles at the divertor target plates is termed the divertor strike point, while the area below the X-point, between the inner and outer divertor legs, is referred to as the private flux region. This region is isolated from the core plasma, shielded by the adjacent SOL plasma, which rapidly carries away particles flowing from the core toward the private flux region. The private flux region is predominantly populated by neutral particles originating from the divertor target plates, not bound to the magnetic field, resulting in a low plasma density Clever [2010], Krasheninnikov and Kukushkin [2017].

The geometry of the poloidal divertor can be more or less open or closed depending on the fraction of neutrals that can penetrate into the central plasma. Mechanical baffles near the X-point can stop neutrals, affecting the openness of the configuration.



(a) Limiter configuration **(b)** Divertor configuration

Figure 1.6: (a) Tokamak Limiter configuration with LCFS defined by the limiter structure. (b) Tokamak divertor configuration schematic depicting the various tokamak terminology depicting the ions in red arrows forming in the core and moving radially outwards. Image from Clever [2010]

Poloidal divertors have a relatively small plasma-wetted area, leading to high localized particle and heat fluxes. The advantages of the poloidal divertor configuration over the limiter configuration primarily include improved energy confinement and the generation of high neutral densities in the divertor region for enhanced pumping Clever [2010].

1.4 Overview of the DIII-D Tokamak

The DIII-D tokamak, first proposed in 1970s and completed in late 1980s, has the capacity to achieve plasma with current up to 2 MA. The DIII-D tokamak program was developed to improve scientific understanding of the high temperature plasmas that attains high performance and high confinement times (Luxon [2002]) (as of today, the DIII-D machine can contain high temperature plasmas up to 8 seconds).

A cross-section of the DIII-D tokamak is shown in Figure 1.7. As pointed out in the figure, there are three types of magnetic coils encompassing the DIII-D tokamak: the toroidal, ohmic and field shaping coil. (Luxon [2002]). The DIII-D tokamak is enclosed in a vacuum vessel that is sheathed with water cooled graphite tiles and divertor baffles. There are neutral beam heating systems that provides 16MW of deuterium power for at least 5 seconds. There is an Anti-torque structure to support the tokamak from overturning and twisting and eventually breaking down fur to the forces generated by the toroidal coils and their interaction with poloidal coil field and plasma. Overall, there are more than 50 diagnostics implemented on the DIII-D tokamak that provide temporal and spatial plasma parameter (Luxon [2002]).

DIII-D currently provides up to eight distinct divertor geometries. Among these, four conventional types include the Lower Single Null (LSN) with high triangularity on the floor (Figure 1.8(a)), LSN with low triangularity on the shelf (Figure 1.8(b)), Upper Single Null (USN) with high triangularity on the floor (Figure 1.8(c)), and USN Small Angled Slot (SAS) divertor Guo et al. [2019] (Figure 1.8(d)).

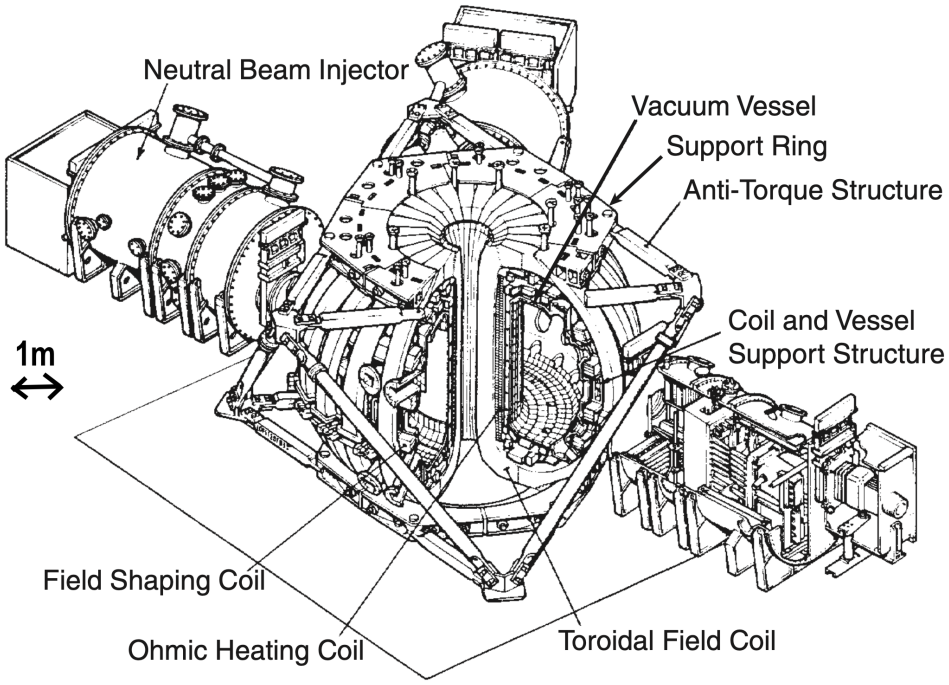


Figure 1.7: A cutaway schematic of the DIII-D tokamak. The image shows supporting structures used for the tokamak. Image from Luxon [2002]

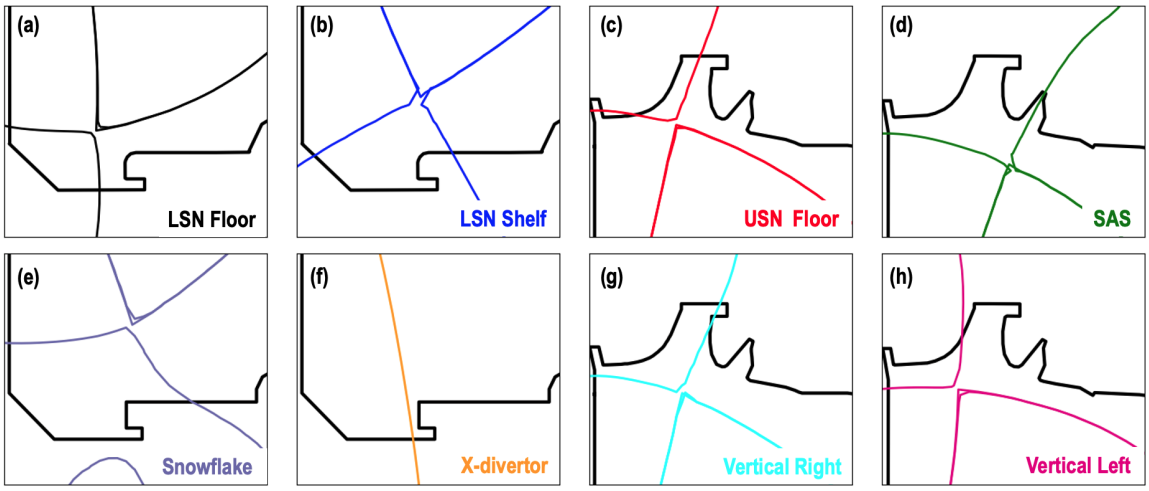


Figure 1.8: Types of divertor targets available in DIII-D. (a) LSN Floor, (b) LSN Shelf, (c) USN Floor, (d) SAS, (e) Snowflake, (f) X-divertor, (g) vertical right, and (h) vertical left

Three out of the four conventional divertor geometries, excluding SAS, provide various physical baffling options with accompanying pumping mechanisms designed to aid in density control and particle inventory control Maingi et al. [1999]. Additionally, DIII-D can operate in four non-conventional divertor configurations: the snowflake divertor Ryutov [2007], Kolemen et al. [2018], Cowley et al. [2023] (Figure 1.8(e)), x-divertor Cowley et al. [2023], Kotschenreuther et al. [2013] in the vertical right configuration (Figure 1.8(g)), and the vertical right configuration (Figure 1.8(h)). This is the reason DIII-D is chosen to answer the hypothesis questions with regards to the divertor closure.

To quantify neutral particle fluxes at the main chamber and at the divertor, there are three main things that needs to be observed: electron density and temperature from Thomson Scattering, Langmuir probes and the Deuterium Balmer emission from atomic spectroscopy - Filterscope. The following subsections will detail out the diagnostics utilized in this thesis to quantify neutral particle fluxes at the main chamber and at the divertor region.

Chapter 2

Tokamak divertor closure: fundamentals, measurements and modeling

This chapter delves into the foundational aspects of neutral dynamics within the tokamak. It comprehensively explores the nature and formation of neutrals, followed by an intricate examination of neutral measurements, recycling processes in both the divertor and main chamber regions. Subsequently, it delves into the impact of divertor design on recycling phenomena. The chapter also provides insights into the models employed within the fusion community to comprehend the intricate interplay between neutrals and the edge. Concluding the discussion, it presents a succinct overview of diagnostic tools employed in the DIII-D tokamak. The knowledge gleaned from these insights forms the basis for addressing the core thesis question, involving the analysis of magnitude of fluxes within the window frame and the quantification of neutral restriction within the divertor region through the utilization of the geometric restriction parameter.

2.1 Tokamak Divertor and SOL physics

The Scrape-Off Layer (SOL) as seen in Figure 1.6(b) can be effectively categorized through two distinct approaches: firstly, by considering particle transport and edge turbulence, resulting in subdivisions into plasma and sheath regions; and secondly, by examining density and temperature gradients, leading to a division into near and far SOL. But before delving into these classification, here the topics that are discussed in this section: fundamentals of the Simple SOL, The SOL 2-Point Model, the role of collisionality within the SOL, the significance of drifts in the SOL, physics regimes of tokamak divertors, and relationship between divertor regimes and SOL collisionality, offering valuable insights into the interconnected dynamics shaping the behavior of tokamak SOL and divertor plasma.

2.1.1 SOL particle transport and edge turbulence

In terms of charged particles and their effect in the tokamak SOL, the SOL can be divided into two major types: (1) SOL plasma; and (2) Sheath. The SOL plasma occupies the majority of the space and is quasi-neutral, i.e., $n_e \approx n_i$, the electron and ion density are the same, making the plasma electrically neutral. Whereas the sheath is a region of net charge and is usually a thin region closer to the wall surface where $n_e < n_i$. The sheath can be broken down into three parts: (1) Debye Sheath; (2) Magnetic Pre-Sheath (MPS); and (3) Pre-Sheath Stangeby [2000].

(1) The Debye sheath, or commonly called sheath, is a region where $n_e < n_i$ with a width of few Debye lengths

$$\lambda_{\text{Debye}} \equiv \sqrt{\frac{\epsilon_0 k T_e}{e^2 n}} \tag{2.1}$$

where, T_e is the electron temperature, n is the density of the electron and ions.

(2) The MPS, or commonly known as Chodura sheath, is quasi-neutral in nature and has a width of few ion Larmor radii ($\rho_i \approx \frac{m_i c_s}{eB}$), where B is the magnetic field, m_i is the mass of an ion and c_s is the sound speed Stangeby [2000]

$$c_s = \sqrt{\frac{kT_e + kT_i}{m_i}} \tag{2.2}$$

(3)The pre-sheath is also known as plasma. As mentioned, it is also quasi-neutral in nature, just like the Chodura sheath. The E-field is dominated in the Debye sheath compared to the B – field, as the width of the Debye sheath, is smaller than the ion Larmor radius. It is to note that ions entering the Chodura sheath has velocities higher than sound speed c_s.

There are three main consequences of the sheath. (1) The sheath cools down electrons faster than ions making the ion temperature in the SOL higher than the electron temperature. (2) The sheath increases the solid material sputtering. (3) The sheath strongly influences the tokamak edge properties as it acts as an electron well that does not have the electron density the same as the ion density Stangeby [2000].

2.1.2 SOL Density and temperature gradients

The community also divides SOL based off the density and temperature in the SOL. It can be divided into two regions: (1) near SOL and (2) far SOL. The near SOL region is characterized by the steep gradient of temperature and density near the separatrix, and the far SOL is characterized by the flatter temperature and density profile from the separatrix to the wall. In a schematic form, we can describe the near SOL region as to be between the LCFS and the red line in Figure 1.6(b) and the far SOL region is the SOL region between the red line and the wall.

The SOL exhibits turbulence in the form of bursts and has events that carry the plasma to the first wall with velocities greater than 100 ms^{-1} Loarte et al. [2007]. The cross-field particle transport increases in the far SOL with increase in density, which leads to an increase in PMI. The increase in PMI is stronger during transient events

such as Edge Localized Modes (ELMs) discharge in H – mode operation compared to L – mode operation. This is due to the fact that ELMs account for 30% – 90% of particle flux into the main chamber, depending on the discharge conditions and the cross-field fluxes that travel radially outwards in the far SOL lead to sputtering and production of neutral species Rudakov et al. [2005].

2.1.3 The Two-Point SOL Model

An intuitively simple model for SOL divides itself between two points: upstream (u) and target (t) (As seen in Figure 2.1). Upstream (u) refers to the point that is halfway between the two divertor targets (t) in a single null plasma configuration. The two points are represented in a flattened-out SOL Figure 10. It is noted that the divertor was developed to achieve lower temperatures in the SOL near the targets compared to upstream Stangeby [2000].

The two-point model defines three 'control parameters' by assuming particle, pressure, and power balance, as shown in Equation 2.3, 2.4, and 2.5. The model assumes that the target acts only as a particle sink, with no volume recombination, and the power flux density ($q_{\parallel}[Wm^{-2}]$) is carried by only conduction. The upstream and target density and temperature follow equation 2.3, as seen:

$$n_u\, T_u = 2\, n_t\, T_t \tag{2.3}$$

$$T_u^{7/2} = T_t^{7/2} + \frac{7}{2}\left(\frac{q_{\parallel} L}{\kappa_{0_e}}\right) \tag{2.4}$$

$$q_{\parallel} = \gamma\, n_t\, k\, T_t\, c_s\, t \tag{2.5}$$

Here, n_t and n_u represents density and T_t and T_u represents the temperature at the target and upstream respectively. $q_{\parallel}$ is the parallel power flux density with units $[Wm^{-2}]$ and L, γ, and κ_{0_e} are constants Stangeby [2000].

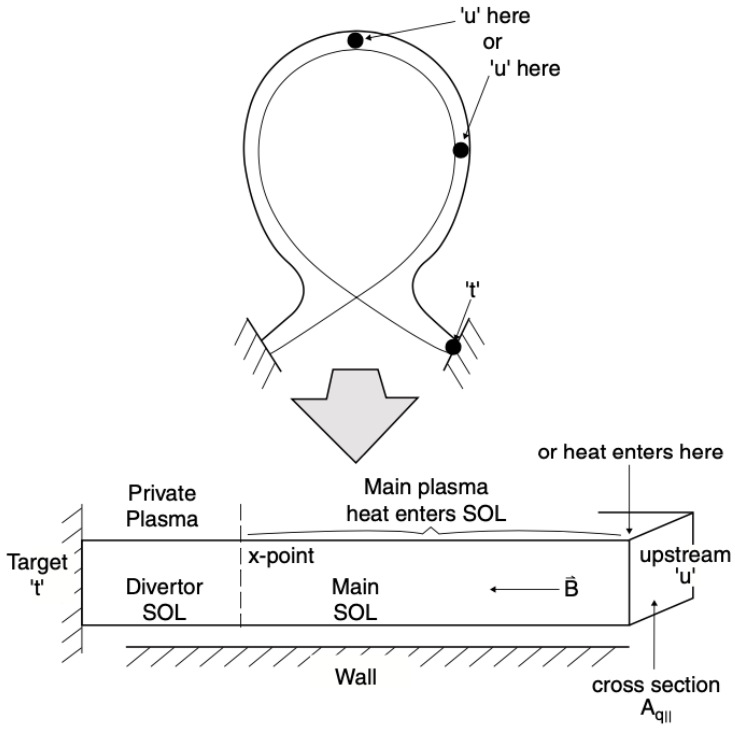


Figure 2.1: A flattened-out SOL from target T till the upstream location u. The length of this flattened SOL is of length L. Image from Stangeby [2000]

2.1.4 SOL collisionality regimes

Since the mass of an ion and mass of an electron are different, the temperature of ion (T_i) and electron (T_e) are different. When the plasma is said to be collisional, the temperature of ion tends to be similar to that of an electron ($T_i \rightarrow T_e$). The time taken for this process is called temperature equilibration time (τ_{eq}) given by Stangeby [2000]:

$$\tau_{eq} \approx 4.2X10^{13}\frac{T_e^{\frac{3}{2}}}{n_e} \tag{2.6}$$

As the τ_{eq} decreases, the collisionality increases, due to increase in density as seen by Equation 2.6. It is to note that $\tau_{\mathrm{eq}} \ll \tau_e^{\mathrm{SOL}}$, where τ_e^{SOL} is the SOL energy confinement time and is given by

$$\tau_e^{\mathrm{SOL}} \approx \frac{3L}{\gamma c_s} \tag{2.7}$$

Which gives

$$\frac{n_{\mathrm{LCFS}}L}{T_{\mathrm{LCFS}}^2} \gg 10^{18} \tag{2.8}$$

There are four different ways where the collisionality can force the transition from $T_i \rightarrow T_e$: Type A, B, C, and D. These four types of SOL are defined with respect to the temperature gradient and collisionality: Table 2.1 describes these SOLs Stangeby [2000].

But in order to understand the effect of temperature gradient on collisionality, we must define SOL collisionality ($\nu^*_{\mathrm{SOL},e}$):

$$\nu^*_{\mathrm{SOL},e} \equiv \frac{L}{\lambda_{ee}} \approx \frac{n_u L}{T_{eu}^2} \times 10^{-16} \tag{2.9}$$

$$\nu^*_{\mathrm{SOL},i} \equiv \frac{L}{\lambda_{ii}} \approx \frac{n_u L}{T_{iu}^2} \times 10^{-16} \tag{2.10}$$

when $T_i = T_e$,

$$\nu^*_{\mathrm{SOL}} \equiv \frac{L}{\lambda_{ee\,ii}} \approx \frac{n_u L}{T_u^2} \times 10^{-16} \tag{2.11}$$

where, λ_{ii} and λ_{ee} are the electron and ion self-collisionality lengths defined as

$$\lambda_{ee} \approx \frac{T_e^2}{n} \times 10^{16} \tag{2.12}$$

$$\lambda_{ii} \approx \frac{T_i^2}{n} \times 10^{16} \tag{2.13}$$

As seen in Table 2.1, Type A SOL is isothermal in nature where $T_i = T_e$ With no temperature gradient. With constant L, n_{LCFS}, and T_{LCFS}, equation 2.8 would give $\nu^*_{\mathrm{SOL},e} \gg 100$ whereas, on the other hand, from equation 2.9 and 2.10, $\nu^*_{\mathrm{SOL},e} \leq 10$. This is unlikely to happen, and hence type A SOL is not likely to exist. The other types of SOL – Type B, C, and D are depicted in Figure 2.2 with respect to the upstream electron temperature, density, and collisionality.

Type B type of SOL has a significant temperature gradient; however, it has $T_i = T_e$. This is possible only when $\nu^*_{\mathrm{SOL},e} \geq 50$. Hence type B SOL has strong collisionality. Type C SOL has no significant temperature gradient $\nabla_{\parallel} T = 0$ and has $T_e < T_i$. This is opposite to what is seen in Type B, i.e., it has weak collisionality ($\nu^*_{\mathrm{SOL},e} < 10$). Type D SOL has both a significant temperature gradient and has an unequal electron and ion temperatures. This type of SOL has intermediate collisionality as $10 \leq \nu^*_{\mathrm{SOL},e} \leq 50$. In this intermediate collisionality regime, the electron temperature gradient is significant compared to the ion temperature gradient, and the ion temperature near the target is greater than electron temperature at the target near the weak collisionality, whereas the ion and electron temperature at the target are similar to each other as the collisionality approaches to highly collisionality regime Stangeby [2000].

Table 2.1: Four different types of SOL defined with respect to its temperature (T) gradient and isothermal property

	No T-gradient	Significant T-gradient
$T_i = T_e$	Type A	Type B
$T_i \neq T_e$	Type C	Type D

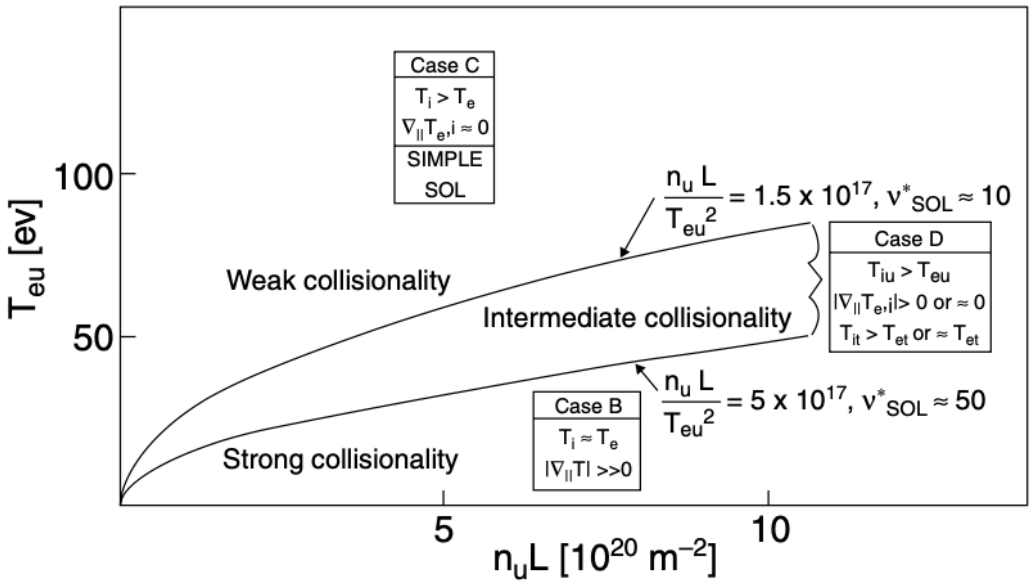


Figure 2.2: Different SOL collisionality regimes shown in simple SOL, and other SOL with varying temperatures - Details shown in Table 2.1. Image from Stangeby [2000]

2.1.5 A simple SOL

The simple SOL is characterized by (1) constant electron, and ion temperatures in each flux tube in the SOL; (2) electrons and ions are thermally decoupled; (3) No ionization occurs in the SOL, i.e., all the hydrogenic species are being ionized in the core plasma; (4) there is no volumetric recombination; (5) There is no neutral friction present in the SOL; and (6) The sheath acts as particle sink Stangeby [2000]. It is to note that the aforementioned near and far SOL does not come under the simple SOL approximation.

The most common way to understand the SOL in a diverted tokamak is by flattening it out, as shown in Figure 2.1. It neglects the toroidal magnetic curvature and neo-classical effects to help understand the parallel and perpendicular flows in the SOL. The flattened SOL has a length of 2L, where L is the connection length (defined as the length from divertor target to upstream SOL) and terminates at two divertor targets with width w. The top of the LCFS faces the core plasma, whereas the bottom of the LCFS faces the tokamak vessel walls. The coordinate w is perpendicular to the r direction and parallel to the B magnetic direction. The simple SOL attains particles only through cross-field diffusion, and the number of particles flowing from the core plasma towards the SOL through the LCFS is given by

$$\Gamma_{\perp} = -D_{\perp}^{\mathrm{SOL}} \left.\frac{dn}{dr}\right|_{\mathrm{LCFS}} 2L_w \,[\mathrm{particles}\, s^{-1}] \tag{2.14}$$

Where $D_{\perp}^{\mathrm{SOL}}$ is called the cross-field transport coefficient, which is empirically derived Stangeby [2000].

2.1.6 SOL Drifts

Recall, the toroidal field is denoted by ϕ and the poloidal field is denoted as θ in Figure 1.4. There are two main types of nomenclature that is used in tokamak physics. Normal Grad B X ∇B_{ϕ} and reverse Grad B X ∇B_{ϕ} drift. The normal

∇B_ϕ drift has the ions move towards the bottom, i.e., towards the target, whereas in contrast, reverse ∇B_ϕ has the ions move away from the bottom, i.e., towards the crown/upstream location of the tokamak. Figure 2.3 shows four different combinations of drift in a tokamak via a poloidal view and a toroidal view. The 'E X B' drift is affected by the electric and the magnetic field in the tokamak SOL. As seen in Figure 2.3, the ion drift because of B_ϕ is always on the inside leg of the divertor and the ion drift because of E_ϕ is always on the outside leg of the divertor Stangeby [2000].

There are two types of E x B drifts: (1) poloidal and (2) radial. The poloidal drift is due to the radial electric field, while the radial drift is due to the poloidal electric field along the SOL. The particle fluxes density due to poloidal E x B drift is defined as shown in Equation 2.15, and the particle fluxes density due to radial E x B drift is defined as shown in Equation 2.16 Stangeby [2000].

$$\Gamma_\theta^{dr} \approx \frac{3kT_e n}{e\lambda_{T_e} B} \tag{2.15}$$

$$\Gamma_r^{dr} \approx \frac{B}{B_\theta} \frac{nkT_{eu}}{eLB} \tag{2.16}$$

2.2 Physics regimes of the tokamak divertor

Figure 2.4 depicts the three main physics regimes of a tokamak divertor: Sheath limited (Figure 2.4(B)), Conduction Limited / High Recycling (Figure 2.4(C)), and detached (Figure 2.4(D)). To understand these physics regimes, let us consider a flattened-out SOL (Figure 2.4(A)) with magnetic field 'B' and heat flux $q_\parallel$, both of which are parallel to the first wall and the heat flux entering the SOL Q_{SOL} is perpendicular to the SOL. The density, n, and temperature, T, ranges from upstream u to the divertor target t on the x-axis.

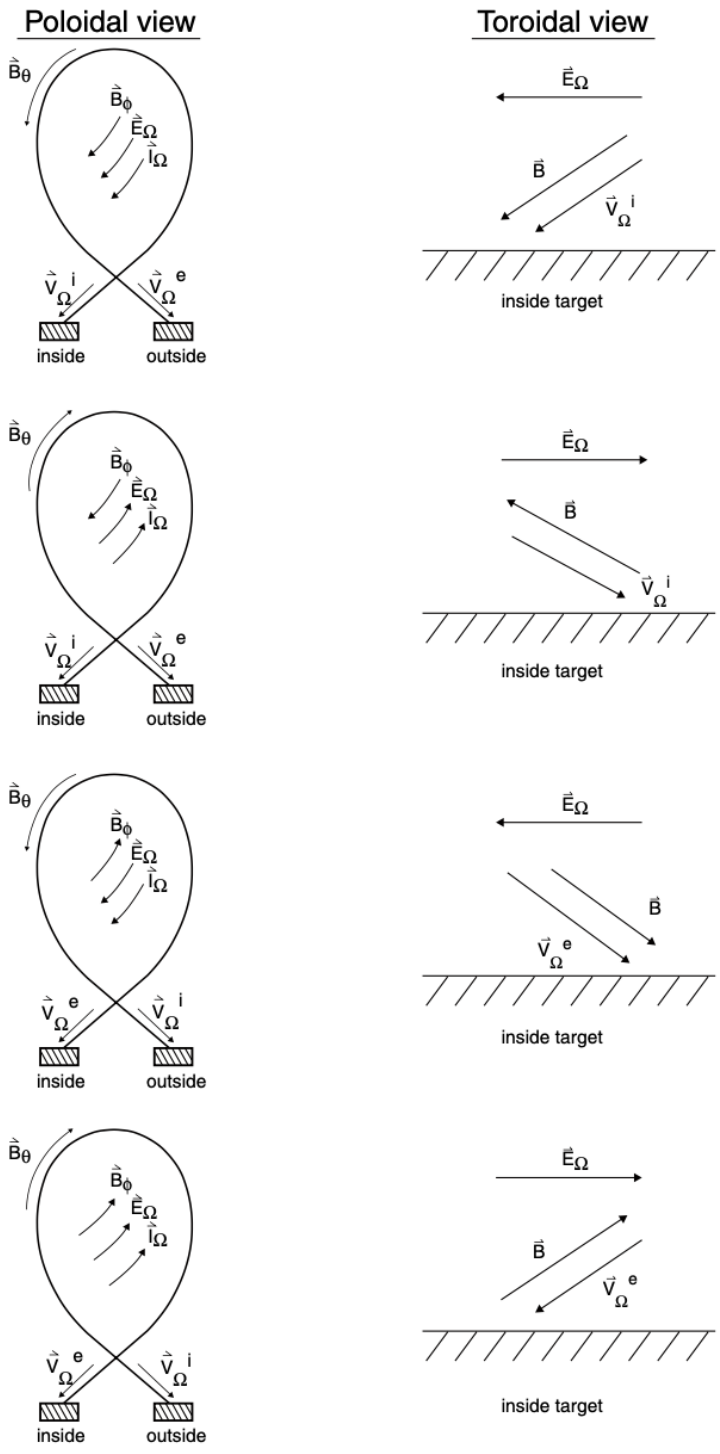


Figure 2.3: Depiction of various drifts in poloidal and toroidal magnetic field. Image from Stangeby [2000]

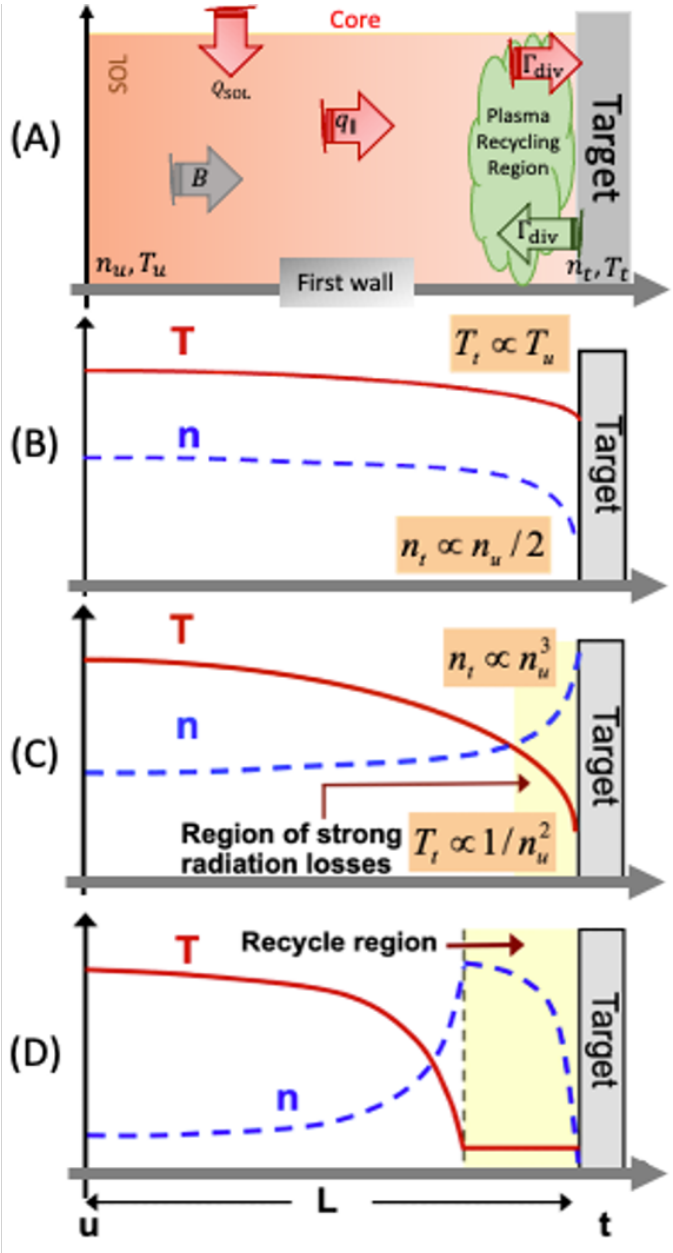


Figure 2.4: A cartoon depiction of the SOL along the connection length 'L'. (A) Flow of heat and particle fluxes in the SOL with the plasma recycling region near the divertor target. Variation of temperature and density profiles along the connection length are depicted in (B) Sheath limited (C) Conduction limited and (D) Detached regimes. Image adapted from Krasheninnikov [2018] and Pitts [2007]

Figure 2.4 displays the relationship between the upstream density n_u, target density n_t, upstream temperature T_u and target temperature T_t in the respective physics regimes. The following sub-sections explain the different physics regimes in detail.

2.2.1 Relationship between divertor regimes and SOL collisionality

Diverse divertor regimes, namely Sheath Limited, Conduction Limited, and Detached, are contingent on upstream temperature (T_u) and target temperature (T_t), which are, in turn, influenced by collisionality. The transition from the Conduction Limited regime to the Sheath Limited regime occurs when $\nu^*_{SOL} \approx 10$, while the transition to the Detached regime takes place when $\nu^*_{SOL} \approx 85$. As illustrated in Figure 2.5, analogous to Figure 2.2, the graph showcases upstream electron temperature values as functions of upstream electron density and connection length L. The data points from Langmuir probes on JET are displayed, with solid lines delineating the boundaries between different divertor regimes, and the red dotted line indicating the average trendline of the dataset. In summary, the relationship between SOL collisionality and divertor regimes can be encapsulated by the following generalizations: the Sheath Limited regime correlates with weak collisionality (Figure 2.2, top left part), the Detached regime is associated with high collisionality (Figure 2.2, bottom right part), and the Conduction Limited regime aligns with intermediate collisionality (Figure 2.2, central part).

2.2.2 Sheath Limited Regime - weakly collisional

Temperature drop along the connection length of the SOL is the main factor that differentiates different SOLs (simple vs. non-simple). The sheath limited regime is defined by the constant temperature along each flux tubes in the SOL, i.e. plasma is isothermal along each flux tube Stangeby [2000]. The Sheath limited regime is

defined by low density, high temperature and high power in SOL. In this regime, the target temperature is proportional to upstream temperature and the target density is proportional to half of the upstream density, as seen in Figure 2.4(B). This regime also has weak collisionality (upper left part of Figure 2.2) Pitts [2007].

2.2.3 Conduction Limited / High Recycling Regime - intermediately collisional

In the conduction limited/high recycling regime (Figure 2.4(C)), the collisionality rises, as the upstream density rises, and parallel temperature gradients rises. But since the pressure is maintained, the target temperature decreases, which makes the target density increase. As the target density is increased, the recycling in the target region increases, amplifying the particle flux in the process. As the target temperature decreases, the radiation loss increases, which decreases the target temperature even more. This is shown in Figure 2.4(C) the temperature and density profiles crosses path, making a region of strong radiation loss in the process Pitts [2007].

The recycling regime is the foundation for the SOL and divertor plasma. It comprises different types of neutral interaction (such as the plasma-neutral interaction, ion-plasma interaction, and neutral – neutral interaction), ionization of hydrogenic species, and plasma neutral interactions with the PFC Krasheninnikov and Kukushkin [2017]. Plasma density in the high recycling regime is $10^{15} m^{-3}$ with the mean free path of neutrals around 1 mm Krstic and Schultz [1999]. The high recycling regime of the divertor performance was theorized in the late 1960s Lehnert [1968] but was discovered around the same time as the discovery of the H model in a tokamak in the early 1980s Keilhacker et al. [1982], Lackner et al. [1984]. In the high recycling regime, neutrals deposit back onto the divertor target in the form of energetic ions many times before they have been pumped out, deposited on the PFC, or penetrated into the core. The highly recycled divertor is envisioned to be implemented in future tokamaks as it is characterized by low plasma temperature and

large plasma flux. This helps the divertor have a low sputtering yield from its PFC Krasheninnikov and Kukushkin [2017].

There are two types of recycling regimes: (1) high recycling and (2) low recycling. Recycling conditions are described by the ratio of total plasma flux to the PFC of the divertor and walls (Γ_{div}) to the plasma flux entering SOL from the plasma core (Γ_{SOL}). If $\Gamma_{div} > \Gamma_{SOL}$, the recycling regime is labeled as low recycling and when $\Gamma_{div} \gg \Gamma_{SOL}$, the recycling regime is termed as high recycling regime. A cartoon is shown in Figure 2.6 depicting the Γ_{div} and Γ_{SOL} in a tokamak divertor.

In a high recycling regime, the neutrals (shown in green in Figure 2.6) ejected from PFC ionize close to the target. Since the open magnetic field brings the ions back to the divertor target, the newly ionized particles bombard onto the divertor, making the divertor highly recyclable. High recycling conditions lead to a significant increase in particle flux on to the divertor and, in turn lead to changes in energy transport in the upstream and downstream SOL Krasheninnikov and Kukushkin [2017]. Hence high recycling conditions are preferable for the divertor.

During the ionization process in the recycling regime, there is an interaction between old neutrals and newly ionized electron-ion pairs resulting in a transfer of energy from the newly ionized to the cold old neutrals. Due to this, plasma flux (Γ_{div}) increases towards the divertor while the temperature on the divertor target T_t decrease. This leads to decrease in heat flux on the target ($q_{\parallel}$) while the heat flux coming into the SOL from the core (Q_{SOL}) increases. The plasma energy transported from SOL to the divertor target changes from being convective in nature in a low recycling regime to conductive in nature in a high recycling regime Mahdavi et al. [1981], Krasheninnikov [2018].

To reiterate, a high recycling regime is good as there is a fast flow of plasma on the divertor targets along the magnetic lines that encourage the recirculation of plasma. Plasma flow near the magnetic sheath must satisfy the Bohm criteria – given by Stangeby [2000]:

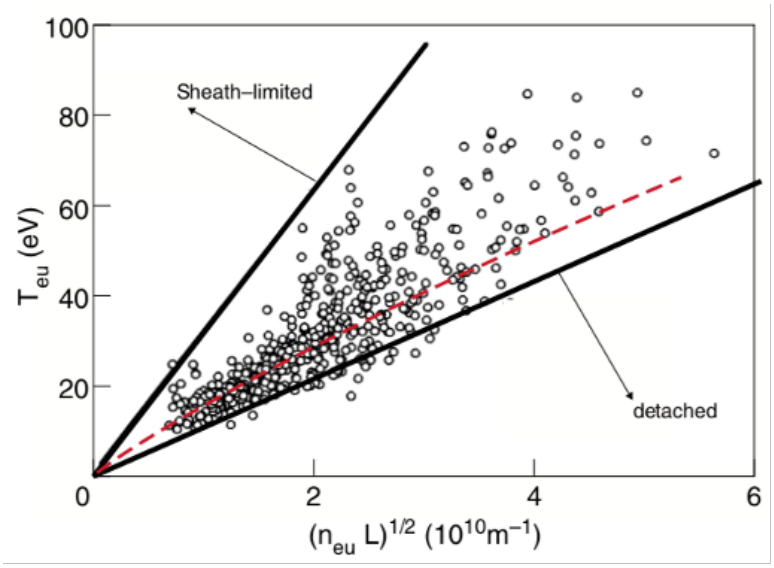


Figure 2.5: Langmuir probe data points showing upstream electron temperature as a function of upstream electron density and its connection length on JET. Solid lines show the boundaries between different divertor regimes, and the red dotted line indicates the average trend line of the dataset

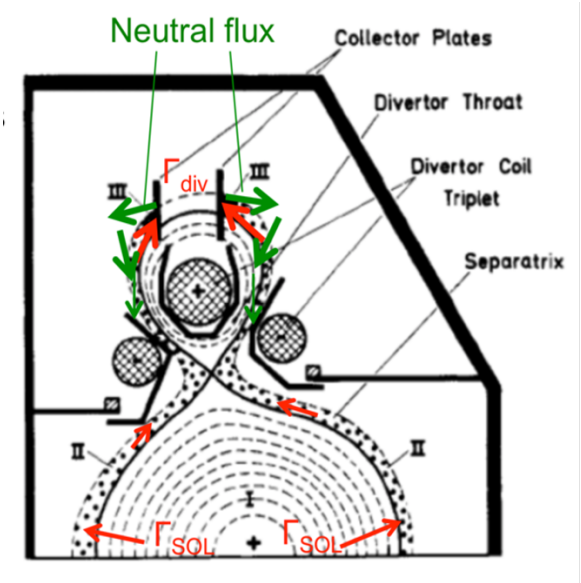


Figure 2.6: Schematic depiction of a high recycling regime pin-pointing the neutral, divertor and plasma flux in a typical tokamak divertor. Image from Krasheninnikov [2018]

$$\int_0^\infty \frac{f_{se}^i(v)dv}{v^2} \leq \frac{m_i}{kT_e} \tag{2.17}$$

Where $f_{se}^i(v)$ is the ion velocity distribution at the edge of the sheath, v is the velocity component perpendicular to the PFC, m_i is the ion mass and T_e is the electron temperature Krasheninnikov and Kukushkin [2017]. When the plasma velocity is greater than the square root of the ratio of T_e and m_i, there is a non-oscillatory evolution of the electrostatic potential within a Debye length (length at which the electrostatic potential is shields the PFC from the plasma) distance from the PFC Stangeby [2000]. This leads to instability which is weak in nature and can be stabilized easily by warming the plasma.

As mentioned earlier, the plasma – neutral interaction effects the divertor detachment. In a high recycling divertor, plasma recycling occurs due to the following conditions: (1) Production of neutrals from the divertor PFC and subsequent volumetric recombination due to the neutralization. (2) Ionization of the neutrals formed and (3) availability of power to maintain the ionization process Krasheninnikov and Kukushkin [2017]. This regime has intermediate collisionality (central part of Figure 2.2).

2.2.4 Detached Regime

When both heat and particle fluxes are reduced in the divertor region, Krasheninnikov and Kukushkin terms this as the ultimate divertor detachment Krasheninnikov and Kukushkin [2017]. However, the term ultimate divertor detachment and divertor detachment will be used interchangeably through this document. When there is an increment in the impurity radiation loss along with an increase in the plasma density in the divertor and the SOL, the plasma temperature reduces at the divertor and the target $< 5eV$. This in turn strongly reduces physical sputtering. At lower target temperatures, the ionization rate of the neutrals is lower than the charge exchange processes and recycling increases. Due to which the density at the target begins to

reduce and the plasma pressure falls across the recycling region as seen in Figure 2.4(D). Once the target temperature reduces below 1-2 eV, volume recombination process 'extinguishes' the plasma, and reduces the target power flux and reaching the 'detached' state Pitts [2007].

Although, in high recycling regimes, the edge plasma density increases leading to an increment in the particle flux at the divertor target Krasheninnikov et al. [2016]. This increment increases the ion recombination at the target surface making the heat load on the divertor exceed the 10 MW/m^2 material limit as proposed for an ITER scale reactor Basis [1999]. To decrease this heat load on the divertor target, the only possible way is to decrease the incoming particle flux. This is achieved by increasing the edge plasma density further more than previously inputted, leading to a 'detached divertor regime' Krasheninnikov et al. [2016]. It is characterized by the rollover of the plasma flux on to the target by increased edge plasma density Loarte et al. [1998] supplemented by large pressure drop and low plasma temperature at the target as shown in Figure 2.7 Basis [1999]. Figure 2.7 shows the loss in plasma pressure and target temperature as the electron density is increased in upstream and divertor target with respect to ρ (x – axis in terms of plasma coordinates) in Alcator C-MOD. As seen in Figure 2.7, the pressure and temperature in a sheath limited regime would drop after 15mm in ρ, whereas, the pressure and temperature would drop at 5mm in the detached conditions with density kept constant Basis [1999].

In the detached divertor regime, the plasma is virtually quenched before reaching the divertor leading to lowered heat and particle fluxes on the divertor target PFC. Radiation loss due to the presence of impurities, the plasma–neutral interaction and volumetric recombination in the divertor region led to a detached divertor. In H-mode operation, there is energy and particle loss due to ELMs that can produce high heat flux incoming from the plasma core to the SOL (Q_{SOL}) that can burn through detachment Basis [1999]. Radiation loss due to impurity production also creates thermal instabilities that link to loss of detachment Krasheninnikov and Kukushkin [2017].

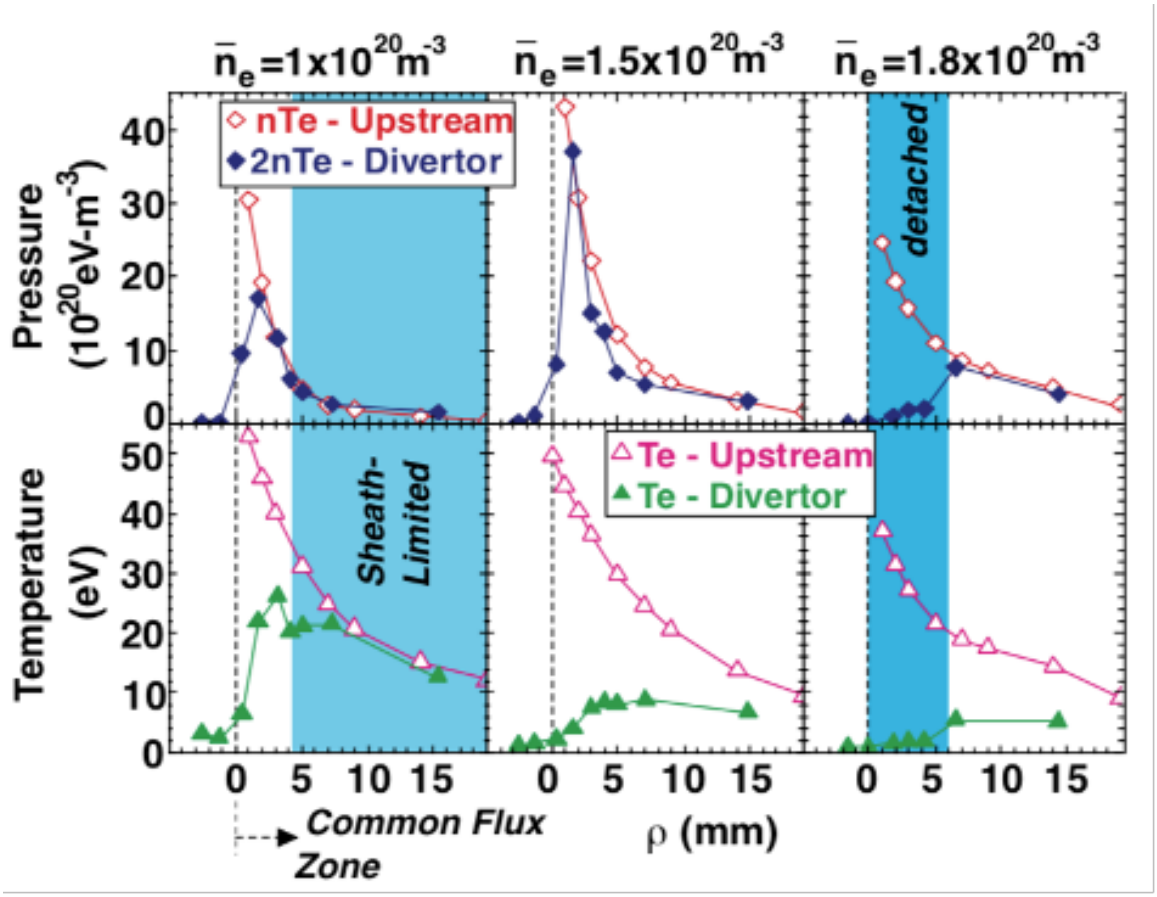


Figure 2.7: Increase in plasma density from left to right in the figure leading to loss in plasma pressure and target temperature (green and blue data sets) showcasing the sheath-limited temperature transitioning to detached divertor. Image from Basis [1999]

2.3 Divertor closure, leakage and design

2.3.1 How are neutrals formed and measured?

Recall, two out of the four ways D – T reaction occur are depicted in Equations 1.2, and 1.3 in Section 1.3. It is seen that the reaction produces an energetic neutron that is produced during the fusion of D – D and D – T reactions. When the energetic electrons, and the other plasma particles such as ions interact with the material surface, a neutral hydrogen atom (will be referred to as '*neutral*') is formed Stotler et al. [2017] and this process is called as recycling. There are several other ways a neutral is introduced in the plasma such as: neutral gas puffing, neutral beam injection, and pellet injection Dey et al. [2019].

Recycling refers to neutrals and other ions released from the PFC by various PMI processes Stotler et al. [2017] as shown in Figure 2.8. It shows various recycling reactions at the PFC, such as neutral back-scattering, adsorption, dissociation, ionization and resonant charge exchange.

The rate at which the aforementioned reactions occur can be seen in Figure 2.9. It shows the reaction rate coefficients for atomic and molecular hydrogen in seven different processes. (1) $e^- + H_2 \rightarrow H_2^+ + 2e^-$ shows the ionization process, (2) $e^- + H_2 \rightarrow 2H^0 + e^-$, shows the Franck-Condon dissociation by electron impact, (4) $e^- + H_2^+ \rightarrow 2H^0$ depicts the thermal release of molecule, (3) $e^- + H_2 \rightarrow H^0 + H^+ + 2e^-$ and (5) $e^- + H_2^+ \rightarrow H^0 + H^+ + e^-$ depict ionization process of hydrogen molecule, (6) $e^- + H^0 \rightarrow H^+ + 2e^-$ and (7) $H^0 + H^+ \rightarrow H^+ + H^0$ depict the resonant charge exchange process. As shown in Figure 2.9, it is evident that Equation (7) exhibits the highest cross-section across all electron and ion temperatures on the x-axis of the plot. Equation (7) specifically represents charge exchange (CX), signifying the exchange of charge between a neutral particle and an ion during their interaction. The graphical representation in Figure 2.9 indicates that the rate of charge exchange is notably higher when compared to other reactions.

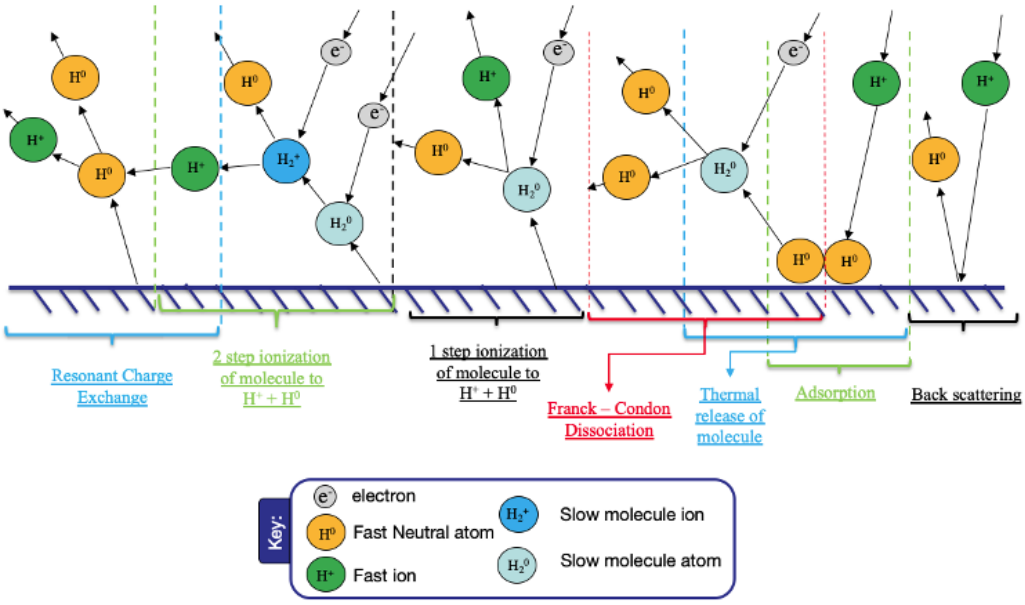


Figure 2.8: Cartoon depicting various PMI processes occurring in the SOL. Adapted from Stangeby [2000]

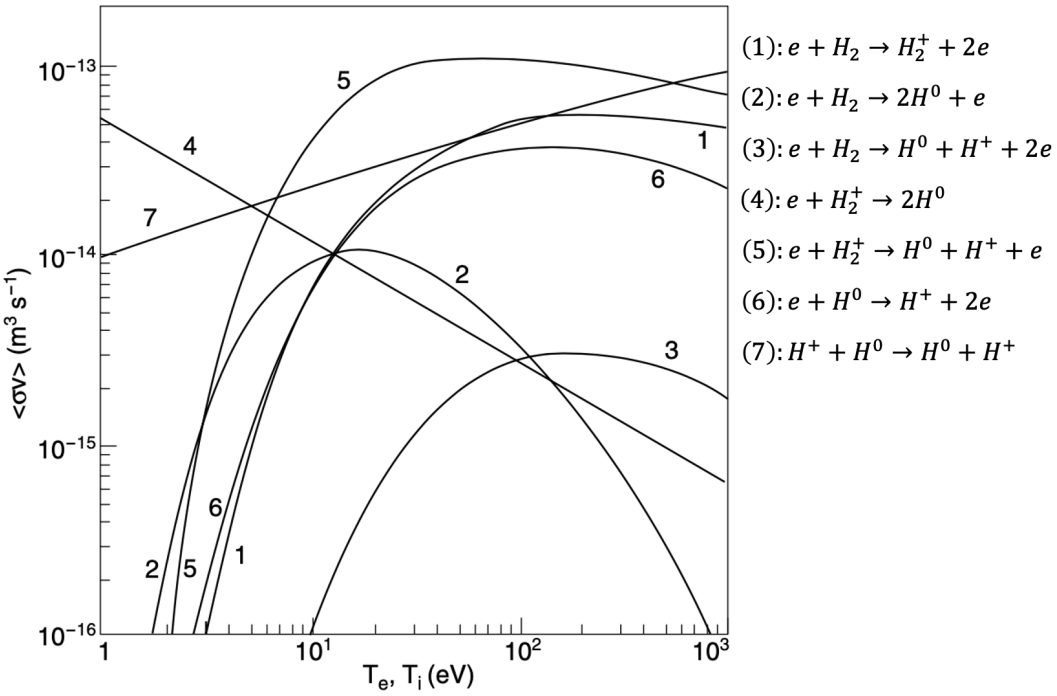


Figure 2.9: Reaction rate coefficients on Hydrogen in both atomic and molecular state. Image from Stangeby [2000]

However, it is crucial to emphasize that charge exchange between a neutral and an impurity ion does not occur due to the lower density of the impurity compared to the neutral in typical tokamak experiments Stangeby [2000]. Neutrals play a role in achieving H-mode as they can help in the pedestal formation Boivin et al. [2000]. Neutrals also increase the plasma density during the L-H mode transition in a tokamak when there is an increment in neutral density in the SOL. This increase leads to opaque plasma and decrease in neutral penetration Carreras et al. [1998].

In general, there are two types of neutrals produced from the PMI processes: (1) Reflected neutrals and (2) thermal neutrals. Reflected neutrals produced from the PFC travel back to plasma volume instantaneously. Thermal neutrals are produced by thermal desorption and can have some time dependencies. While many thermal neutrals travel back to plasma radially outwards, some neutrals deposit into the PFC by diffusion. This is the reason there is a constant need to refuel the plasma in a tokamak Krasheninnikov and Kukushkin [2017].

The fusion plasma consist of hydrogen isotopes (H, D, or T), which in a quasi-steady state has electron densities of 10^{13}–$10^{14}\,cm^{-3}$ and electron temperatures up to 10 keV in the center of the plasma core. All of these fueling sources and impurity ions emit photons at a particular wavelength, which can be measured using spectroscopic approaches. These emitted photons can provide the following information: (1) ion temperatures and velocities; (2) concentration of impurities in the plasma; (3) effect of the impurities on the fueling source; (4) understanding of impurity production; and (5) operating scenarios of the plasma. Spectroscopic techniques utilize accurate atomic data (such as transitional probabilities, rate coefficients for excitation, ionization, recombination, and charge exchange) to infer the intensities of the atomic species Denne [1989].

Understanding the Electromagnetic Radiation

The determination of rate coefficients and cross sections for various processes within a plasma constitutes an entire subfield of physics, which I will not delve into extensively

here. However, for the present requirement, particularly with hydrogen plasma in consideration, the rate coefficients have been consolidated as Photon Emissivity Coefficients (PEC) for each collisional process. These coefficients are accessible in atomic databases such as ADAS. Henceforth, in this document, the terms 'PEC' and rate coefficients $\langle \sigma_{ik} v \rangle$ will be used interchangeably. The primary focus of this document is on neutrals produced from Balmer hydrogen.

From a spectroscopic perspective, there are three things a spectrum should have: (1) The line of interest should have high intensity and should be unblended, (2) the line should have longer wavelength; and (3) the relevant atomic cross section data should be available Denne [1989]. In order to understand the spectrum, we must understand the radiation coming from an atom with an electron.

Consider two energy levels of transitions: 'i' and 'k,' where 'i' represents the upper/higher energy level, and 'k' is the lower energy level. Any electron capable of completing a transition from '$i \rightarrow k$' can do so through three mechanisms: (1) an electron may decay from an upper energy level 'E_i' to a lower energy level 'E_k' by emitting a photon in the process, with a frequency of 'ν_{ik},' i.e., $h\nu_{ik} = E_i - E_k$. The likelihood of this spontaneous transition occurring in unit time can be denoted by 'A_{ik}'. (2) An electron in the lower energy level could absorb an incoming photon, leading to excitation to an upper energy level, contingent on the probability of absorption per unit time '$B_{ki}\rho(\nu_{ik})$'. 'B_{ik}' is a function of the energy density per unit frequency of the electromagnetic radiation at the atom, denoted by '$\rho(\nu_{ik})$'. (3) A radiation-induced decay from 'E_i' to 'E_k,' with the probability of this event occurring being '$B_{ki}\rho(\nu_{ik})$' Hutchinson [2002].

The terms 'A_{ik}', 'B_{ki}', and 'B_{ik}' are called the Einstein Coefficients and can be defined as:

$$A_{ik} = \frac{8\pi h \nu_{ik}^3}{c^3} B_{ik} \tag{2.18}$$

$$g_k B_{ki} = g_i B_{ik} \tag{2.19}$$

$$B_{ik} = \frac{8\pi^3}{3h^2(4\pi\epsilon_0)} \mathcal{LS}_{ik} \tag{2.20}$$

Where, c is the speed of light, g_k and g_i represent the number of states in the k-th and i-th levels respectively, and $\mathcal{LS}_{ik}$ is the line strength dependent on the atomic dipole moment. The Einstein coefficients can also be calculated using the absorption oscillator strength f_{ki}, which is defined as follows Hutchinson [2002]:

$$f_{ki} = \frac{m_e h}{\pi} \frac{4\pi\epsilon_0}{e^2} \nu_{ik} B_{ki} = \frac{4\pi\epsilon_0}{e^2} \frac{m_e c^2}{8\pi^2 \nu_{ik}^2} \frac{g_i}{g_k} A_{ik} \tag{2.21}$$

f_{ki} is a dimensionless quantity that describes the strength of the transition; in other words, if a transition is stronger, f_{ki} approaches the value 1. Table 2.2 provides spectral line data for Hydrogen, including its Lyman and Balmer series Hutchinson [2002].

There are two main types of electron process that occur in a plasma: Collisional and Radiative. The electron transition between bound states, and free bond transitions such as recombination and photoionization come under the radiative processes. Whereas, the electron impact ionization, de-excitation, impact ionization, three-body recombination, dielectronic recombination, autoionization fall under the collisional electron processes Hutchinson [2002]. Some of these processes are shown in Figure 2.8.

The collisional processes of electron impact ionization, de-excitation, impact ionization and three-body recombination are basically radiative in nature with one difference: the transitions are stimulated by electron collisions without any spontaneous decay. The Dielectronic recombination collisional process is a process by which an atom excites an electron from itself into an upper energy level using the energy loss from an external electron that is captured in an upper energy level.

Table 2.2: Spectral Line Data for Hydrogen (Lyman & Balmer)

Line	Wavelength [nm]	A_{ik} $[10^8 s^{-1}]$	f_{ki}	g_i
L_α	121.57	4.699	0.4162	8
L_β	102.57	0.558	0.0791	18
L_γ	97.25	0.128	0.029	32
H_α	656.28	0.441	0.641	18
H_β	486.13	0.0842	0.119	32
H_γ	434.05	0.0253	0.044	50

The reverse is known as autoionization. This, however, does not apply to hydrogen as it has only 1 electron Hutchinson [2002]. The transition probabilities of radiative processes can be determined using Einstein coefficients. However, for collisional processes such as radiative recombination, it is best described by rate coefficients, which are a component of a discrete cross-section $\sigma_{ik}(\nu)$. The cross-section $\sigma_{ik}(\nu)$ for such a process is defined by the number of collisions occurring in a density of atoms n_i, where the electron has the velocity ν, per unit path length (Hutchinson 2002). The rate at which these collisions occur with an atom containing all types of electrons can be defined as:

$$\int_{\mathbb{R}^3} \sigma_{ik} f(v) v \, \mathrm{d}^3 v = n_e \langle \sigma_{ik} v \rangle \tag{2.22}$$

where

$$\langle \sigma_{ik} v \rangle \equiv \frac{\int_{\mathbb{R}^3} \sigma_{ik} v f \, \mathrm{d}^3 v}{\int_{\mathbb{R}^3} f \, \mathrm{d}^3 v} \tag{2.23}$$

$\langle \sigma_{ik} v \rangle$ is called the rate coefficient. The $\langle \sigma_{ik} v \rangle$ is formulated for a Maxwellian distribution with temperature T. Therefore, rate coefficients can be used to calculate the equilibrium population for each process, termed as collisional. Equation 2.22 describes an equation that encompasses both radiative and collisional processes. To solve Equation 2.22, some simplification is needed and can be solved by finite matrix algebra Hutchinson [2002].

$$\sum_{k \neq i} [n_i A_{ik} - n_j A_{ki} + n_i B_{ik} \rho(v_{ik}) - n_j B_{ki} \rho(v_{ik}) + n_e n_i \langle \sigma_{ik} v \rangle - n_e n_k \langle \sigma_{ki} v \rangle] = 0 \tag{2.24}$$

Now that we know how different electron processes and radiation occurs through any atomic species, we must understand the equilibria in which the radiation occurs in order to predict the radiative behavior of a plasma environment. By predictive the radiative behavior, we can learn about the expected population of an atomic

species in the said plasma environment. There are four major types of equilibria: (1) Thermal; (2) Local – Thermal; (3) Coronal; and (4) Time – Dependent Situations Hutchinson [2002].

Local Thermal Equilibrium

A plasma is said to be in a state of complete thermal equilibrium when the atoms in the plasma adopt the Boltzmann distribution between all its possible states and emits radiation energy density corresponding to a blackbody of the system temperature. The radiation in a complete thermal equilibrium tends to be weakly coupled and hence is not seen in a laboratory generated plasma, however, it is possible in inter-stellar objects. Therefore, a Local Thermal Equilibrium (LTE) is a widely used concept in the plasma physics community. In LTE, the atoms are Boltzmann distributed, but the radiation is not thermal. This, however, is also restrictive to laboratory plasma. Therefore a Saha – Boltzmann distribution is adopted which determines the relative population of the ionized states of atoms in a thermal equilibrium Hutchinson [2002]. LTE can be achieved by the presence of high density of collisional transitions over radiative transition between all the states of the atoms in a plasma. This can be written as follows:

$$n_e \gg 10^{19} \sqrt{\frac{T}{e}} \left(\frac{\Delta E}{e} \right)^3 \ [\mathrm{m}^{-3}] \tag{2.25}$$

Where '$\Delta E/e$' and 'T/e' are the energy levels and temperature difference in eV. For magnetic fusion plasma, Equation 50 is satisfied only when 'ΔE' is very small. Therefore, to predict the radiative population, a more generalized equilibrium is to be used, i.e., using rate coefficients for a specific atom process Hutchinson [2002].

Coronal Equilibrium

In coronal equilibrium (word derived from solar corona), the upward transitions are considered to be collisional, as the radiation density is low; and all the downward transitions are considered to be radiative, as the electron density is low. When a downward transition occurs, a photon is emitted that is absorbed by another atom

elsewhere in the plasma for an upward transition. Therefore, in a plasma that is optically thin (low on density), the photon emitted in a downward transition is lost as it is not absorbed. Therefore, in an optically thin plasma, the upward radiative transitions are neglected (Hutchinson 2002).Therefore, Equation 2.24 can be rewritten for coronal equilibrium as

$$\sum_{j\neq i}[n_i A_{ij} - n_j A_{ji} + n_i B_{ij}\rho(v_{ij}) - n_j B_{ji}\rho(v_{ij})] = 0 \tag{2.26}$$

Time-Dependent Equilibrium

Most of the time, the plasma is not always constant and is dependent on time. Hence for a time dependent solution we can rewrite Equation 2.24 as

$$\sum_{j\neq i}[n_i A_{ij} - n_j A_{ji} + n_i B_{ij}\rho(v_{ij}) - n_j B_{ji}\rho(v_{ij}) + n_e n_i\langle\sigma_{ij}v\rangle - n_e n_j\langle\sigma_{ji}v\rangle] = \frac{dn_i}{dt} \tag{2.27}$$

Where the only difference is a change from right hand side of the Equation. Equation 2.27 encompasses the change in density over time to derive the population in an equilibrium. If the excited state is in equilibrium with the ground state, even if ground states of different species are not in equilibrium with one another, the system can be simplified. This would help use Equation 2.27 as a part of a coronal model or a less restrictive model. One such model is called the Collisional Radiative Model (CRM) Hutchinson [2002].

Measurements of Neutrals

The study of Electro-Magnetic (EM) radiation emitted by ionized media is known as plasma spectroscopy and is a powerful diagnostic technique available to any plasma physicist. The only difference between normal spectroscopy and plasma spectroscopy is that the latter has a dependence on the surrounding plasma properties near the radiating species along with the radiating atomic/ionic species. This dependence is due to the fact that the radiation emitted by the species is due to the interaction

of the electrons/ions with the plasma to produce the radiation. This interaction can be due to several processes, as described in Figures 2.8 & 2.9 – such as ionization, recombination, excitation, de-excitation, and charge exchange Michelis and Mattioli [1984].

Degree of Dissociation

Figure 2.9 depicts reaction rates of several processes that occur in plasma through which neutral particles are formed. These processes, as seen, has both atomic and molecular neutral particle. In a laboratory made low temperature hydrogen/deuterium plasma, the neutral particle is dominantly molecular (H_2, D_2) in nature with a degree of dissociation (δ) around 1%. The molecular hydrogen dissociates into atomic hydrogen via a process of direct excitation and a process of dissociative excitation (shown as Curve 5 in Figure 2.9). The relevance of ion H_2^+ (curve 5 in Figure 2.9) is of less importance as its density is 3 times lower than the atomic density at 1% degree of dissociation and ionization degree of 10^{-5}, where degree of dissociation (δ) is given by

$$\delta = \frac{n_H}{n_{H/2} + n_{H_2}} \tag{2.28}$$

Where, n_H is the atomic hydrogen density, and n_{H_2} is the molecular hydrogen density. Generally, the 'δ' is 4%-6% for hydrogen plasma compared to 5.5%-7.5% for deuterium plasma. The rate coefficients for hydrogen and deuterium originating from direct excitation are similar to one another, however, the rate coefficients for deuterium are lower in case of dissociative excitation Fantz [2002].

The neutral density is calculated by analyzing Balmer and Lyman series. However, utilizing Balmer series is advantageous to calculate neutral density as opacity in plasma (which makes it impenetrable to radiation) predominately influences the Lyman series. Figure 2.10 shows neutral density of hydrogen and deuterium in a Helium plasma with and without the taking into account of opacity of Lyman lines on the Balmer series. It is to note that, the plasma was made from a mixture of

10% H_2/He and 10% D_2/He gas. It can be seen that three main Balmer lines were analyzed: α, β, and γ. As seen in the figure, in an optically thin plasma (some penetration of radiation is possible), Balmer α deviates the most (especially in D_2 plasma) due to the high re-absorption and small Doppler profile whereas, Balmer γ deviates the least, i.e., it is the least influenced line as it contains smallest molecular contribution and is least affected by opacity. It is to note that Balmer γ has some drawbacks, i.e., it has weak intensity as it is susceptible to recombination and is sensitive to electron density Fantz [2002].

Neutral Opacity

Plasmas exhibiting minimal self-absorption of radiation are referred to as "optically thin" or "less opaque". These plasma, often found in low-temperature environments, are primarily governed by collisions and can initially be treated as optically thin. However, a notable occurrence arises from the high population density residing in the ground state relative to the excited states. This phenomenon may lead to the re-absorption of robust resonance lines of Balmer and Lyman hydrogen Fantz [2002].

For a homogeneous plasma, it is assumed that the the length of the plasma l have uniform T_e, n_e and n_i. The radiation through this plasma can be quantified by

$$\frac{dI_v}{dl} = \epsilon_v - \kappa(v) I_v \tag{2.29}$$

Here, the change in intensity I_v over a unit path length is defined by the spectral emission coefficient ϵ_v and the absorption coefficient $\kappa(v)$ per unit meter. Adding a source function $S_v = \epsilon_v/\kappa(v)$, the above equation 2.29 can be rewritten as Fantz [2002]

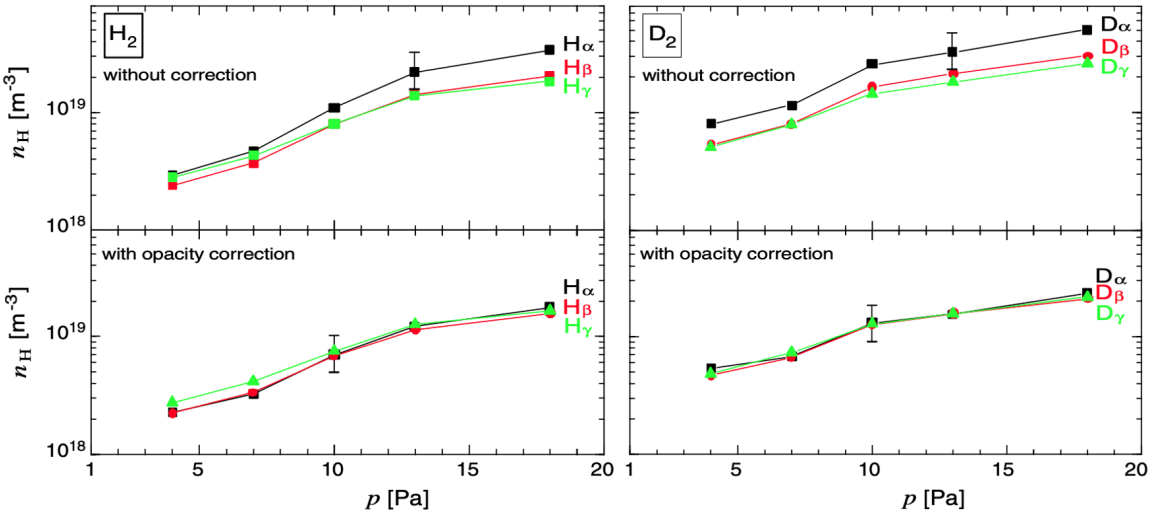


Figure 2.10: Neutral hydrogen and deuterium density measurement with and without accounting for the influence of opacity on Lyman lines. Image from Fantz [2002]

$$\frac{dI_v}{d\tau} = S_v - I_v \tag{2.30}$$

$$d\tau = \kappa(v)dl$$

$d\tau$ is the optical depth, $\tau(v)$ is the optical thickness at given ν frequency and can be defined as follows. Fantz [2002]

$$\tau(\nu) = \kappa(\nu)l \tag{2.31}$$

Here, κ is a function of density and l is a function of distance. Integrating Equation 2.30 with $I_v(0) = 0$, we get

$$I_v = \frac{\epsilon_v}{\kappa(\nu)}(1 - exp(-\kappa(\nu)l)) = S_\nu(1 - exp(-\tau(\nu))) \tag{2.32}$$

An optically thin plasma can also be defined as $\kappa(\nu)l = \tau(\nu) \ll 1$ where the exponential function can be approximated to be linear and the intensity can relate the spectral coefficient. The area under the absorption coefficient $\kappa(\nu)$ can be written as a function of the Einstein's transition probability for absorption $B_{k,p}$ or with the oscillator strength f as shown below. Fantz [2002]

$$\int_{line} \kappa_{\kappa,p} d\nu = n_\kappa B_{\kappa,p} \frac{h\nu_0}{c} = n_\kappa f \frac{e^2}{4\epsilon_0 m_e c} \tag{2.33}$$

Here, ν_0 is the frequency of the line, c is the speed of light, ϵ_0 is the permittivity of free space. The transition probabilities in optically thin environments are affected by factors known as population escape factors, denoted as $\theta_{p,\kappa}$, which signify the ratio of absorbed to emitted radiation power. These factors elucidate how the radiation field within the plasma volume influences the population of electronic states. It's important not to confuse these with escape factors used in radiation transfer calculations along a line of sight through the plasma, crucial for analyzing observed line radiation affected

by self-absorption. The population escape factor is always less than 1 and varies based on the absorption coefficient, line shape, and plasma geometry Fantz [2002]. It is given by

$$\theta(p,\kappa) = \int_{line} P_\lambda exp(-\kappa_{k,p}(\lambda)b)d\lambda \tag{2.34}$$

with

$$\int_{line} P_\lambda d\lambda = 1$$

here, P_λ is the spectral line profile, b is the characteristic length of about half of the shortest dimension in plasma, and as mentioned before, $\kappa(\lambda)$ is the absorption coefficient in the line center and is defined as

$$\kappa(\lambda_0) = n_1 \frac{\lambda_0}{c} \frac{fe^2}{4\epsilon_0 m_e} \sqrt{\frac{\mu m_p}{2\pi\kappa T_g}} \tag{2.35}$$

here, μ is the atomic mass number, n_1 is the number density in lower state Fantz [2002].

Figure 2.11(a) shows population escape factor θ as a function of $\kappa(\lambda_0)b$ for Lyman alpha, beta, gamma and delta for density of $10^{20}m^{-3}$, temperature of 1eV and a characteristic length of 5cm. Here, observations indicate that the initial lines within the Lyman series exhibit optical thickness in scenarios characterized by typical parameters of low-density plasmas. This circumstance could potentially impact the population density of higher energy levels as well. The Figure 2.11(b) depicts correction factors for opacity pertaining to each Balmer line under conditions of $n_e = 10^{17}, \mathrm{m}^{-3}$ and $T_e = 2, \mathrm{eV}$, applicable for a Doppler profile of 1 eV. These factors must be adjusted to match the actual ionization grade, with additional scaling necessary for deuterium due to the mass-dependent nature of the absorption coefficient. The absorption coefficient, primarily dependent on electron density and to a lesser extent on electron temperature, is a key determinant. Correction factors have been derived for both atomic and molecular components, revealing hydrogen's

lesser susceptibility to opacity compared to deuterium or hydrogen-alpha. This, along with the reduced influence of dissociative excitation on population, suggests hydrogen as the preferred option for diagnosing atomic hydrogen densities Fantz [2002].

Balmer Line Ratio

Each Hydrogen emission spectral line emit photons due to the electron transitioning between two energy levels. The energy levels are divided into two state: higher (n) and lower (n'). The emission spectrum of hydrogen is divided into seven spectral line series based on their lower energy levels (n'): Lyman ($n' = 1$), Balmer ($n' = 2$), Paschen ($n' = 3$), Brackett ($n' = 4$), Pfund ($n' = 5$), and Humpherys ($n' = 6$) and others ($n' > 6$). For example, the transition from energy level 2 to energy level 1 has the spectral line called Lyman alpha, and the transition from 3 to 2 is called Balmer alpha Nave [2005].

Three most common hydrogen spectral series analyzed in a tokamak are the Lyman, Balmer and Paschen. These series are used to understand the sourcing fuel (Deuterium) in UV, visible and IR range respectively Nave [2005]. The Lyman and Balmer series electron transition and their wavelength are described in Table 2.2. Do note that the wavelength for hydrogen and Deuterium Blamer series are very similar to each other of Edinburgh [2020].

When Balmer α and γ are measured, the neutral particles are predominately molecules, however, with dissociate excitation occurring simultaneously along with taking into the effects of opacity, the measurement becomes insensitive and hence taking line ratio (H_α/H_γ or D_α/D_γ) comes into play. Figure 2.12 shows the line ratio with respect of electron temperature ranging from 1 eV to 4eV. Figure 2.12(a) shows line ratio of H_α/H_γ and H_α/H_β and Figure 2.12(b) shows line ratio of D_α/D_γ and D_α/D_β, both of which has degree of dissociation taken into account. The hollow data points represent the H_α/H_γ and D_α/D_γ ratio whereas the filled data points represent the H_α/H_β and D_α/D_β Fantz [2002].

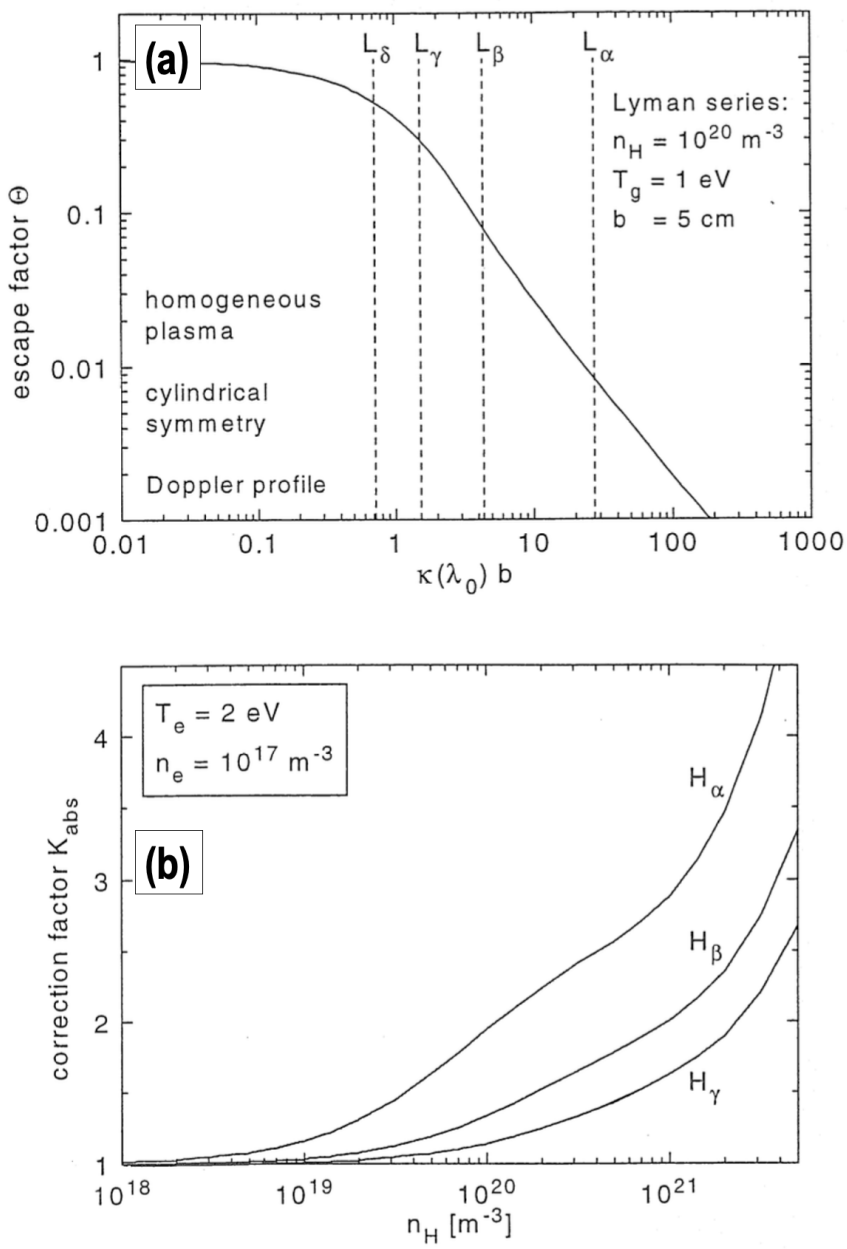


Figure 2.11: (a) Escape coefficients for a hydrogen plasma of radius 'b', with the locations of the initial four Lyman lines highlighted. (b) Adjustment coefficients for three Balmer lines attributable to the opacity stemming from Lyman lines. Image from Fantz [2002]

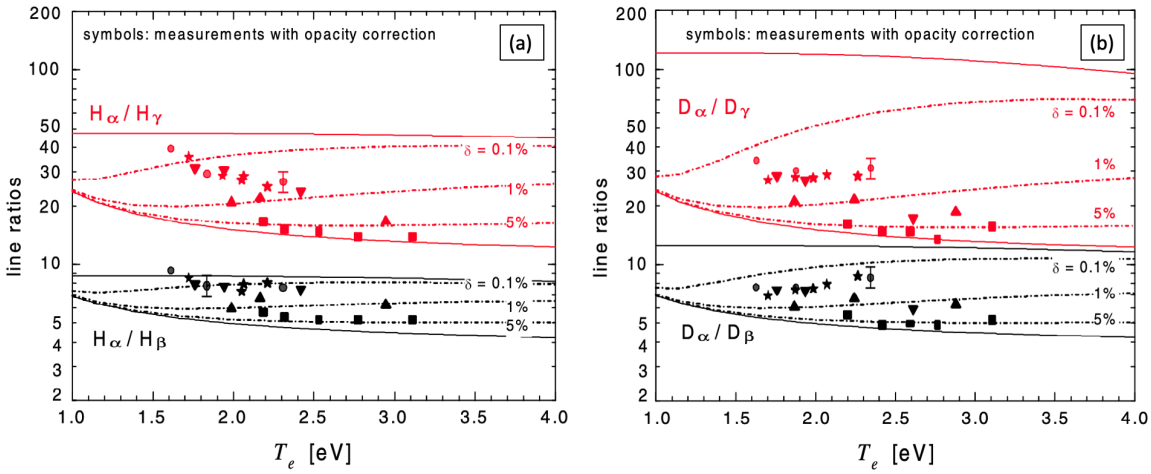


Figure 2.12: Balmer line ratio of H_2 and D_2 as a function of electron temperature and degree of dissociation. Image from Fantz [2002]

The data points represent the percentage of H_2/D_2 molecules in Helium with ■: 10%, ▲: 20%, ▼: 50%, •: 80%, and ★: 90%. It can be seen from Figure 2.12(a) and 2.12(b) that H_α/H_γ ratio is superior to H_α/H_β . The hydrogen ratio tends to increase its dependency on electron density as it increases. The atomic and molecular excitation is different in deuterium compared to that of hydrogen, giving a more accurate result for line ratio for deuterium Fantz [2002].

Atomic and Molecular Fluxes

The temperature at the divertor varies from 10 eV to sub eV where it can be attached or detached or can be highly recycling. With the different divertor regimes, the atomic and molecular hydrogen / deuterium varies. Therefore, to determine the atomic hydrogen / deuterium flux Γ_H, Balmer line radiation is measured. Atomic hydrogen / deuterium flux is measured by using the S/XB coefficient, where 'S' is the effective rate coefficient for ionization, 'X' is the excitation rate coefficient and 'B' is a branching ratio for the H_α/D_α line and is available in atomic databases Fantz [2002]. The Γ_H is given by

$$\Gamma_H = \frac{S}{XB}\Gamma_{H_\alpha} \tag{2.36}$$

Similar to Atomic flux, molecular flux can be found using molecular bands, i.e., along with ionization process, the process of dissociation will also be considered Fantz [2002]. The molecular flux is given by:

$$\Gamma_{H_2} = \frac{S_{eff} + D_{eff}}{XB}\,\Gamma_{Fulcher} \tag{2.37}$$

Where, S_{eff} and D_{eff} are the effective ionization and dissociation rate coefficients, and $\Gamma_{Fulcher}$ is the Fulcher alpha particle flux (Fulcher alpha band is a molecular band of Balmer alpha that ranges from wavelength 600 – 640 nm). The effective ionization and dissociation processes per effective Fulcher alpha system is calculated with collisional radiative model and the data is available in Fantz [2002]. In general, the molecular fluxes were found between 1 to 20 eV and for temperature less than 1

eV, the radiation emitted by the hydrogen molecule is weak Denne [1989], Johnson and Hinnov [1973], Fantz [2002].

Molecular Assisted Recombination (MAR)

During the onset to detachment, the temperature at the divertor falls below 5eV and is followed by volumetric recombination of neutrals (majority of which are molecular in nature). The molecular neutrals produced at the surface by recombining atoms and ions leak into the main chamber plasma and play a defining role in divertor dynamics. This process, where the volumetric recombination is enhanced due to the presence of molecular neutrals is known as Molecular Assisted Recombination (MAR). The vibrationally excited molecules (H_2 (ν) and D_2 (ν)) enhance the volumetric recombination by the following processes Fantz [2002]:

$$H_2(\nu) + e^- \rightarrow H^- + H \qquad followed\ by \qquad H^- + H^+ \rightarrow H + H^* \tag{2.38}$$

Dissociative Attachment — Mutual neutralization

$$H_2(\nu) + H^+ \rightarrow H_2^+ + H \qquad followed\ by \qquad H_2^+ + e^- \rightarrow H + H^* \tag{2.39}$$

Ion Conversion — Dissociative Recombination

Equation 2.38 and 2.39 shows that in each reaction an electron and/or ion recombines to a neutral H atom and the molecule is dissociated, with an electronically excited state (H^*) as a byproduct of the reaction. This excited state can vary in three ways which can either lead to Molecular Assisted Recombination – MAR (Equation 2.40, Molecular Assisted Dissociation – MAD (Equation 2.41), and Molecular Assisted Ionization – MAI (Equation 2.42) Fantz [2002].

Only Equation 2.40 – MAR contributes to volumetric recombination compared to MAD and MAI. Rate coefficients for MAR, MAD and MAI are available in atomic

databases and it is to note that the rate coefficients for MAI are too small compared to MAR and MAD. The rate coefficients of MAR and MAD differ by a factor of 1 to 2. The MAD and MAR decreases away from the divertor wall, whereas in comparison, the radiative recombination rate remains constant even away from the divertor volume.

$$H_2(\nu) + H^+ \rightarrow H_2^+ + H \qquad followed\ by \qquad H_2^+ + e^- \rightarrow H + H \tag{2.40}$$

$$H_2(\nu) + H^+ \rightarrow H_2^+ + H \qquad followed\ by \qquad H_2^+ + e^- \rightarrow H + H^+ + e^- \tag{2.41}$$

$$H_2(\nu) + H^+ \rightarrow H_2^+ + H \qquad followed\ by \qquad H_2^+ + e^- \rightarrow H^+ + H^+ + 2e^- \tag{2.42}$$

The decrease in MAD and MAR away from the divertor wall is due to the high electron temperature and low molecular density away from the divertor wall. MAD dominates over all reaction chains which confirms that the molecules dissociate (MAD) and ionize (MAI) before they recombine (MAR). A thin layer of molecules closes to walls contribute to plasma recombination. Since the MAD and MAI dominates more than MAR, the ionization lengths of the particles reduce, making the potential energy stored in the divertor increase leading to plasma re-attachment Fantz [2002].

Reflection Coefficients (R)

The atomic and molecular hydrogen and deuterium present in the plasma edge can be used to find diffusive Γ_{diff} and molecular Γ_{mol} flux, which are given by:

$$\Gamma_{\text{diff}} = D_n \frac{dn}{dz} \quad \text{and} \quad \Gamma_{\text{mol}} = n_H \frac{v_{\text{th}}}{4} \tag{2.43}$$

Where, D_n is the diffusion coefficient, D_n for hydrogen is 4.3 m^2/s and D_n for deuterium is 3.3 m^2/s at 20 Pa and 650K temperature. The atomic flux Γ_H or Γ_D derived from above values is same for both hydrogen and deuterium at value 2.6x10^{21} $m^{-2}s^{-1}$. The particle flux is termed molecular when the mean free path of

the particle is shorter than the distance of line of sight to the surface, thus molecular flux takes atomic neutral density n_H into account. The term v_{th} is the mean particle velocity, and the $\nu_{th}(H) = 3700m/s$, and $\nu_{th}(D) = 2600\ m/s$ at 650 K temperature. It is to note that the molecular fluxes are considerably higher than diffusive fluxes Fantz [2002].

Calculating both diffusive and molecular fluxes help determine a term called 'Reflection Coefficient' (R), defined as:

$$R = \frac{\Gamma_{mol} - \Gamma_{diff}}{\Gamma_{mol}} \tag{2.44}$$

Since both diffusive and molecular fluxes are influenced by the surface of the wall, the fluxes for both hydrogen and deuterium are different. For graphite wall, hydrogen had a reflection coefficient of 91% and deuterium had a reflection coefficient of 95%. For stainless steel wall, reflection coefficient for hydrogen is 73% and 93% for deuterium. Therefore, reflection coefficient (R) is important to calculate, in order to understand the wall and plasma parameters as it influences the atomic density of hydrogen and deuterium near the surface that leads to change in recycling and degree of dissociation Fantz [2002].

Particle Source Ionization Rate

One of the main goals for current and future fusion reactors is to reduce the particle and heat fluxes on the PFC of the divertor target. The main drivers of the particle and heat fluxes are the power and neutrals pressures balance at the plasma edge region that is controlled by radiation and charge exchange. One way to reach the goal is by divertor detachment – i.e., very low heat and plasma flux on the divertor as outlined in section 2.2.4. Remember, in the detachment regime, plasma–neutral interaction plays a major role with interaction directly affecting the power radiated by the hydrogen resulting in the momentum transfer from the ion-fluid to the neutrals through charge exchange and other processes Kurz et al. [1997].

The D_α emission rate is defined by the following equation. Where, 'S_α' is the H_α emissivity (H_α photons/m^{3}s), 'n_e' is the electron density, 'n_n' is the neutral density, and '$\langle\sigma\nu\rangle$' is the rate coefficient (as seen in Figure 2.9) for various atomic processes such as excitation, dissociation, and charge exchange Kurz et al. [1997].

$$S_\alpha = n_e \cdot n_n \cdot \langle\sigma\nu\rangle \tag{2.45}$$

In the SOL, there are two main mechanisms that usually dominate the particle sourcing: (1) Plasma electrons locally ionizing the neutrals; and (2) cross-field diffusion. Describing just the electron ionization process, one can rewrite equation 2.45 as

$$S_{iz} = n_e \cdot n_H \cdot (\sigma\nu_{iz}) \tag{2.46}$$

Where, 'S_{iz}' is the ionization rate of hydrogen atoms due to electron impact and is measured in ionization events/m^3/s. The value '$\sigma\nu_{iz}$' is an ionization cross-section that encompasses the rate coefficient for the ionization process (rate coefficient is shown in Curve 6 in Figure 2.9).

For primary results for the experiments conducted for this document, Equation 2.46 will be used to calculate the particle source ionization rate. However, for future experiments, the '$\langle\sigma\nu\rangle$' from Equation 2.45 can/should consist of all the seven atomic and molecular processes described in Figure 2.8 – such as dissociation and charge exchange Stangeby [2000].

In summary, understanding how neutrals are formed and measured play a role in understanding the hypothesis question that is poised in this thesis. The first hypothesis questions mentions understanding neutral leakage and its correlation with divertor closure. The information provided by this section helps us understand and measure neutrals in terms of ions and utilize the information to infer the results to answer the hypothesis question.

2.3.2 Divertor closure

A considerable fraction of neutrals emitted from the divertor target undergoes re-ionization within the divertor region before reaching the SOL or the core, owing to an opaque plasma, rendering the divertor highly recycling, as detailed in Section 2.3.3. Furthermore, the physical geometry, particularly the re-emission of neutrals perpendicular to the recycling surface Pitcher and Stangeby [1997], influences the recycling nature of the divertor. A highly recycling divertor aids in reducing power load on the divertor plate, lowering temperature by enhancing neutral density, thereby promoting detachment. This detachment proves advantageous for prolonged material endurance in future devices. Thus, the concept of divertor closure becomes pivotal in this context.

Historically, the term "divertor closure" has been associated with separatrix electron density and exhaust efficiency. The prevailing understanding posited that lower closure corresponded to increased particle leakage from the divertor, and conversely, higher closure indicated improved particle exhaust. In the late 1990s, Jones and colleagues from JET (Joint European Torus) introduced the concept of divertor closure in the context of enhanced particle exhaust, highlighting that superior particle exhaust was synonymous with higher closure, as documented in their work Jones [1997].

Subsequently, Bosch and the ASDEX team in 1999 expounded on divertor closure, drawing an analogy to electron separatrix density. This quantification approach for divertor closure found application in the early 2000s, as exemplified by research teams at JET Guo et al. [2000] and JT60-U Sakasai et al. [2001]. These teams quantified divertor closure indirectly by measuring higher separatrix density.

In the following years, researchers from HT-7U Zhu and Zha [2003] and JET Rapp et al. [2008] redefined divertor closure with respect to recycled neutrals. Their findings indicated that lower recycled neutrals were associated with higher divertor closure. In 2008, the JET team Fundamenski [2008] established a widely adopted definition

of divertor closure, which involved measuring neutral pressure inside and outside the divertor and quantifying neutral compression. According to their definition, higher divertor closure corresponded to increased trapped neutrals and greater neutral compression.

The concept of divertor closure was later linked to geometric baffling by the MAST-U team Fishpool et al. [2013], Havlíčková et al. [2015], marking the first instance of such an association. Subsequently, the DIII-D team defined closure by considering an increase in separatrix density and combining it with higher baffling Sontag et al. [2017], Casali et al. [2019, 2020, 2022].

The lack of consensus within the community regarding the definition of divertor closure is evident from the diverse approaches taken by different research teams. Consequently, there is a pressing need for a standardized definition of divertor closure, a gap that this thesis aims to address.

A general widely accepted definition of divertor closure, as defined by Horton et al. [1999], Loarte [2001], pertains to neutrals emitted from the divertor target that escape the divertor region. The level of neutral escape is inversely proportional to divertor closure, with higher closure resulting in lower neutral escape. Increased closure enhances particle pumping within the divertor region, diminishes neutral density in the main chamber, and augments plasma confinement. The closure is contingent upon both magnetic and physical geometry.

Generally, a divertor characterized by tight baffling and a closed structure prevents neutrals from escaping the region. Achieving a closed structure involves adjusting baffle positions, directing emitted neutrals to ionize toward the Private Flux Region (PFR). Figure 2.13 illustrates the re-ionization pattern of neutrals in connection with a horizontal divertor (depicted at the outer divertor) and a vertical divertor (depicted at the inner divertor). In the case of vertical divertors, neutrals are recycled toward the separatrix, where the power flux is at its maximum. Conversely, for horizontal divertors, neutrals generated at the separatrix strike point are recycled in the outer region of the SOL.

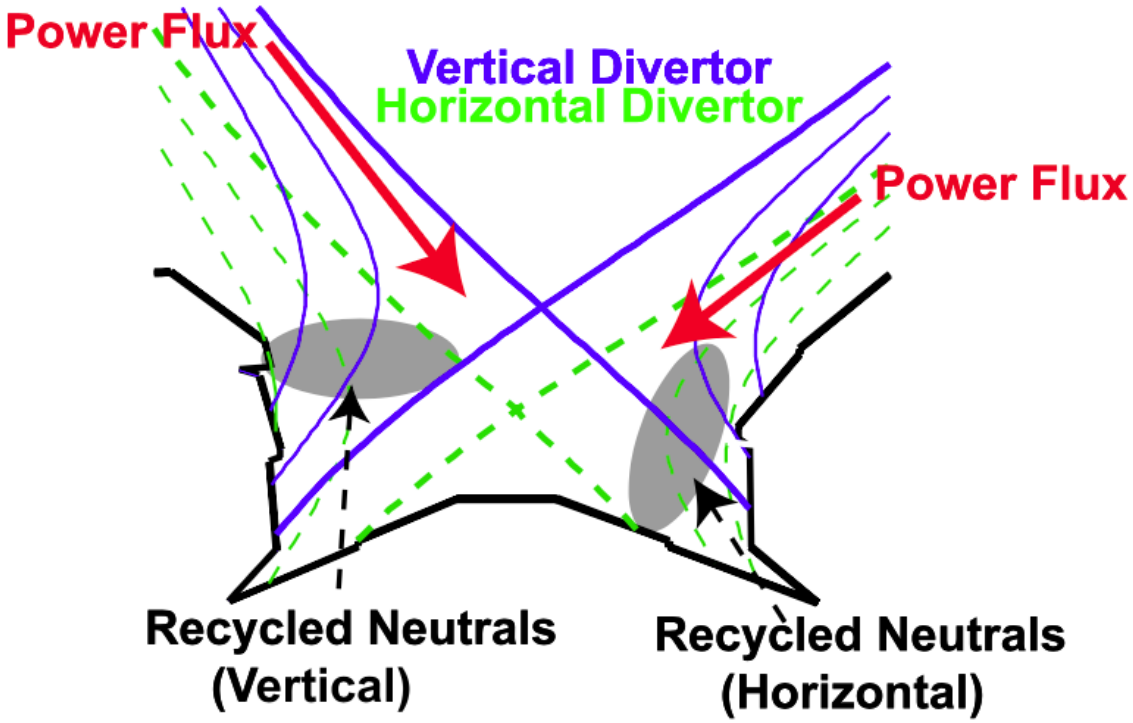


Figure 2.13: A cartoon depiction of neutral ionization pattern related to Vertical and Horizontal divertor target plate. For Vertical target, the neutrals re-ionize near the separatrix and for horizontal target, the neutrals re-ionize near the outer SOL. Loarte [2001]

It should be emphasized that ELMy plasma discharge tends to elevate recycling in the main chamber. The extent of divertor closure's influence on recycling neutrals outside the divertor region would be contingent on the magnitude of ELMs.

2.3.3 Divertor Leakage

Neutral divertor leakage refers to the neutrals that have 'leaked' or 'escaped' the divertor closure Casali et al. [2020]. Figure 2.14 depicts a generic tokamak cross-section with the neutral leakage path. Loop 1 in Figure 2.14 depicts the ions impinging on the divertor plate that are recycled as neutrals, which are then again ionized and returned to the divertor. Loop 2 shows the ions pathways that leak from the divertor region and later ionize in the core. Loop 3 shows the location outside the divertor where ions moving radially outwards recycle with the main chamber. These neutrals ionize and travel back to the PFC or into the plasma core. Loop 4 depicts the ions that recycle at the divertor but leak directly to the main SOL, where they are ionized into the core Lipschultz and LaBombard [2005].

Neutral leakage is different in open and closed geometry. In a closed divertor geometry, the neutrals are efficiently trapped at the target and are recycled. Whereas, in open geometry, the neutrals scatter into the SOL and private flux region higher power dissipation and pedestal fueling Casali et al. [2020].

In order to quantify the divertor leakage, Casali et al. came up with a 'Divertor Leakage Parameter' or 'DLP'. It is defined as the ratio of the number of neutral particles leaking from the divertor to the number of neutral particles being produced in the divertor and can be formulated as:

$$DLP\,[\%] = \frac{\int \Gamma_{i,belowX-point}\, dy}{\int S_{neutral}\, dy}\, X100 \tag{2.47}$$

Where, $S_{neutral} = S_{recycling} + S_{recombination}$ is the neutral originating at the divertor and $\Gamma_{i,belowX-point}$ is the loss of neutrals just below X-point in the divertor. $\Gamma_{i,belowX-point}$ represents the ion flux below the X – point. DLP is calculated (in

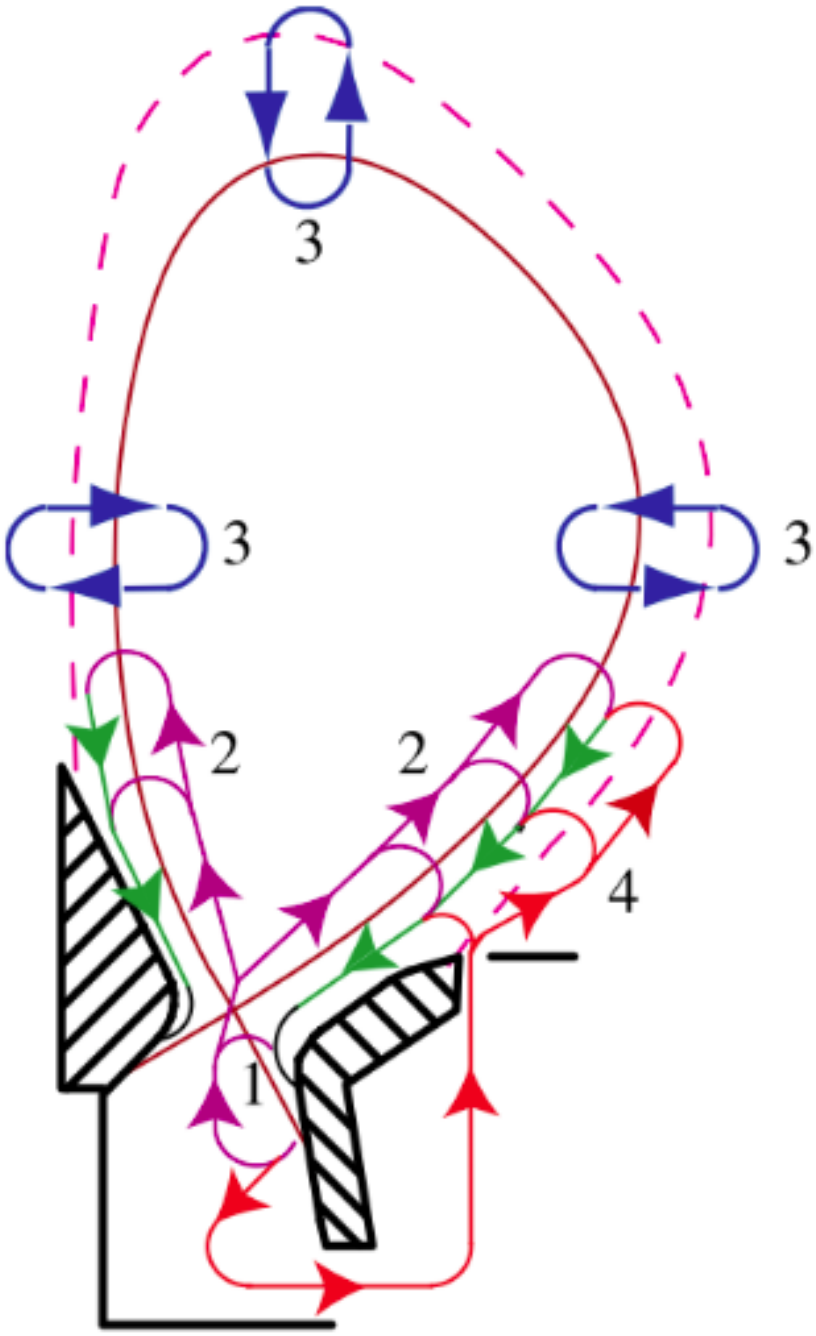


Figure 2.14: Flow of neutrals through SOL, divertor and core plasma. Image from Lipschultz and LaBombard [2005]

percentage (%)) as a function of separatrix density from attached to detached conditions and is depicted in Figure 2.15 with open (blue) and closed (green) divertor. The neutral leakage in open divertor is 30% and in closed divertor is 2% in attached plasma condition. However, at the onset of detachment, the neutral leakage increases in closed divertor geometry to 12% and 35% for the open divertor configuration. Also, in detached conditions, the neutral leakage is increased further to 20% in closed divertor and up to 60% in the open divertor configuration. This is summarized in Table 2.3 and it concludes that the divertor geometry is important for the neutral leakage Casali et al. [2020].

Main Chamber Recycling

Main chamber recycling (MCR) refers to the recycling of neutrals and PMI at the main chamber (located at loop 3 in Figure 2.14). The neutral source at the main chamber occurs due to a combination of three main processes – (1) plasma ion flux moving radially outwards impacting the wall (Figure 2.14, Loop 3); (2) neutrals that leak through vessel walls bypassing the vessel structure (Figure 2.14, Loop 4); and (3) neutrals leaking from the divertor through charge exchange and wall collision and reflections Kallenbach et al. [2003]. MCR has damaging effects on plasma performance and on particle and plasma control, which is an issue for future reactors such as ITER Groth et al. [2003].

Understanding SOL transport & Onset to MCR

The energy and particle from the core enter the SOL through slow cross-field transport, and once the particle and energy are in the SOL, it travels to the divertor target quickly with the help of the parallel B field transport Stangeby [2000]. Cross-field particle fluxes extend from the far SOL to the near SOL at the main chamber and help balance neutral density and, in turn, ionization source rates at the main chamber.

Table 2.3: Comparison of DLP values in different divertor geometry with different divertor plasma conditions Casali et al. [2020]

	Open (LSN)	Closed (USN)
Attached	30% Leakage	2% Leakage
Onset to Detachment	35% Leakage	12% Leakage
Detached	60% Leakage	20% Leakage

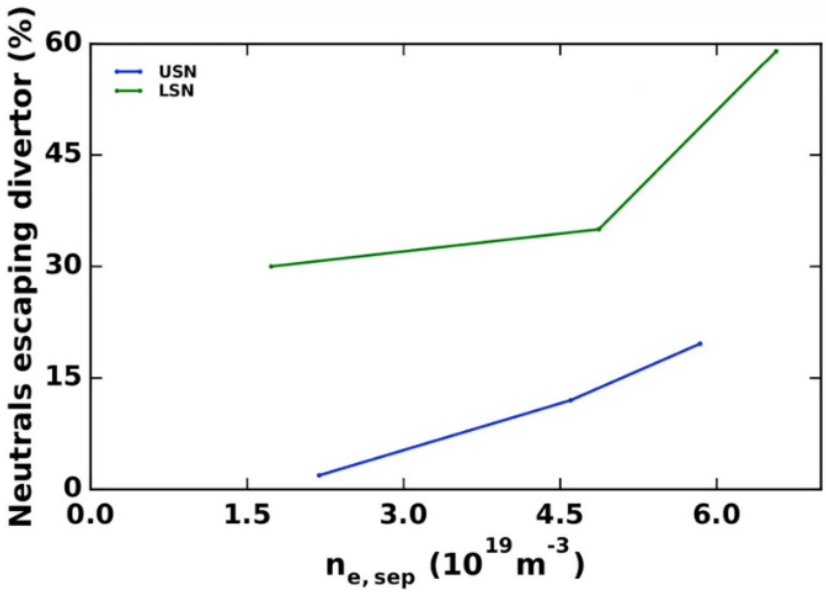


Figure 2.15: The DLP as a function of separatrix density in Open (LSN) and Closed (USN) DIII-D divertor geometry. Image from Casali et al. [2020]

Assuming the molecular recombination is neglected, the conservation of plasma and neutral species requires the following equations to satisfy LaBombard et al. [2000].

$$\nabla \, . \, \Gamma_{div} = n_0 \, n_e \, \kappa_{ion} \tag{2.48}$$

$$\nabla \, . \, (\Gamma_{div} + \Gamma_0) = 0 \tag{2.49}$$

In equation 2.48, Γ_{div} is the divertor plasma flux, n_0 is the atomic density, n_e is the plasma electron density and κ_{ion} is the ionization rate coefficient. In Equation 2.49, Γ_0 is the neutral atomic flux.

Figure 2.16 shows the SOL laid out flat with length 2L extending from one divertor surface to another. SOL can be divided into series of flux tubes adjacent to each other with constant electron density and temperature. It is noted that MCR occurs in both low and high recycling regimes. Averaging Equations 2.48 and 2.49, we get the following equations:

$$\frac{\partial}{\partial r_\perp} \langle \Gamma_\perp \rangle = n_e \left(\langle n_0 \rangle \, \kappa_{\text{ion}} - \frac{C_s}{2L} \right) \tag{2.50}$$

$$\frac{\partial}{\partial r_\perp} \langle \Gamma_\perp \rangle + \frac{\partial}{\partial r_\perp} \langle \Gamma_{(0_\perp)} \rangle = 0 \tag{2.51}$$

Equation 2.51 states that the average plasma flux density that crosses any magnetic field that terminates on an axisymmetric wall perpendicular to $\overrightarrow{B}$ (magnetic field) (Figure 2.15) is balanced by neutral flux density from the opposite direction. Equation 2.50 shows that the average plasma flux decreases as the flux travels deeper (in the 'r' direction) into the SOL if the averaged ionization source does not exceed the parallel flow losses at the divertor surface. $\langle \Gamma_\perp \rangle$ increases with distance in the SOL if the averaged neutral density in a flux tube $\langle n_0 \rangle$ exceeds a critical value $\langle n_0 \rangle_{\text{crit}}$. If $\langle \Gamma_\perp \rangle$ increases with distance in SOL, $\langle n_0 \rangle$ increases as the overall recycling over the SOL increases. If $\langle n_0 \rangle_{\text{crit}}$ value is surpassed at one location in the SOL, then $\langle n_0 \rangle_{\text{crit}}$ will increase in all the SOL until $C_s/2L$ increases sufficiently. When $\langle n_0 \rangle$ in the LCFS

is almost equal to $\langle n_0 \rangle_{\text{crit}}$, the source ionization rate becomes uniform throughout the SOL due to cross-field fluxes. These cross-field fluxes increase to the nearest main chamber leading to main chamber recycling (LaBombard et al. 2000). This MCR regime is dominated by cross-field plasma density, which is given by Equation 2.52, where T_e is the temperature of electron or ion in eV, q is the safety factor, and R is the major radius in meters LaBombard et al. [2000].

$$\langle \Gamma_\perp \rangle_{\text{crit}} \approx 2 \times 10^{20} \left(\frac{T_e}{qR} \right) \text{ m}^{-2}\,\text{s}^{-1} \tag{2.52}$$

When $\langle \Gamma_\perp \rangle$ is close to $\langle \Gamma_\perp \rangle_{\text{crit}}$, the cross-field plasma fluxes dominate the plasma particle balance in the SOL. When $\langle \Gamma_\perp \rangle_{\text{crit}}$ is achieved near the LCFS, the SOL achieves MCR with radially dominated transport LaBombard et al. [2000].

MCR measured in ASDEX-Upgrade, Alcator C-Mod, and DIII-D

This section will describe neutral measurement in terms of Balmer alpha, neutral pressure, and/or both of the above in the ASDEX-Upgrade, Alcator C-Mod, and DIII-D.

Starting with ASDEX-Upgrade, the neutral flux density is measured using ionization gauges and derived using Balmer alpha spectroscopy. The neutral flux measured in the divertor is found to be 200 times higher than at the midplane, as seen in Figure 2.17. However, the neutral flux densities at the high flux side are 40 times higher than the midplane. These results originate due to the presence of bypass neutral leakage (Loop 4 from Figure 2.14). The neutral density measurement is difficult to quantify between the high and low flux sides due to wall reflection. However, the 10-30% of bypass neutrals originating from the divertor lead to MCR at the midplane Kallenbach et al. [2003].

Alcator C-Mod measures neutral pressure at both divertor and midplane regions. The Alcator C-Mod team measured neutral pressures in low and high recycling regimes with plasma operating conditions being both attached and detached.

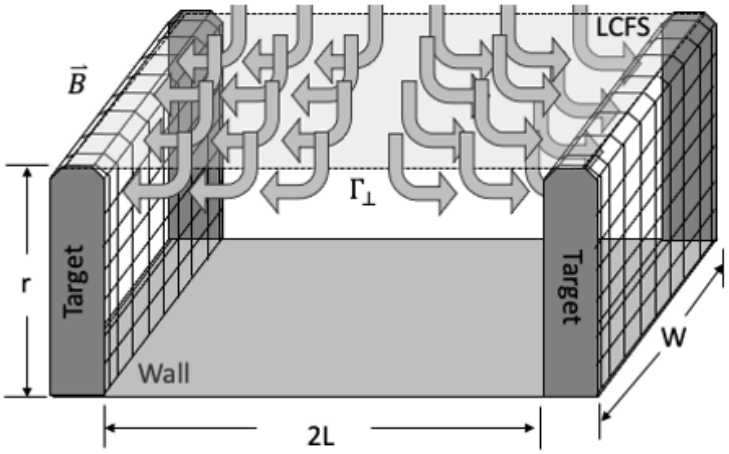


Figure 2.16: Flattened out SOL depicting the cross-field plasma flux moving towards the divertor targets. Adapted from Stangeby [2000]

The neutral pressure in the divertor is 100 times more than that in the main chamber. However, the upper neutral pressure is only three times higher than the midplane. The MCR dominates in the main chamber SOL, and the neutral pressure in the main chamber SOL is comparable to that found near the divertor LaBombard et al. [2000].

The DIII-D team utilized cameras to observe the divertor and midplane areas of the DIII-D vessel, enabling the measurement of inner and outer emission wall profiles. Balmer alpha measurements were also conducted using a filterscope. In low-density discharges with attached plasma (L mode), the D_α emission exhibited a peak further upstream in the inner divertor leg, with twice the D_α emissivity at the inner strike point compared to the outer strike point. It is noteworthy that the D_α emission peaked near the X point within the separatrix. Additionally, the D_α emission at the midplane was three times lower than that on the divertor plate. In recycling low and medium ELMy H mode plasma, the D_α emission was found to be twice as high in the divertor region. In a double null configuration, the D_α emission remained uniform in both the inner and outer divertor legs. However, the magnitude of D_α was twice as high in the lower divertor compared to the upper divertor. Also, in the double null configuration, the emission from the lower X point was twice as high as that from the upper X point Groth et al. [2003]. In summary, a detached divertor regime is advantageous as it provides high collisionality at the target with lower MCR (refer to Figure 2.2). This condition can enhance pedestal performance and contribute to a better understanding of particle and plasma control.

2.3.4 Effects of Divertor Design on Divertor Physics

The divertor designs in various experimental tokamaks worldwide as seen in Figure 2.18 have evolved over decades to maximize benefits, aiming for regimes with low power load on the divertor target, minimal material erosion, and effective energy and core confinement. These designs also integrate effective particle and helium

ash removal, essential for future reactor designs Loarte [2001]. Figure 2.18(a) shows schematic representation of three divertor geometries investigated in JET: Mk I, Mk IIA, and Mk II Gas Box. During the Mk IIA exploration, the conductance of the bypass leaks was reduced (referred to as Mk IIA/P, denoting Mk IIA with plugged divertor leaks).

In all geometries, divertor pumping is conducted using a divertor cryo-pump [prepared by R.D. Monk]. Figure 2.18(b) depicts the divertor geometry in ASDEX-U with Div I (open) and the Div II 'Lyra' (closed). Pumping in Div I involves turbo-molecular pumps connected to the vacuum vessel near the outer divertor through the shown ports. Additionally, a cryo-pump has been installed in Div II to enhance pumping Gruber et al. [1999]. Figure 2.18(c) illustrates the divertor geometry in Alcator C-mod, delineating the positions of the bypass divertor leaks and the locations of gauges for measuring neutral pressure (G) Pitcher et al. [2000]. Figure 2.18(d) Divertor geometry in DIII-D with magnetic equilibria for the bottom (open) and top (closed) divertors. Lastly, Figure 2.18(e) the two divertor geometries explored in JT-60U: (open) divertor and W-shape divertor (closed). In the W-shape divertor, pumping occurs through the private flux region Asakura et al. [1999a].

This section explores the non-linear dependencies of divertor design on neutral transport, impurity transport at the divertor, SOL, and edge plasma. It discusses the impact of x-point location on target power load, considering horizontal and vertical targets (2.3.4). Additionally, it explains divertor geometry effects on detachment and divertor radiated power (Appendix F), influences on deuterium and impurity pumping (2.3.4), and the impact of neutral pressure in the main chamber on plasma confinement (2.3.4).

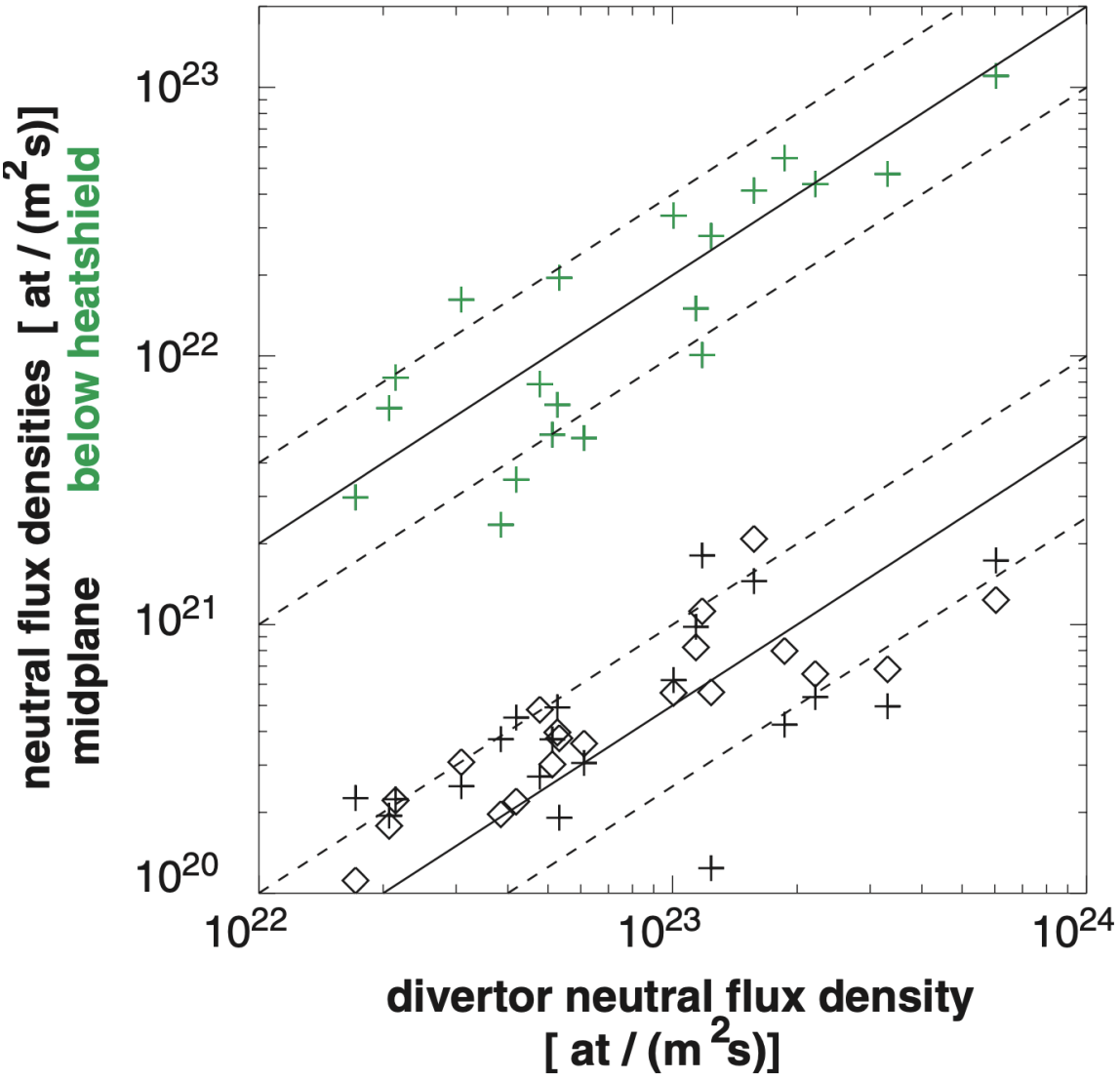


Figure 2.17: Neutral flux densities from midplane D_α spectroscopy (♢), ionization gauges below the inner heat shield at the HFS (+), and behind structures in the main chamber on the LFS (+) are compared with the neutral flux measured using an ionization gauge in the divertor below the roof baffle for ASDEX Upgrade. Solid lines denote fluxes equivalent to 1/200 and 1/5 of the divertor flux, while dotted lines indicate a deviation by a factor of 2. Image from Kallenbach et al. [2003]

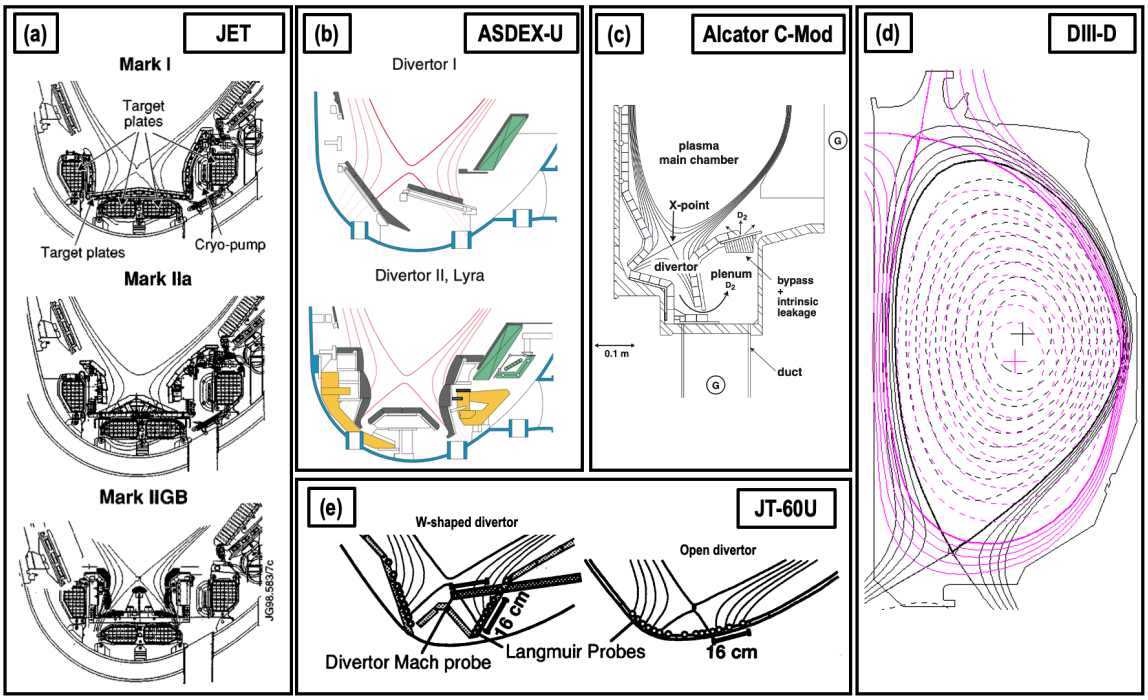


Figure 2.18: Divertor designs in various experimental tokamaks worldwide: (a) JET [prepared by R.D. Monk], (b) ASDEX-U Gruber et al. [1999], (c) Alcaor C-Mod Pitcher et al. [2001], (d) DIII-D and (e) JT-60U Asakura et al. [1999a]

Effect of divertor magnetic geometry on target power load via flux expansion and X-point height

Upstream power and particle fluxes exhibit dependence on x-point formation, divertor target flux expansion, and divertor geometry—whether configured with a flat horizontal or vertical target featuring a specific angle of incidence. Flux expansion inversely correlates with x-point height, associated with longer divertor legs. Consequently, an augmented divertor leg length or increased x-point-to-target distance correlates with elevated peak power deposition on the divertor target. This outcome arises from an enlarged angle of incidence on a flat divertor target and diminished flux expansion, with concentrated deposition of particle and heat fluxes. Loarte Prieto [1992], Loarte and Harbour [1992], Loarte [2001]. This is illustrated in Figure 2.19, presenting normalized flux measurements commencing from $Z_t = 0cm$, where the x-point-to-target is set as 0 as a reference, signifying direct contact between the x-point and divertor target. The measurement extends up to $Z_t = 30cm$ depicting increased flux deposition as distance increases.

Another influential factor affecting power deposition on the target, in conjunction with varying x-point height, is the diffusion of particle fluxes into the Private Flux Region (PFR). Upon diffusion into the PFR, the maximum parallel power flux diminishes by a factor of 2 when mapped to the outer mid-plane Lasnier et al. [1998], Loarte [2001].

Effect of divertor geometry on neutral pumping

Adding to the previous sections mentioning the effects of divertor geometry, another important parameter is neutral pumping, which is a requisite for achieving precise density control in ongoing experiments and facilitating the removal of helium ash in subsequent devices. Enhanced divertor closure diminishes the likelihood of recycled neutral atoms/molecules escaping to the bulk plasma, thereby elevating divertor neutral pressure and, consequently, enhancing divertor pumping efficiency. Figure

2.20 [prepared by R.D. Monk] illustrates the escalating divertor neutral pressure across similar L-mode plasma, progressing from JET-Mk I to JET-Mk IIA and culminating in the JET-Mk II Gas Box divertor.

Numerous effects of divertor geometry on pumping efficiency have been discerned since the initial pumping experiments conducted in DIII-D Klepper et al. [1993]. The probability of a recycled neutral being pumped hinges on its likelihood of reaching the pumping plenum compared to being ionized in the plasma, particularly contingent upon the distance between the strike point and the entrance of the pumping plenum Klepper et al. [1993]. In a study by Loarte [1997b], divertor pumping exhibited a pronounced dependence on the plasma's precise position concerning the pumping plenum entrance only when neutral transport to the plenum was dominated by the initial flight neutral contribution. Conversely, when neutral transport was dominated by diffusive processes, such as charge-exchange and multiple collisions with divertor/vessel walls, the transport process displayed a naturally weaker dependence on the neutral source location Loarte [2001].

Influence on main chamber neutral pressure and confinement

In addition to augmenting divertor neutral pressure and thereby enhancing pumping efficiency, a closed divertor has the potential to reduce main chamber neutral pressure. Initial findings in PDX by Kaye et al. [1984] and ASDEX by Wagner [1991] demonstrated that diminishing the conductance of by-passes for divertor neutrals back into the main chamber improved access to H-mode (lower power threshold) and enhanced H-mode energy confinement. This led to the expectation that employing more closed divertors could lower main chamber neutral pressure, yielding positive effects on H-mode confinement. The reduction of main chamber neutral pressure and recycling could also play a role in decreasing impurity production resulting from charge-exchange sputtering by energetic atoms on the main chamber walls. Hence understanding the influence of divertor geometry on main chamber neutral pressure and plasma confinement is important.

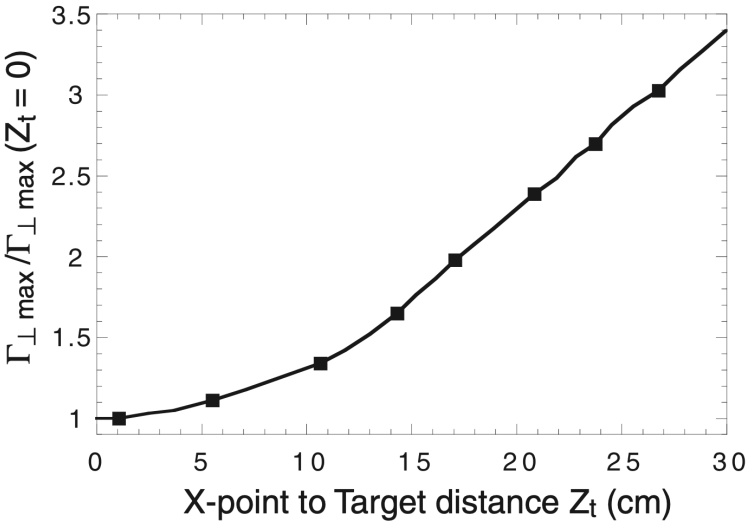


Figure 2.19: Normalized flux on the divertor target plotted versus x-point-height on a JET divertor Loarte Prieto [1992]

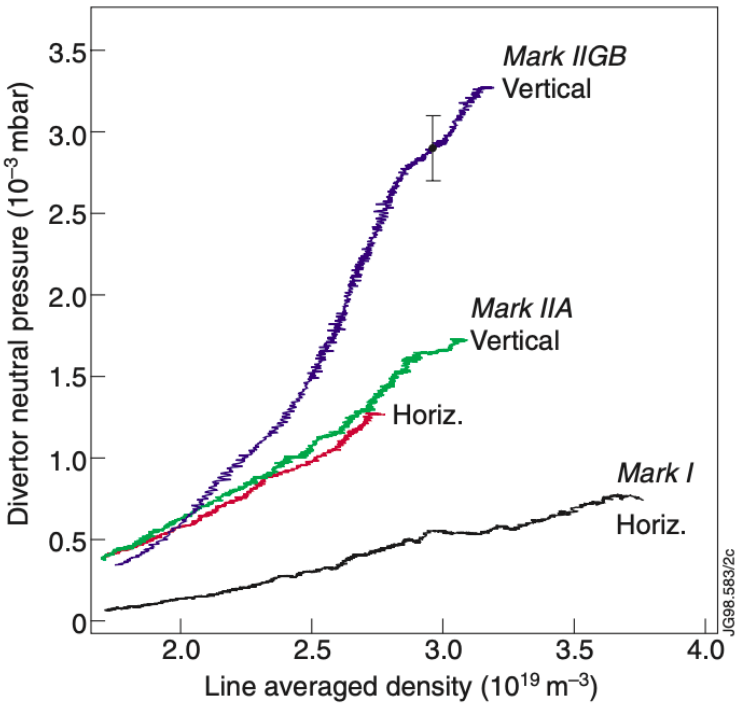


Figure 2.20: Measured neutral pressures in horizontal and vertical divertor ranging from most open divertor (JET-Mk I, to the most closed divertor JET-Mk II Gas box. This shows neutral pressure increases with increase in plasma density. [prepared by R.D. Monk], Loarte [2001]

In principle, it is not inherently evident that the installation of a closed divertor in a device will result in a lower main chamber neutral pressure, as Main Chamber Recycling (MCR) is independent of recycling in the divertor, see Section 2.3.3. Moreover, a more closed divertor configuration leads to an elevated divertor neutral pressure, potentially intensifying the flow of neutrals leaking back from the divertor to the main chamber through by-passes in the divertor structure in case of Alcator C-Mode Pitcher et al. [2000].

If the divertor structure lacks sufficient tightness to prevent neutral back-leakage, the main chamber neutral pressure may remain unaffected even with the installation of a more closed divertor in the device. Observations in Alcator C-Mod by Pitcher et al. [2000] and ASDEX-U by Bosch et al. [1999] indeed demonstrate that a more closed divertor results in larger divertor neutral pressures without influencing the main chamber neutral pressure. Consequently, the neutral compression (ratio of divertor to main plasma pressure) increases with a more closed divertor due to the elevated divertor pressure rather than a reduction in the main chamber pressure.

The role of by-pass leaks from the divertor into the main chamber (Loop 4 in Figure 2.14) has been experimentally investigated in Alcator C-Mod by implementing a system allowing changes in the conductance of the divertor by-pass leaks during a shot Pitcher et al. [2000]. The results suggest that in Alcator C-Mod, the neutral escape from the divertor back into the main chamber through the divertor leaks follows a 'flux-limited' phenomenon Pitcher et al. [2001]. Increasing the conductance of these leaks reduces the divertor pressure, ensuring that the neutral flux escaping the divertor through the leaks remains constant, thereby leaving the main chamber neutral pressure unchanged (see Figure 2.21).

The findings in JFT-2M Kawashima et al. [1999], DIII-D Allen et al. [1999], and particularly JET Horton et al. [1999], [prepared by R.D. Monk] are more in accordance with the expected behavior of a closed divertor in relation to main chamber neutral pressure. An apparent trend indicates that an increase in divertor closure is accompanied by a concurrent decrease in main chamber neutral pressure.

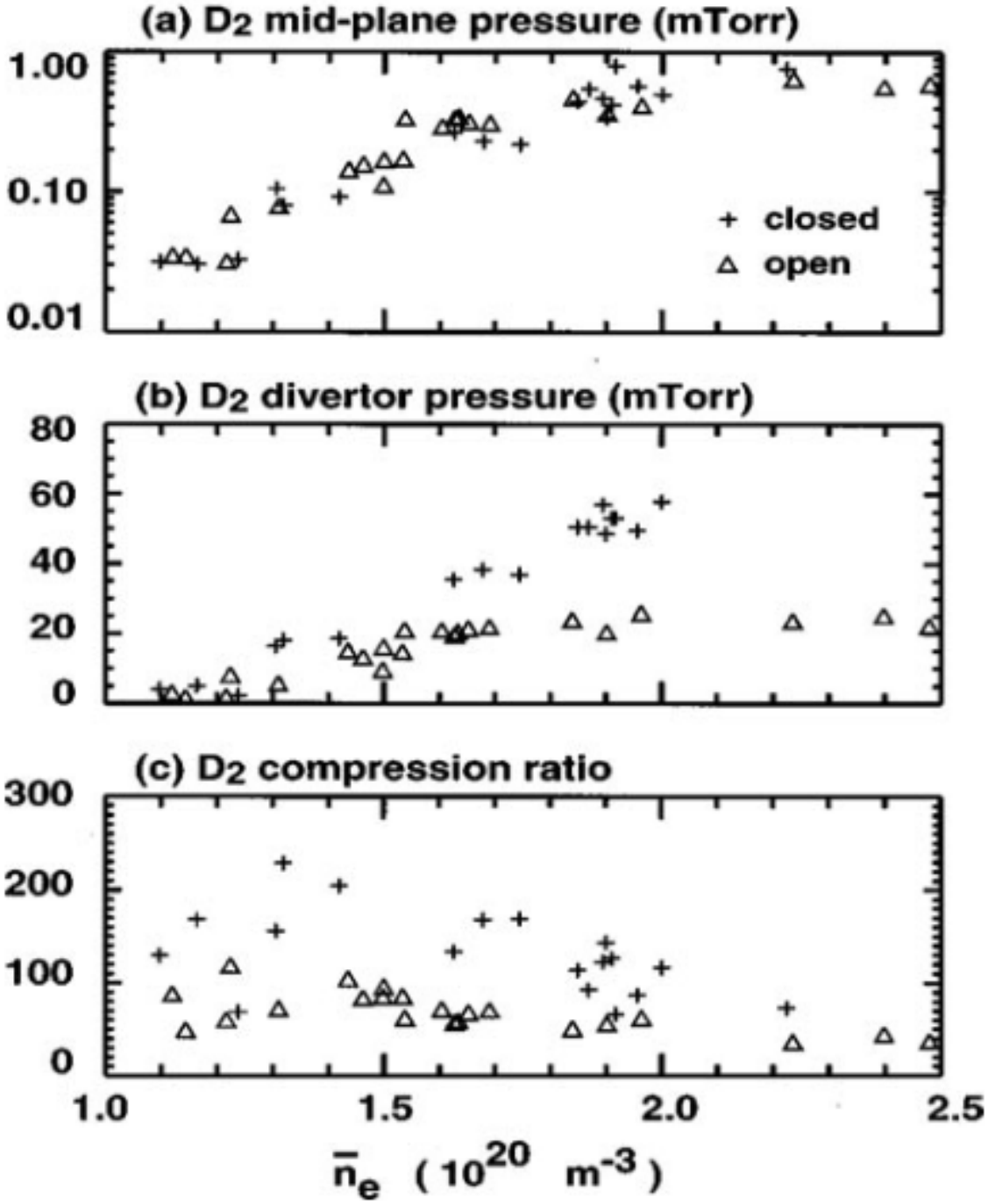


Figure 2.21: Plots of (a) midplane neutral pressure,(b) divertor neutral pressure, and (c) neutral compression are presented against line-averaged density in Alcator C-Mod experiments. Crosses denote experiments with closed divertor by-pass leaks, while triangles represent with open by-pass leaks. Neutral compression is significantly reduced when the by-pass leaks are open Pitcher et al. [2000]

This suggests that the neutral pressure in the main chamber is primarily influenced by neutral escape directly from the divertor plasma, rather than through leaks in the divertor structure Loarte [2001].

2.4 Edge and divertor modeling for tokamak closure

Due to the critical role of the SOL in shaping the performance of fusion devices, a comprehensive understanding of its physics is paramount for the success of the entire fusion program. The challenges faced by fusion today are closely linked to the intricate dynamics of the plasma within the SOL region. While codes have traditionally served as valuable design tools, there is a growing recognition within the community of the need to augment their use with insights from first-principles simulations, particularly in the context of designing future fusion devices like ITER Ricci [2015].

Despite the significant progress made in first-principle simulations of SOL dynamics, current designs of tokamak divertors and wall systems still heavily rely on empirical extrapolation from observed SOL plasma and neutral dynamics in existing devices, complemented by fundamental theoretical considerations. While empirical codes, even when fully validated against measurements from existing devices, cannot reliably predict SOL dynamics under conditions far from existing experience, their value lies in identifying trends for extrapolations rather than providing detailed quantitative predictions. A recent review of the status of empirical SOL modeling can be found in Loarte et al. [2007].

In their simplest form, these codes solve a reduced set of Braginskii fluid equations for plasma density (n), ion temperature (T_i), electron temperature (T_e), and parallel ion velocity ($V_{\|i}$), assuming quasi-neutrality and ambipolar flow. They can also incorporate a multi-species fluid description. Transport across magnetic field lines is described through an *ad hoc* diffusion-advection process, while parallel transport

is modeled using classical heat conductivity with flux limit factors to simulate kinetic effects. When run in an interpretative manner, free diffusive and convective parameters are adjusted to fit experimental data. These fits are then used to evaluate SOL profiles when the codes are run in predictive mode. In recent years, the description of plasma dynamics was improved by including stationary $E \times B$ and ∇B drifts and currents. Plasma description is coupled with a Monte Carlo model for neutral particles, crucial for describing pumping, fueling, and detailed plasma–material interactions Ricci [2015].

Among the empirical SOL modeling codes are SOLPS (formerly B2-Eirene) Reiter et al. [1991], Schneider et al. [1992], EDGE2D Simonini et al. [1994], UEDGE Rognlien et al. [1994], and SOLDOR Shimizu et al. [2003]. Widely used in both interpretative and predictive modes, these codes represent a significant investment by the fusion community. For instance, the primary SOL simulation code used for ITER divertor design Pitts et al. [2009], SOLPS, consists of about 200,000 lines of source code, with over 100 professional-years invested in its development Kukushkin et al. [2011].

The modeling of the SOL has highlighted the key parameters influencing SOL profiles, including the power entering the SOL, fusion fuel pressure, pumping speed, helium concentration-based fusion power, the ratio of gas puffing to core fueling, and the magnetic field's connection length Loarte et al. [2007]. The outcomes of modeling efforts have significantly influenced the design of the ITER divertor Kukushkin et al. [2011]. For instance, SOLPS simulations demonstrated that a V-shaped intersection of the target plates with the divertor floor promotes partial detachment. Additionally, to mitigate the load imbalance between the outer and inner divertor legs, structures supporting the divertor dome have been designed to allow high gas conductance Ricci [2015].

Plasma exhaust codes such as SOLPS-ITER effectively simulate the multi-physics phenomena in the SOL. However, given the numerous design and operating parameters and the lengthy simulation run times, it is impractical to simulate all possible scenarios. Additionally, certain simulation parameters, such as anomalous

transport, are unknown for new reactors. To address this challenge, surrogate models come into play. These machine learning models are trained on simulation data, allowing them to interpolate in the parameter space and provide fast results for various scenarios. The key objective in surrogate modeling is to train a model with minimal data, considering that each training datapoint requires computationally intensive simulations. Although surrogate modeling still entails running numerous simulations for training, the overall computational effort is expected to be less than exploring the high-dimensional parameter space through simulations alone. Moreover, certain surrogate models, like neural networks, are differentiable, enabling their use in gradient-based design optimization. Surrogate modeling finds applications in various fields, including engineering Sun and Wang [2019], medicine Pruett and Hester [2016], neuroscience Zhang and Young [2020], plasma physics van de Plassche et al. [2020], and has been explored in scrape-off layer simulations Preuss and Toussaint [2016], Gopakumar and Samaddar [2020], Zhu et al. [2022], Dasbach and Wiesen [2023]. This is however, a current topic of research and out of scope for this thesis.

2.4.1 SOLPS

SOLPS is a comprehensive simulation code designed to depict both the edge plasma and neutral transport. It comprises two interconnected codes: B2, a two-dimensional fluid code capable of handling species with varying ionization levels Braams [1996], and EIRENE Reiter et al. [2005], a three-dimensional Monte Carlo kinetic neutral transport code. Although coupled with EIRENE, B2.5 possesses the capability to simulate neutral transport as a fluid interacting with the plasma, departing from the kinetic treatment of EIRENE. The interaction between EIRENE and B2.5 involves the simulation of various atomic processes, including ionization, recombination, charge exchange, and radiation. Recent enhancements to B2.5 include the incorporation of radiation-enhanced sublimation, thermal evaporation, and impinging particle backscattering for interaction with plasma-facing surfaces

Coster et al. [2006]. SOLPS has demonstrated utility in simulating detachment Coster [2011], Guo et al. [2007], H-mode plasmas Chankin et al. [2006], Ohmic plasmas Chankin et al. [2008], and contributing to ITER design and scenario development Kukushkin et al. [2011]. However, despite its effectiveness in edge modeling, SOLPS currently lacks consideration for any potential influence that the core might have on edge dynamics, suggesting a potential avenue for future extensions Leddy [2016].

Constructing a basic SOLPS-ITER run involves following the workflow outlined in Figure 2.22, progressing from top to bottom. The primary plasma solver, represented by the blue box, is B2.5-Eirene, a coupling of the standalone executables "b2mn" and "Eirene." The steps for building a SOLPS-ITER run are as follows Bonnin et al. [2016]:

- Geometry Definition: Utilize the DivGeo utility to establish the location of vacuum vessel walls, their properties, pumping locations, equilibrium topology, and plasma species presence.

- Plasma Mesh Generation: Use the Carre mesh generator to create a structured quadrangular mesh for the plasma solver. This mesh covers an area extending from the edge of the confined region to the line of first tangency with a limiting (non-divertor) wall structure.

- Input File Generation: Employ the Uinp utility to generate corresponding Eirene (and some B2.5) input files based on the provided data.

- Neutral Mesh Generation: With the input files, use the Tria and Triageom programs to create an unstructured triangular grid covering the Carre-gridded area plus the outer SOL domain up to the actual vacuum vessel wall.

- Physics Input: Translate additional plasma parameters into the internal format used by B2.5 using utilities such as "b2ag" (geometry), "b2ah" (transport and boundary conditions), "b2ai" (initial state), and "b2ar" (atomic physics tables).

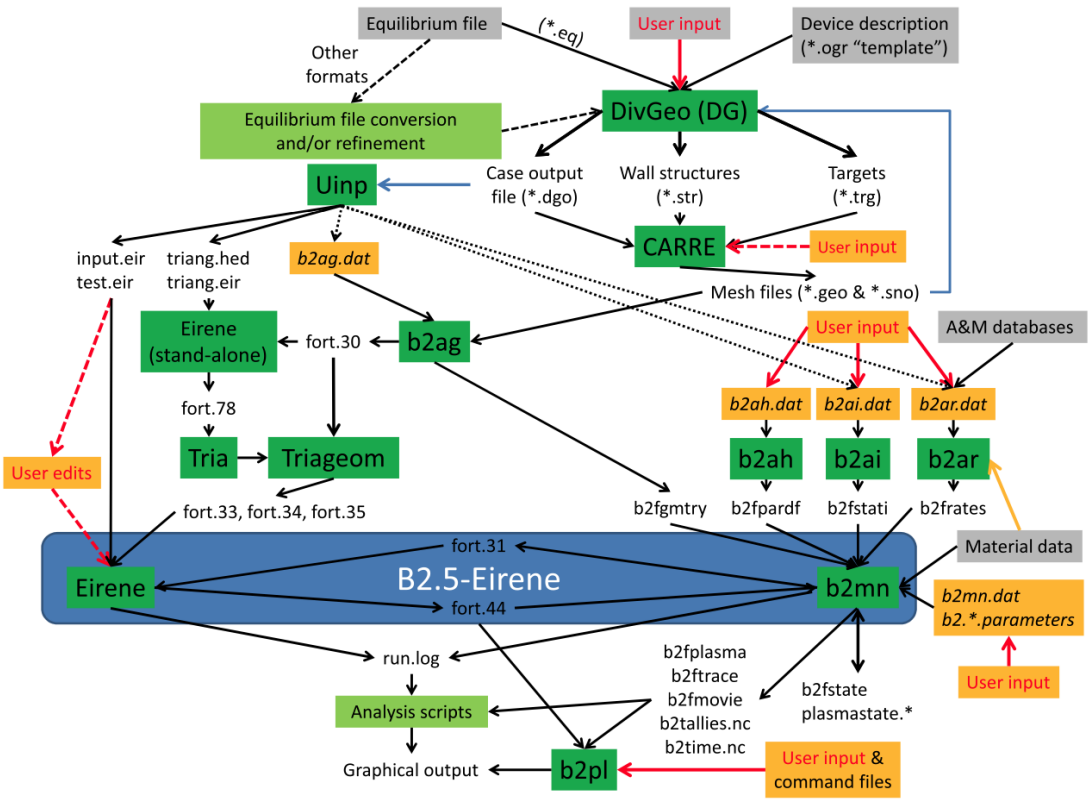


Figure 2.22: The workflow of SOLPS-ITER is illustrated, where the primary code B2.5-Eirene is encapsulated within the blue box. Each green box corresponds to a distinct executable, while grey boxes denote data sourced from external databases. Orange boxes signify steps within the new user interface Bonnin et al. [2016]

Supplement these with a list of run switches and additional name lists provided as human-readable input files.

Once the input files are prepared, launch standalone runs of Eirene or B2.5, or coupled B2.5-Eirene runs. One can analyze and plot the results using the b2plot utility. SOLPS-ITER includes converter utilities that facilitate the translation of input and output files from previous SOLPS versions into the expected format, enabling the continuation of older runs with minimal user intervention Bonnin et al. [2016].

2.4.2 EIRENE Model

EIRENE is a multispecies code designed to solve either a system of time-dependent (optional) or stationary (default) linear kinetic transport equations with considerable complexity in a specified host medium (background). Initially developed in the mid-1980s, a basic model for transporting ionized particles along magnetic field lines was included to address applications related to hydrocarbon breakup via intermediate charged states (hydrocarbon molecular ions). EIRENE is linked to external databases providing atomic and molecular data, as well as surface reflection data.

The code incorporates various user-supplied routines, facilitating data exchange with other fluid transport codes. While the primary objective of its development was to investigate neutral gas transport in magnetically confined plasmas, its flexibility allows for the solution of more general linear kinetic transport equations using a stochastic method of solution rather than numerical or analytical approaches. Notably, the code retains options to simplify model equations for the essential case of the one-speed transport problem, particularly in radiation transfer, such as photon transport. A flowchart structure outlining the code's organization is available on the website `http://www.eirene.de`. The iterative mode, as indicated in Figure 2.23, becomes essential for addressing nonlinear effects within the neutral particle model under fixed plasma conditions, involving considerations like neutral-neutral collisions.

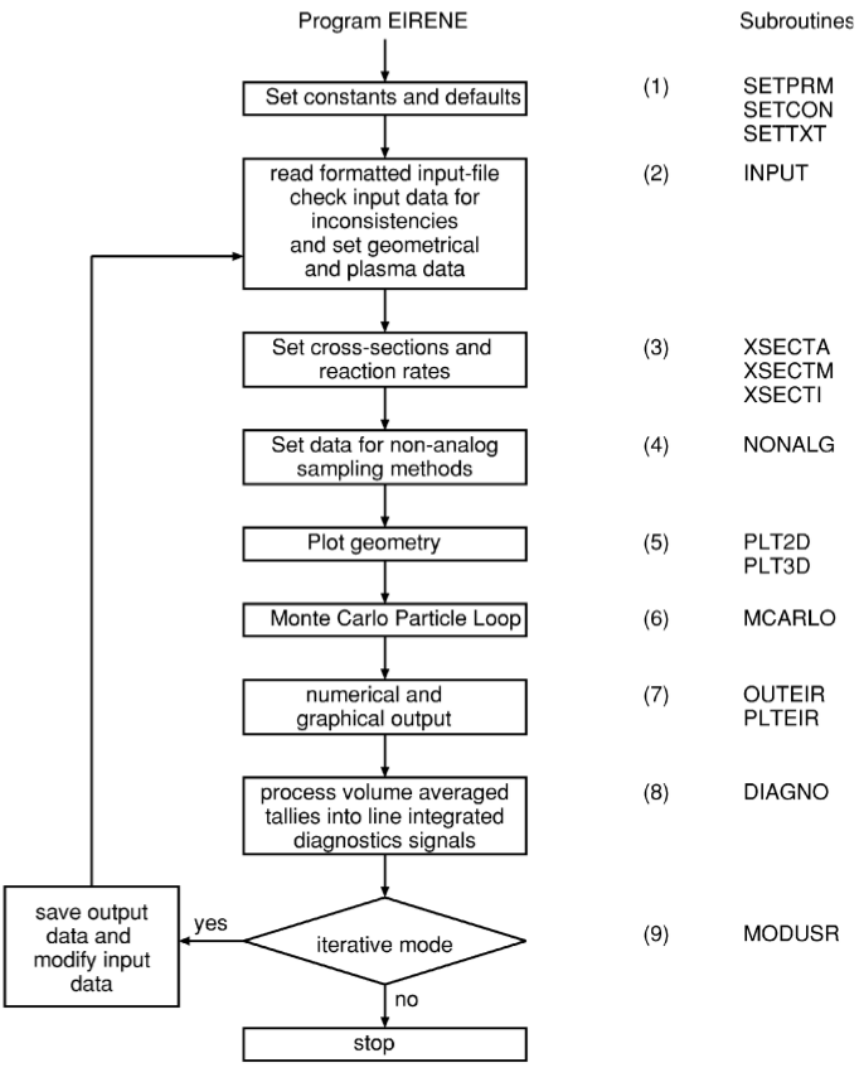


Figure 2.23: Diagram depicting the fundamental structure of the EIRENE Monte Carlo Solver for the Boltzmann equation at its lowest level. The numbers and program names on the right correspond to additional flowcharts at more advanced levels within a comprehensive tree of flowcharts. Reiter et al. [2005]

These internal iterations become unnecessary if the plasma background response to neutral gas transport is explicitly considered, as the coupled neutral-plasma problem is resolved through iterations between EIRENE and the plasma code.

The EIRENE Monte-Carlo neutral code, developed by Reiter and colleagues, is utilized in this study. The OSM code provides a hydrogenic "background" plasma solution, serving as input for EIRENE. EIRENE determines the neutral distribution function (see Equation 2.53) by solving the steady-state Boltzmann transport equation, considering position (r), velocity (v), and particle species (i) as seen in Equation 2.54

$$f(\overrightarrow{x}) = f(\overrightarrow{r}, \overrightarrow{v}, \overrightarrow{i}) \tag{2.53}$$

$$\overrightarrow{v}\nabla_r f(\overrightarrow{x}) = C(f)\overrightarrow{x} \tag{2.54}$$

The collision term $C(f)$ represents neutral particle interactions in phase space with a state x. Neutral transport modeling in fusion devices, and an introduction to the EIRENE formalism by Reiter et al. [2005], are essential references for this work. EIRENE calculates volumetric source terms for particle, momentum, and energy resulting from plasma-neutral interactions. The OSM code iterates with EIRENE to achieve self-consistency in plasma and neutral solutions (assuming convergence), exemplified by the SOL22 plasma solver. D and D_2 are explicitly included, and D_{2+} is incorporated via a collisional equilibrium approximation (excluding transport along field lines). Neutral-plasma interactions relevant to fusion plasmas are extensively reviewed by Harrison and Post. A valid neutral solution requires comprehensive neutral collisions in the model, contingent on accurate cross-section data. An assessment suggested the atomic data's adequacy for fusion modeling ($\sim$25% uncertainty), but the molecular database was deemed "weak." Krstic and Schultz provided a comprehensive set of cross-sections for elastic collisions, contributing to

EIRENE. The code can operate in a time-dependent mode, accommodating non-steady-state phenomena such as ELMs Reiter et al. [2005].

2.4.3 Onion Skin Model (OSM)

As mentioned previously, OSM solves 1D background plasma conservation equation that are along the B-field using data from Langmuir probes from the experiment to produces a 2D edge plasma solution that is toroidally symmetric. It utilizes a concept of flux tubes, which is defined as a constant value of magnetic induction enclosed within the flux tube, denoted as $BA_{\parallel} = constant$, where $A_{\parallel}$ represents the cross-sectional area of the flux tube perpendicular to B. The notion that transport is highly anisotropic in plasmas subjected to strong magnetic fields might suggest the validity of the flux-tube concept. However, it's important to note that anisotropic transport only guarantees that the scrape-off layer (SOL) will exhibit elongated and narrow characteristics. This leaves open the question of the applicability of an analysis grounded in individual flux tubes within the SOL Stangeby [2000].

The OSM can be dealt in two ways: non-terative way and an ietrative way. The most straightforward form of non-iterative Onion-Skin Method (OSM) modeling employs the two-point model for individual flux tubes. In this approach, it is assumed that all entering power is concentrated either at the upstream end or uniformly along the length (L) of the flux tube. While this assumption is not critical for iterative OSM methods, adopting the OSM approach of separately and sequentially treating perpendicular and parallel balances can reduce the computational time required to reach a converged solution Stangeby [2000]. In iterative OSM, the perpendicular flux densities of particles, momentum, and power can be proportionally related to the local values of second derivatives in the perpendicular direction, following the standard assumption of diffusive cross-field transport. In such cases, the OSM approach essentially serves as an alternative numerical procedure for conducting 2D modeling.

However, it retains a significant advantage – the radial span of the SOL is covered by boundary condition information obtained from experiments Stangeby [2000].

OSM in modelling SOL

In the onion-skin method (OSM), the boundary conditions are typically defined at the target and involve parameters such as electron temperature (T_e), ion temperature (T_i), and electron density (n_e) across the targets. Ideally, this information is obtained experimentally. The key aspect of OSM lies in inputting boundary condition information from experiments across the SOL radially, thus constraining each individual flux tube Stangeby [2000].

OSM modeling can be implemented at various levels of sophistication. In initial applications, simple analytic OSM models were incorporated into the DIVIMP code to create "plasma backgrounds" for launching Monte Carlo particles, without employing actual experimental data as boundary conditions. Subsequent developments involved the use of experimental measurements of n_e and T_e across limiters as boundary conditions, still employing simple analytic OSM models. The evolution of OSM continued with the introduction of full 1D fluid models, incorporating experimental boundary conditions Stangeby [2000].

One can begin by considering a straightforward scenario where each flux tube in the SOL is assumed to be in the sheath-limited regime, with constant T_e and T_i along each flux tube but varying radially based on the boundary values at the target. This involves using balance equations that yield values of T_e, T_i, n_e, velocity (v), and electric field (E) at each location along the flux tube. As T_e, T_i, and n_e typically vary across the targets, the OSM generates a 2D solution of the SOL. Notably, the information needed for radial variations enters the solution directly from the target boundary conditions. In contrast to the standard 2D fluid model approach, this method does not rely on imposed cross-field transport coefficients ($D_\perp$, $\chi_\perp$, etc.), which, in fact, are not imposed in the OSM. Instead, these coefficients can

be effectively extracted from the target boundary conditions using the OSM Stangeby [2000].

The standard 2D fluid code approach involves imposing boundary conditions at specific points or along a single flux surface, such as the density at the upstream separatrix location or the power flow across the separatrix. In contrast, the Onion-Skin Method (OSM) adopts a different approach. In OSM, boundary conditions or solution-constraining information are specified radially across the entire Scrape-Off Layer (SOL), eliminating the need to assume values for cross-field transport coefficients. This spatially distributed constraint input can come from probes at targets, upstream, spectroscopic measurements, and more. To handle an abundance of experimental information that could over-constrain solutions, algorithms are employed to minimize variance between total experimental input and computed values Stangeby [2000].

SOL 22 - an OSM plasma solver option for attached plasma conditions

The 1D plasma solver generates 2D SOL solutions, which are then iterated with a neutral hydrogen code such as EIRENE. Impurity effects can be included by extending the 1D plasma equations to a multi-fluid mode or by using a Monte Carlo impurity code like DIVIMP iteratively with the 1D plasma solver. OSM modeling simplifies by disregarding particle and momentum cross-field sources and sinks, attributing all cross-field power input to a simple distribution. More sophisticated versions include spatially distributed sources and sinks for particles, momentum, and energy, balanced through iteration. Cross-field contributions, even at basic levels, typically have minimal impact on the solutions Stangeby [2000]. In other words, the OSM code offers the flexibility to employ distinct solution methods for each "half-ring," defined from the target to a designated "symmetry" point on the ring denoted as s_{sym}. This adaptability is a benefit of the 1D approach, as it doesn't strictly mandate local cross-field flux conservation on a cell-by-cell basis. The choice of solver can be tailored to specific plasma regions based on the plasma conditions, determined

through the analysis of experimental data, such as: SOL22 addresses the standard conservation equations and typically employed in OEDGE for attached plasmas, and SOL24/SOL28 to incorporate prescription-based, semi-empirical methods designed for approximating detached plasmas.

SOL22 is designed to solve a particular set of 1D Braginskii plasma fluid equations, yielding results for electron temperature (T_e), ion temperature (T_i), electron density (n_e), and parallel velocity ($v_\parallel$) along a half-ring. The assumptions made in this calculation are that T_e is equal to T_i and n_e is equal to n_i.

$$\frac{\partial}{\partial s}(n_e v_\parallel) = S_{ion}(s) + S_{rec}(s) + S_\perp(s) \tag{2.55}$$

$$\frac{\partial}{\partial s}(p + m_i n_e (v_\parallel)^2) = S_{mom}(s) \tag{2.56}$$

$$\frac{\partial}{\partial s}(q_{i,conv.} + q_{i,cond.} + q_{e,cond.}) = Q_i(s) + Q_e(s) + Q_\perp(s) \tag{2.57}$$

In the above equations, s represents the position along the magnetic field line, p denotes static pressure, m_i is the mass of the plasma ion, $q_{i,\mathrm{conv}}$ signifies the power carried by ions through convection, and $q_{i,\mathrm{cond}}$ and $q_{e,\mathrm{cond}}$ are the conducted powers for ions and electrons, respectively. The volumetric sources taken into account consist of ionization (S_{ion}), recombination (S_{rec}), momentum (S_{mom}), and the power terms for ions (Q_i) and electrons (Q_e). Additionally, $S_\perp$ and $Q_\perp$ represent the cross-field particle and power fluxes, playing roles as volume sources in the 1D formulation.

SOL22 is iteratively coupled with the EIRENE neutral code, which calculates the volumetric source terms for plasma-neutral interactions (S_{ion}, S_{rec}, S_{mom}, Q_{i}, and Q_{e}). The magnitudes of Γ_{ion} and Γ_{pow} can then be calculated from conservation principles: with known target fluxes - assigned from LP measurements for a given half-ring - and volumetric source terms, the particle and power balance for a specific ring must be satisfied by the net cross-field flux into or out of the ring. The temperature gradient

is computed using a 5th order Runge-Kutta method which begins computation at the target and proceeds spatially in the upstream direction. It is to note that since Γ_{ion} and Γ_{pow} are poorly characterized due to nature of anomalous cross-field transport, the distribution is assumed to be uniform.

2.4.4 OEDGE

The OSM-Eirene-Divimp-EdGE (OEDGE) modeling code measures edge plasma of magnetic fusion devices iteratively. As the name suggests, OEDGE combines onion-skin analysis (OSM) with EIRENE and DIVIMP codes for edge analysis. The OSM code solves 1D background plasma conservation equation that are along the B-field using data from Langmuir probes from the experiment to produces a 2D edge plasma solution that is toroidally symmetric. The OSM analysis is insensitive to convective or diffusive transport assumptions which can be extracted out of the solution provided by the code. The solution is then coupled with a neutral hydrogen Monte Carlo code called EIRENE and also coupled with impurity neutral and ion Monte Carlo code called DIVIMP. In simpler terms, using OEDGE one gets iteratively solved edge diagnostic measurement for n_e, T_e, T_i, n_0 and other quantities that are desired for understanding physics related to main chamber recycling, tritium retention, detachment onset etc.

The approach taken while making OEDGE was that of an iterative model rather than a predictive model. The predictive model expects to have calculated everything including the plasma hydrogenic species, impurity species in the core and the edge. The predictive model would have to model the whole machine with all the impurities in the 3D space of the tokamak. This however, is not only computationally expensive, but is riddled with uncertainties. On the other hand, the interpretative model approach helps reduce those uncertainties regarding the fuel and impurity species. The background / plasma core can be made from experimental measurements with

known 2D n_e, T_e, T_i from diagnostics such as Thomson Scattering that are present both in the core and the edge.

The idea behind OEDGE is to model impurity species and hydrogenic species in the edge which can be understood by adjusting the 'controlling knobs' or 'input options' which would launch impurity in the known plasma background and see how the edge measurements change. This helps in diagnosing the edge measurements where actual experimental measurements are not possible. Measurement of edge plasma has been sparse due to multiple reasons such as cost of implementation and fewer diagnostic locations available to lease in a tokamak. OEDGE take multiple experimental inputs options and plug them into the plasma background to refine and better diagnose the edge Stangeby et al. [2003], McLean et al. [2005], Stangeby [2000].

OEDGE code initially started as an impurity ion transport model for limiter source specifically called LIM around 25 years from today Stangeby et al. [1988], Stangeby and Farrell [1990]. Eventually the code was modified to understand impurity ions from a divertor and was labelled as DIVIMP Stangeby and Elder [1992]. Over the next decade, in the 1990's, the DIVIMP code was used to calculate impurity retention in the divertors Stangeby and Elder [1995] and was used to compare with other model codes such as EDGE2D Stangeby et al. [1997]. The next decade, early 2000's, saw DIVIMP being used with Onion Skin Model (OSM) and EIRENE model and was re-branded as OEDGE Stangeby et al. [2003] to estimate fuel species along with impurity species in the edge region. It is to note that a standalone DIVIMP system was being used to model different impurities from different plasma machines such as DIII-D, ASDEX-Upgrade, ITER and NSTX up until late 2010's. While OEDGE helped understand edge impurity from divertor region in fusion devices around the world, LIM was revived into a 3-dimensional code called 3DLIM by Carpentier Carpentier et al. [2011] and was later resurected again by Zamperini et al. [2020, 2022], Shawn Zamperini and Crowe [2023]. Figure 2.24 shows n_e from an example case from OEDGE run.

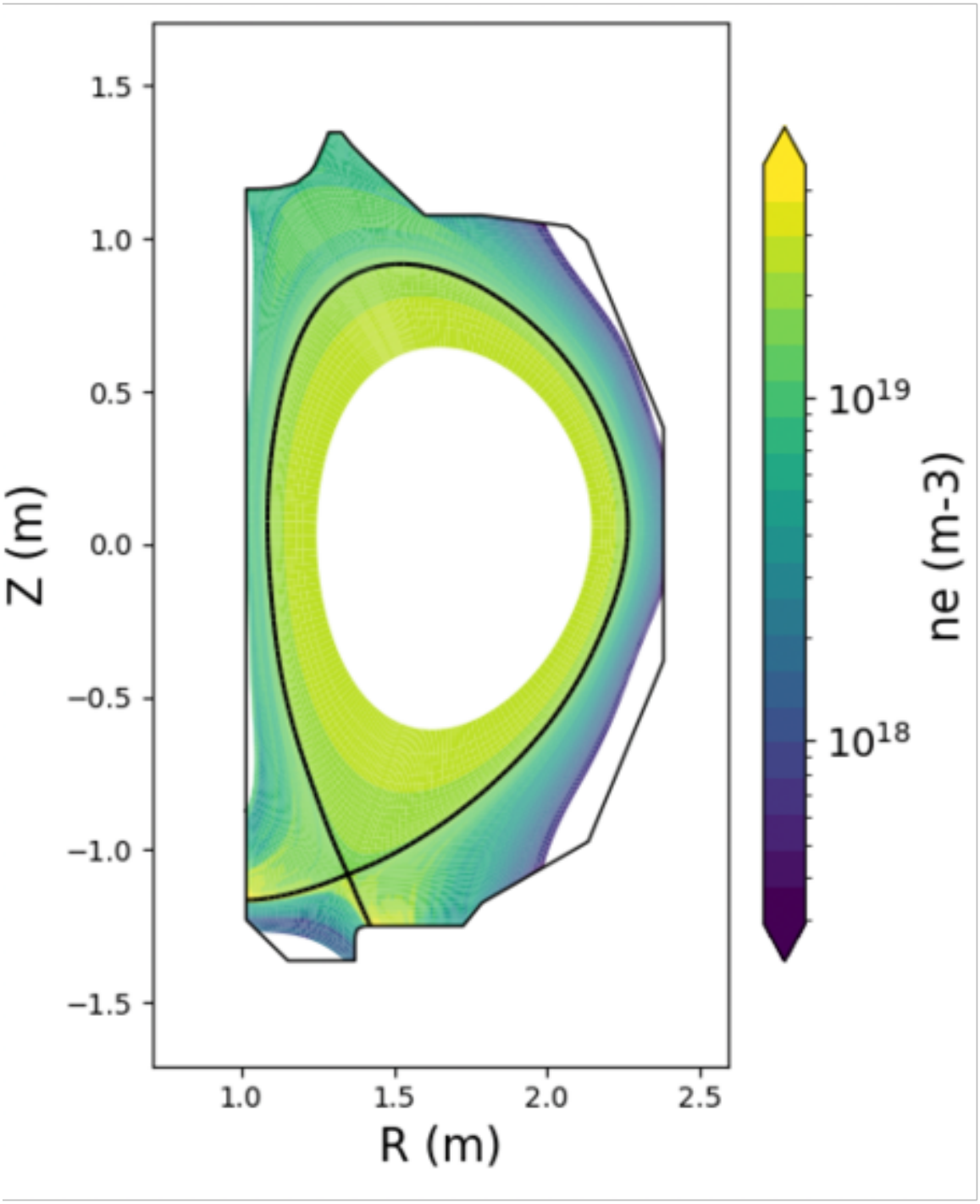


Figure 2.24: Plasma solution depicting n_e from an OEDGE simulation poloidally across DIII-D tokamak

2.5 DIII-D Tokamak Diagnostic Suites used to quantify ion fluxes in main chamber and divertor region

2.5.1 Thomson Scattering

A charged particle is set into motion by Lorentz force exerted by the electric and magnetic components of an electromagnetic wave. This particle, which moves in a specific periodic time just like the wave, is accelerated and emits radiation consequently. This radiation occurs due to the fact that the charged particle has absorbed the energy from the wave and remits as an electromagnetic radiation. The process by which the wave is deflected by free electrons and emits radiation is known is Thomson Scattering (TS) Richard [2014].

This technique on DIII-D tokamak measures the temperature and density of the electron in the plasma core and the divertor Carlstrom et al. [1992], Glass et al. [2016]. It uses multiple Nd:YAG pulsating lasers to make measurements rapidly during a plasma discharge that could help measure electron temperature and density during L – H transition and ELMs. The TS system incorporates polychromator with digitizing modules to help acquire and analyze data at plasma core and the divertor as shown in Figure 2.25 Ponce-Marquez et al. [2010]. The data is available to any user using the REVIEW code in the DIII-D data acquisition system. A normal measuring range for the electron temperature is 10 eV to 20 keV and a minimal electron density about 2 x $10^{18} m^{-3}$ Carlstrom et al. [1992].

In the last four years, to characterize the temperature and density of the electron in the divertor, Divertor Thomson Scattering (DTS) system has been added that inputs 8 channels to the divertor region from the main TS system. It was implemented in parallel to the Langmuir probes as the probes had complications in the data. However, the main goal of the DTS system is to measure temperature and density of

the electron at the divertor to help understand important physics phenomenon such as: divertor detachment, and advanced tokamak physics Glass et al. [2016].

Figure 2.26 depicts sample data from Thomson scattering data for L mode and H mode discharges in DIII-D. As seen, the electron temperature and density are higher in H mode compared to that in L mode. The measurement, however, show the decrease in electron temperature and density when moving radially outwards across the separatrix.

2.5.2 Langmuir Probes

Langmuir probe is a simple electrostatic probe that perturbs plasma and measures local electron density, electron temperatures and their fluctuations. Essentially, it is a wire inserted into plasma that is held via an insulator that measures the current and voltage present at the probe tip. This tip is surrounded by sheath or an electrostatic charge layer. Dolan [2013]

The working theory of Langmuir probes depends solely on the voltage applied to the probe. With varying voltage, there is a distinct I-V curve that is produced as shown in 2.27. The reference point, called the space potential (V_{pl}) is when the voltage applied to the probe is equal to the plasma potential. When voltage to the probe is greater than the space potential, ions will be repelled and electrons will be attracted towards the probe.

The sheath around the probe will have non-zero electric field and the electron saturation current can be measured depending on the acceleration of the electrons into the sheath. If the probe voltage is lower than the space potential, the opposite will happen, i.e., ions will be attracted to the probe and ions will be repelled. Once enough ions are attracted to the probe that equals the number of electrons, a floating potential (V_{fl}) is created. This is different from the plasma potential as the voltage would be different as seen in 2.27.

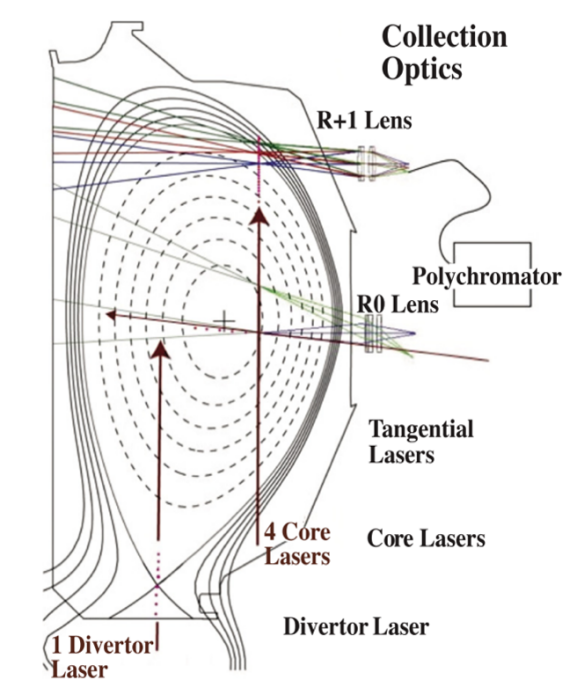


Figure 2.25: Cross-section of DIII-D with Thomson system laser path and view ports. Image from Ponce-Marquez et al. [2010]

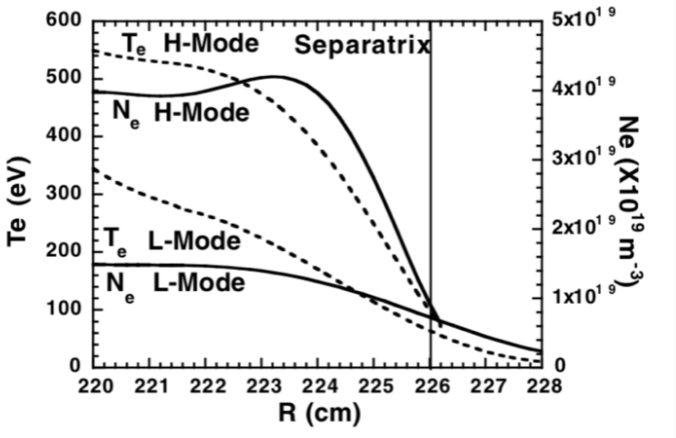


Figure 2.26: Plot depicting the electron temperature (dashed) and density (solid) measured via Thomson Scattering. Image from Colchin and Owen [2003]

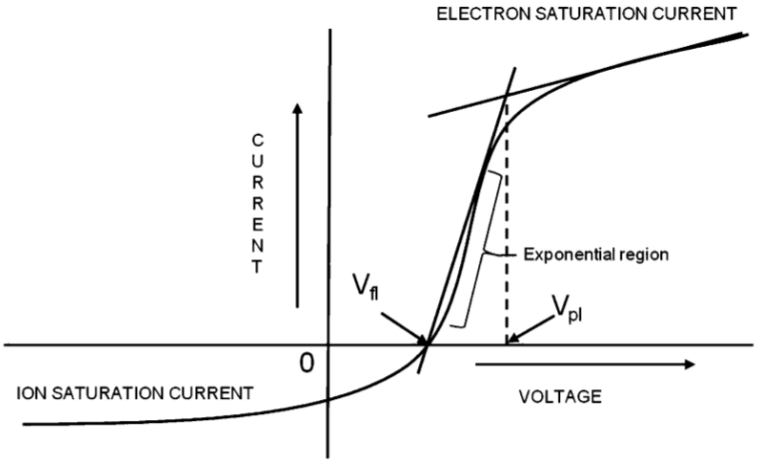


Figure 2.27: I-V characteristic for the Langmuir probe. Image from Dolan [2013]

Similar to how the electron saturation current is achieved due to positive voltage applied to the probe, if strong negative voltage is applied to the probe, ions are attracted and electrons are repulsed to reach the ion saturation current. In DIII-D, there are 72 fixed Langmuir probes and two reciprocating Langmuir probes that measure local density, temperature, floating potential, heat flux and particle flux. Out of the 72 probes, 30 probes are located at the Upper divertor and the rest are on the Lower divertor. There are two translating probes that plunge 15cm into the device from midplane location and x-point location in the lower divertor. The translating probes measures density and temperatures as the probe plunges into the plasma. The midplane probe is a double Langmuir probe system that utilizes two probe tip at high frequency upto 2.5MHz and has a plunge speed of 150ms. The x-point probe is also a double Langmuir probe system and has a plunge speed of 300ms DIII-D [2023]

Now that we are aware of the fact that a Langmuir probe generates an I-V curve, let's explore the process of deriving electron density (n_e) and electron temperature (T_e) from this curve. The electron energy distribution is directly related to the second derivative of the electron current to the probe, as illustrated in Equation 2.58 Ruzic [1994].

$$f_E(E) = \frac{-4}{A_p \cdot e^2} \cdot \frac{m_e(V_{plasma} - V)^{\frac{1}{2}}}{2e} \cdot \frac{d^2 I_e(V)}{dV^2} \tag{2.58}$$

This electron energy distribution function provides the count of electrons within the energy range of E to E+dE. Assuming a Maxwellian distribution for the electron energy, Equation 2.58 can be integrated twice, allowing the theoretical electron current as a function of probe voltage to be determined for voltages below the plasma potential. Given that $\mathrm{E} = e(V_{plasma} - V_{probe})$, the integration yields Equation 2.59. In this equation, I_{sat} represents an exponential decline in current from its value at the plasma potential Ruzic [1994].

$$I_e(V_{probe}) = I_{e,sat} \cdot e^{\frac{-e(V_{plasma} - V_{probe})}{kT_e}} \tag{2.59}$$

where $I_{e,sat}$ is given by

$$I_{e,sat} = eA_p n_e \sqrt{\frac{kT_e}{2\pi m_e}} \tag{2.60}$$

The determination of T_e is not based on a single I-V point at the plasma potential, as per Equation 2.60, but instead relies on a series of I-V points. Taking the natural logarithm of Equation 2.59 and plotting $ln|I_e(V)|$ against V, T_e can be extracted as the inverse of the slope, eliminating the need for electron density (n_e). Equation 2.60 can be reformulated, as shown in Equation 2.61 Ruzic [1994].

$$ln(|I_e(V)|) = \frac{-e}{kT_e}(V_{plasma} - V) + ln(|I_{e,sat}|) \tag{2.61}$$

If the energy distribution is non-maxwellian, the T_e is then given by the follwing equation:

$$\bar{E} = \frac{3}{2}kT_e \tag{2.62}$$

Now that we have the T_e from 2.61 and 2.62, let us get to getting the n_e. It can be found out using the I-V curve using the following equation Ruzic [1994]:

$$n_e[m^{-3}] = 3.73 \times 10^{13} \cdot \frac{I_{e,sat}[A]}{A_{probe}[m^2]\sqrt{T_e[eV]}} \tag{2.63}$$

It is to note that the $J_{e,SAT}$ and $I_{e,SAT}$ are assumed to be the same as $J_{i,SAT}$ and $I_{i,SAT}$ throughout this thesis.

2.5.3 The Filterscope

Filterscope is a band-pass radiometer that is used in high temperature plasmas, such as DIII-D as a spectroscopic tool to monitor different measurements such as, effective ion charge of the plasma, SOL temperature and densities, and PMI Unterberg et al. [2019]. One of the main utilization of the Filterscope is to detect Dα light that is

primarily produced at the plasma edge and divertor to help quantify plasma edge conditions and divertor recycling Colchin et al. [2003]. Filterscope was developed by ORNL two decades ago and have been deployed on various fusion devices around the world: including DIII-D, NSTX-U, KSTAR and Proto-MPEX, due to its remote, compact, cost-efficient and modular design Brooks et al. [2008], Unterberg et al. [2019], Colchin et al. [2003].

Filterscope is made up of three main components: (1) Endoscope – like fiber optic cable (2) narrow – bandpass filter and (3) a Photomultiplier Tubes (PMT) detector. The fiber optic cable allows for highly sensitive measurements at remote locations in the fusion device. The line of sights for these fiber optics are seen in Figure 2.28. The narrow bandpass filter allows the user to measure the specific line of interest in the visible spectra and the PMT detector along with its associated electronics help convert the incoming light into voltage signal. The Filterscope uses a National Instrument DAQ (Data acquisition and Control) system to help acquire data from up to 96 channels at a sampling rate of 1 MHz for up to 10 minutes Vacaliuc et al. [2005], Unterberg et al. [2019]. The fast sampling rates help study various transient effects such as Edge Localized Modes (ELMs) and SOL turbulence Colchin et al. [2003]. More details about the calibration philosophy of the Filterscope can be found in Appendix A.

2.5.4 Neutral pressure gauges

The concept of ASDEX gauges was developed by Haas and team at Germany ASDEX Team et al. [1984] and Klepper and team applied it to the DIII-D system in 1993 Klepper et al. [1993]. Since then DIII-D has six fast neutral pressure gauges positioned strategically in the upper and lower divertors, as well as at the vessel midplane. These gauges are all commercial adaptations of gauges from ASDEX tokamak and hence are also called the 'ASDEX gauges'. These gauges are capable of measuring pressures ranging from 10^{-3} mtorr to 10 mtorr at higher magnetic fields and temperature ranges.

As detailed in Klepper et al. [1993], Haas and Bosch [1998], the ASDEX gauge employs a tetrode configuration, a type of electronic vacuum tube featuring four active electrodes: a cathode, a control grid, a screen grid, and a plate (anode) as seen in Figure 2.29(a). Positioned between the cathode and the anode, an aperture plate modulates the emission current, crucial for extracting signals in noisy environments like tokamaks.

This modulation, typically at 10kHz, is facilitated by electronics derived from ASDEX's data acquisition system. Operating within a magnetic field, the gauge's alignment within 15°ensures enhanced sensitivity of ion current to neutral pressure. The filament operates with a heating current of 15 ($\pm$5) A, reaching 25-30 A during startup, while the accelerator grid maintains a fixed potential of +250 V. The modulator oscillates between +25 and +125 V to modulate the emission current, which is feedback-controlled based on its modulation amplitude. Transformers isolate the vessel ground from electronics chassis ground to measure modulation amplitude accurately. The electronics amplify and demodulate both ion and electron currents, with ion current being pressure-sensitive and regulated by a feedback circuit controlling filament heating current.

During rapid pressure changes, such as edge-localized modes (ELMs), filament cooling may temporarily reduce emission current, corrected by the feedback circuit Klepper et al. [1993]. Figure 2.30 shows the pressure measurement from the midplane pressure gauge from plasma discharges that are utilized to investigate the magnitude of fluxes in the divertor and midplane region throughout the thesis. Pressure measurements were taken for plasma discharges exhibiting $B \times \nabla B$ orientation toward the target in both L-mode (subfigure a) and H-mode (subfigure b), as well as for discharges with $B \times \nabla B$ directed away from the target in L-mode (sub-figure c) and H-mode (sub-figure d). The discharges represented in blue correspond to divertor geometries of LSN Shelf, those in red represent the USN Floor, and those in black illustrate the LSN Floor condition. The pressure measurements, as seen, range from 10^{-9} to 10^{-6} Torr.

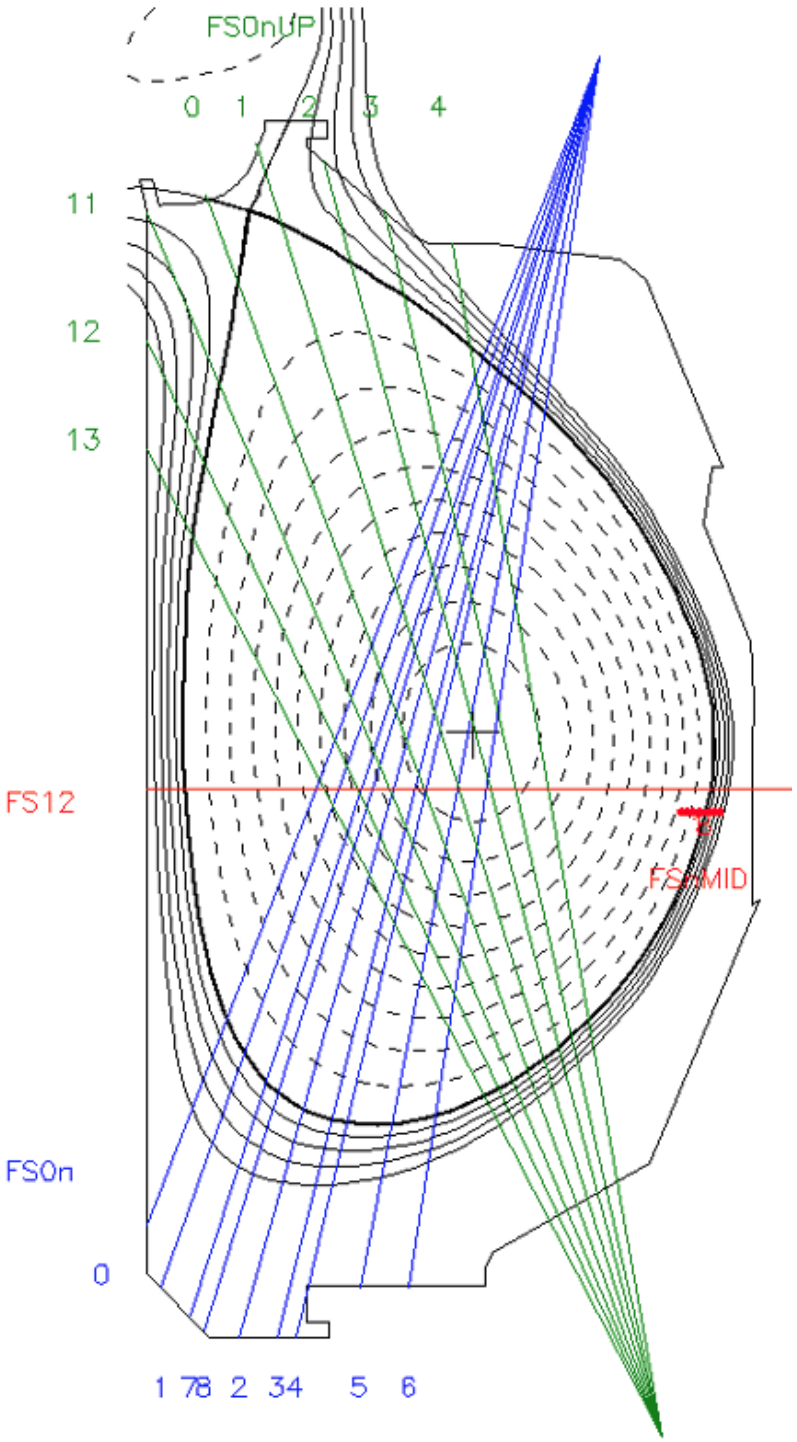


Figure 2.28: Line of sights (LOS) for Filterscope on the DIII-D tokamak showing LOS for LSN (blue), USN (green), midplane (red)

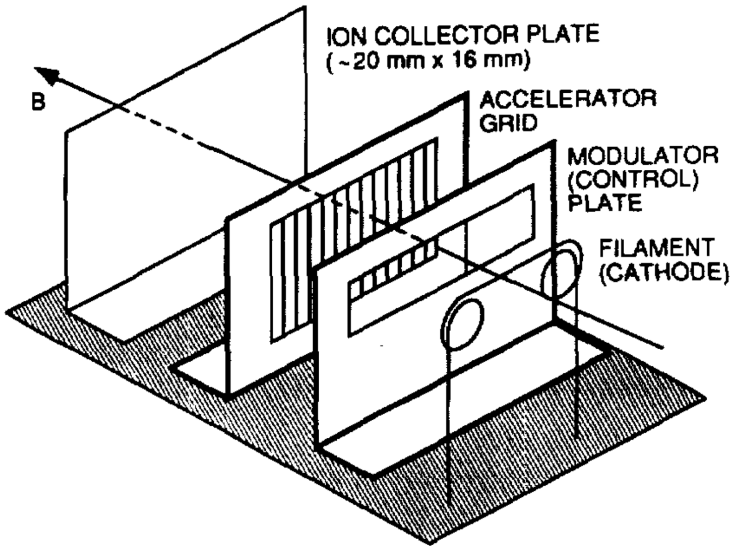


Figure 2.29: Detailed schematic of the ASDEX gauge. Image from Klepper et al. [1993]

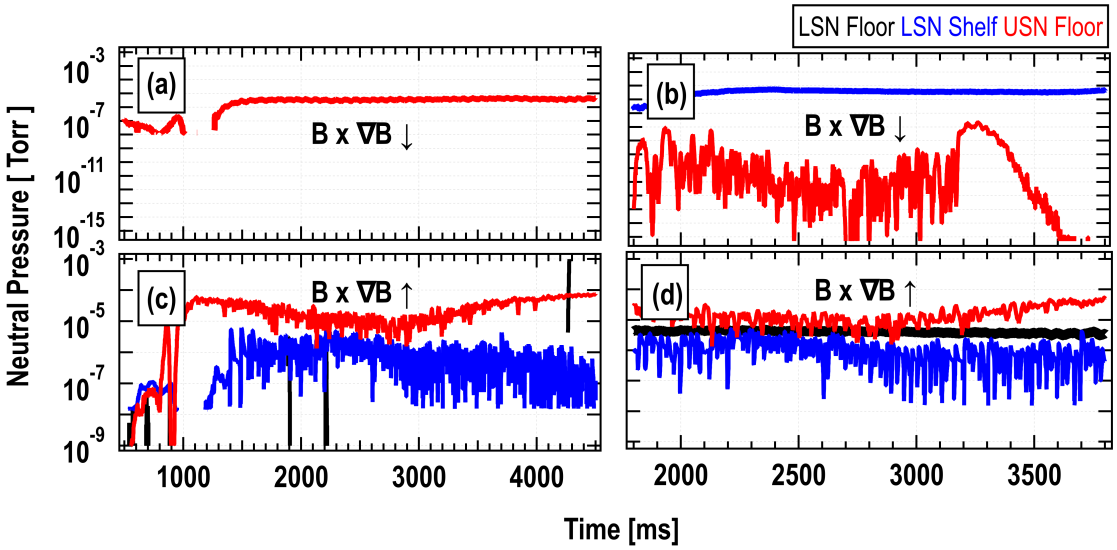


Figure 2.30: Midplane pressure measurements for plasma discharges with $B \times \nabla B$ towards the target in L-mode (subfigure a) and H-mode (subfigure b) and with $B \times \nabla B$ away from the target in L-mode (sub-figure c) and H-mode (sub-figure d). The discharges in blue are from divertor geometries of LSN Shelf, red depict the USN Floor and Black show LSN Floor condition.

Chapter 3

Analysis framework for tokamak closure interpretation

In this chapter a systematic examination is undertaken to elucidate the nuanced intricacies inherent in divertor physics and neutral transport. The chapter is divided into two sections. Section 3.2 meticulously details the GRP and WFA. The WFA section details the steps to get f_{wall}, the ratio of particle flux magnitudes between the main chamber and the divertor region (Equation 3.8) while the GRP subsection unveils insights into divertor restrictions for conventional and non-conventional divertors on DIII-D. In the second section 3.3, the empirical analysis is replicated using the OEDGE model. This is intended to reproduces the empirical WFA methodology. It also calculates the magnitude of poloidally averaged fluxes in the main chamber versus the divertor thanks to the availability of data in the model.

3.1 Understanding the neutral pathways in the tokamak edge

The fundamental principles governing divertor recycling, leakage, and main chamber recycling are elucidated in Section 2.3.2. Building upon this comprehension and

drawing inspiration from Figure 2.14, we present Figure 3.1, illustrating the flow of neutrals and their evolution to ions in the scrape-off layer (SOL) and edge region of the DIII-D tokamak. In Figure 3.1, neutral and ion pathways are represented by 'o' and '+', respectively.

Pathway 1 (orange) describes divertor recycling. A combination of pathway 1 (orange), 2 (green-near the main chamber region) and 6 (maroon) involves ions directed towards the divertor plate, recycling upon arrival, traversing through the divertor region, undergoing ionization within the core, and necessitating radial transport out of the core, followed by their return to the divertor plate via the SOL. Pathway 3 (blue) represents the radial transport of ions to first-wall surfaces outside the divertor, where they recycle as neutrals, and the ions that do not recycle on the first-wall surface and are lost to the core are labeled by pathway 4 (black). It is assumed here that although pathway 2 neutrals penetrate the core in close proximity to the divertor, they uniformly exit the core as ions. This assumption applies equivalently to pathway 3 as well.

While the aforementioned pathways primarily serve to explain neutral transport within the SOL region, it is imperative to provide a comprehensive depiction that encompasses the pathways of ionized neutrals beyond the divertor, extending poloidally across the tokamak. In Figure 3.1, three additional pathways are depicted:

- The pathway denoted as 'sep' in red illustrates the magnitude of ions at the separatrix, representing ions emitted from the core region and reaching the separatrix.
- The pathway labeled 'Core' in teal color illustrates the magnitude of ions originating from the core-confined plasma.
- Pathway 5, depicted in purple, illustrates the magnitude of ions reaching the tokamak wall.

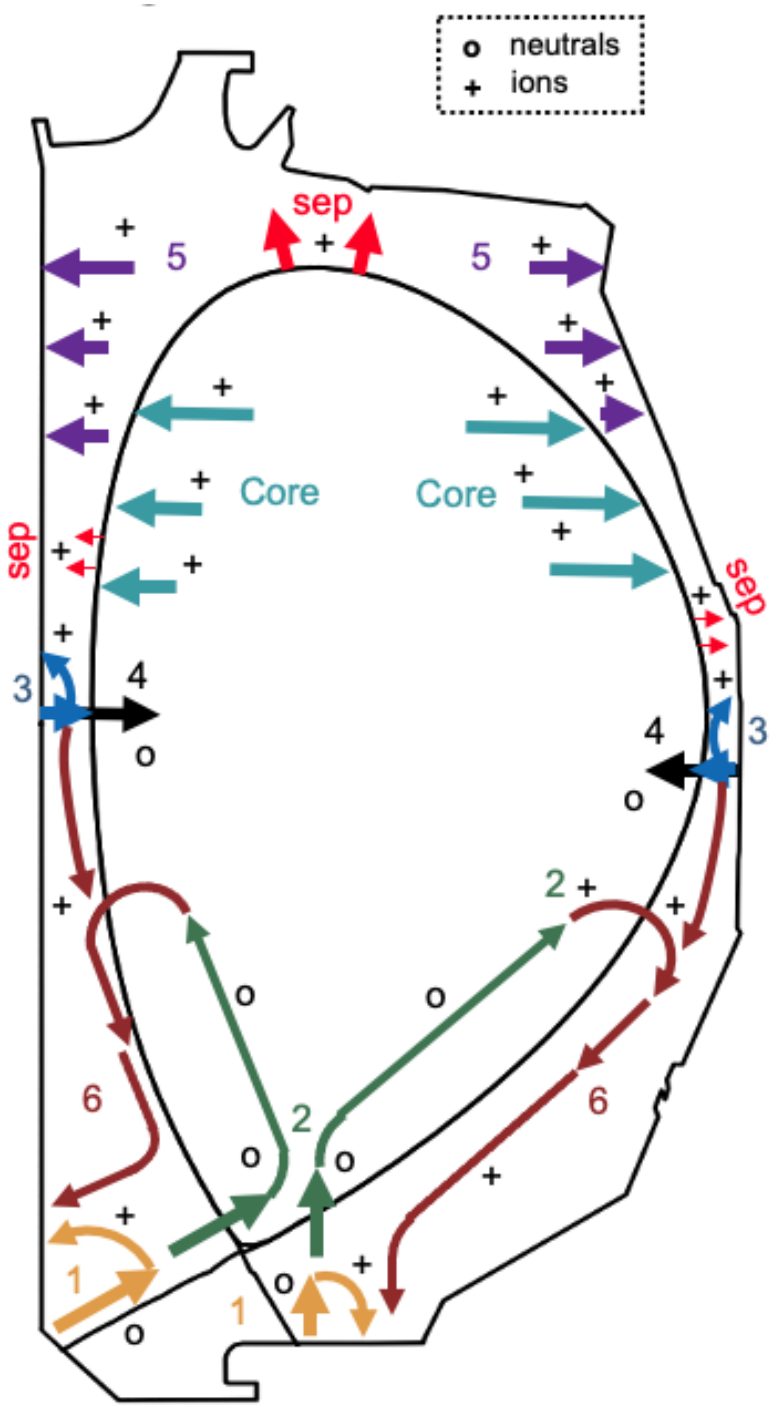


Figure 3.1: Neutral and ion pathways at the edge of the tokamak. Neutrals are depicted as 'o' and ions are depicted as '+'. The pathways range from 1 to 6 in the edge with divertor recycling depicted in orange as loop 1 and main chamber recycling loop depicted with blue as loop 3. There is a divertor leakage recycling loop that is depicted as Loop 1, 2, and 6 with colors ranging from orange, green, and maroon

These interconnected pathways play a crucial role in advancing the understanding of the analysis conducted in Chapter 4. However, for the sake of simplicity, we assume both poloidal and toroidal symmetries in the ionization sources and radial ion fluxes.

Defining the ion fluxes through the pathways is crucial for understanding the specific roles of each pathway under different conditions. For instance, in the scenario where the divertor is tightly restricted with a baffle structure, the flux at pathway 2 would be expected to decrease, while the flux at pathway 1 would increase. This is because higher restriction facilitates more recycling by trapping the neutrals generated in the divertor within the divertor itself. Similarly, with pathway 2 experiencing reduced flux due to higher restriction, the fluxes in pathways sep, 5, and 6 would also vary accordingly.

However, in order to quantify these effects and gain a deeper understanding of the underlying physics, it is necessary to express the pathways in simple mathematical formulations. It is to note that the particle (ion) flux at any given pathway is labeled as 'I'. There as three main loops created by the neutral pathways:

- Divertor recycling (DR) loop: $I_1 + I_2$
- Divertor Leakage Recycling (DLR) loop: $I_2 + I_6$
- Main Chamber Recycling (MCR) loop: I_3

There are two major fueling pathways where neutrals emitted ends up as a fueling source: I_2^0, and I_4^0.

The wall flux can be defined as:

$$I_{wall} = I_3^+ + I_5^+ \tag{3.1}$$

The divertor flux can be defined as:

$$I_{div} = I_1^+ + I_6^+ \tag{3.2}$$

The SOL flux can be defined as:

$$I_{SOL} = I^{+}_{sep} - I^{+}_{5} \tag{3.3}$$

The flux for pathway 6 can be defined as:

$$I^{+}_{6} = I^{+}_{core} + I^{+}_{SOL} + I^{+}_{2} + I^{+}_{4} \tag{3.4}$$

Recall Equation 3.8, it is the ratio of magnitude of fluxes at the wall and at the divertor. Substituting Equations 3.1 and 3.1 to the Equation 3.8, we can rewrite it as:

$$f_{wall} = \frac{I_{wall}}{I_{div}} = \frac{I^{+}_{3} + I^{+}_{5}}{I^{+}_{1} + I^{+}_{6}} = \frac{I^{+}_{3} + I_{SOL} - I^{+}_{sep}}{I^{+}_{1} + I^{+}_{core} + I^{+}_{sep} + I^{+}_{2} + I^{+}_{4} - I^{+}_{5}} \tag{3.5}$$

Equation 3.1 provides insights into which pathways influence the magnitude of fluxes in both the wall and divertor regions. One of the key questions addressed in this thesis is understanding the impact of divertor design and operation on the magnitude of neutral particle fluxes. Specifically, it aims to comprehend the balance between divertor recycling and main chamber recycling and how this balance varies under different restrictions (GRP).

This balance can be comprehensively understood through the measurement of particle fluxes in both the divertor region and the outer midplane region, accounting for varying restrictions. By employing this method, we can grasp the collective trend of I_{div} and its consequential effects on divertor performance. One approach to achieve this is by analyzing the D_{α} signal and subsequently calculating the particle flux in both the divertor region and the outboard midplane region, thus elucidating the implications of neutral ionization. It is however important to note that isolating one pathway for the leakage or recycling in divertor or main chamber is complicated and

is not understood properly. There, in order to understand the balance between the neutral pathways, we can measure ion fluxes in main chamber and divertor region and indirectly understand the role and dominace of neutrals. the following sections talk about the methodology in detail.

3.2 Methodology - Measurement of ion fluxes in main chamber and the divertor to interpret divertor closure

This section explains the methodology to obtain f_{wall} using Filterscope and Langmuir probes and also details the estimation of the geometric restriction parameter for the quantification of divertor restriction.

3.2.1 Window Frame Analysis

The Window Frame Analysis (WFA) technique, based off of theoretical work done by Stangeby [2002], has been developed and implemented previously on DIII-D Whyte et al. [2005], Leonard et al. [2003] to quantify the accurate time-averaged particle flux to wall surfaces outside the divertor region on the Low Flux Side (LFS) of the tokamak Whyte et al. [2005]. The utilization of axisymmetric limiter surfaces beyond the divertor is aimed at minimizing the need for extrapolation when measuring the overall plasma-wall flux. The peripheries of two continuously toroidal baffles, situated at the entry points of the upper divertor (labeled as A in figure 3.2 and 3.3) and lower divertor (labeled as B in figure 3.2 and 3.3), delineate a flux surface resembling a 'window-pane.' Just like an actual window frame and window pane (see figure 3.2), the concept of creating a window frame and pane is similar. The window-pane/surface facilitates the passage of the cross-field ion flux density ($\Gamma_{\perp} \equiv j_{wall}$, [ions $s^{-1}m^{-2}$]), averaged over the window-pane, toward the main chamber wall much like the glass

pane through wich one can see outside the window. The region radially situated 'behind' the window-pane is denoted as the shadow plasma region and the baffles make up the window frame. These baffles act as plasma ion sinks for the primary wall. I_{wall} based off of previous work from LaBombard et al. [2000], calculates radial particle flux [ions s^{-1}] towards the far SOL and the main wall and is unaffected by any geometric assumptions regarding the reception of plasma flux through the window-pane. I_{wall} is defined as follows.

$$\Gamma_{\perp} \equiv j_{wall} = \frac{I_{wall}}{2\pi R L_{pol}} \tag{3.6}$$

Here, both average major radius of the device (R) and poloidal extent of the windowpane are in meters. For simplicity, we will use the term 'window-frame' to describe this axisymmetric configuration of magnetic geometry and primary-wall surfaces, with the primary-wall surfaces referred to as 'baffles'.

In an ideal scenario, employing an array of embedded probes within the surface of the window-frame would be the preferred method to directly measure the incoming plasma flux on the window-frames. This would allow for a straightforward spatial integration to derive I_{wall}. However, the current setup in DIII-D only features a solitary embedded probe in the LFS of the upper baffle. Consequently, we have devised methodologies to calculate I_{wall} using plasma measurements taken in the shadow plasma, situated at locations far removed from the surfaces of the window-frame. This approach considers variations in geometry and accounts for the sink effect of the window-frame surface using a reciprocating probe near the outboard midplane. Using this, I_{wall} can be defined as:

$$I_{wall} \cong C_{geom}(n_e T_e^{1/2})_{window-pane} \lambda_{shadow}) \tag{3.7}$$

Here, C_{geom} is a constant that can be obtained from the Appendix in Ref. Whyte et al. [2005]. The Electron temperature and density and the radial decay length of

the density in the shadow region is obtained from the reciprocating Langmuir probes as previously stated.

While the ion flux in the main chamber is given by Equation 3.7, the total ion flux received on the divertor target I_{div}, outside the window-frame is measured using an array of embedded Langmuir probes in the divertor region. For the sake of simplicity, the ratio of plasma flux received at the main-wall to that received at the divertor is defined as

$$f_{wall} = \frac{I_{wall}}{I_{div}} \tag{3.8}$$

f_{wall} acts as a simple indicator for making rough estimations of plasma-wall contact by providing the magnitude of fluxes in the main chamber and at the divertor. The magnitude of f_{wall} is directly proportional to the line averaged core plasma density and ranges from 0.1 to 1, where 1 indicates detached plasma conditions and most likely that the main chamber wall acts as particle sink instead of the divertor target.

Calculating f_{wall} through WFA

The general Window Frame Analysis (WFA) outlined in Section 3.2.1 involves the computation of particle flux using a single reciprocating Langmuir Probe (RCP) situated near the outboard midplane within the primary chamber region of the DIII-D tokamak. This method is valuable for estimating parameters such as I_{wall} and f_{wall}. However, the RCP is contingent upon diagnostic availability and needs. Due to this unavailability of RCP in every plasma discharge, a significant volume of data from DIII-D remains untapped and underutilized. To address this limitation, utilizing Filterscope system close to the location of RCP was introduced.

In Figure 3.4, the main-wall D recycling fluxes, Γ_D, measured at various locations at the LFS main chamber are compared with the averaged plasma ion flux density to the main wall, j_{wall}.

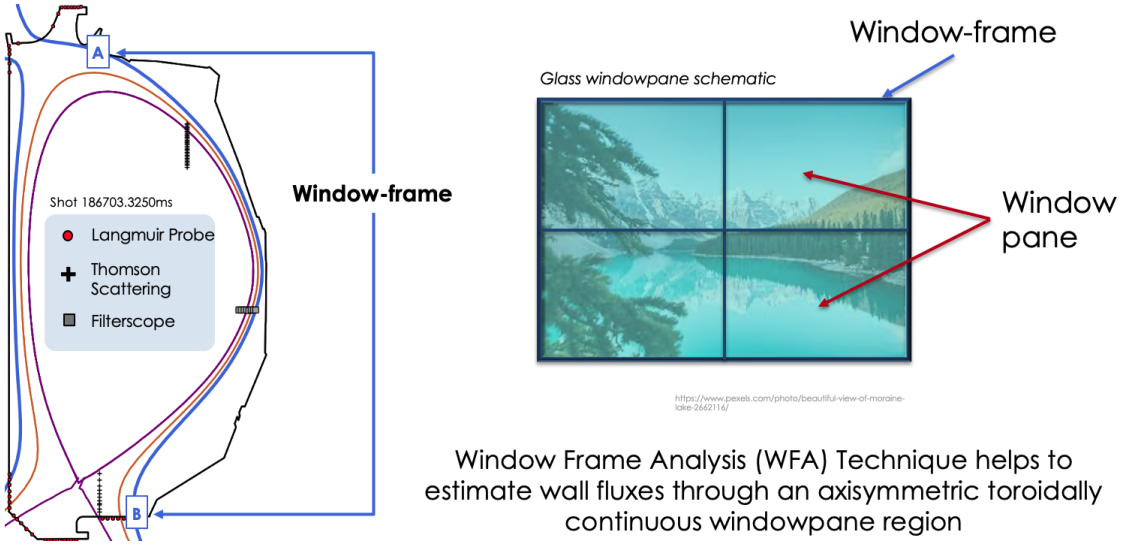


Figure 3.2: A schematic representing window frame analysis in terms of actual window frame. Figure on the left shows a poloidal cross-section with window-frame depicted as point A-B as seen in the analogy from the figure on the right. The flux surface between points A and B is the windowpane

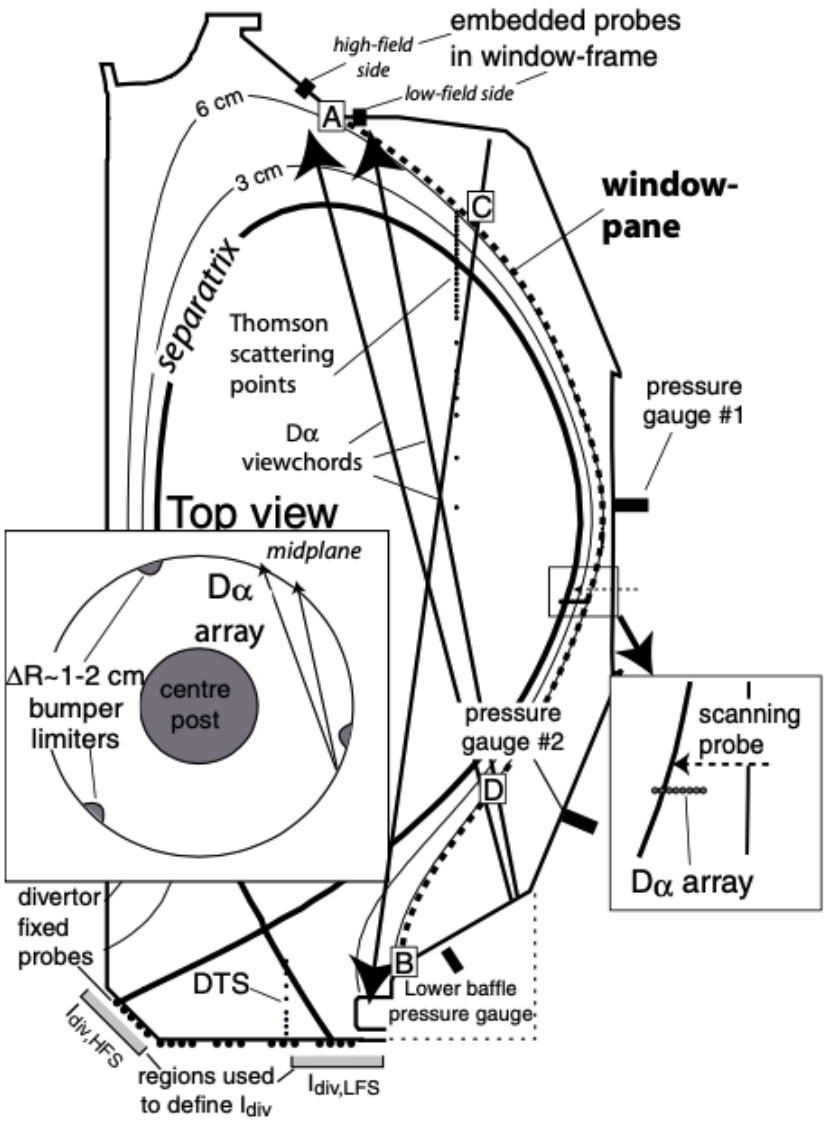


Figure 3.3: Standard DIII-D lower single null plasma configuration and diagnostic points are illustrated. The poloidal position of the toroidally continuous surface forming the 'window-frame' flux surface (approximately $\delta = 60$ mm) is indicated by the thick dashed line. The intercepting upper and lower divertor baffle structures (designated as 'A' and 'B') are symmetrical and establish the core of the primary window-frame. Surfaces denoted as A and B delineate the boundaries of the window-frame. It's worth noting that the outer midplane wall exhibits non-axisymmetric characteristics, as depicted in the top view inset.

Since $j_{\text{wall}} \equiv I_{\text{wall}}/A_{\text{window-pane}}$ we can view this as a test of the accuracy of extrapolating local recycling measurement, i.e., $\Gamma_D \times A_{\text{window-pane}}$, for measuring main-wall plasma contact. We first note that all of the measurements of Γ_D are strongly correlated in their relative magnitude with j_{wall} as $\bar{n}$ increases. The magnitude of the midplane D (Γ_D based on midplane $D-\alpha$ and pressure gauges), the measurement of which is distributed at different toroidal locations, turns out to be quite close in absolute magnitude to j_{wall} (Figure 3.4). This might be expected for the pressure gauges that tend to average out the local recycle flux density due to their remoteness from the edge plasma. Since the factor of ~ 2 agreement between midplane $D-\alpha$ measured Γ_D and j_{wall} exists, Filterscope is utilized to assess the fluxes in the main wall in this thesis instead of RCP probe Whyte et al. [2005].

While similar assessments were conducted by Whyte and colleagues in 2005, it is imperative to estimate comparable quantities to enhance the understanding of plasma discharge values pertinent to this thesis. The thesis examines 12 specific discharges, detailed in Tables 4.2 and 4.3. Particle fluxes from these discharges, as measured by midplane pressure gauges and Filterscope, are juxtaposed against fluxes from an embedded Langmuir probe situated on the divertor target adjacent to the windowpane location (Figure 3.5).

Although this comparison does not directly align with Figure 3.4 due to the absence of RCP data for a direct match, notable observations emerge: (a) fluxes recorded by Filterscope are approximately an order of magnitude higher compared to those from the Langmuir probe, and (b) fluxes measured by ASDEX gauges are approximately an order of magnitude lower. These disparities stem from differences in measurement locations, occurring either in the divertor or the main chamber. Nonetheless, the linear trend persists, as depicted in Figure 3.4. By leveraging the average trend between ASDEX pressure gauges and Filterscope diagnostics, one can utilize Filterscope as a surrogate diagnostic, replacing Langmuir probes for flux measurements.

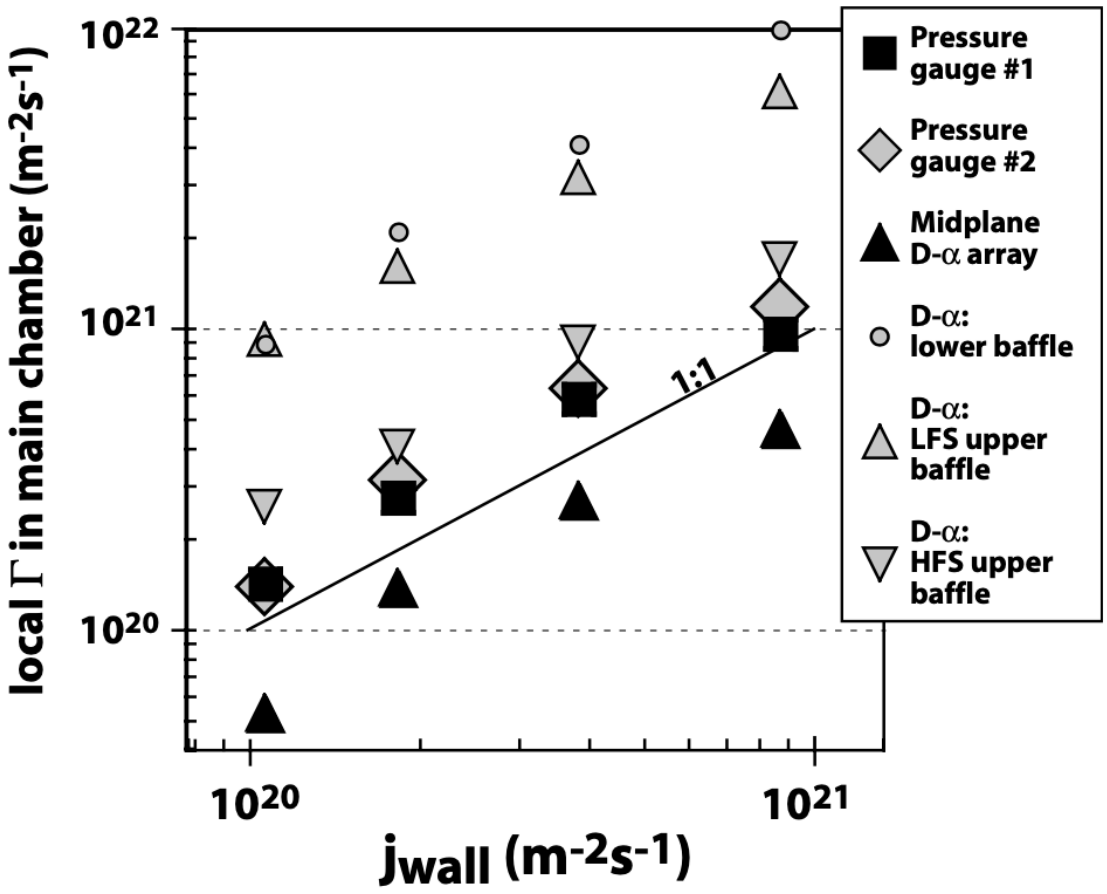


Figure 3.4: Local influx of neutrals, Γ_D, inferred from $D-\alpha$ and pressure gauges located at various main chamber locations, are compared with j_{wall} measured with the window-frame technique for the L-mode core density scan. Local flux densities correlate well with j_{wall} but can vary in absolute magnitude by a factor of 10. The magnitude of $D-\alpha$ LFS upper baffle was obtained by cross-calibration to a lower divertor $D-\alpha$ signal on another shot, with the cross-calibration verified by comparing local ion fluxes from probes. Image from Whyte et al. [2005]

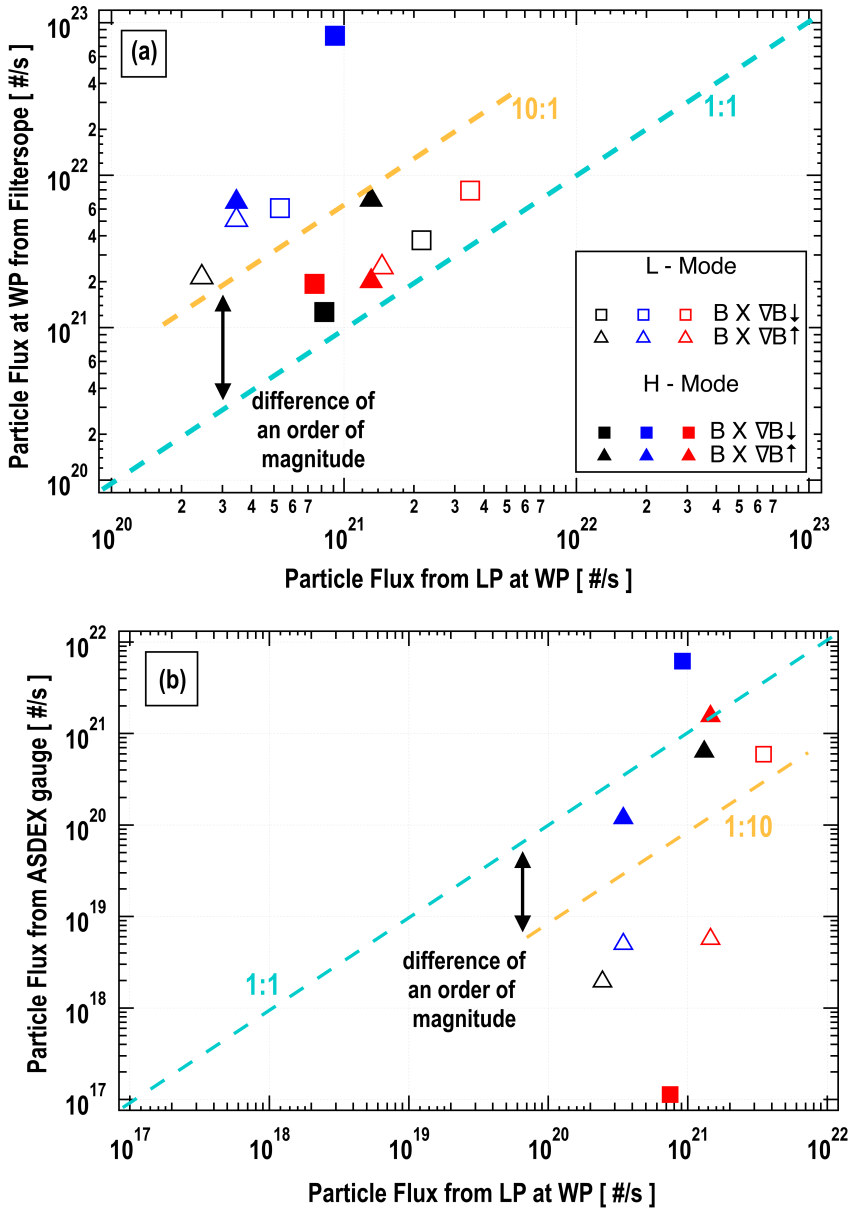


Figure 3.5: Local influx of neutrals, Γ_D, inferred from $D-\alpha$ and pressure gauges located at various main chamber locations, are compared with particle fluxe measured with the window-frame technique for 12 plasma discharges in $B \times \nabla B$ towards and away from the target conditions for LSN Shelf, LSN Floor and USN Floor divertor geometries. Local flux densities correlate well with fluxes from LP but vary in absolute magnitude by a factor of 10.

The primary objective of the window frame analysis remains the calculation of ion flux, a quantity also obtainable from Filterscope measurements. However, certain fundamental assumptions must be acknowledged and addressed to appropriately consider and quantify flux, ultimately deriving f_{wall} through this alternative method. It is important to note that, for clarity and consistency, we adopt the nomenclature from Whyte et al. [2005]. In this context, we define f_{wall} as:

$$f_{wall} = \frac{I_{wall}}{I_{div}} \tag{3.9}$$

Here, I_{wall} represents the particle flux measured with the mid-plane Filterscope system and can be calculated as follows:

$$I_{wall}\left[\frac{\#}{s}\right] = \Gamma_{wall}\left[\frac{\#}{m^2.s}\right] \times 2\pi R[m] \times LWP[m] \tag{3.10}$$

$$\Gamma_{wall}\left[\frac{\#}{m^2.s}\right] = 4\pi[str] \times \frac{S}{XB}\left[\frac{\#}{ph.}\right] \times I_0\left[\frac{ph.}{s - str - m^2}\right] \tag{3.11}$$

Here, Γ_{wall} is the neutral deuterium particle flux obtained from Filterscope system using a deuterium Balmer line emission. S is the ionization rate coefficient, X is the excitation rate coefficients and B is the branching Ratio and the S/XB ratio is calculated from ADAS data Whyte et al. [2005], Mertens et al. [2001] and the Emission intensity I_0 in units of [photons/s-str-cm2] Unterberg et al. [2019], Denne [1989], Johnson and Hinnov [1973]. $2\pi R$ is the circumference of the windowpane region around the tokamak nearest to the wall with R = RWP = 2.3305 [m] and LWP is the length of the WP region from point A to point B in Figure 3.6(a) which is approximated to be 3m.

$$I_{div}\left[\frac{\#}{s}\right] = \int_{separatrix}^{windowpane} \Gamma_{div}\left[\frac{\#}{m^2.s}\right] dR \tag{3.12}$$

$$\Gamma_{div}\left[\frac{\#}{m^2.s}\right] = JSAT\left[\frac{A}{m^2}\right] \times 6.24e18 \tag{3.13}$$

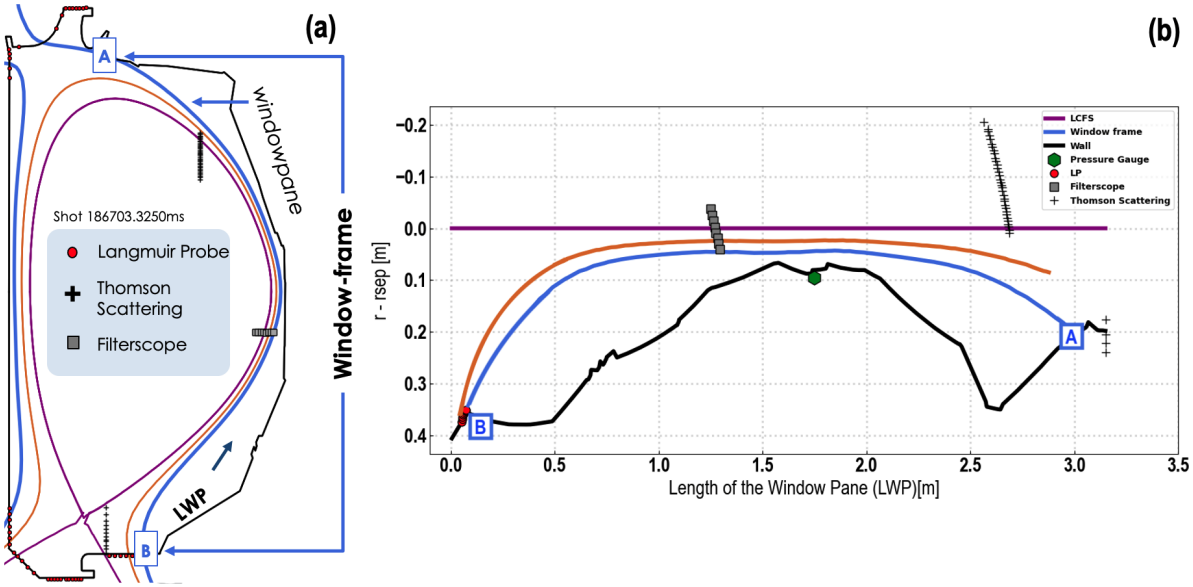


Figure 3.6: (a) 2D flat layout of the DIII-D LFS depicting the separatrix, windowpane region, the wall shadow region, and the main chamber wall along with the numerous diagnostics used for Shot 186703 in DIII-D. (b) Typical DIII-D cross-section of a LSN plasma configuration depicting diagnostics used to calculate particle flux inside the Windowpane region (dashed line from Point A to Point B) in the LFS. The windowpane region is assumed to be axisymmetric and is toroidally continuous.

I_{div} is estimated using the Langmuir probes available on the divertor target and using Equation 3.12. The particle flux in the divertor region utilizes the Langmuir probes on the divertor target and I_{div} is estimated by considering the area under the Langmuir probe data set on the divertor target. Since Γ_{div} is the particle flux density, it is multiplied by the area covered by the Langmuir probes on the divertor target to obtain the particle flux in terms of particles/s as shown in Equation 3.13.

Assumptions made for the Window Frame Analysis

1. Main Chamber wall surfaces inside the windowpane region is assumed to be toroidally axisymmetric.

2. I_{wall} measured at the windowpane from the midplane Filterscope is assumed to be the same poloidally throughout the length of the windowpane (LWP) region, from point A to point B (see Figure 3.6).

3. I_{wall} is assumed to be moving radially outward towards the wall.

Figure 3.6(a) illustrates a cross-section of the DIII-D tokamak during a Lower Single Null (LSN) discharge, presenting the nomenclature employed in the window frame analysis. The diagram shows the diagnostics instrumental in computing I_{wall} and I_{div}, including the Filterscope system, Thomson Scattering system, and Langmuir probe system. Additionally, it highlights the designated window pane region spanning from point A to point B, depicted in blue.

In Figure 3.6(b), the SOL region is represented in a flattened configuration with respect to r-rsep [m], and the Length of the Separatrix or Length of the Windowpane (LWP) space is plotted alongside relevant notations against the LWP. The figure delineates key features such as the Separatrix/Last Closed Flux Surface (LCFS) in purple, the windowpane region indicated by the blue line, and the DIII-D wall in black. The primary axisymmetric windowpane is precisely defined by the intersection of the magnetic line leading to a main chamber wall outside the divertor region (from point A to point B along the blue line).

3.2.2 The Geometric Restriction Parameter (GRP)

Diverted tokamaks redirect plasma along open field lines outside the confined region termed as the SOL towards the divertor target where the open field lines interact with PFC in order to: (a) dissipate power from the core plasma on a target away from the vessel wall, (b) improve neutral pressure near the exhaust pump duct to enhance helium ash removal from the system, and (c) control impurity production near the main chamber region Pitcher and Stangeby [1997], Whyte et al. [2005]. Diverted tokamak concentrates heat and particle fluxes on the PFC at the divertor target which leads to particle (neutral and impurity) production at the divertor target through recycling and sputtering. On average, recycled neutrals are emitted perpendicularly to the divertor target Pitcher and Stangeby [1997] potentially 'leaking' them from the divertor region into the region between the core and the main chamber wall. These leaked neutrals travel towards the main chamber where they may be ionized via charge exchange and other processes and may influence recycling near the main chamber Lipschultz and LaBombard [2005] which potentially could deteriorate core plasma performance Casali et al. [2022].

A method to control divertor (neutral) leakage and thus improve neutral retention is by increasing the divertor closure Loarte [2001]. A divertor with good closure has physical baffling that aids in incrementing neutral content inside the divertor region while enhancing neutral recycling Horton et al. [1999] driving the divertor into a high recycling state (i.e., neutrals are born and re-ionize inside the divertor region Loarte [2001]). Increased closure helps to increase neutral pressure inside the divertor, which improves the particle exhaust Horton et al. [1999], Maingi et al. [1999]. Another advantage of divertor closure is that the detached regime better protects the divertor PFCs Casali et al. [2019, 2020], Maingi et al. [2004]. Historically, divertor closure refers to the degree to which neutrals can escape where higher the closure, lower the neutral leakage Loarte [2001]. More recently, one can quantify closure by examining the electron density in the divertor region and the efficiency of removal

of particles through exhaust pumps in the divertor Bosch et al. [1999], Sontag et al. [2017], Stangeby [2000], Jones [1997], Guo et al. [2000], Rapp et al. [2008], Havlíčková et al. [2014].

Quantifying the ratio of ion flux in the main chamber (I_{wall}) to the divertor region (I_{div}) through a technique called WFA Whyte et al. [2005], Stangeby [2002], Leonard et al. [2003], Rudakov et al. [2005] helps determine the total ion flux crossing the far SOL toward the main chamber wall and the total ion flux measured by the Langmuir probes on the divertor target. The ratio of these fluxes could give an insight into the amount of restriction present at a divertor target and thus provide an insight in the divertor closure provided by a divertor target. Historically, three-dimensional plasma and neutral codes with high fidelity have been implemented for tokamaks around the world to understand and quantify divertor closure Loarte [2001], Renner et al. [2002], Sang et al. [2017], Schneider et al. [1997], Kawashima et al. [2007], Kukushkin et al. [2002]. However, these codes have limitations, such as requiring an expert to operate them and taking months to present an outcome. Also, these codes are computationally expensive and need access to latest specific machine geometry to work efficiently Kukushkin et al. [2002], Lore et al. [2019]. Hence, a simplified method is required to quantify divertor closure that characterizes and quantifies the geometric restriction present at the divertor due to baffling and magnetic geometry.

GRP quantifies the effect of physical restriction on neutral particles present at a divertor target due to physical baffling and the magnetic field structure, such as the location of the strike point, height of the outer divertor leg, flux expansion, and angle of the strike point at the divertor target. GRP approximates the ballistic path for the neutrals Ntampaka et al. [2021] present at the outer divertor leg that considers the neutrals hitting the PFC directly after they are born Kadomtsev et al. [a,b]. GRP and the ion fluxes determined using WFA provide a thorough insight regarding divertor leakage and closure in different divertor configurations in DIII-D. The aim of GRP is to define, justify and quantify the restriction present at each divertor target to optimize divertor closure needed for future fusion devices.

GRP is coined in order to quantify the effect of physical restriction on neutral particles present at a divertor target due to physical baffling and the structure of the magnetic field such as strike point location, height of the x-point, flux expansion factor, and angle made by the strike point on the divertor target. In this section, we will walk through a model for an outer divertor leg restriction in the DIII-D tokamak. Here, we on four conventional types of divertor geometries: the Lower Single Null (LSN) with high triangularity on the floor as seen in Figure 1.8(a), LSN with low triangularity on the shelf (Figure 1.8(b)), Upper Single Null (USN) with high triangularity on the floor as seen in Figure 1.8(c), and USN Small Angled Slot (SAS) divertor Guo et al. [2019] (Figure 1.8(d)). It is to note that multiple divertor options are available on DIII-D as seen in Figure 3.7.

Three out of four conventional divertor geometry, except SAS, offers a range of physical baffling with pumping mechanisms near it to help in density control and particle inventory control Maingi et al. [1999]. DIII-D also can operate in four other divertor configurations that are non-conventional, viz., snowflake divertor Ryutov [2007], Kolemen et al. [2018], Cowley et al. [2023] - seen in Figure 1.8(e), x-divertor Cowley et al. [2023], Kotschenreuther et al. [2013] (Figure 1.8(f)), vertical right configuration as seen in Figure 1.8(g) and vertical right configuration (Figure 1.8(h)). Figure 3.8 shows a DIII-D cross-section representing two plasma discharges: Shot 188492 (solid line) and Shot 188501 (dashed line) at 3100ms and 4800ms respectively. Both plasma discharges have the outer divertor leg hitting the same divertor target – LSN Floor, but at different strike point location of 1.18m and 1.35m respectively. The angle made by the outer divertor legs with respect to the PFC target geometry for both these plasma discharges are $\alpha_1 = 105.1°$and $\alpha_2 = 108.4°$respectively. It is evident from Figure 3.8 that the strike point location of plasma discharge 188492 is closer to the baffle PFCs compared to that of plasma discharge 188501. Despite having the strike point on the same divertor target, the location of the strike point impacts the restriction present for the plasma discharge.

Detailing the Outer Divertor GRP

GRP incorporates the physical PFC geometry and the magnetic geometry of the diverted tokamak. It considers the PFC present next to the divertor target, i.e., physical baffling, and the angle subtended between the outer divertor leg reaching the strike point location and the divertor target. For now, we focus on the reproduced neutral on the low field side of the outer divertor leg until it reaches the angle of the strike point in the poloidal direction. GRP is defined as shown in Equation 3.14. Here, ϕ_T, the total number of neutral particles emitted from the divertor target per second assumes neutrals travel ballistically and are isotropic in nature. This model essentially considers first-flight neutral transport, i.e., collisionless neutral transport towards the PFC Maingi et al. [1999], Lore et al. [2019].

$$GRP = \frac{\phi_B}{\phi_T} = \frac{\text{\# of particles hitting the divertor PFC per second}}{\text{Total \# of particles emitted from the divertor target per second}} \tag{3.14}$$

Here, ϕ_T is calculated by quantifying the recycled neutral flux, $\Gamma_0(x)$, emitted from the strike point location x_{OSP} at a fraction of solid angle $F(x,\theta)$. It can be written mathematically as:

$$\phi_T = \int_0^{x_{max}} \Gamma_0(x)\, 2\pi R\, F(x,\theta)\, dx \tag{3.15}$$

Here, as seen in Figure 3.9(b), ϕ_T is the recycled neutral flux crossing the plane present at x_{max}, the maximum value to which the flux profile exists. It is defined as $5\lambda_n$, meaning it accounts for 5 times the e-folding length of the neutral flux profile ($\Gamma_0(x)$, and accounts for all the particles present under the curve. $\Gamma_0(x)$ is the poloidally distributed recycled neutral current present at the OSP. The probability that the particles emitted from the Outer Strike Point (OSP) reaching the LFS of the tokamak at x_{max}, is given by a geometric solid angle fraction $F(x,\theta)$, which is defined as

$$F(x,\theta) = \frac{\int_0^{\theta_{max}} dA(\theta)}{\int_0^{\pi} dA(\theta)} \tag{3.16}$$

Where, $dA(\theta)$ is the differential area present at the height of the x-point. $dA = 2\pi R sin(\theta) d\theta$, where R is major radius of the tokamak. Assuming the particles emitted are ballistic in nature, i.e., particles do not undergo any other ionization or charge exchange processes during their path towards the divertor PFC, the geometric solid angle would depend only the poloidal angle at which the particle are emitted. Therefore, the geometric solid angle can be simplified as

$$F(\theta) = \frac{\int_0^{\theta_{max}} sin(\theta) d\theta}{2} = \frac{1 - cos(\theta_{max})}{2} \tag{3.17}$$

Here, θ_{max}, is the maximum acceptance of the solid angle that takes the neutrals originating from the OSP into account. It is defined as

$$\theta_{max} = tan^{-1}\left[\frac{\Delta Z}{\Delta X}\right] = tan^{-1}\left[\frac{Z_{XPT} - Z_{OSP}}{X_{max} - X_{OSP}}\right] \tag{3.18}$$

To understand Equation 3.17 and 3.18 better, let us assume θ_{max} to be 90°, that would make Equation 3.17 equal to 1/2. This would imply, 50% of the particles produced at that OSP and traveling through that solid angle would travel to LFS and other 50% would travel towards the private flux region.

Next, let us compute ϕ_B (see Figure 3.9(c)), the number of particles hitting the divertor baffle PFC. It is calculated by adding the flux reaching the divertor PFC at every discretized segment. In each segment, recycled neutral flux, $\Gamma_0(x)$, is emitted from x_{OSP} reaching the PFC baffles at every infinitesimally small poloidal solid angle, $d\theta$. Assuming the particles that originate at X_{OSP}, mostly atoms and molecules, dissociate instantly to produce a longer mean free path neutrals are then dominated by ballistic neutral transport would give us a transmission probability $T(x,\theta)$ that quantifies the particles reaching the baffle structure are not ionized. It can be written mathematically as follows:

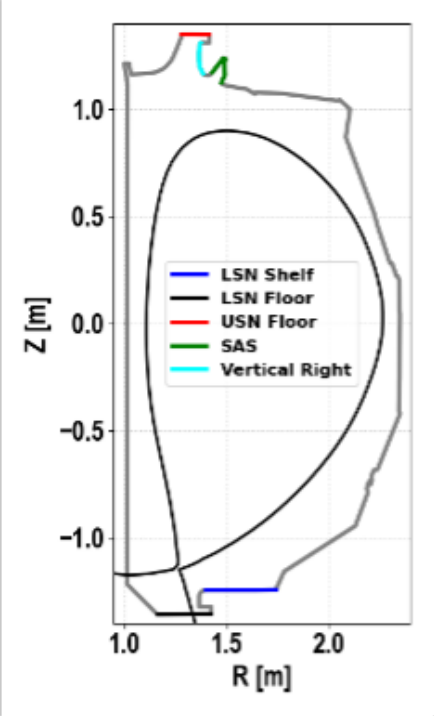


Figure 3.7: DIII-D cross-section depicting different divertor targets location. There are two divertor targets in the Lower Single Null (LSN) configuration, viz., LSN Floor (Black) and LSN Shelf (Blue) and there are three divertor targets in the Upper Single Null (USN) configuration, viz., USN Floor (Red), Single Angled Slot - SAS (Green), and Vertical Right (Cyan)

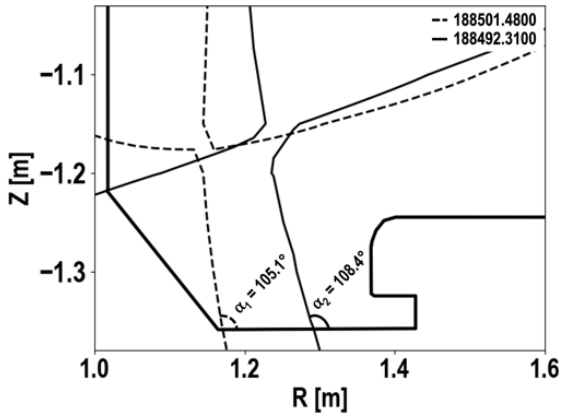


Figure 3.8: DIII-D Lower Single Null (LSN) divertor geometry with the strike point hitting the floor portion of the divertor target depicting two different plasma discharges, viz., Shot 188492 (solid) and Shot 188501(dashed) with varying strike point

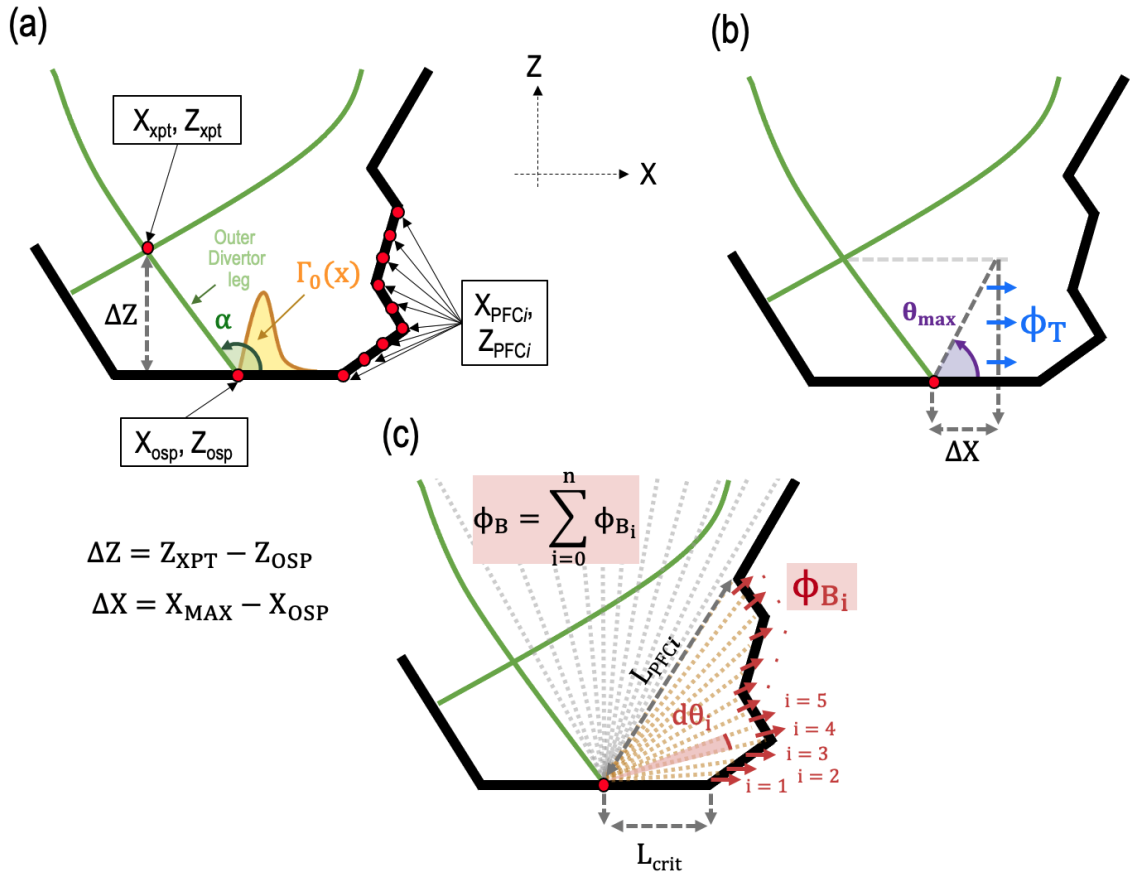


Figure 3.9: Illustration depicting the geometric configuration of a divertor, highlighting the elements utilized in the derivation of the GRP. (a) Schematic defining the elements of the divertor geometry such as location of strike point (R_{OSP}, Z_{OSP}) in X,Z space, the height of x-point (ΔZ) along with the location of x-point (R_{XPT}, Z_{XPT}), angle made between the divertor target and the strike point , α, the location of each PFC location (R_{PFCi}, Z_{PFCi}) and the neutral flux profile $\Gamma_0(x)$. This flux profile depicted in orange is used to map the location of X_{max}, a maximum value at which flux profile can extend upto. Here $X_{max} = 5\lambda_n$.(b) The same cross section now showcasing the features needed to quantify the recyced neutral flux ϕ_T. Some features shown are: divertor target $\Delta X = X_{max} - X_{OSP}$, and the solid angle θ_{max} at which the flux is emitted. (c) This cross-section showcases the features needed to quantify the recycled neutral flux ϕ_B = sum of ϕ_{Bi}. Here, the tokamak divertor is discretized into 'n' points with each discretized segment having a poloidal angle '$d\theta$' until 'α'. Here, the length of the path taken by a netural that is ballistically transported is given by 'L_{PFCi}'.

$$\phi_B = \sum_{i=1}^{n} \phi_{Bi} = \phi_{B1} + \phi_{B2} + \phi_{B3} + ... + \phi_{Bn} \tag{3.19}$$

where,

$$\phi_{Bi} = \int_0^{x_{max}} \Gamma_0(x)\, 2\pi R\, F_i(x,\theta)\, T_i(x,\theta)\, dx \tag{3.20}$$

Γ_{Bi} is derived from: (a) transmission probability, *T(x, θ)*, of neutrals that are produced at the strike point that travel to LFS without getting ionized and, (b) the geometric solid angle *F(x, θ)* of the neutrals that were ballistically produced and travel poloidally uniform towards the divertor baffling without collisions Dunn and Shultis [2011], Maingi et al. [1999], Lore et al. [2019]. Figure 3.9(c) depicts a cross-section of an arbitrary tokamak divertor. It shows 'α' as the angle between the tangent made from the outer strike point location poloidally and the divertor target plate. It also depicts the LFS side of the tokamak being discretized into 'i' sections, each having a small poloidal solid angle, $d\theta$.

We assume that the neutral flux originates at the OSP and defined as a fitted functional form of current density measured through Langmuir probes data as described in Equation 1 of Maingi et al. [2004]. Hence, we can say the factor '$\Gamma_0(x)$' is assumed to be a averaged constant number that is the peak flux present at OSP throughout the divertor target wetted area, $< \Gamma_0 >$. Also, using the base assumptions of isotrpoic ballistic distribution of neutrals, and assuming the neutral flux produced over the divertor target remains constant, we can rewrite Equation 3.20 as:

$$\phi_{Bi} =< \Gamma_0 >\, 2\pi R \int_{x_{osp}=0}^{x_{max}} F_i(\theta)\, T_i(\theta)\, dx \tag{3.21}$$

It is to note that in Equation 3.21, the term 'dx' can be rewritten as $L_{PFCi}\cos(\mathrm{d}\theta)$. Next, similar to Equation 3.17, $F(\theta)$ is the geometric solid angle, but this time it is the solid angle for the discretized segment, there we can rewrite Equation 3.17 as:

$$F_i(\theta) = \frac{\int_0^{d\theta} sin(\theta) d\theta}{2} = \frac{1 - cos(d\theta_i)}{2} \tag{3.22}$$

The probability of transmission of neutrals, $T_i(\theta)$, from the OSP location towards the said indexed PFC location without going through any interactions also is dependent on the poloidal angle and the distance of the neutral path. This can be defined as follows:

$$T_i(\theta) = \begin{cases} 1 & \text{if } L_{PFCi} \leq L_{crit} \\ 0 & \text{if } L_{PFCi} > L_{crit} \end{cases} \tag{3.23}$$

In Equation 3.23, L_{crit} is the width of the divertor wetted area and is taken as 5 λ_n. The grey (for $T_i = 0$) and orange (for $T_i = 1$) dashed lines in Figure 3.9(c) show L_{PFCi}, the path of the ballistic neutral originating at the OSP which is estimated as the distance between the indexed PFC location x_{PFC} and the x_{OSP}. In Cartesian plane, it can be defined as

$$L_{PFCi} = \sqrt{(Z_{PFCi} - Z_{OSP})^2 + (R_{PFCi} - R_{OSP})^2} \tag{3.24}$$

Substituting Equation 3.15 and Equation 3.19 in Equation 3.14, we get

$$GRP = \frac{< \Gamma_0 > \, 2\pi R \sum_{i=1}^{n} \int_0^{x_{max}} F_i(\theta)\, T_i(\theta)\, dx}{\int_0^{x_{max}} \Gamma_0(x)\, 2\pi R\, F(x,\theta)\, dx} \tag{3.25}$$

Assuming similar assumption for ϕ_T as made for ϕ_B, we can rewrite equation 3.25 as

$$GRP = \frac{< \Gamma_0 > \, 2\pi R \sum_{i=1}^{n} \int_{x_{osp}=0}^{x_{max}} F_i(\theta)\, T_i(\theta)\, dx}{< \Gamma_0 > \, 2\pi R \int_{x_{osp}=0}^{x_{max}} F(\theta)\, dx} \tag{3.26}$$

Further simplification gives us,

$$GRP = \frac{\sum_{i=1}^{n} F_i(\theta)\, T_i(\theta)\, cos(d\theta_i) L_{PFCi}}{F(\theta)} \tag{3.27}$$

Since, the arbitrary discretization is constant throughout the tokamak geometry, $d\theta$ is constant over 'n' index values. Hence we can rewrite 3.27 as:

$$GRP = \frac{cos(d\theta_i) \sum_{i=1}^{n} F_i(\theta)\, T_i(\theta) L_{PFCi}}{F(\theta)} \tag{3.28}$$

Substituting Equation 3.17 and Equation 3.22, we get

$$GRP = \frac{cos(d\theta_i)(1 - cos(d\theta_i)) \sum_{i=1}^{n} T_i(\theta) L_{PFCi}}{(1 - cos(\theta_{max}))} \tag{3.29}$$

If $\theta_{max} \approx 90°$, and $d\theta \approx 5°$, then GRP $\rightarrow$ 0. This would mean, the number of particles hitting the divertor baffle is very small compared to the particles emitted from the OSP. This implies there are no restrictions present at the divertor, suggesting little to no baffling present. If the divertor is closed, GRP $\rightarrow$ 1, implying complete baffling.

3.3 Methodology - Interpretive analysis of poloidally averaged ion fluxes in the main chamber

The intricate interactions between the central and peripheral regions of plasma play a crucial role in governing the confinement and heating processes in fusion plasma. Nevertheless, models of the SOL can be time-consuming and necessitate substantial human involvement for result generation. Hence, a simplified model, mappable to a 2D grid, can effectively address SOL neutral dynamics challenges, encompassing issues such as edge neutral sourcing. The objective is to assess the ratio of particle fluxes in the main chamber compared to the divertor by employing the modified window frame analysis through the window pane region. It is important to note that this analysis relies on the assumption that the measured wall flux, I_{wall}, remains constant poloidally across the windowpane region. This assumption is necessitated by the absence of spatially available diagnostics in the LFS of the tokamak. While this approximation holds reasonably well, it is acknowledged that SOL physics operates differently across flux tubes in distinct poloidal regions.

For instance, the SOL physics is primarily influenced by divertor recycling in the region near the divertor, while it is dominated by main chamber recycling outside this region. Given the variations in temperature and density poloidally in a tokamak, assuming constant I_{wall} is a practical approximation for experimental determination of f_{wall}. However, a more nuanced understanding can be achieved with the assistance of the modeling approach using OEDGE.

3.3.1 Ratio of poloidally average flux densities at the main chamber to the divertor

As elucidated in Section 2.4, the interpretability of the OEDGE model can enhance the comprehension of edge physics while considering experimental boundary conditions. Here $f_{wall-OEDGE}$ can be defined as:

$$f_{wall-OEDGE} = \frac{I_{wall-OEDGE}}{I_{div}} \tag{3.30}$$

With the help of OEDGE, we can get the $I_{wall-OEDGE}$ information at the windowpane using the basic particle flux equation

$$I_{wall-OEDGE}\left[\frac{\#}{s}\right] = \Gamma_{wall-OEGDE}\left[\frac{\#}{m^2.s}\right] \times 2\pi R[m] \times LWP[m] \tag{3.31}$$

where Γ_{wall} is given by:

$$\Gamma_{wall-OEDGE}\left[\frac{\#}{m^2 \cdot s}\right] = n_e\left[\frac{\#}{m^3}\right] \times v\left[\frac{m}{s}\right] \tag{3.32}$$

where, n_e is the electron density across the length of the windowpane, and v is the velocity of particles at the windowpane. Since the boundary condition given to the OEDGE for OSM and EIRENE model includes the Langmuir probe data, the calculation of I_{div} remains the same as seen in Equation 3.12.

Figure 3.10 displays the electron density for a representative Lower Single Null (LSN) Shelf configuration discharge, highlighting the positions of the Filterscope,

Langmuir Probe, and Thomson Scattering diagnostic tools. Additionally, the figure identifies the windowpane region, denoted from point A to point B, which represents the last region considered in the OEDGE simulation convergence. This figure delineates three Regions of Interest (ROI): $ROI\#1$ corresponds to the Filterscope location, $ROI\#2$ is situated just inside the divertor beneath the x-point, and $ROI\#3$ is located at the divertor target. To calculate $f_{\text{wall-OEDGE}}$ using Equation 3.30, we can express it in a simplified form as follows:

$$f_{wall-OEDGE} = \frac{I_{wall-OEDGE}\, at\, ROI\#1}{I_{div-OEDGE}\, at\, ROI\#3} \tag{3.33}$$

Equation 3.33 yields the f_{wall} value derived from OEDGE calculations. This value is determined in reference to experimental calculations outlined in Equation 3.8, allowing for a detailed examination of the disparities between the model predictions and experimental observations across the entire physics domain encompassing $ROI\#1$ and $ROI\#3$.

As elucidated in the preceding paragraph, the true strength of the OEDGE model lies in its ability to estimate $I_{\text{wall-OEDGE}}$ along the poloidally symmetric window pane, extending from point A to point B, as depicted in Figure 3.10. Consequently, we can express this averaged flux ratio in equation form as:

$$\langle f_{wall-OEDGE} \rangle = \frac{I_{wall-OEDGE}\, across\, AB}{I_{div-OEDGE}\, at\, ROI\#3} \tag{3.34}$$

3.3.2 Critical Considerations in OEDGE Simulation Setup

Figure 3.11 illustrates a flowchart outlining the standard steps for an OEDGE run scenario and the procedures required to obtain a dictionary output from the OEDGE file. As depicted in the flowchart, fundamental knowledge of the IRIS setup on the DIII-D server is essential. A detailed explanation of this setup is provided in Appendix C.1. Once the server is configured, understanding the process of creating a DG-Carre-based grid, a crucial component in the OEDGE model, becomes necessary. This

grid generation process, though time-consuming and possessing a learning curve, is extensively described in Appendix C.2.

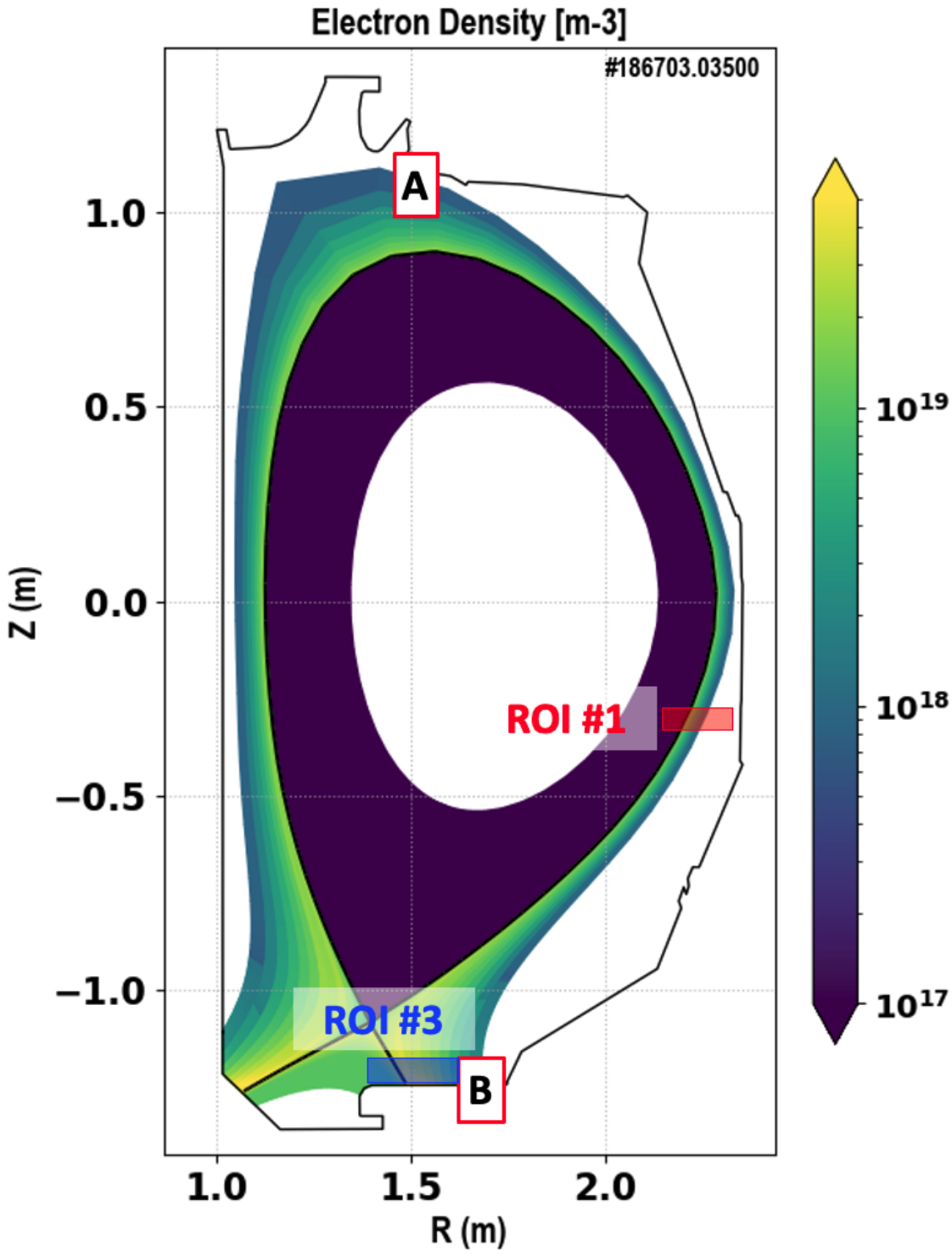


Figure 3.10: A plasma solution depicting n_e for a LSN Shelf divertor configuration showing the windowpane region from Point A to Point B along with the regoins of interest (ROI) for f_{wall} estimation

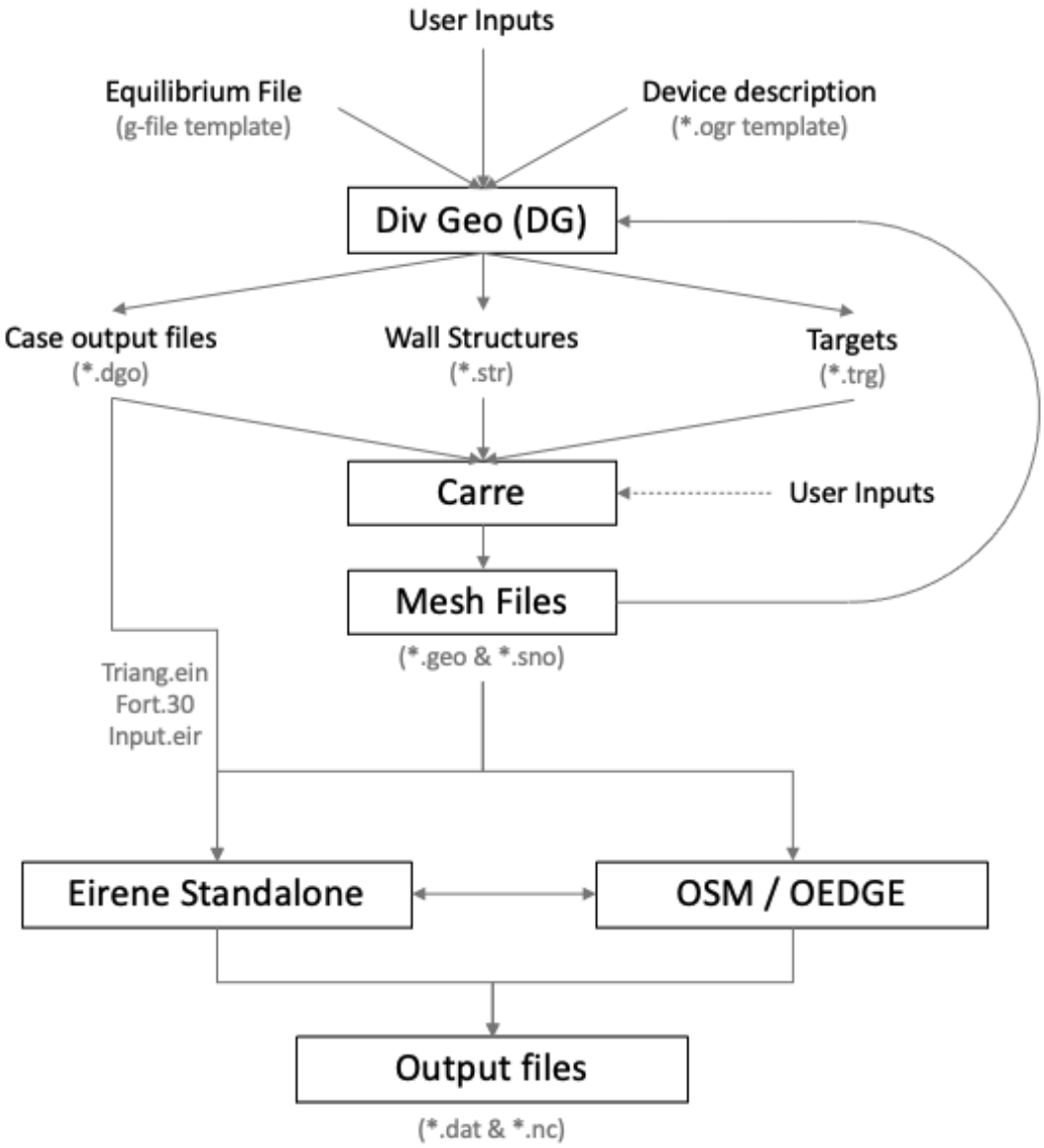


Figure 3.11: Flowchart depicting scenarios for a successful OEDGE run.

Chapter 4

DIII-D Database development for closure interpretation

The aim of this chapter is to conduct a comprehensive comparative analysis between experimental and modeled data, with the objective of elucidating the characteristics of f_{wall} and $f_{\text{wall-OEDGE}}$, and identifying any disparities between the two. The chapter meticulously presents an in-depth analysis of plasma discharges in both L-mode and H-mode, providing a step-by-step account of the procedures employed to determine f_{wall}, and $f_{\text{wall-OEDGE}}$.

Section 4.1 presents a detailed step-by-step analysis leading to the calculation of I_{wall}, incorporating results from the Filterscope calculation to derive particle flux density at the window pane region. Subsequently, the chapter discusses the results leading to the calculation of I_{div}, contributing to a comprehensive understanding of the determination of f_{wall}. The section then outlines the meticulous estimation process for $f_{wall-OEDGE}$, poloidally averaged $< f_{\text{wall-OEDGE}} >$ through the OEDGE modeling setup, providing a sequential procedure for obtaining results from a successful OEDGE run.

Section 4.2 offers an overview of the shots utilized in the comparative study, spanning three distinct divertor geometries - LSN shelf, LSN floor, and USN floor.

Moving forward, Section 4.3 delves into the results of the GRP estimation, exploring various divertor types and their respective GRP variations.

4.1 Systematic investigation of empirical and model-derived f_{wall} for one plasma discharge

This thesis documents 12 plasma discharges or shots characterized by diverted, single-null magnetic equilibrium, where the $B \times \nabla B$ ion drift is directed both towards (Reverse B_T) and away (Forward B_T) from the target. The primary focus of this study centers on conventional divertor geometries, namely the LSN Shelf, LSN Floor, and USN Floor, with the aim of estimating f_{wall}. It is noteworthy that Section 4.3 comprehensively outlines GRP values for non-conventional divertors as well. It is crucial to emphasize that this section provides detailed information for a single plasma discharge—Shot # 186703 in the LSN Shelf configuration—for the sake of clarity. Calculations for additional plasma discharges can be found in Appendix D.

Figure 4.1 presents the fundamental global parameters for the LSN shelf plasma discharge (Shot #186703) in an H mode configuration, where the $B \times \nabla B$ ion drift is directed towards the target. The figure illustrates key aspects such as density, pedestal temperature, injected power, outer gap, and outer strike point location within the time slice of 2500 - 3500 ms (shaded region). Within this region of interest we see in Figure 4.1, (a) the electron density of the plasma discharge is 8e19 m^{-3}, (b) the pedestal temperature is 3.0 keV, (c) the injected power is 6 kW, (d) the outer gap between the plasma and the main chamber measures 6.6 cm, and (e) the average strike point location of the outer divertor leg on the target is 1.5 m. Additionally, it is important to highlight that this discharge exhibits a B_t of 2 T and I_p of 1.3 MA. It is noteworthy that the global parameters at the selected time slices are intentionally maintained to demonstrate consistency among values.

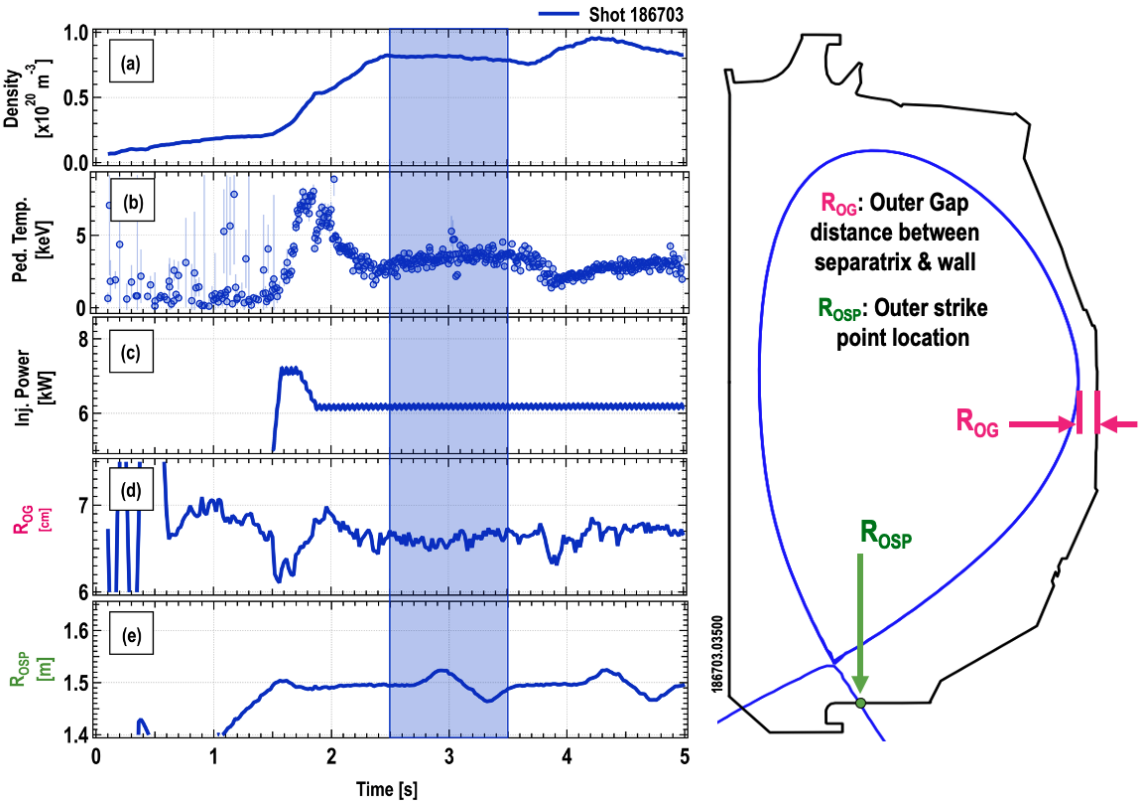


Figure 4.1: Global Parameters of Plasma discharge #186703 in with $B \times \nabla B$ ion drift directed both towards the target in H mode configuration are depicted here. (a) shows Line averaged density, (b) shows pedestal temperature, (c) shows injected power, (d) shows the outer gap of plasma to the main chamber wall and (e) shows the location of the outer strike point. The location of R_{OSP} and R_{OG} are shown in the cross-section of DIII-D

This deliberate approach facilitates a more meaningful comparison of results, particularly in cases where the underlying physics appears ostensibly similar, with variations primarily attributed to differences in divertor geometry.

4.1.1 Empirical estimation of f_{wall}

As seen in Chapter 2.5, there are three main diagnostics useful in understanding and calculation of f_{wall}, namely, Thomson Scattering to inform n_e and T_e data inside the separatrix which is useful to understand the SXB values and the Filterscope data that is useful in estimating I_{wall} as seen in Equation 3.11. Langmuir probe measurements to inform the ion current density, J_{sat}, data at the divertor target which is useful for estimating I_{div} as seen in Equation 3.13.

In Figure 4.2(a), the mean electron density (n_e) obtained from Thomson Scattering data is presented for time slices between 2500 - 3500 ms. The data illustrates electron density ranging from approximately 6e19 m^{-3} near the core to about 1.2e19 m^{-3} near the window pane region. The n_e values are plotted with respect to the psiN value, representing the location of the separatix at psiN of 1 and that of the window-pane region at psiN of 1.1.

Similarly, Figure 4.2(b) displays the mean electron temperature (T_e) values obtained from Thomson Scattering for the specified time range. The temperature data shows a range from approximately 1 keV near the core region to about 5 eV near the window-pane region.

Lastly, in Figure 4.2(c), SXB values (left axis) and PEC values (right axis) derived from n_e and T_e are mapped at every psiN value. As mentioned earlier, these values are employed to calculate particle flux density and neutral density from Filterscope, respectively. The SXB values range from about 25 near the core to approximately 8 near the window-pane region, while the PEC values span from 10^{-9} near the core to 10^{-13} near the window-pane region.

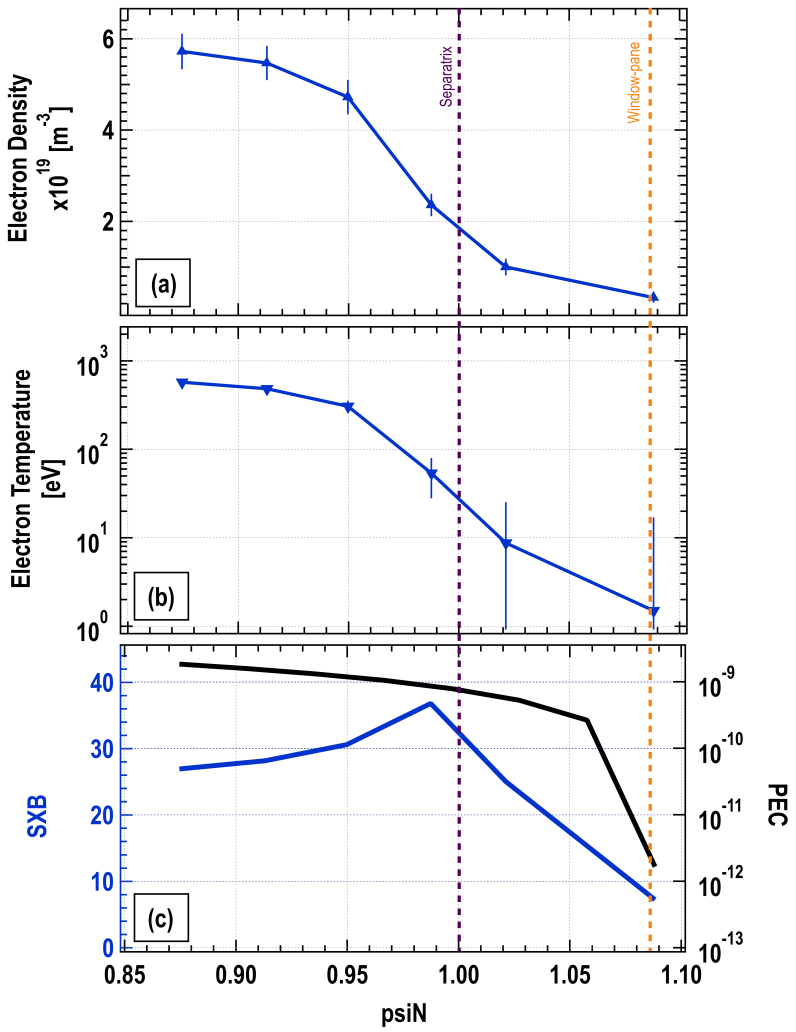


Figure 4.2: (a) n_e and (b) T_e along with (c) SXB (left axis - blue) and PEC values (right axis - black) for plasma discharge #186703 in the time of interest between 2500 - 3500 ms.

4.1.2 Estimation of I_{wall}

Recalling the equations:

$$I_{wall}\left[\frac{\#}{s}\right] = \Gamma_{wall}\left[\frac{\#}{m^2.s}\right] \times 2\pi R[m] \times LWP[m]$$

$$\Gamma_{wall}\left[\frac{\#}{m^2.s}\right] = 4\pi[str] \times \frac{S}{XB}\left[\frac{\#}{ph.}\right] \times I_0\left[\frac{ph.}{s - str - m^2}\right]$$

$$n_{D0}(r) = \frac{4\pi \frac{d}{dr}(I_0)}{n_e(r)PEC(r)}$$

Recalling Equations 3.10 and 3.11 we see that in order to get I_{wall} we need to obtain particle flux density (Γ_{wall}) and and radiance (I_0). Figure 4.3 shows a 2D cross-section of the DIII-D tokamak. Here, the separatrix is depicted in purple, the window-pane region from A-B is highlighted in orange, and the diagnostic location on the DIII-D tokamak is indicated. Sub-figures (a-d) provide detailed information necessary for obtaining I_{wall} from the Filterscope location. (a) Illustrates the radially varying radiance (I_0) across the midplane Filterscope system. (b) Displays the emissivity of the radiance, obtained through the Abel inversion process. (c) Depicts the particle flux density calculated using the emissivity and SXB values, and (d) Shows the neutral density n_{D0} emission at the midplane location - see Figure 4.2 for reference. These sub-figures collectively contribute to a comprehensive understanding of the radiative properties and diagnostic measurements at the midplane location within the DIII-D tokamak.

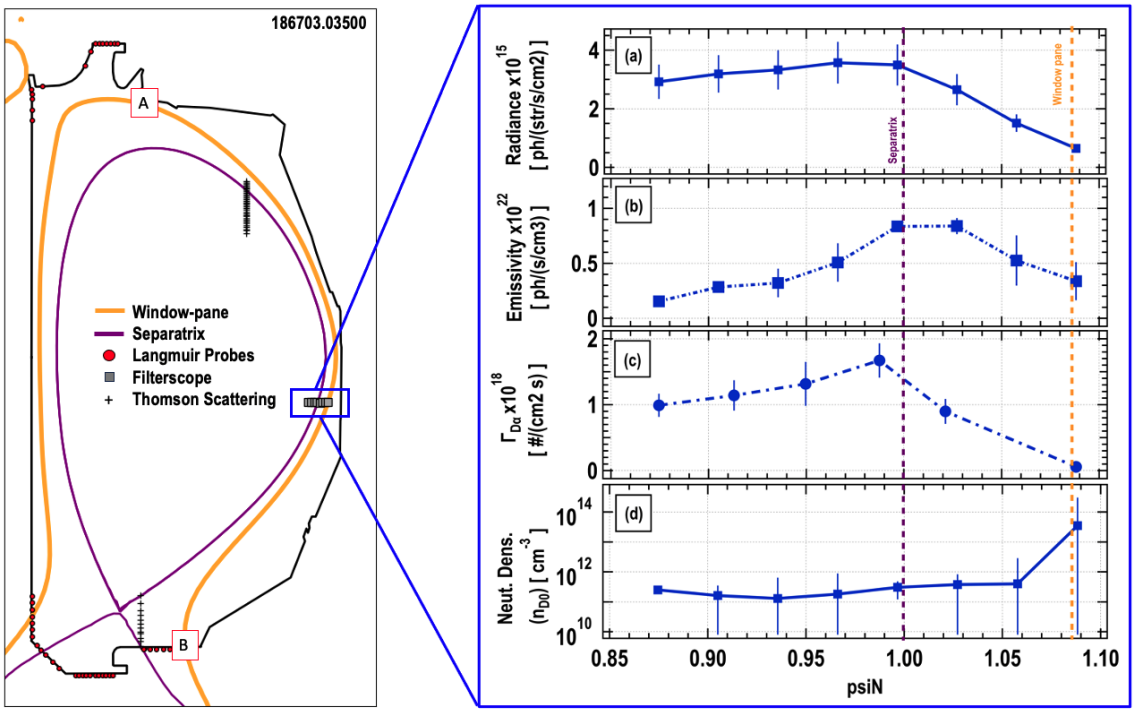


Figure 4.3: 2D cross section of DIII-D tokamak depicting the separatrix (purple), window-pane region from A-B (orange) and the diagnostic location on the DIII-D tokamak is shown. The sub-figure (a-d) shows details needed to get the I_{wall} from the Filterscope location. (a) shows the radiance (I_0) radially across the midplane filterscope system. (b) shows the emissivity of the radiance obtained through Abel inversion process, (c) shows the particle flux density calculated using the emissivity and SXB values and (d) shows the neutral density emission at the midplane location

4.1.3 Estimation of I_{div}

Recalling the equations:

$$I_{div}\left[\frac{\#}{s}\right] = \int_{separatrix}^{windowpane} \Gamma_{div}\left[\frac{\#}{m^2.s}\right] dR \times \pi(R^2 - r^2)[m^2]$$

$$\Gamma_{div}\left[\frac{\#}{m^2.s}\right] = JSAT\left[\frac{6.24e18[\#/s]}{m^2}\right]$$

Figure 4.4 provides a detailed overview of the estimation process for I_{div} in Shot 186703 during the time slice of interest from 2500 to 3500 ms. (a) Displays the particle flux density obtained via Langmuir probes, presenting all measured data with gray circle markers, median values with blue circle markers, and the fit data represented by the black dashed line, achieved through Maingi fit. The fit exhibits a reduced χ^2 value of 1.51. (b) Presents the Maingi fit parameter values utilized for fitting the median data. (c) Illustrates the weights obtained during the fitting process. (d) Shows the residuals of the fit plotted against psiN. The particle flux density is delineated by the separatrix (purple dashed line) and the windowpane (orange dashed line), calculated using the specified equations. The estimation of I_{div} involves determining the area under the curve between the separatrix and the windowpane region, multiplied by the area of the annulus between the windowpane and the separatrix. Figure 4.4 incorporates a goodness-of-fit measure that includes data averaged over ELMs, enhancing the reliability of the estimation process.

For the Maingi fit, The temporal profiles are transformed into spatial profiles with respect to the separatrix position through utilization of the EFIT equilibrium reconstruction at each time point of the profile. Then, the spatial profiles are subjected to fitting procedures based on functional representations as shown in Figure 4.4(e)

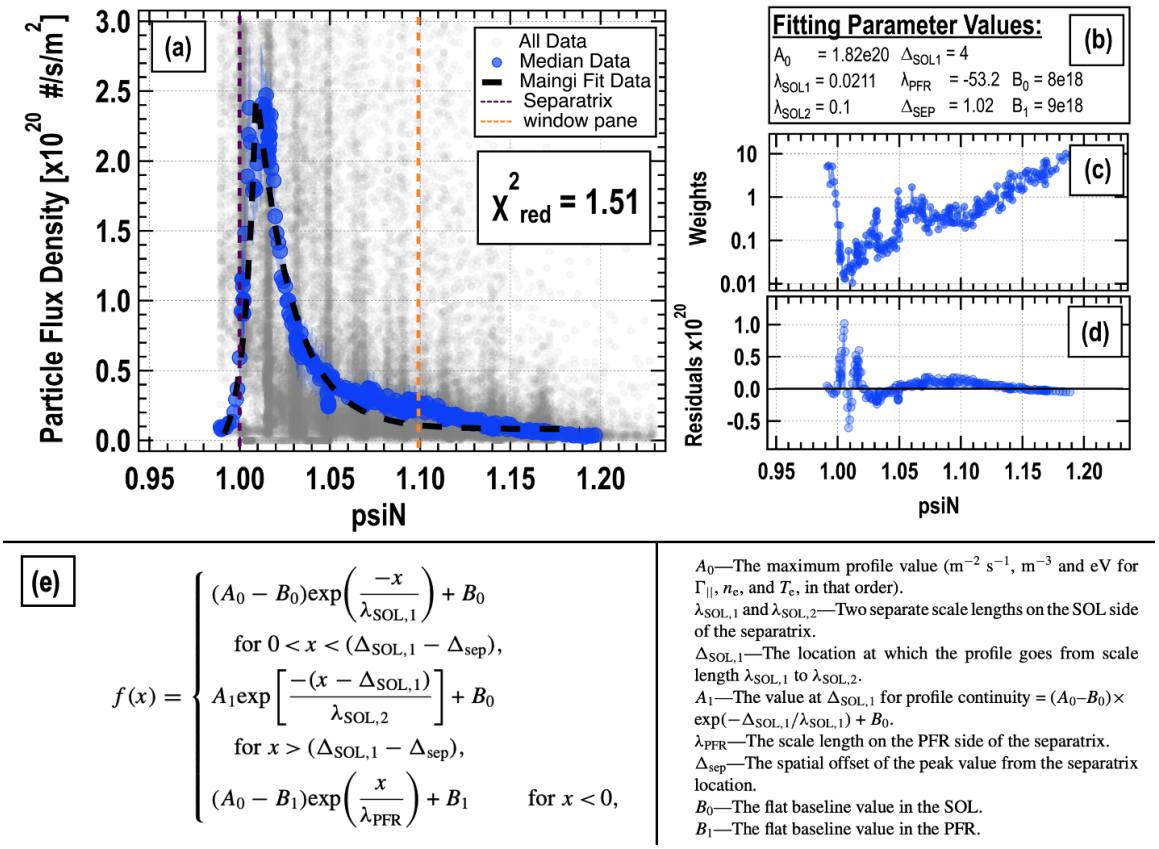


Figure 4.4: (a) Particle flux density obtained via Langmuir probes shown with all measured data (gray circle markers), median values (blue circle markers) and fit data (black dashed line) done using Maingi fit. The fit has a reduced χ^2 value of 1.51. (b) Maingi fit parameter values used for fitting the median data. (c) weights obtained while fitting the data along with (d) the residuals of the fit plotted against psiN. The particle flux density shows the separatrix (purple dashed line) and the windowpane (orange dashed line). (e) Subfigure defines the Maingi fit - taken from from Maingi et al. [2004] utilized to make the fit on the flux density data

4.1.4 Modeled f_{wall}: Introduction to OEDGE results

In this thesis, our primary focus is the understanding of f_{wall} values across different divertor targets. While the preceding section approached this empirically, we also delve into it using the modeling approach. Here a divertor plasma solution is generated using OEDGE for specific divertor configurations in both $B \times \nabla B$ towards and away from the target in L mode and H mode configurations. In the earlier segment, we scrutinized the experimental values of I_{wall} and I_{div} for the LSN shelf configuration of Shot 186703 in H mode. Similarly, mirroring the empirical approach, we will now guide through Shot 186703 in H mode for a time slice at 3500 ms using OEDGE. Following the execution of the OEDGE case, as outlined in Appendix C, and a thorough understanding of the steps necessary for calculating the required f_{wall} values from Section 3.3, we will proceed to examine the results obtained from the OEDGE run.

4.1.5 Estimation of $f_{wall-oedge}$

The initial step in obtaining a modeled-derived f_{wall} involves creating a mesh through DG-Carre, with detailed procedures outlined in Appendix C. Figure 4.5(a) displays the DG-Carre surface with the mesh superimposed, illustrating the mesh configuration for Shot 186703 at the 3500 ms time slice. An important observation from this figure is the presence of a limiting surface near the SAS divertor, restricting the mesh due to the presence of the wall surface. This limitation is crucial in defining the window-pane region, as depicted in Figure 4.5(b) from point A-B.

After running the OEDGE case, numerous output variables become available for visualization. Figure 4.6 presents key results, including: (a) Electron density, (b) Electron temperature, (c) Plasma velocity and (d) Calculated plasma flux density using the equation $\Gamma = n \times v$. It's important to highlight that the OEDGE case assumes the plasma to be quasineutral. These plots offer valuable insights into the distribution and characteristics of electron density, temperature, plasma velocity, and

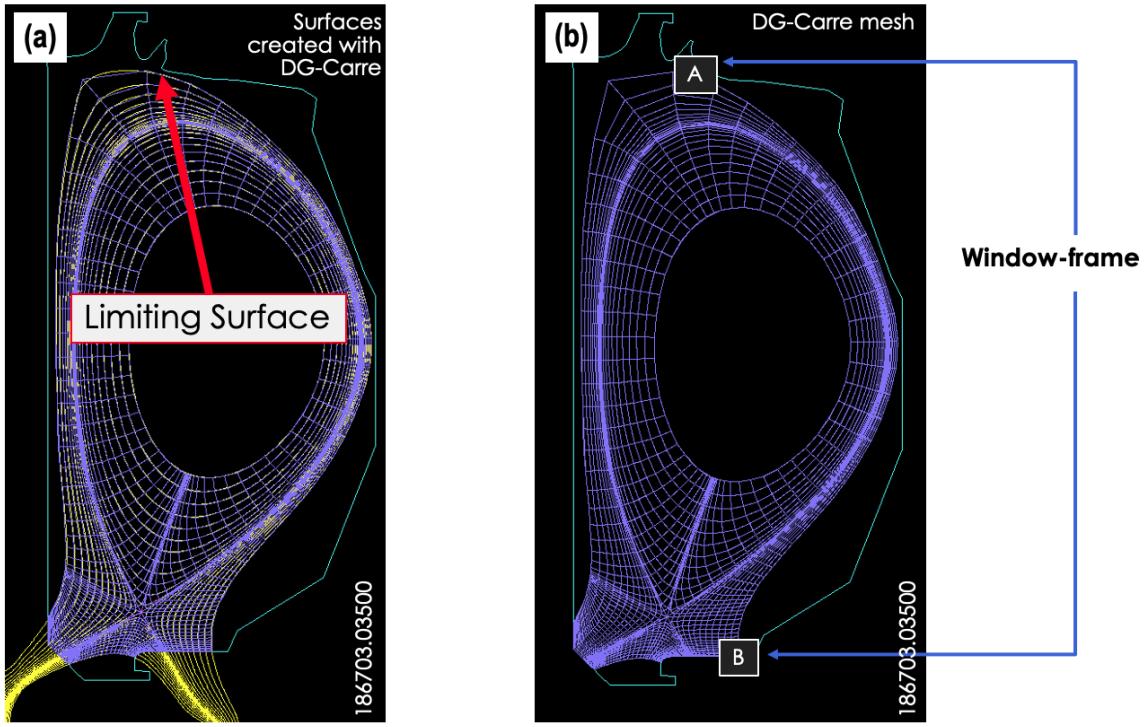


Figure 4.5: Cross-section of DG-Carre created (a) surface and (b) mesh depicting the limiting surface for mesh generation near the SAS divertor and windowpane region from point A-B as seen in sub figure (b)

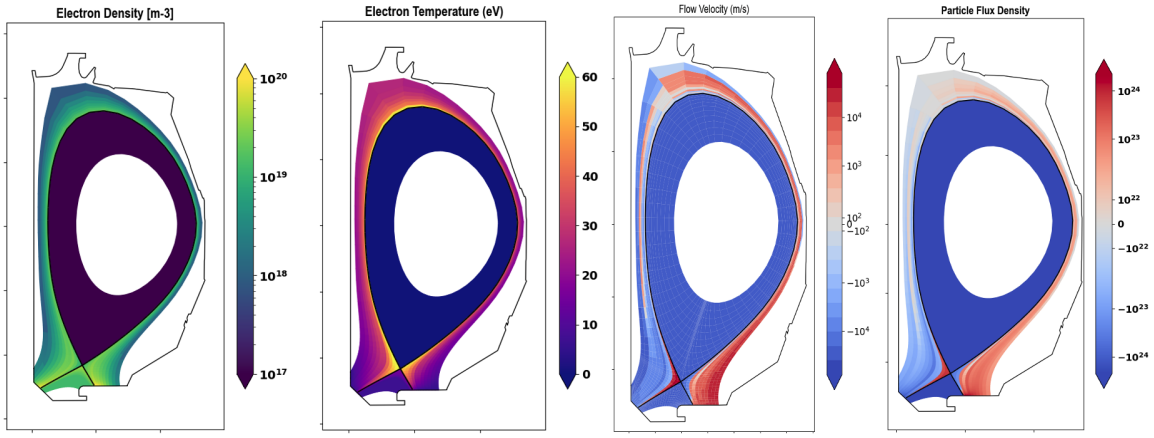


Figure 4.6: 2D profiles of shot 186703 showing data that is used to calculated particle flux density from n_e and velocity v. (a) shows the electron density, (b) shows the electron temperature, (c) shows the plasma flow velocity, and (d) shows the calculated plasma flux density poloidally across the DIII-D tokamak

flux density within the modeled scenario in a 2D poloidal cross-sectional view. Upon successfully running the model, the initial validation involves assessing the deviation between the modeled data and diagnostic data.

Figure 4.7 displays the electron density (n_e) and electron temperature (T_e), along with the goodness-of-fit between experimental data and OSM model data. The χ^2 values between the model and the data are reported as 1.34 for n_e and 5.70 for T_e. These χ^2 values serve as indicators of the agreement between the model and experimental data, with lower values generally suggesting better alignment. Figure 4.8 shows the validation for Langmuir Probe diagnostic with (a) n_e, (b) T_e and (c) J_{SAT} for outer divertor target.

Referring to Equation 3.33, we can compute $f_{wall-OEDGE}$ by evaluating the particle flux density in region 1 over the particle flux density in region 3, as illustrated in Figure 4.9. Sub-figure (a) represents the electron density (n_e) for region 1, (b) for region 2, and (c) for region 3. Additionally, Figure 4.9 includes a n_e cross-section obtained from the OEDGE run.

Similarly, Figure 4.10 presents the plasma velocity for the corresponding regions. These visualizations provide valuable insights into the variations in electron density and plasma velocity across different regions, aiding in the calculation of $f_{wall-OEDGE}$. Figure 4.11 shows particle flux density in region 1, region 2 and region 3 calculated from Figure 4.9 and 4.10. It also plots a 2D cross-section of particle flux density in three regions.

In this context, the estimation of modeled $f_{wall-OEDGE}$ facilitates a robust comparison with experimental f_{wall} by evaluating the particle flux density at the windowpane region, ensuring an 'apples-to-apples' comparison. This approach enhances the assessment of the model's predictive capabilities against experimental data, providing a comprehensive understanding of the agreement between the two.

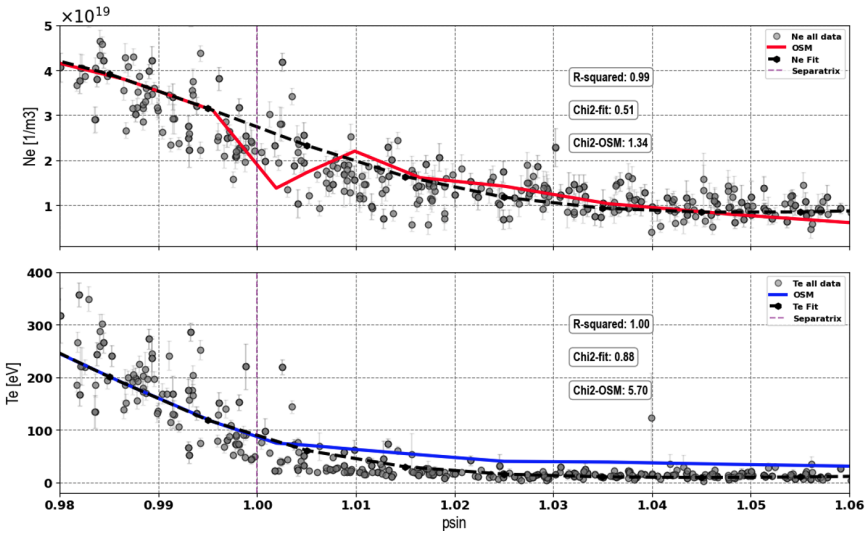


Figure 4.7: Validation of (a) n_e and (b) T_e through OSM with the Thomson Scattering data with χ^2 for n_e being 1.34 and for T_e being 5.70.

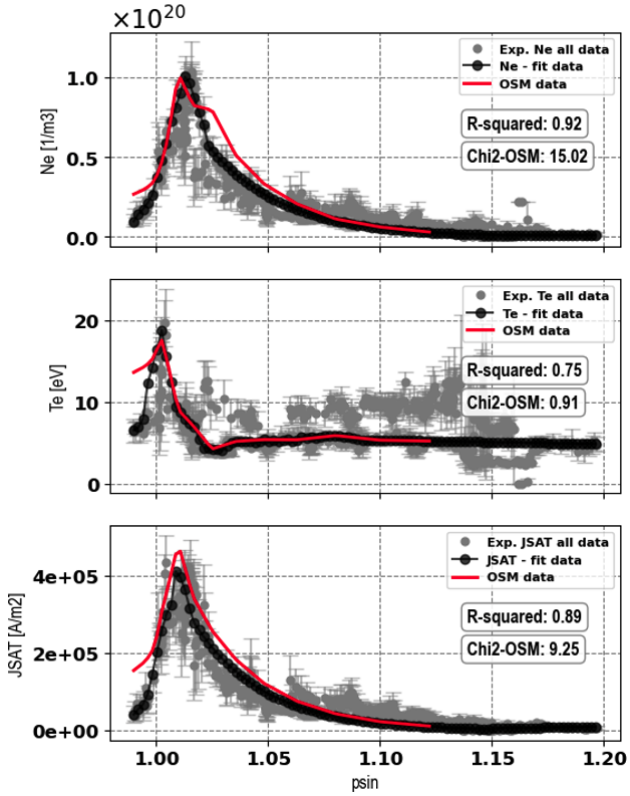


Figure 4.8: Validation of (a) n_e, (b) T_e and (c) J_{SAT} through OSM with the Langmuir Probe data with χ^2 for n_e being 15.02 and for T_e being 0.91 and for J_{SAT} being 9.25

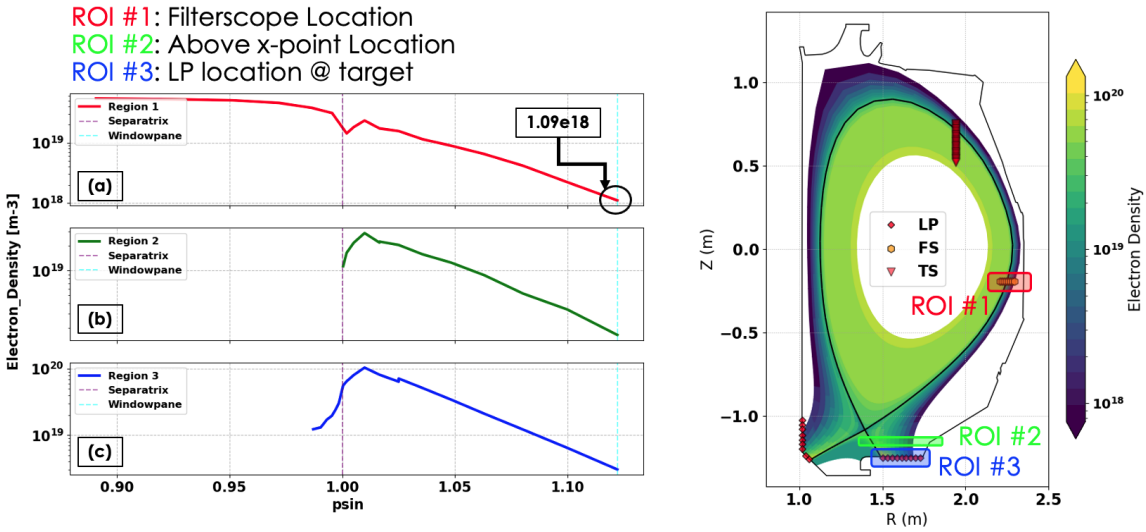


Figure 4.9: n_e estimation in three regions using OEDGE as seen in sub-figure a, b and c. Region 1 is defined on the Filterscope location, Region 2 is defined as the region just below the x-point and Region 3 is the region on the divertor target

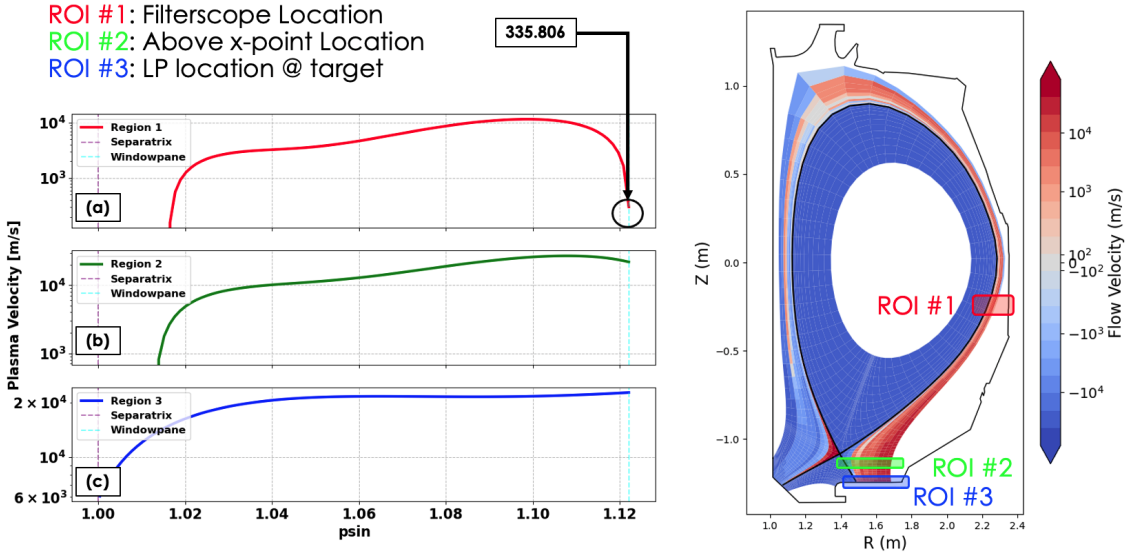


Figure 4.10: v estimation in three regions using OEDGE as seen in sub-figure a, b and c. Region 1 is defined on the Filterscope location, Region 2 is defined as the region just below the x-point and Region 3 is the region on the divertor target

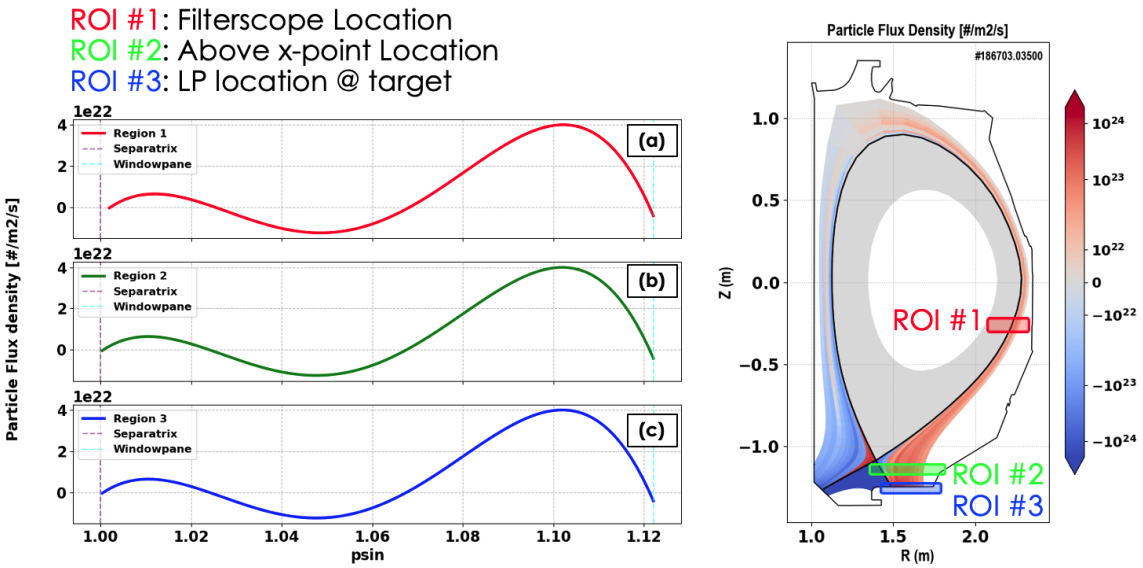


Figure 4.11: Γ_{wall} estimation in three regions using OEDGE as seen in sub-figure a, b and c. Region 1 is defined on the Filterscope location, Region 2 is defined as the region just below the x-point and Region 3 is the region on the divertor target

4.1.6 Estimation of poloidally averaged $< f_{wall-oedge} >$

An advantageous aspect of having a modeling case lies in the capability to estimate quantities across a 2D cross-section where diagnostic data may be sparse during experimental runs. Referring to Equation 3.34, we can estimate the poloidally averaged $f_{wall-OEDGE}$ radially across the window frame A - B, as depicted in Figure 4.12. The figure illustrates the density and velocity plotted across the S-coordinate, representing the flux surface. In Figure 4.12, the S-coordinate values between the windowpane are observed to span from 30 to 45 m. The values averaged across the S-coordinate are then utilized to calculate the poloidally averaged $f_{wall-OEDGE}$. This approach enables a comprehensive assessment of the quantity across the specified region, offering insights into its radial distribution.

4.2 Summary for Shot 186703 and database of plasma discharges for comparative study between divertor design

The table below summarizes the results obtained from both empirical and model-driven estimations of f_{wall}. Notably, the empirically derived and model-driven f_{wall} values are quite similar, hovering around 0.7. However, the calculated value of $f_{wall-OEDGE}$, obtained by poloidally averaging the particle flux across the windowpane, exhibits a decrease to approximately 0.55.

This observation may suggest a greater interaction of particles crossing the window pane radially, possibly unaccounted for during the experiments. As previously stated, the goal of this thesis is to do a comparative study between divertor design for multiple plasma discharges. By laying down the step by step process and results for estimation of quantities shown in Table 4.1, one can follow up with more plasma discharges to calculate the same. The details are shown in Appendix E.

Table 4.1: Summary of calculation of f_{wall} via experiment and OEDGE model for Shot 186703

Shot	I_{wall} [# /s]	I_{div} [# /s]	f_{wall}	$f_{wall-oedge}$	$< f_{wall-oedge} >$
186703	1.01e19	1.45e19	0.7	0.71	0.55

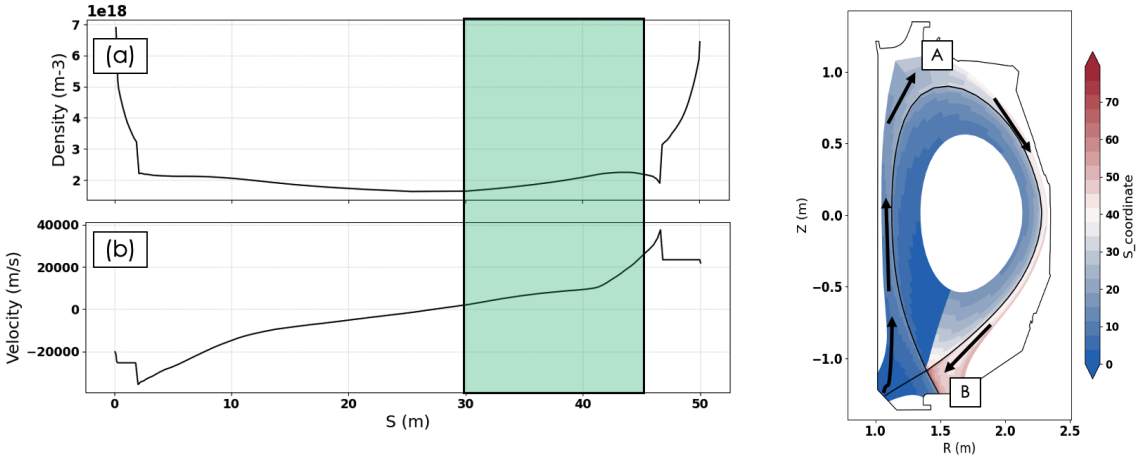


Figure 4.12: average n_e and v estimation across the poloidal cross-section using OEDGE as seen in sub-figure a, and b. The cross-section figure on the right shows the 2D plot of the s-coordinate with flux surface and showing window pane region

Here, Table 4.2 shows details about the plasma discharges with $B \times \nabla B$ towards (reverse B_T) the data and Table 4.3 shows details about the plasma discharges with $B \times \nabla B$ away (forward B_T) the data.

4.3 Results from GRP estimation for conventional and non-conventional divertor

GRP is quantified on seven different types of divertor configurations present at DIII-D – four conventional divertor types: LSN Floor, LSN Shelf, USN SAS, and USN Floor; and three non-conventional divertor types: Snowflake, X-divertor, and a sub-divertor category of USN Floor - Vertical right. All seven divertors range in divertor target size, baffling, slot presence, and x-point height. Figure 4.13 (a-g) shows all seven divertor cross-sections along with their GRP value present in that selected time arranged in increasing value of divertor structural restriction. As seen in Figure 4.13, the snowflake configuration has the lowest median GRP value at 0.13, and the SAS divertor configuration has the highest median GRP value at 0.82.

Figure 4.14 (a-b) shows a breakdown of $\alpha^{\circ}$and $\theta_{max}{}^{\circ}$ for LSN Floor plotted as a function of time respectively. The data seen in Figure 4.14 consists of 58 plasma discharges sampled from 1000 – 6000 msec at every 20 msec. In Figure 4.14 (a) the angle of the strike point ranges from 91°- 116° with the median value at 104.94°. Figure 4.14(b) the $\theta_{max}{}^{\circ}$ ranges from 2.1°– 142.1° with a median value of 37.94°. Each data point in Figure 4.14(b) has a $\theta_{max}{}^{\circ}$ that is made of a summation of transmission factors of all 58 plasma discharges, one of which is represented in Figure 4.15 for Shot 174795 at 3940ms time slice. The summation of transmission factors is calculated as LPFC below the critical length (L_{crit}) at every discretized index value of the DIII-D wall geometry. Figure 4.15 shows the outer strike point (OSP) location and indicates the hypotenuse length from the point of strike point location to the index value to the next plasma-facing component.

Table 4.2: Details of plasma discharges in L-mode and H-mode for $B \times \nabla B$ towards the target

L-mode						
Type	Shot #	Time	B_T	I_p	$P_{inj.}$	n_e
		[ms]	[T]	[MA]	[MW]	$[10^{19} m^{-3}]$
LSN Floor	167234	2000-4000	2	1.19	0.5	2.4
LSN Shelf	163210	3000-4000	2	1	1.1	2.25
USN Floor	184533	2000-4000	-2	1	4	3.4
H-mode						
LSN Floor	167245	3000-4000	2	1.19	3.9	5.2
LSN Shelf	186703	2500-3500	2	1.3	6	8
USN Floor	179974	2000-3100	-2	1.3	6.5	6

Table 4.3: Details of plasma discharges in L-mode and H-mode for $B \times \nabla B$ away from the target

L-mode						
Type	Shot #	Time	B_T	I_p	$P_{inj.}$	n_e
		[ms]	[T]	[MA]	[MW]	$[10^{19} m^{-3}]$
LSN Floor	174803	450-600	-2	0.9	1.7	1.4
LSN Shelf	186791	900-110	-2	1	Ohmic	2.8
USN Floor	179760	600-750	2	1	1.32	1.45
H-mode						
LSN Floor	175937	2000-4000	-2	1.3	5.1	6.2
LSN Shelf	186791	3000-4000	-2	1.3	5.7	6.8
USN Floor	179760	2500-3200	2	1.3	6.15	4.8

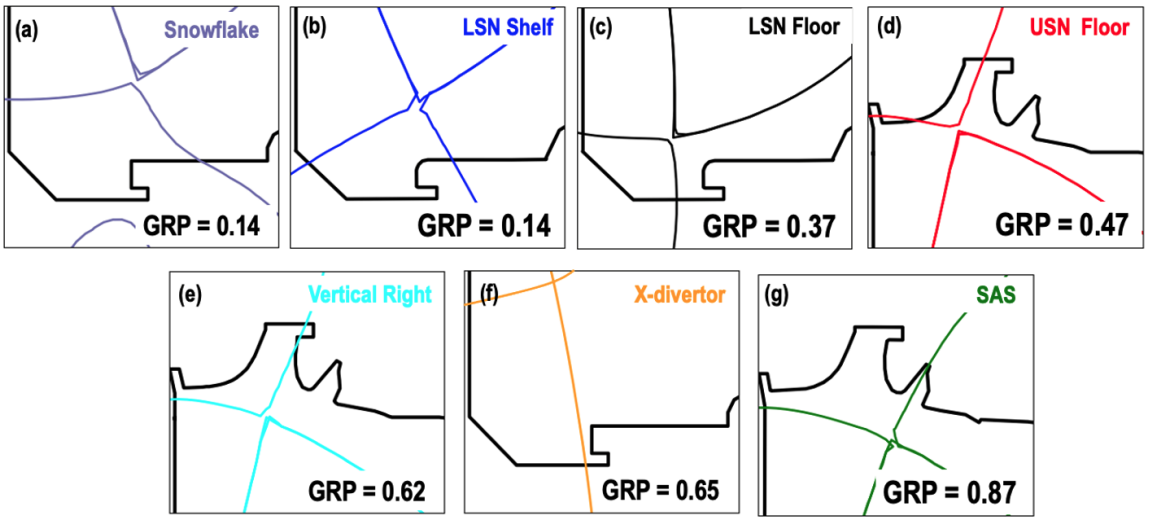


Figure 4.13: Seven different DIII-D divertor configuration, viz., (a) Snowflake with GRP = 0.14, (b) LSN Shelf with GRP = 0.14, (c) LSN Floor with a GRP of 0.37, (d) USN Floor with GRP = 0.47, (e) Vertical right with GRP = 0.62, (f) X-divertor with a GRP of 0.85, (g) SAS with GRP = 0.87. The seven sub-figures show the location of the strike point for each divertor configuration for one example plasma discharge

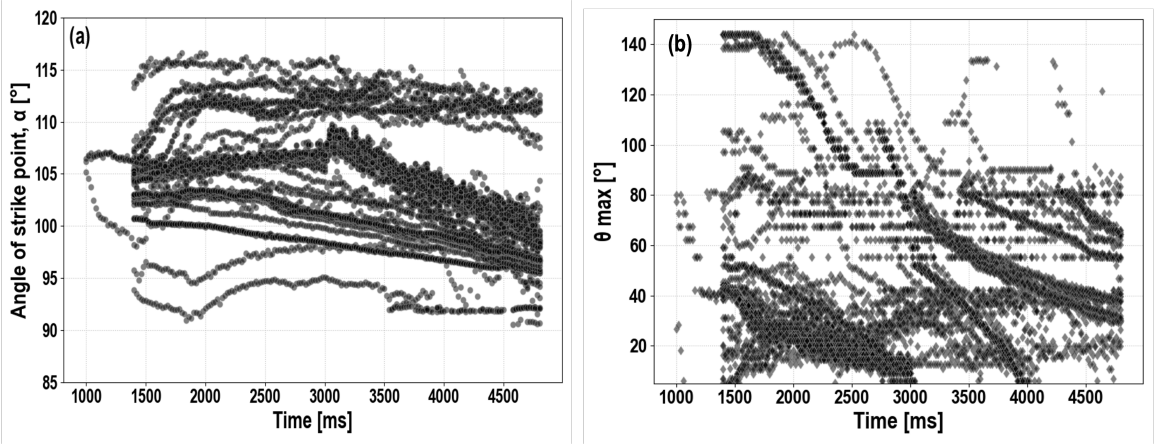


Figure 4.14: Variation of (a) α, angle of strike point and (b) θ_{max} as a function of time for LSN Floor configuration for 58 plasma discharges at every 20msec

Figure 4.16 shows the relationship of the GRP values with the different divertor configurations as a function of time with Kernel Density Estimate (KDE) showing the population density of data points with respect to GRP on the right side of the plot. A KDE plot serves as a visual tool to depict the distribution of observations within a dataset, akin to a histogram. Unlike a histogram, a KDE utilizes a continuous probability density curve in one or more dimensions, offering a less cluttered and more interpretable representation, particularly when illustrating multiple distributions. Figure 8 consists of more than 250 plasma discharge shots ranging from 1000 msec to 6100 msec, with high-fidelity data analyzed every 20 msec. It depicts the variation of restriction present on four conventional divertor geometries, viz., LSN Floor (black), LSN Shelf (blue), SAS (green), and USN Floor (red). Figure 4.17 depicts the variation of restriction of three non-conventional divertors, viz., Snowflake (purple), X-divertor (orange) and a sub-divertor types: of USN Floor: vertical right (cyan). The reason for bifurcating the USN Floor configuration is the location of the strike point, which for the cases of vertical right, has the strike point between the divertor target and SAS. Figures 4.16 and 4.17 also show the KDE plot on the right of the GRP scatter plot, which shows each divertor configuration's population density with its median value.

As mentioned, GRP ranges from 0 to 1, where if the GRP value is closer to 0, the restrictions present at the divertor are almost none. Figure 4.16 shows the lowest GRP value ranging from 0.05 to 0.25, with a median value of 0.14 for LSN Shelf configuration. The neutrals and impurities born here could easily leak into the main chamber region, due to absence of baffling / restricting structure present for this divertor configuration.

Kernel Density Estimate (KDE)

KDE offers a method for visualizing univariate or bivariate distributions, akin to histograms but providing a continuous probability density curve representation.

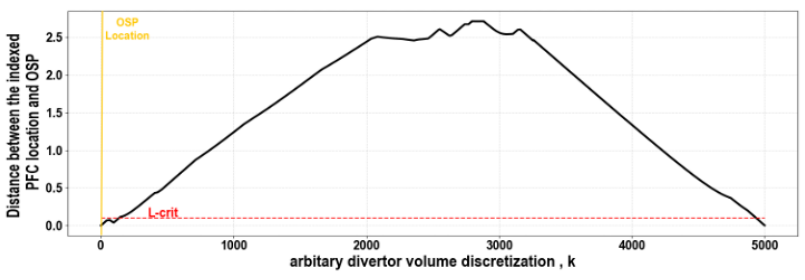


Figure 4.15: Variation of the hypotenuse (length between OSP to the PFCi value) plotted as a function of discretized wall index values that make up the DIII-D geometry for Shot 174795 at 3940ms. Summation of the L_{PFC} (the hypotenuse length) below the critical length (L_{crit}) makes the transmission factor.

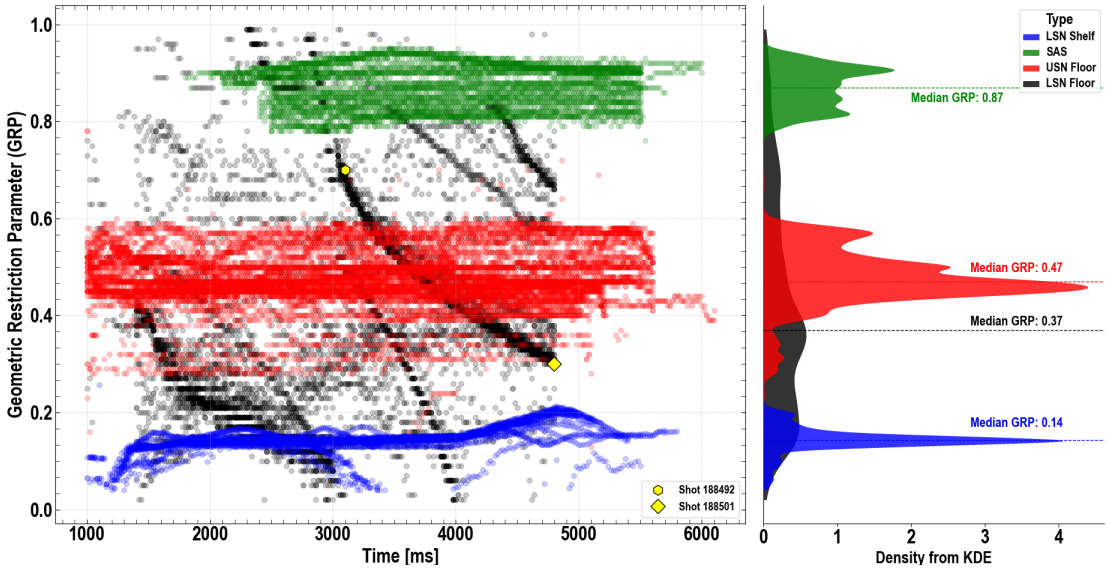


Figure 4.16: GRP values for different divertor configurations depicted as a function of time along with KDE for each configuration with median value. There are four conventional divertor configurations plotted here, LSN Shelf (blue), LSN Floor (black), USN Floor (red), and SAS (green).The figure also depicts two LSN Floor discharges depicted in Figure 2: Shot 188501 (yellow diamond marker) and Shot 188492 (Yellow hexagon marker) and it can be seen the variation in GRP value with just change in OSP location in same divertor configuration

Unlike histograms, KDE plots are less cluttered and more interpretable, particularly when illustrating multiple distributions. However, the effectiveness of KDE relies on appropriate smoothing parameters, and it may introduce distortions if the underlying distribution is bounded or not smooth. Key features of KDE include its reliance on a single kernel function for representation, its nonparametric nature determined by the dataset, and its sensitivity to the bandwidth parameter Weglarczyk [2018].

Unlike histograms, KDE does not require an optimization technique for fitting to the data. Compared to histograms, KDE offers advantages such as smoother curves that better capture details and potential non-unimodality, utilization of all sample points for improved information retrieval, more convincing depiction of multimodality, and a higher level of bias reduction.

In two-dimensional applications, KDE outperforms histograms by avoiding the need to specify bin orientations, thereby reducing subjectivity in representation Weglarczyk [2018].

The bandwidth, representing the standard deviation of the smoothing kernel in KDE, holds significance as it influences the accuracy of the data representation. An incorrectly specified bandwidth can lead to distortions in the visual depiction of the dataset. The default bandwidth is most effective when the underlying distribution is smooth, unimodal, and approximately bell-shaped Weglarczyk [2018].

Interpreting the density axis units (see Figures 4.16 and 4.17 right subplots) can be confusing as the curve represents a density rather than a probability at each point. Probabilities can only be derived by integrating the density over a range. The curve is normalized to ensure that the integral across all possible values equals 1, thereby making the scale of the density axis contingent on the data values Weglarczyk [2018].

The kernel density estimator can be defined as

$$\hat{f}_h(x) = \frac{1}{n}\sum_{i=1}^{n} K_h(x - x_i) = \frac{1}{nh}\sum_{i=1}^{n} K\frac{x - x_i}{h} \tag{4.1}$$

The samples $x_1, x_2, x_3 ... x_n$ are drawn independently and with the same distribution, originating from an univariate distribution with an unknown density function f at any given point x. Here, K represents the kernel, a non-negative window function, and $h > 0$ denotes a smoothing parameter known as the bandwidth. The kernel with the subscript h is referred to as the scaled kernel and is defined as $K_h(\mathrm{x}) = 1/\mathrm{h}\ \mathrm{K}(\mathrm{x}/\mathrm{h})$. In essence, one aims to select h as small as feasible based on the data; nevertheless, there exists a constant trade-off between the estimator's bias and its variance Weglarczyk [2018].

The smoothing parameter, h, is a function of sample standard deviation $\hat{\sigma}$ and the sample size n. It is given as:

$$h = 1.06\hat{\sigma}n^{\frac{-1}{5}} \tag{4.2}$$

Coming back to the GRP estimation, the second lowest GRP value ranges from 0.1 to 0.2, with a median value of 0.14 for the Snowflake configuration, as seen in Figure 4.17 – purple markers. We know the strike point of the snowflake divertor (Figure 5c) is on a similar LSN Shelf target with little to no baffling. However, the variation of GRP of this divertor configuration is more varied than LSN Shelf due to its difference in magnetic geometry, which has higher flux expansion in this kind of divertor geometry. It implies that with higher flux expansion, the neutral particles could get more region to get ionized before leaking in the main chamber region.

USN Floor (Red) and LSN Floor (Black) divertor configurations have GRP values ranging from 0.25 – 0.6 and 0.1 – 0.98, respectively in Figure 4.16. These divertor geometries provide a range of baffling around the divertor target that lets the restriction vary by such a significant margin. As understood until now, the value of GRP is lower when the strike point is away from the baffling structure, providing an easier leakage path. In contrast, GRP is higher when the strike point is near the baffling structure, implying the neutrals born at the strike point are restricted due to the baffling. We see a higher variation in GRP value for the LSN Floor

configuration than USN Floor due to a higher flat divertor surface area in the LSN Floor configuration. In contrast, USN Floor has a bottleneck structure around it, providing a unique geometry to keep the neutrals from leaking into the main chamber. Also, the angle of the strike point 'α' might be similar in each configuration, but the presence of physical restriction provided by the baffling structures impact the estimation of GRP.

X-divertor (orange), similar to LSN Floor divertor configuration has a GRP value ranging from 0.15-0.95 with a median of 0.65, making it the second most restrictive divertor configuration present at DIII-D. There is some variation in the GRP values, as seen in Figure 4.17, for similar reasons as LSN Floor. This configuration has a longer divertor leg compared to other configurations which provides particles a longer path to leak, during which they could quickly get ionized and hence would potentially 'leak' less.

The highest GRP value with a median of 0.87 ranges from 0.75-0.95 for SAS divertor configuration due to its restrictive geometry implied by its name – Small Angled Slot (SAS) divertor (green in Figure 4.16). The main reason for the higher restriction is the baffling position (see Figure 4.13 (g)), which significantly restricts neutrals born in the divertor and limits leakage to the main chamber region.

Vertical right (cyan) divertor configurations essentially are part of the USN Floor configuration but have the strike point far out to the right of the divertor target (Figure 4.13f). Figure 4.17 shows that the vertical right configuration has a median GRP value of 0.62 with a range of 0.3 – 0.9. This shows the target (bottleneck structure) acts as a divertor with varied restrictions mostly depending on the angle of the strike point on the divertor structure. Note that the number of data points for the sub-divertor category is fewer compared to other divertor scenarios and are not widely used divertor configurations. These were used here to show the impact of strike point location to quantify divertor restriction.

4.3.1 Effect of geometry on neutral particle restrictions

We see that divertor restriction varies based off the physical PFC geometry and the magnetic geometry of the diverted tokamak. This can be noted by comparing two plasma discharges: Shot 188492 (yellow hexagon) and Shot 188501 (yellow diamond) in Figure 4.16. The location of OSP for the two plasma discharges are depicted in Figure 4.14 and we can see both the plasma discharges have similar x-point height and are on same divertor configuration – i.e., LSN Floor. However, the only varying factor between the two plasma discharges is the location of their OSP. As seen in Figure 4.16, Shot 188492 (yellow hexagon) has the GRP value as 0.7 with the OSP at 1.35m and Shot 199501 (yellow diamond) has the GRP value as 0.3 with the OSP at 1.18m. We see that as the OSP location was near to the baffling structures, the GRP value that incorporates the structure to calculate GRP has higher value.

In conclusion, geometric restriction was calculated using a new technique for seven divertor configurations at DIII-D. The GRP value varies for all divertor configurations with snowflake providing the lowest divertor restriction and SAS providing the most divertor restriction. Table 4.4 shows median GRP and std to the GRP for all divertor configurations. Also, Table 4.5 shows summary of the GRP values for the selected plasma discharges for this thesis where we see the lowest restriction provided for LSN Shelf configuration, and the most restriction configurations is provided by LSN Floor. The table shows the mean GRP and the standard deviation of the GRP for each plasma discharges in both $B \times \nabla B$ away and towards the target.

Table 4.4: Summary table of calculated GRP values for conventional and non-conventional divertor geometry in DIII-D

Divertor Type	Median GRP	Std. GRP
LSN Shelf	0.14	0.08
LSN Floor	0.37	0.3
USN Floor	0.47	0.14
SAS	0.87	0.09
snowflake	0.14	0.1
X divertor	0.65	0.45
Vertical right	0.62	0.3

Table 4.5: Details of plasma discharges in L-mode and H-mode for $B \times \nabla B$ towards the target and away from the target

Towards	**the**	**target**		
L-mode				
Type	Shot #	Time	GRP	std GRP
		[ms]		
LSN Floor	167234	2000-4000	0.58	0.116
LSN Shelf	163210	3000-4000	0.03	0.006
USN Floor	184533	2000-4000	0.42	0.084
H-mode				
LSN Floor	167245	3000-4000	0.58	0.116
LSN Shelf	186703	2500-3500	0.03	0.006
USN Floor	179974	2000-3100	0.42	0.084
Away	**from**	**the target**		
L-mode				
LSN Floor	174803	450-600	0.58	0.116
LSN Shelf	186791	900-110	0.03	0.006
USN Floor	179760	600-750	0.42	0.084
H-mode				
LSN Floor	175937	2000-4000	0.58	0.116
LSN Shelf	186791	3000-4000	0.03	0.006
USN Floor	179760	2500-3200	0.42	0.084

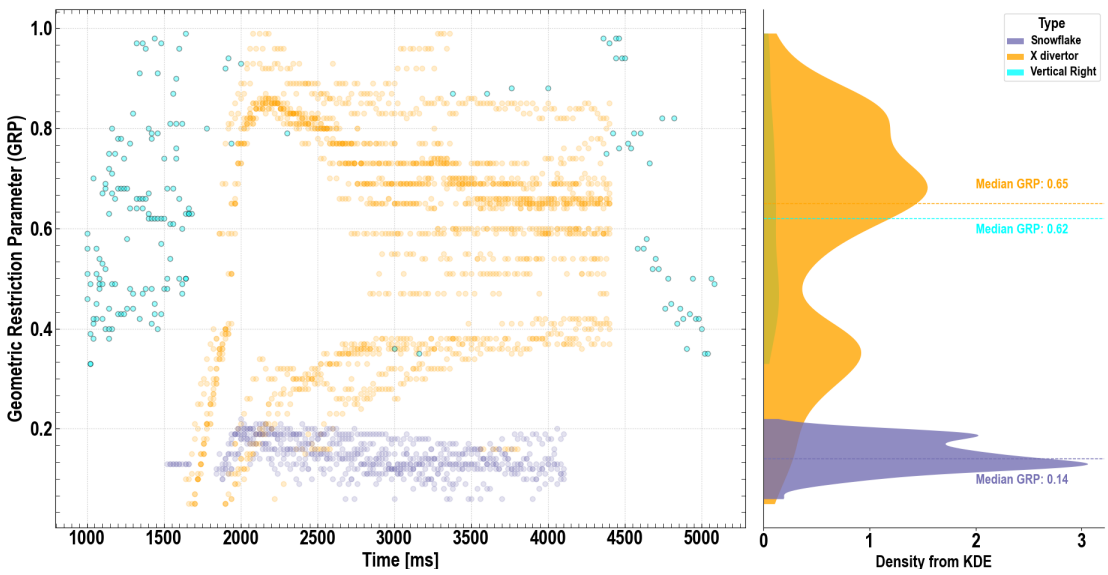


Figure 4.17: There are three non-conventional divertor configurations plotted here, Snowflake (purple), x-divertor (orange), and Vertical Right (cyan). GRP values for different divertor configurations are depicted as a function of time, along with KDE for each configuration with a median value.

Chapter 5

Conclusions from DIII-D divertor closure analysis

Changes in the divertor configuration have been quantified through the evaluation of the divertor restriction, measured along with the magnitude of plasma fluxes in the main chamber (I_{wall}), and over the divertor region (I_{div}), as detailed in Chapter 4. This observation underscores the influence of divertor geometry on the ratio of flux magnitudes in the main chamber to the divertor — an indicator of neutral leakage. Such variations can potentially lead to differences in main chamber recycling. To investigate the impact of divertor geometry on potential neutral leakage, we need to understand the neutral pathways and recycling paths on a tokamak cross-section.

5.1 Restrictions influencing main chamber and divertor recycling as measured by Filterscope

The detection of a D-alpha signal at the midplane suggests the presence of a neutral population undergoing ionization at the plasma edge, with potential contributions from divertor leakage recycling (DLR) and main chamber recycling (MCR). While prior research by Whyte in 2005 Whyte et al. [2005] indicates that MCR likely

dominates based on their dataset, this conclusion is limited to a specific divertor closure level, warranting further investigation.

Recent hypotheses by Wynn, Lipschultz, et al. Lipschultz and LaBombard [2005], Wynn [2017] propose that divertor recycling might contribute to the formation of SOL density shoulders by reducing the parallel flow of ions from the SOL to the divertor. Their analysis of JET cases suggests divertor recycling as a probable cause for shoulder formation and MCR. This underscores the importance of exploring potential correlations with divertor recycling in the DIII-D dataset.

Currently, there is insufficient data to draw conclusions regarding the impact of wall interactions (I_{wall}) or direct measurements of MCR. However, existing data may shed light on the significance of DLR in midplane ionization. Specifically, examining correlations between midplane ionization rates (measured by OMP filterscope D-α)) and divertor recycling rates (measured from divertor D-α) could provide insights, particularly as divertor closure levels vary.

Figure 5.1 presents a comparison between main-wall D-α and divertor D-α as a function of GRP. This serves as a test to understand the impact of varying restrictions on neutral ionization. It is observed that the particle flux measured on the LFS of divertor remains constant with varying restrictions, whereas the particle flux measured at the outboard midplane decreases by a factor of 10 as restrictions increase.

Figure 5.1 presents data from the Filterscope diagnostic at varying GRP with different divertors. The LSN shelf divertor cases have a GRP of 0.03, the USN floor has a GRP of 0.43, and the most restricted divertor LSN Floor has a GRP of 0.58. The magnitude of particle fluxes measured by the midplane filterscope are measured toroidally across the separatrix whereas the filterscope measurement from the divertor target is measured poloidally across. Our measurements of particle flux at the midplane location align with recent findings Groth et al. [2003], Whyte et al. [2005], who observed weak midplane main-chamber D_α emissions compared to the divertor flux.

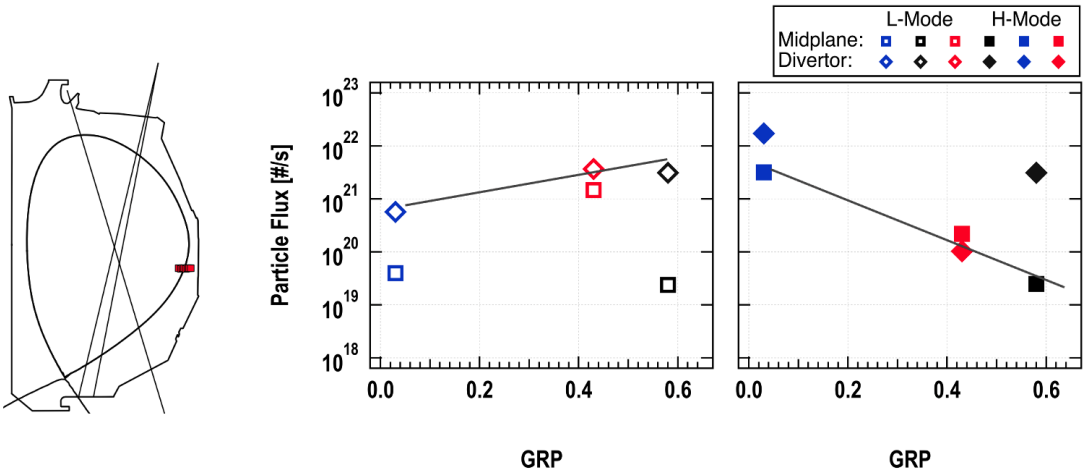


Figure 5.1: The particle flux, as measured by the Filterscope D_α (subfigure (a) for measurement location), reveals the influence of divertor restriction on neutral ionization in the outboard midplane. (b) While divertor recycling (diamond markers) remains consistent across varying divertor restrictions (GRP) in H-mode (filled markers), the ionization of neutrals (square) exhibits a tendency to decrease with increased divertor restriction. The opposite is true for L-mode scenrio (open markers)

A significant consequence of plasma main-wall contact is the consequent release of recycled D molecules and neutrals from the main wall, which contribute to plasma fuelling. The influx of D neutrals, (measured in D molecules per square meter per second), is estimated at discrete main-wall locations using D_α brightness and neutral pressure gauges. Typically, the gas pressure in the main chamber during these experiments is around 10^{-4} Torr, which is interpreted as a D_2 molecular flux density ($\dot{D}_2 = \frac{1}{4} n_{D2} \bar{v}$), assuming room temperature D_2 molecules from the DIII-D wall. Half of this flux is directed towards the plasma and contributes to local D atom ionization in the plasma after molecular dissociation, i.e., $\dot{D} \approx 2(\text{D/molecule}) \times \frac{1}{2} \dot{D}_2$ Whyte et al. [2005].

For divertor D_α views approximately normal to recycling surfaces, the D_α brightness, $B_{D-\alpha}$, can be directly interpreted as D atom influx using the well-known ionizations per photon ratio (also known as SXB ratio), i.e., $\dot{D} \approx 4\pi B_{D-\alpha} \frac{S}{XB}$. This straightforward interpretation is possible because the deuterium atoms are ionized and excited in the same viewing volume Whyte et al. [2005].

The scenario is somewhat different for the midplane D_α array, as it does not directly view a recycling surface but rather has view chords tangent to the SOL. Here, the measured brightness profile must be inverted to obtain a radial emissivity (photons per cubic meter) profile, which is then converted to a volumetric ionization profile (ionizations per cubic meter) using S/XB based on local n_e and T_e. The ionization profile is then radially integrated through the SOL to determine a local, outer midplane. These fluxes from divertor and midplane are plotted in the Figure 3.1.

As seen in Figure 5.1, the local recycling flux at the divertor is 100 times greater than at the window-frame location in the main chamber. While this trend follows the results from Whyte et al. [2005], one thing that data from Figure 5.1 differs from previous results is adding in the understanding of restriction variation. With the addition of increased restriction, one can potentially call out Equation 3.1 and decipher what flux pathways play a major role. As seen in Figure 5.1, the highest

restricted divertor has the particle flux lower by a factor of 4 compared to the divertor whereas with lower restriction the difference is a factor of two. This implies ionization reduces by a factor of 2 with an increase in restriction by 60%.

We can also offer speculative remarks to bolster our hypothesis concerning a direct linkage between main chamber recycling (MCR) and divertor leakage recycling (DLR) with varying restrictions. The MCR flux does not exhibit a non-linear decrease, which would suggest a variation in neutral pathways as described in Equation 3.1. According to this equation, a reduction in main chamber fluxes could stem from lower local recycling or fewer incoming ions deposited through the I^+_{SOL} to I^+_2 pathway, as depicted in Figure 3.1. Previous studies have highlighted the correlation between increased restrictions and reduced particle leakage Loarte [2001], Casali et al. [2019]. In this context, the divertor's "shielding" of neutrals could precisely adjust the number of particles transported into the main chamber region. Thus, it can be suggested that MCR is influenced by changes in divertor restrictions and DLR.

Another way to understand the influence of DLR on to MCR is by quantifying the density pedestal with varying divertor restrictions. Experiments conducted on JET and DIII-D, where the divertor configurations were manipulated, demonstrated a significant alteration in the density pedestal structure. JET studies Joffrin et al. [2017] indicated a close correlation between overall density and the availability of neutrals in the device and also showed the impact of recycled neutrals with varying divertor restriction Loarte [2001]. In an open divertor configuration, neutrals can move more freely into the main chamber, whereas in a closed divertor, they tend to remain trapped in the private flux region and the divertor area. Dedicated studies on DIII-D comparing plasmas in open versus closed divertor configurations showed that, for similar divertor conditions (density and temperature), the density at the top of the pedestal was much lower for the open divertor configuration. Achieving similar divertor conditions necessitated significantly more fueling using gas puff in the open divertor configuration, leading to increased electron density not only in the divertor but also in the pedestal, while the SOL densities remained similar between

the two cases. Addition of gas puff in the closed divertor configuration raised the density but also resulted in an outward shift of the electron density profile, similar to observations on JET and AUG Dunne et al. [2016], Stefanikova et al. [2018], Beurskens et al. [2011]. However, no such outward shift was observed in the open divertor configuration. The electron density continued to increase with increased fueling, but no increase or decrease in the shift between the electron density and temperature profiles was observed. The common factor between the shift in the electron density and temperature profiles is $\eta_e = \frac{L_n}{L_{Te}}$, a measure for the drive in Electron Temperature Gradient (ETG) turbulence, suggesting that the shift is not solely linked to changes in main chamber fueling or neutral pressure but also to changes in transport Wang et al. [2018].

SOLPS modeling of these experiments revealed a large difference in ionization between closed and open divertor configurations and a distinct poloidal distribution of the neutral density, yet the average ionization inside the separatrix for attached conditions remained similar Sontag et al. [2017]. While the divertor configuration strongly impacted the pedestal density, whether the divertor was attached or detached seemed to have less influence Moser et al. [2019]. The relative density increases with increased fueling were independent of whether the divertor was attached or detached. The increase in the pedestal density was directly linked to the increase in the separatrix density, which increased with increased gas fueling and continued to increase after detachment was observed, in any configuration Casali et al. [2019].

Another factor impacting the density pedestal structure is the grad-B drift direction T.H. Osborne [2019]. In DIII-D closed divertor experiments where the pedestal density was matched, an outward shift of the pedestal density occurred for $B\nabla B$ away from the X-point (unfavorable drift direction), resulting in a much higher SOL density. SOLPS simulations studying the effects of the $B\nabla B$ drift direction showed a strong effect on the radial particle flux at the midplane Sontag et al. [2017]. Simulations with $B\nabla B$ toward the X-point displayed a similar increase (although less

pronounced) in the SOL density compared to the case with $B\nabla B$ away from the X-point and also exhibited a small outward shift. This is shown via empirical approach in section 5.3 Mordijck [2020].

In summary, these experiments involved varying divertor geometry from 'open' to a more 'closed' configuration and altering the coupling of the strike point to the cryopump. Changes in divertor geometry and coupling to the pump directly impacted fueling of the core plasma through alterations in neutral pressure in the main chamber as well as the divertor, subsequently affecting the separatrix and pedestal density leading to higher MCR. The absence of a 'simple' model to predict how this would affect the pedestal density underscores the limitations in the predictive capabilities of any MHD model. These findings emphasize the role of the divertor and SOL conditions in determining the pedestal structure and the necessity for models predicting the pedestal structure to incorporate information on divertor and SOL characteristics to help understand the role of DLR for MCR.

5.2 Understanding the neutral opacity with respect to closure using OEDGE

In the evolving landscape of fusion research, the burgeoning size of tokamak devices brings them closer to emulating conditions akin to those within a reactor. This shift towards larger devices profoundly alters the interplay between neutrals and the edge pedestal structure. Neutrals, both recycled and introduced via gas puffing, find their efficacy in penetrating the confined plasma region considerably diminished. This diminishment, in turn, restricts their role as particle sources on closed flux surfaces. To quantitatively assess this damping effect of fueling neutrals, a parameter known as the neutral attenuation coefficient, or neutral opacity, represented by the symbol η is introduced. Details about opacity is shown in Section 2.3.1, however in a simplistic approach, analogous to optical opacity, η is directly proportional to both the local

electron density (n_e) and a generic cross-section for neutral-plasma interaction (σ). A neutral population introduced into a uniform plasma experiences exponential decay with a characteristic length scale (L_D) inversely related to η, and thus approximately proportional to $\frac{1}{n_e}$. Consequently, higher absolute edge densities render plasmas more impervious to neutrals. We further define an opaqueness screening parameter, $\eta \times \Delta = \frac{\Delta}{L_D}$, where Δ signifies the approximate boundary region width Mordijck [2020].

The screening effect of neutrals can vary significantly within individual devices and especially between devices of varying size and density. For a given toroidal device, opaqueness is directly proportional to the product of n (density) and a (minor radius), assuming the boundary region thickness scales with a. Considering $n = \frac{1}{2}(n_{eped} + n_{esep})$, the opaqueness in ITER is projected to be approximately $\sim 1.2 \times 10^{20}\,\mathrm{m}^{-2}$. In contrast, DIII-D typically operates at $\sim 1.5 \times 10^{19}\,\mathrm{m}^{-2}$, while JET, with a larger minor radius but similar pedestal densities, operates at twice the opaqueness of DIII-D. Alcator C-Mod, characterized by a high magnetic field, operates naturally at high density, resulting in opaqueness values of up to $7.0 \times 10^{19}\,\mathrm{m}^{-2}$. Thus, while devices like DIII-D, AUG, and JET typically operate at an opaqueness an order of magnitude lower than that expected on ITER, the opaqueness on C-Mod is only a factor of 2 lower. We adopt the term "opacity" to describe the reduced ability of neutrals to penetrate the plasma and "opaqueness" to represent $n \times a$, facilitating comparison across various experimental conditions Mordijck [2020].

Looking ahead, the larger physical size of future tokamak devices inherently increases opaqueness, thereby significantly diminishing the impact of divertor conditions on fueling. With neutrals' mean free path shortened, the pedestal essentially operates independently of the divertor, diverging from the close connection observed in current devices. In the scaled-down SOLPS version, an increase in divertor neutral concentration leads to a constant rise in upstream separatrix electron density, whereas in full ITER, the separatrix density saturates and remains constant, unaffected by changes in divertor neutral pressure. However, the divertor can still influence fueling, as evidenced by LaBombard et al.'s work LaBombard et al. [2017]. Therefore, if

divertor conditions directly affect plasma flows in the SOL, they will significantly impact fueling via gas puffing in the main chamber Mordijck [2020].

In the quest to enhance predictive capabilities of density pedestal structures in reactor regimes, several avenues emerge. In current devices characterized by low opacity, direct measurements of neutrals are paramount for providing a more realistic estimate of the particle flux source Mordijck [2020]. However, with the help of code experiments in OEDGE we can vary the opacity of the divertor and see how it impact the neutral density in the divertor and upstream region. Figure 5.2 shows the ratio of neutral density, measured both upstream and at the target, is plotted as a function of neutral opacity, defined as the product of plasma density and the minor radius. Subfigure (a) depicts a comprehensive plot encompassing all plasma discharges, showcasing variations in neutral opacity across different divertor configurations: LSN Shelf (blue), LSN Floor (black), and USN Floor (red). Subfigures (b-d) present individual ratios for each divertor configuration. The observed trend indicates that as opacity increases—indicative of a more opaque plasma—there is a decrease in neutrals leaking outside the divertor region. This phenomenon results in higher divertor recycling efficiency.

The significance of this graph lies in its indication that the GRP is most relevant in scenarios where the neutral density upstream correlates linearly with the target neutral production rate, maintaining a consistent ratio due to unchanged geometry. However, when this ratio begins to decline, it suggests that neutrals are becoming entrapped by plasma physics phenomena rather than by geometric constraints. For the GRP to serve as a valuable tool in the field, it is imperative to identify the plasma conditions in which it offers a practical simplified model for neutral closure, and to discern the circumstances where additional physics considerations may be necessary. In order to understand this, multiple code experiments were performed using OEDGE where the density of electrons were increased by a factor of 1, 2, 3, 4 and 5 for L mode and H mode plasma in $B \times \nabla B$ towards the target and away from the target conditions in LSN Shelf (blue), LSN FLoor (Black) and USN Floor (red) divertor configurations.

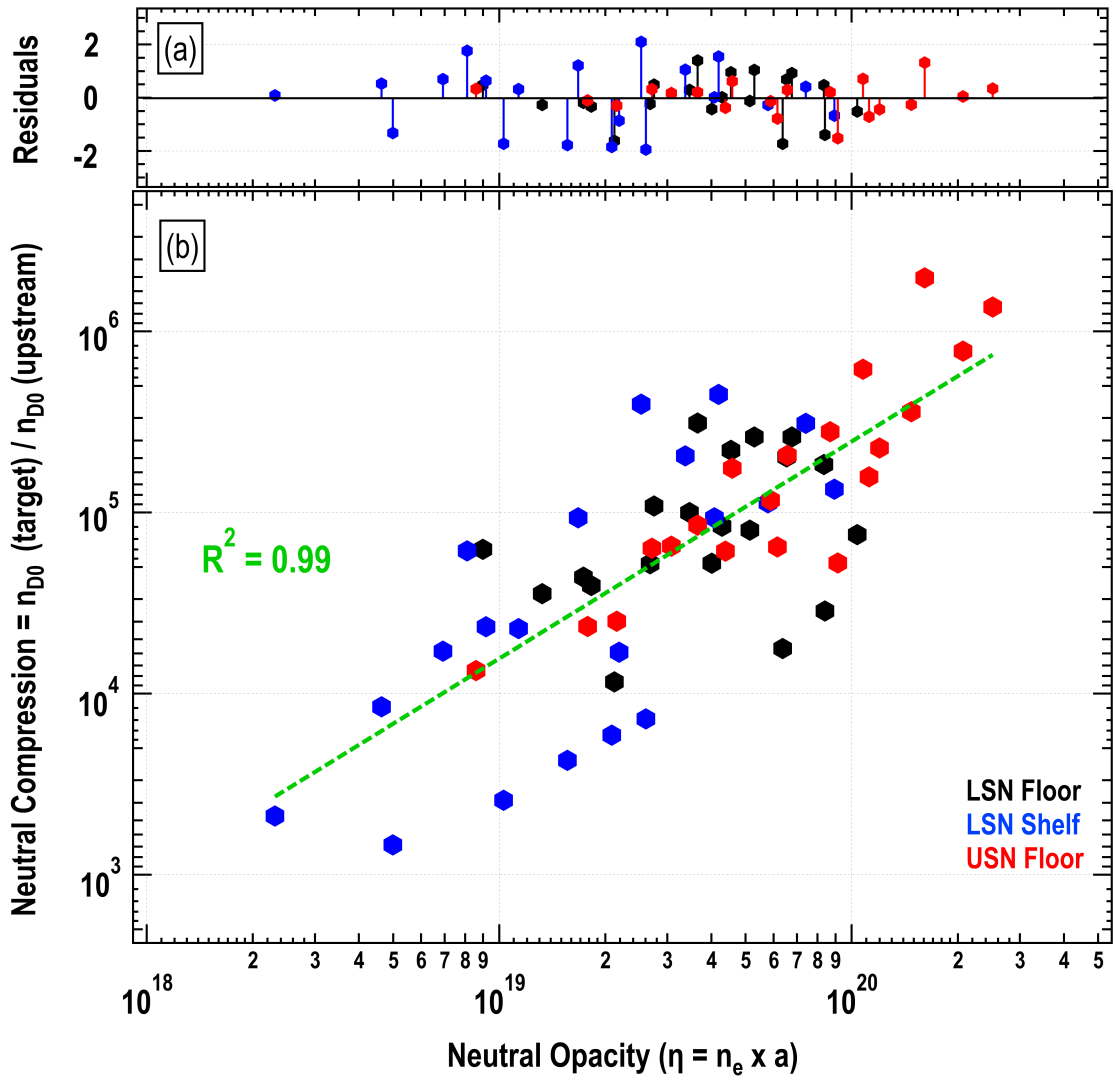


Figure 5.2: The ratio of neutral density, measured both upstream and at the target, is plotted as a function of neutral opacity, defined as the product of plasma density and the minor radius. Subfigure (a) present the residuals for the fit. The observed trend indicates that as opacity increases—indicative of a more opaque plasma—there is a increase in neutrals leaking outside the divertor region. This phenomenon results in higher divertor recycling efficiency. Subfigure (b) depicts a comprehensive plot encompassing all plasma discharges, showcasing variations in neutral opacity across different divertor configurations: LSN Shelf (blue), LSN Floor (black), and USN Floor (red)

The ratio of neutral density, observed upstream (crown) compared to the divertor target, is plotted against the neutral opacity ($n_e \times a$), where 'a' denotes the minor radius of the DIII-D tokamak. Figure 5.2(a) illustrates this ratio for all combined divertor geometries, displaying a linearly declining trend. A green line represents a fit to the data with a χ^2 value of 0.48. The fit suggests that as the plasma becomes more opaque, a possible detachment of the divertor would result in increased neutrals recycling within the divertor region, leading to reduced Divertor Leakage Recycling (DLR) with higher Divertor Recycling (DR). Consequently, this implies a potential decrease in leakage. However, such changes in opacity would invalidate the GRP estimation, which assumes neutrals to travel without undergoing ionization, charge-exchange, or recombination processes before reaching the baffle structure. Hence, it underscores the necessity to quantify GRP separately in detached or highly opaque plasma conditions, highlighting its applicability in assessing restrictions solely in attached plasma conditions.

Figure 5.3 illustrates the ratio of neutral density in the upstream region relative to the target for different divertor configurations: LSN Shelf (blue), LSN Floor (black), and USN Floor (USN) respectively. Both LSN Shelf and USN Floor exhibit a similar trend to subfigure (a), showing a increase in neutral density with increasing opacity. However, LSN Floor displays a notably different pattern, with the ratio of neutral density at the upstream to target remaining relatively constant despite increasing opacity. This observation can be attributed to two factors: (a) the presence of tighter baffling in LSN Floor compared to other divertors, and (b) the existence of exhaust pumps maintaining particle levels constant. Further investigation is required to estimate the GRP for configurations with higher restrictions and opacity, and to determine whether the trendline observed in subfigure (c) remains consistent or undergoes alterations.

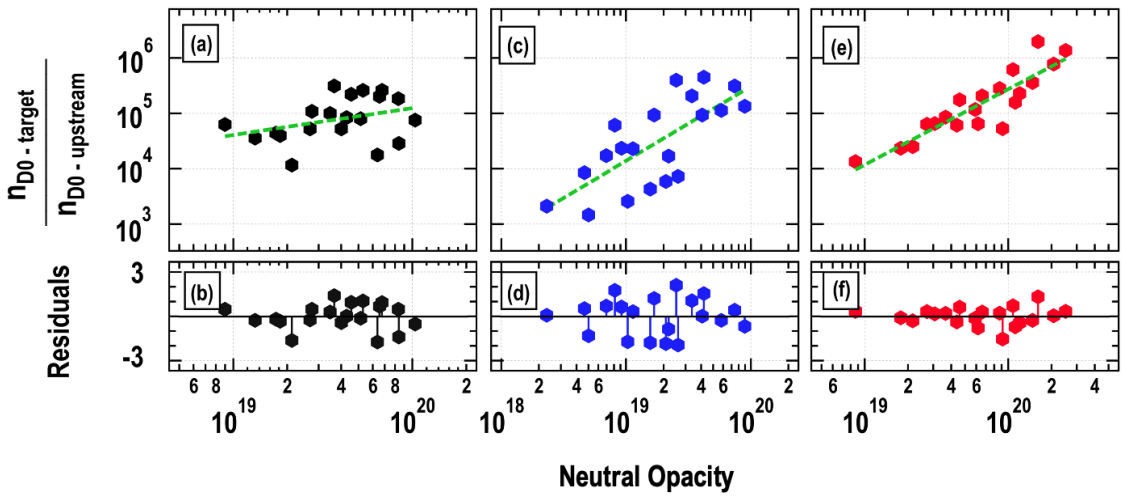


Figure 5.3: The ratio of neutral density, measured both upstream and at the target, is plotted as a function of neutral opacity, defined as the product of plasma density and the minor radius. The plot depicts a comprehensive plot encompassing all plasma discharges, showcasing variations in neutral opacity across (a) LSN Floor (black), (c) LSN shelf (blue), and (e) USN Floor (red). Subfigures (b, d, f) present the residuals for the fit. The observed trend indicates that as opacity increases—indicative of a more opaque plasma—there is a increase in neutrals leaking outside the divertor region. This phenomenon results in higher divertor recycling efficiency. The trend is steep for LSN Shelf and USN Floor configuration compared to the LSN Floor divertor

5.3 Breakdown of wall and divertor fluxes in empirical and modeled procedures

Section 5.3.1 presents a comprehensive plot summarizing the comparison of I_{wall}, I_{div}, and their ratio ($I_{f_{\text{wall}}}$) in both L-mode and H-mode discharges within an experimental setting. In Section 5.3.2, the same comparison is extended using the OEDGE model.

5.3.1 Estimation of main chamber and divertor fluxes using WFA showing lower main chamber fluxes with higher restrictions

The Figure 5.4 illustrates the magnitude of plasma flux in both the main chamber and the divertor target, employing the Window Frame Analysis based on experimental results. The figure displays I_{wall} - Figure 5.4 (a, b), I_{div} - Figure 5.4 (c, d), and f_{wall} data - Figure 5.4 (e, f) under Reverse B_T and Forward B_T conditions, respectively, as a function of GRP.

The observed trend indicates that an increase in GRP correlates with a increase in flux magnitudes in f_{wall}, implying that a higher structural closure at the divertor corresponds to an increased likelihood of particle capture in that region. In Figure 5.4, the three divertors - LSN shelf, LSN floor, and USN Floor - are represented in blue, black, and red, respectively. Figure 5.4(a, b) illustrates I_{wall} as it travels radially across the windowpane region for each plasma discharge. I_{wall} was estimated using Filterscope, averaged over ELMs. The highest particle flux crossing the windowpane region is observed in the LSN shelf configuration, while the lowest is seen in the LSN floor configuration for H-mode, whereas in the L-mode configuration, the highest I_{wall} value crossing the window pane radially is for the USN floor configuration. This is most likely due to the injected power and the outer gap for the USN Floor configuration in L-mode being higher compared to other plasma discharges.

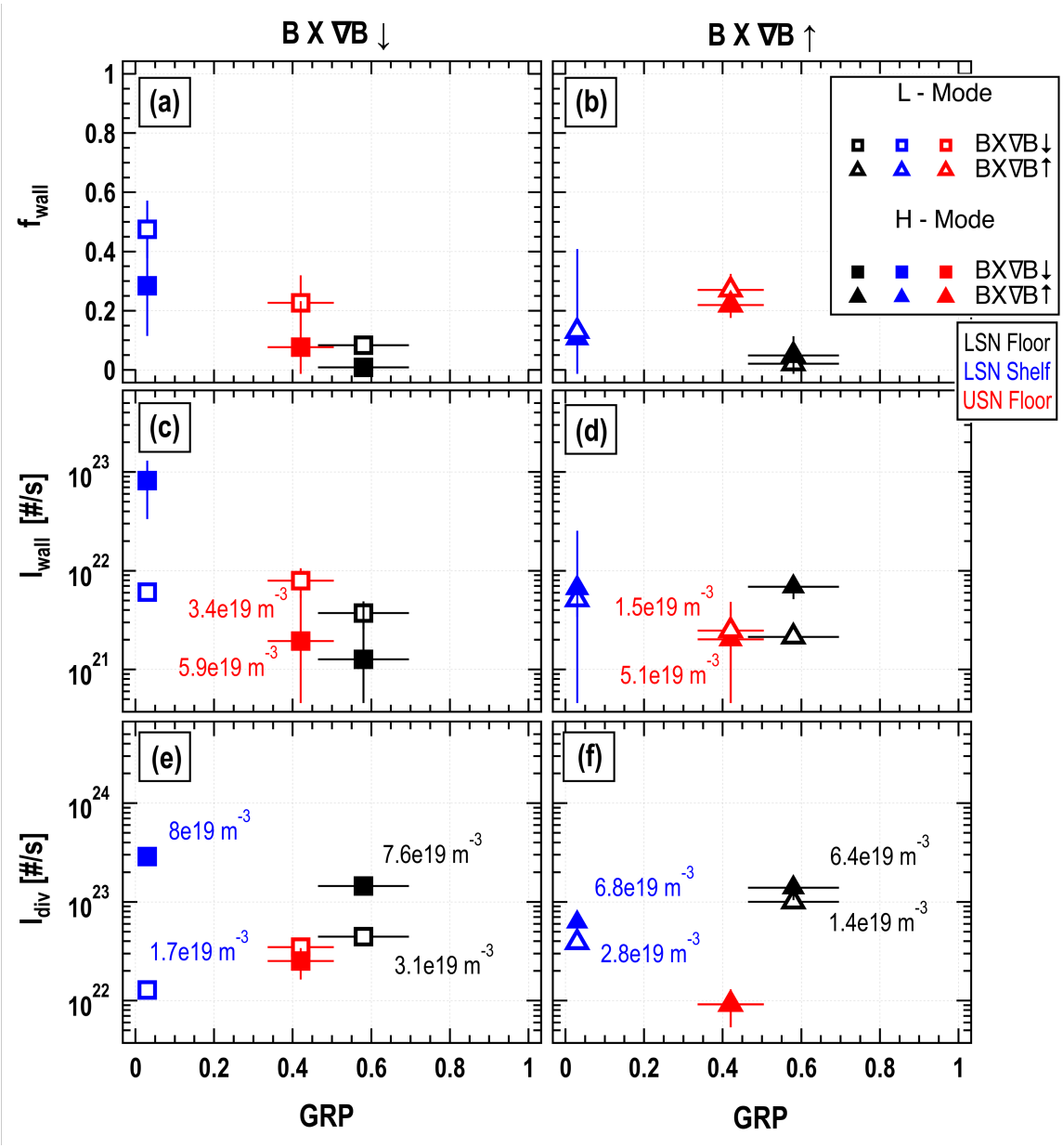


Figure 5.4: (a, b) Plots depicting the relationship between f_{wall} and GRP, (c, d) I_{wall} and GRP, and (e, f) I_{div} and GRP in both L-mode (open markers) and H-mode (filled markers) scenarios. The variations are observed concerning the $B \times \nabla B$ direction, with square markers indicating towards the target and diamond markers representing away from the target. I_{wall} showcases measured data from Filterscope, revealing the prevalence of mid-plane neutral particles in LSN Shelf (Blue), LSN Floor (Black), and USN Floor (Red). Similarly, I_{div} displays neutral particles uniformly across all divertor targets, while f_{wall} illustrates the magnitude of ion fluxes in the main chamber over the divertor region. It can be seen that as GRP increases, f_{wall} decreases in both L-mode and H-mode scenarios.

I_{div}, as depicted in Figure 5.4(c, d), has been measured via Langmuir probes over selected time ranges. As seen, the particle fluxes on the divertor target remain fairly consistent across all divertor configurations, with a notably lower particle flux from the USN Floor configuration in both L-mode and H-mode. It can be observed that a higher restriction on the target provides higher particle fluxes on the target, with the exception of the LSN Shelf (blue) divertor in H-mode. This is largely attributed to twice the density present for the LSN shelf configuration compared to other divertor configurations.

Figure 5.4(e, f) illustrates the f_{wall} values in relation to the GRP values. It can be observed that as GRP increases, f_{wall} decreases as shown by the green dashed and solid arrows for L-mode and H-mode conditions respectively. The LSN Floor divertor (black markers) exhibits the highest closure ($\sim$0.56), while the LSN shelf (blue marker) has the least closure ($\sim$0.08). Importantly, f_{wall} is lowest for LSN Floor (black markers) in both $B \times \nabla B$ conditions in L-mode and H-mode. This result is attributed to the effective restriction present for the LSN Floor divertor and the efficient pumping exhaust near the plenum, facilitating the removal of particles near the target. This implies that the LSN Floor and then USN Floor configuration(s) leak the least amount of neutrals due to the presence of baffles and slot geometry in the divertor. In contrast, the LSN Shelf divertor configuration provides the least closure due to the absence of baffles, resulting in the highest neutrals leakage among the three divertor configurations, as depicted in Figure 5.4 (e, f).

It is noteworthy that the f_{wall} values in L-mode (Figure 5.4(e)) decrease by a factor of five as the restriction increases, where for H-mode conditions f_{wall} values decrease by a factor of only 3. This difference is likely due to the fact that during H-mode conditions, main chamber recycling (MCR) is stronger along with the divertor recycling. But with the presence of ELMs, the I_{wall} is higher, as seen in subfigure (b, d). Hence the f_{wall} values tend to be lower as the magnitude of main chamber and divertor are much similar to each other in H-mode case scenario. Therefore, the outcomes outlined in this comparative study affirm that divertor with baffling, i.e.,

divertor with more restrictions, has the advantages of baffling in constraining neutrals in the divertor and minimizing divertor leakage Casali et al. [2019, 2020]. The findings of this comparative experimental study suggest that the closed configuration proves more efficient in capturing neutrals within the divertor.

In $B \times \nabla B \downarrow$ cases (5.4(a, c, e)) we see the restriction increment leads to decrease in magnitude of fluxes. However, the reason for each decrease in L-mode and H-mode is different. The decrease in L-mode shows constant I_{wall} and increase in I_{div}, whereas decrease in f_{wall} in H-mode shows constant I_{div} and decrease in I_{wall}. This however, is valid for $B \times \nabla B \downarrow$ cases only and not for $B \times \nabla B \uparrow$ cases (b, d, f). The f_{wall} in $B \times \nabla B \uparrow$ cases remains constant with both I_{wall} and I_{div} remaining constant irrespective of L-mode and H-mode plasma scenarios.

Figure 5.5 shows f_{wall} as a function of (a) pedestal density, (b) outer gap, and (c) outer divertor strike point in L-mode (open markers) and H-mode (filled markers) in LSN floor (black), LSN shelf (blue), and USN Floor (USN) divertors. Comparing the aforementioned global parameters with the experimental f_{wall} values show that higher n_e leads to lower f_{wall} which implies that denser plasma provides higher closure.

Data extracted from subfigure 5.5 (a), reveals intriguing observations. Firstly, density consistency in L-mode across different divertors is evident, while variations in H-mode are apparent. Specifically, in L-mode, the LSN Shelf exhibits lower electron density (n_e) but higher wall heat flux (f_{wall}), contrasting with the higher n_e and lower f_{wall} observed in the LSN Floor during H-mode. The implication of higher f_{wall} and lower density and lower f_{wall} with higher density shows GRP varies with density. GRP is proportional to electron density. Furthermore, subfigure 5.5 (b) unveils a consistent trend where the radial offset gap (R_{OG}) remains within a 2cm range for each plasma discharge, indicating stable experimental conditions. Notably, lower R_{OG} values, indicative of higher f_{wall}, are consistently observed in both L-mode and H-mode discharges. Here, we see no significant trend that could relate to GRP, however, we see higher f_{wall} for larger outer gap, and lower f_{wall} for smaller outer gap indicating, GRP could trend similarly to outer gap as well.

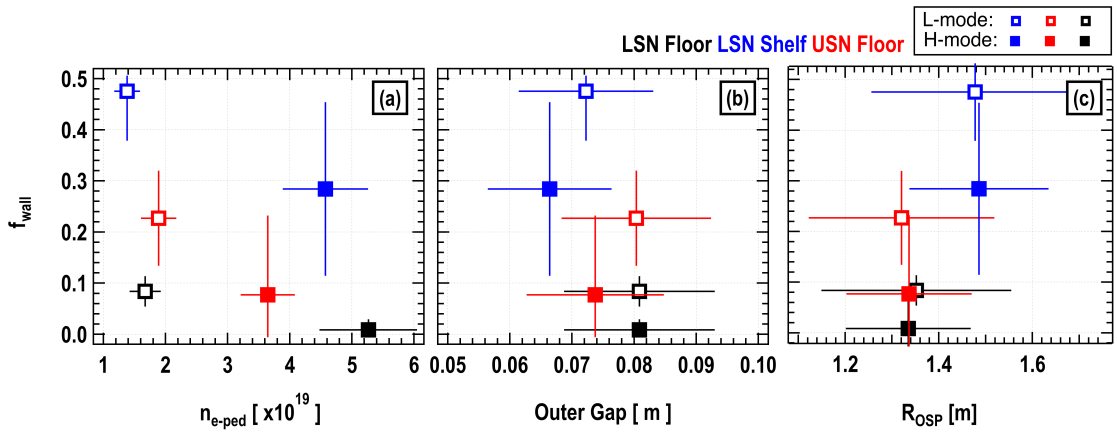


Figure 5.5: f_{wall} plotted as a function of (a) pedestal density, (b) outer gap, and (c) outer strike point. These are plotted in L-mode (open markers) and H-mode (filled markers)

Lastly, subfigure 5.5 (c) illustrates consistent values of the radial offset shoulder power (R_{OSP}) between L-mode and H-mode shots, with no discernible trend line apparent, highlighting the stability of R_{OSP} across different discharge modes. These findings contribute valuable insights into the interplay between plasma parameters and divertor characteristics, shedding light on the complex neutral dynamics governing fusion confinement. From the relationship between f_{wall} and R_{OSP} we see that higher f_{wall} exists as larger R_{OSP}, indicating, inverse proportionality between R_{OSP} and GRP.

5.3.2 Estimation of main chamber and divertor fluxes using OEDGE showing higher main chamber fluxes with higher restrictions for near SOL measurements

The Figure 5.6 depicts the magnitude of plasma flux in both the main chamber and the divertor target, utilizing the Window Frame Analysis based on the OEDGE model. The figure showcases $f_{wall-OEDGE}$ - Figure 5.6 (a, b), and average f_{wall} along the windowpane in poloidal length - Figure 5.6 (c, d) under L-mode (a, and c) and H-mode (b and d) conditions for $B \times \nabla B$ away from the target (triangle markers) and towards the target (square markers), respectively, as a function of GRP.

In Figure 5.6, the three divertors - LSN shelf, LSN floor, and USN Floor - are represented in blue, black, and red, respectively, mirroring the experimental results. Figures 5.6(a, b) depict $f_{\text{wall-OEDGE}}$ as it radially traverses the windowpane region for each plasma discharge, calculated using Equation 3.30. Notably, the LSN Floor configuration exhibits the highest particle flux across the windowpane region in both L-mode and H-mode configurations, while the lowest is observed in the LSN Shelf configuration.

Here, $f_{\text{wall-OEGDE}}$ is calculated with boundary conditions inputted to the OEDGE code and averaged through ELMs. It is evident that $f_{\text{wall-OEGDE}}$ shows higher variation in L-mode configuration compared to H-mode configuration, primarily due

to changing electron temperature and density during the L-H transition. Upon examination, it is noted that, in alignment with the experimental data, the trend of flux magnitudes obtained using OEDGE is inversely proportional; that is, $f_{\text{wall-OEDGE}}$ increases with an increase in GRP. This suggests that a higher structural closure at the divertor corresponds to an increased likelihood of particle escape in that region. However, this is contrary to experimental results.

The main reason for the discrepancy is the creation of the model mesh with DG-Carre without an extended grid that restrains the mesh generation up to the windowpane region. Therefore, the data measured using OEDGE, for most cases (except one case in H-mode, as indicated by the open circle marker), have the mesh created only up to the near SOL region, whereas the experimental windowpane is present in the far SOL. According to Fundamenski [2009], the near SOL has a plasma potential up to 3 times higher compared to the far SOL, indirectly indicating higher temperature in the near SOL, leading to lower density and, consequently, higher flux measurement in region 1 (see Equation 3.33). The only configuration where the model and experimental windowpane match is for Shot 186703 in LSN Shelf configuration (open circle markers in subfigures (b, d, and f)). Further discussion about comparing experimental results and modeled results is presented in the next section.

The poloidally averaged $f_{\text{wall-OEDGE}}$, as illustrated in Figures 5.6(c, d), is calculated by measuring particle flux along the windowpane region and averaging it over poloidal distance. A noticeable difference between sub-figures (a and b) and sub-figures (c and d) is the increase in the magnitude of fluxes for data with $B \times \nabla B$ away from the target, while for data with $B \times \nabla B$ towards the target, the magnitude remains consistent. This highlights the impact of drift conditions on particle transport from the divertor. When $B \times \nabla B$ is away from the target, particles tend to travel more towards the main chamber, in contrast to the case when $B \times \nabla B$ is towards the target, where particles are more constrained in the divertor region.

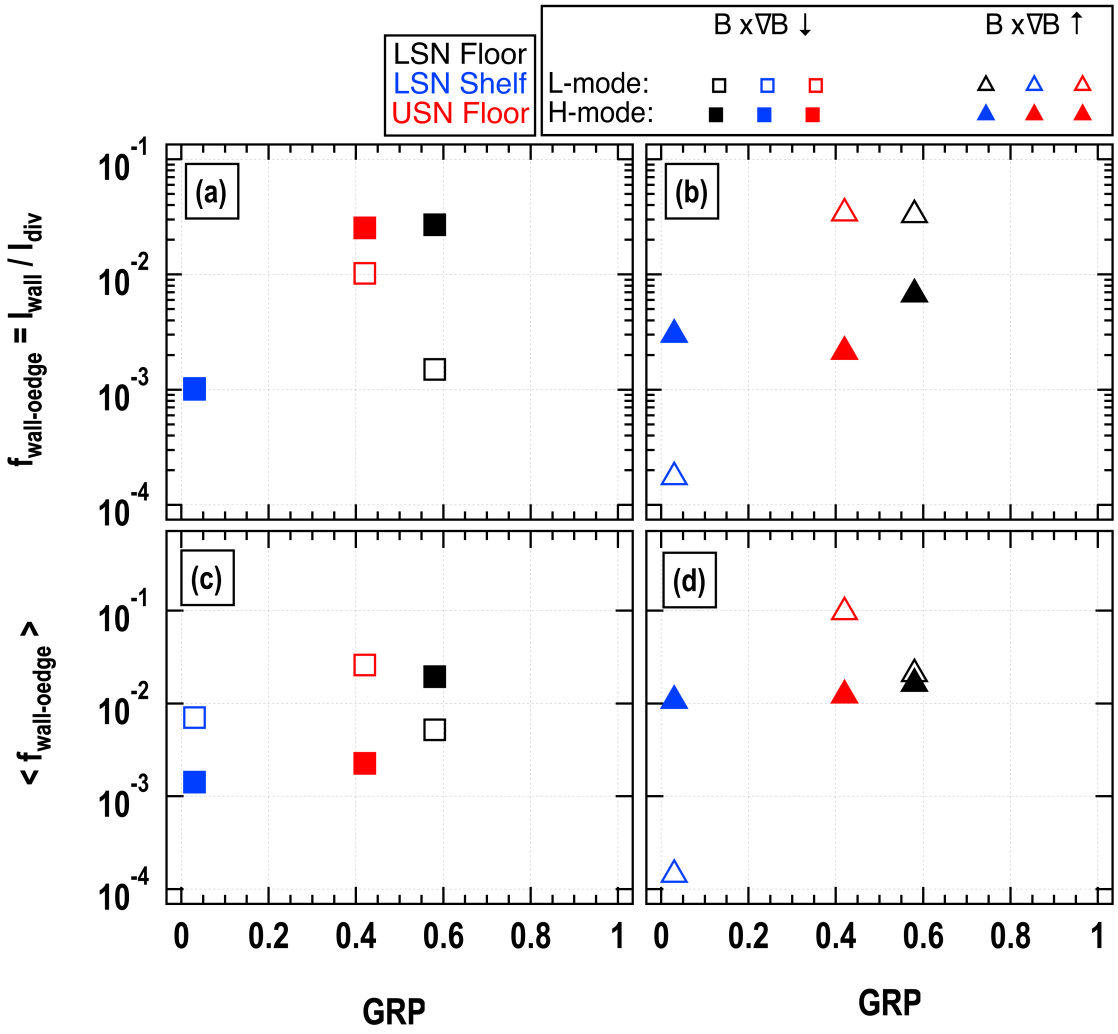


Figure 5.6: (a, b) $f_{wall-oedge}$ vs GRP (c, d) $\langle f_{wall-oedge} \rangle$ along S poloidal vs GRP in L-mode and H-mode. Data shown in LSN Shelf (Blue), LSN Floor (Black) and USN Floor (Red) in $B \times \nabla B$ away from the target (triangle markers) and $B \times \nabla B$ towards the target (square markers) conditions. The trend shows higher f_{wall} modeled values as restriction increase. This is mainly due to modeling constraints

It is crucial to emphasize that the poloidally averaged f_{wall} value follows a consistent trend with both modeled f_{wall} and experimentally calculated f_{wall}, showcasing an increase in the ratio of flux magnitudes as the restriction increases. This approach takes into account flux variations across the entire window-pane region, offering a comprehensive understanding of neutral dynamics. It considers particles near the crown and other locations in the main chamber region, providing a more realistic representation of I_{wall} and a comprehensive understanding of the magnitude of fluxes in the main chamber region. Notably, L-mode and H-mode conditions yield similar normalized values for poloidally averaged f_{wall}, highlighting the thorough consideration of neutral particles across the entire window pane.

5.3.3 Comparing experimental results with Modeled results show deviation

This thesis compared 12 plasma discharges with diverse divertor geometries and varying f_{wall} values obtained through both experimental and modeled results, as illustrated in Figures 5.4 and 5.6. It is crucial to compare the experimental and modeled outcomes, particularly in both L-mode and H-mode configurations. Figure 5.7 presents comparative plots of f_{wall} between experimental and modeled findings. The plots showcase f_{wall} as a function of GRP for (a) $B \times \nabla B \downarrow$ and (b) $B \times \nabla B \uparrow$ in L-mode and H-mode conditions. Both conditions display data for experimental f_{wall} represented by diamond markers, and modeled f_{wall} depicted by 'square' markers. For L-mode the marker is open and for H-mode the markers are filled. In both $B \times \nabla B$ conditions, an increase in restriction corresponds to a decrease in the magnitude of plasma flux in the main chamber over the divertor for experimental calculation where as the with modeled values increase in restriction corresponds to a increase in the magnitude of plasma flux in the main chamber over the divertor. Notably, the modeled data registers lower values compared to the experimental data.

The modeling results exhibit a lack of alignment with the experimental findings when comparing the LSN shelf, LSN floor, and USN Floor configurations with varying restrictions. This discrepancy arises from the measurement of the magnitude of main chamber fluxes at different SOL locations in modeled data versus experimental data. In the experimental calculation, the window-pane is present at the far SOL, whereas for all model data (except one, marked in Subfigure 5.7(b)), the windowpane is present at the last possible mesh generated using the DG-Carre system without the extended grid generator.

The DG-Carre system does not converge grids where it is hindered by a wall surface material. Consequently, when it encounters a wall surface (mainly an issue for divertor geometries with higher restrictions and baffles), the mesh is created that does not extend up to the far SOL region. As mentioned in Fundamenski [2009], the near SOL has three times higher plasma potential, strong radial electric fields, and poloidal flow shear that extend the radial thickness of SOL or the decay lengths beyond the separatrix. In contrast, the far SOL has lower temperature with higher density and lower plasma velocity.

Therefore, quantifying $f_{\text{wall-oedge}}$ in the near SOL could lead to higher I_{wall} measurements and potentially increase the $f_{\text{wall-oedge}}$ value. This discrepancy highlights the importance of considering the specific location of the window-pane in both experimental and modeled data for a more accurate comparison.

However, in the plasma discharge of the LSN Shelf configuration in H-mode, for both towards and away $B \times \nabla B$ directions, the model windowpane is similar to the experimental windowpane, as seen in Subfigure 5.7(b). When comparing the modeled and experimental values for these shots, the true relationship between the model and experimental data becomes apparent. It is observed that the model and experimental values are nearly similar to each other for $B \times \nabla B$ towards the target condition, whereas the model and experimental data differ by a factor of 10%.

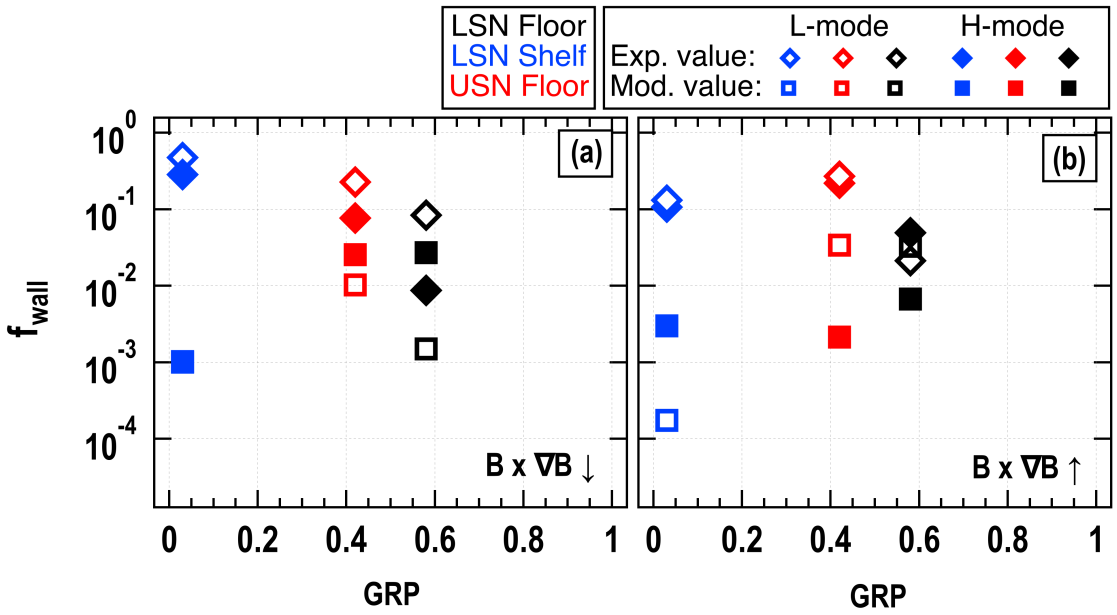


Figure 5.7: Plots depict fwall plotted as a function of GRP for (a) $B \times \nabla B \downarrow$ and (b) $B \times \nabla B \downarrow$ in L mode (open markers) and H-mode (filled markers) conditions. Both the conditions shows data for experimental f_{wall} as shown by diamond markers and modeled f_{wall} shown by square markers respectively. In $B \times \nabla B \downarrow$ conditions, the magnitude of plasma flux in the main chamber over the divertor decreases as restriction increases. The experimental data is higher compared to the modeled data.

This discrepancy can be attributed to the model windowpane being slightly different compared to the experimental windowpane, emphasizing the importance of accurately matching experimental and modeled conditions for a more precise comparison and also the need to re-run the comparison with DG-Carre with extended grids.

From Figure 5.7, the discrepancies between the near SOL (model) and far SOL (experimental) measurements are evident. In the L-mode configuration (5.7(a)), the LSN Shelf mode exhibits the lowest discrepancies between the model and experimental results, attributed to the closer match of the model windowpane compared to the experimental one. The modeled data is two times higher than the experimental data. For USN Floor, the modeled data is three times higher, and for LSN Floor data, the modeled data is four times higher than the experimental data. The discrepancies vary in $B \times \nabla B$ drift conditions, where the $B \times \nabla B$ towards the target drift conditions show model values increasing exponentially, potentially due to measurements near the separatrix. In contrast, in $B \times \nabla B$ away from the target conditions, the model f_{wall} tends to decrease for the LSN Floor configuration. This is likely due to lower electron density for that plasma discharge taken into account. These variations underscore the sensitivity of the model to different conditions and the importance of accurately representing the experimental setup in the modeling process.

The consistency observed between Figure 5.7(a) and 5.7(b) is notable. The LSN Shelf mode consistently exhibits the lowest discrepancies between the model and experimental results, attributed to the closer match of the model windowpane compared to the experimental one. The modeled data is almost similar or 10% higher than the experimental data. For USN Floor, the modeled data is three times higher, and for LSN Floor data, the modeled data is four times higher than the experimental data.

The discrepancies vary in $B \times \nabla B$ drift conditions, where the $B \times \nabla B$ towards the target drift conditions show model values increasing exponentially, potentially due to measurements near the separatrix. In contrast, in $B \times \nabla B$ away from the target

conditions, the model f_{wall} tends to decrease for the LSN Floor configuration. This is likely due to lower electron density for that plasma discharge taken into account. These variations underscore the sensitivity of the model to different conditions and the importance of accurately representing the experimental setup in the modeling process.

Figure 5.7 reveals that the modeled results are at least 2 times higher than the experimental results. This discrepancy could potentially be attributed to variations in the DG-Carre mesh, which might not extensively reach the experimental windowpane. Additionally, the difference may arise from the fact that the divertor particle flux is estimated only in the DG-Carre mesh, which is smaller than the experimentally measured particle flux at the windowpane. This inconsistency between experimental and modeled results might be influenced by these factors. Notably, the LSN shelf H-mode model exhibits the closest mesh condition to the experiments, contributing to the similarity observed between modeled f_{wall} and experimental f_{wall} for LSN Shelf (blue) H-mode data.

5.4 Discussions

This study conducted a comparative analysis involving 12 plasma discharges characterized by diverse divertor geometries, plasma conditions, and drift orientations. The investigation utilized WFA and OEDGE to gain insights into neutral dynamics in the SOL. A novel metric, the Geometric Restriction Parameter (GRP), was developed to assess divertor restriction based on factors such as strike point location, x-point height, and the presence of divertor baffling. GRP calculations were performed for eight divertor configurations in DIII-D, comprising four conventional (LSN Floor, LSN Shelf, USN Floor, SAS) and four non-conventional (Snowflake, X-divertor, Upper Right, Upper Left) designs. This metric serves as an indicator of neutral retention by the divertor, where lower GRP values correspond to reduced neutral restrictions and increased neutral leakage.

In the comparative analysis, the LSN Floor divertor configuration exhibited the highest restriction with a GRP value of 0.58, followed by USN Floor with a GRP of 0.42. These configurations feature multiple baffles and exhaust pumps near the divertor, contributing to enhanced particle control. In contrast, the LSN Shelf divertor, characterized by the absence of baffles, demonstrated the least restriction with a GRP of 0.03. This configuration has direct implications for neutral flow from the divertor region to the main chamber.

While investigating divertor restriction was a primary objective of this thesis, another goal was to quantitatively assess the magnitude of fluxes in the main chamber region over the divertor region over the calculated divertor restriction. This aimed to comprehend neutral dynamics, gain insights into divertor recycling, main chamber recycling, and the potential disentanglement of these phenomena. WFA was employed in piggyback experiments, with a modification utilizing the Filterscope at the midplane location instead of the reciprocating probe to estimate main chamber fluxes.

Publications by Whyte et al. [2005] demonstrated similar values of particle flux magnitudes in the main chamber from reciprocating Langmuir probe and Filterscope measurements. This similarity led us to use D_α measurements from the midplane Filterscope system to calculate particle fluxes at the windowpane in the main chamber, denoted as I_{wall}. Notably, I_{wall} values for LSN Shelf and LSN Floor configurations in H-mode were a factor higher compared to L-mode. This difference is likely attributed to the fact that the measured data was averaged over Edge Localized Modes (ELMs).

The experimental findings indicated that the ratio of fluxes, represented as f_{wall}, reached its highest value for the LSN Shelf configuration— a divertor lacking physical baffles to contain particles. In contrast, the ratio of fluxes was observed to be lowest for the LSN Floor configuration, as depicted in Figure 5.4. It was observed that as closure or restriction increased (higher GRP value), the ratio of fluxes decreased. This implies a higher level of neutral leakage with lower divertor restrictions.

A plausible explanation for the elevated f_{wall} value in the LSN Shelf divertor configuration could be the absence of physical baffles at the divertor location. Notably, the flux in the main chamber decreased across all divertor configurations, exhibiting variation in H-mode plasma. An inverse relationship between structural closure and the magnitude of flux in the main chamber wall was observed—higher closure correlated with a lower flux magnitude in the main chamber wall, assuming no main chamber recycling was present.

However, drawing conclusive findings solely based on GRP as the influencing factor for the variation of I_{wall} would be premature. Therefore, additional experiments are imperative to comprehend f_{wall} values at various GRP values while considering other variables, such as strike point sweep, x-point height variation, etc. This approach will facilitate the identification of a potentially optimal closure for the diverted tokamak and provide insights into the parameters that future fusion devices may operate with.

Despite limitations hindering experimental validation, an iterative modeling approach can offer valuable insights. Consequently, OEDGE was employed for this project, utilizing the Onion Skin Model and EIRENE to solve Braginskii fluid equations and provide a plasma solution for the SOL. As depicted in Figure 5.6 and 5.7, our experimental measurements align with the model for one plasma discharge - LSN Shelf configurtion, showcasing average flux measurements at the windowpane region running poloidally across.

Discrepancies were observed in the magnitude of fluxes between near SOL (modeled) and far SOL (experimental) measurements, emphasizing the sensitivity of the model to different conditions. The comparison between LSN Shelf, LSN Floor, and USN Floor configurations revealed varying levels of deviation, with the LSN Shelf mode consistently showing the lowest discrepancies. However, certain divergences underscored the importance of accurately representing experimental conditions in the model. The need for more spatial diagnostics in the main chamber for precise comparisons and raised awareness about potential inaccuracies in assuming uniform I_{wall} measurements across the windowpane.

Chapter 6

Future Work

This thesis conducted a comparative analysis of various divertor geometries through experimental investigation and modeling. However, the conclusions and discussions highlight the need for further research to enhance our understanding of the physics underlying the influence of divertor design and geometry on neutral leakage.

To achieve a more comprehensive understanding, it is imperative to secure runtime allocation on a suitable facility, preferably DIII-D, given the alignment of this thesis with the tokamak's design specifications. To obtain runtime allocation, researchers must submit a mini-proposal, which will undergo a selection process to align the scientific objectives with the experimental plan endorsed by the DIII-D scientific community. The detailed mini-proposal is provided in Appendix E. As outlined in Appendix E, a crucial aspect that warrants attention is the refinement of the experimental setup to incorporate variations in the outer gap and strike point location. This adjustment is essential for elucidating the influence of divertor constraints on both main chamber and divertor recycling.

For the run day, the hypothesis posits that Neutral Compression (NC), proportional to the divertor-to-main chamber pressure ratio (P_{div}/P_{mc}), increases with greater divertor closure, although this relationship is intricate due to the influence of divertor magnetic and component configurations. To systematically investigate this

phenomenon, our objective is to conduct systematic scans utilizing Window-Frame Analysis (WFA) to meticulously examine the effects on NC and Leakage (NL), which is inversely proportional to NC. Our approach entails employing WFA to analyze particle fluxes in both the main chamber (MC) and divertor across various degrees of closure, progressing from shelf configurations to the Lower Single Null (LSN) floor and the Upper Single Null (USN) floor, culminating with a closed vertical-target at the USN edge. By scanning parameters such as GAPOUT and Z_{XPNT} to modulate fluxes to Regions of Interest (ROIs) alongside magnetic configurations, we aim to glean insights into several key aspects. Firstly, our data aims to validate neutral modeling, particularly in conjunction with the SOLPS simulation.

Additionally, our methodology involves directly measuring flux in the main chamber through WFA employing multiple diagnostics, thereby eliminating the need for extrapolation. The timeliness of this research is underscored by the availability of new diagnostics such as LLAMA and MC ASDEX gauge, which provide more comprehensive measurements than previous WFA experiments. Moreover, the efficient control of particles is inadequately defined yet crucial for the design of pilot plants. Ultimately, the impact of our study lies in its potential to furnish predictive capabilities regarding neutral dynamics in diverted tokamaks, optimize NC for given divertor geometric configurations, and offer insights into enhancing divertor closure without necessitating physical structural changes, thus potentially reducing future divertor costs. A potential expected plot from the stated run day would look something like seen in Figure 6.1. Along with understanding neutral compression, the experimental dataset would allow for one to one comparison with target and upstream neutral densities that could help us decipher role of DLR and MCR.

Furthermore, to enhance the depth of our understanding of the physics involved, it is recommended to substitute the DG-Carre grid, as utilized in this thesis, with the OEDGE extended grid. Employing this extended grid configuration will facilitate the generation of a mesh in closer proximity to the vessel wall. This modification is pivotal for comprehensively investigating and comparing the iteratively estimated

flux magnitudes within the specified regions of interest. Thus, these tasks are pivotal and will be pursued by the author in the near future.

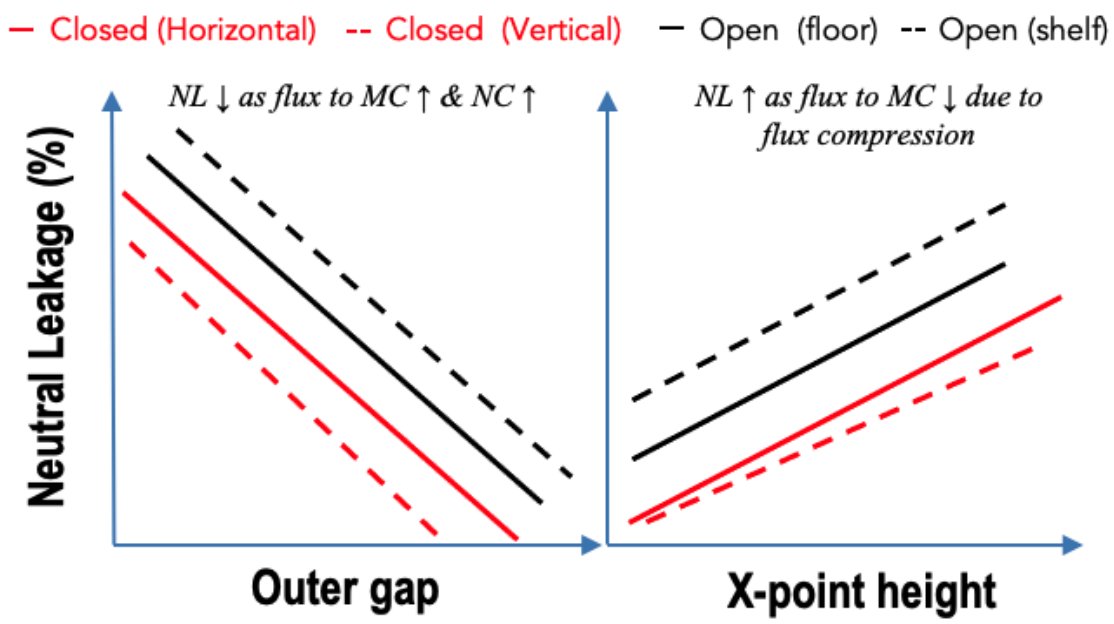


Figure 6.1: Expected results from an experiment slated for future. The results show a percentage of neutral leakage with neutral compression shown with varying outer gap and x-point height

Bibliography

S.L. Allen, N.H. Brooks, R. Bastasz, J. Boedo, J.N. Brooks, J.W. Cuthbertson, T.E. Evans, M.E. Fenstermacher, D.N. Hill, D.L. Hillis, J. Hogan, A.W. Hyatt, R.C. Isler, G.L. Jackson, T. Jernigan, C.J. Lasnier, R. Lehmer, A.W. Leonard, M.A. Mahdavi, R. Maingi, W.H. Meyer, P.K. Mioduszewski, R.A. Moyer, D.G. Nilson, L.W. Owen, T.W. Petrie, G.D. Porter, M.E. Rensink, M.J. Schaffer, J. Smith, G.M. Staebler, R.D. Stambaugh, D.M. Thomas, M.R. Wade, W.R. Wampler, J.G. Watkins, W.P. West, D.G. Whyte, N. Wolf, C.P.C. Wong, R.D. Wood, DIII-D Physics, and Operations Teams. Radiative divertor and scrape-off layer experiments in open and baffled divertors on diii-d. *Nuclear Fusion*, 39(11Y):2015, nov 1999. doi: 10.1088/0029-5515/39/11Y/348. URL `https://dx.doi.org/10.1088/0029-5515/39/11Y/348`. 82

ANS. Nuclear fusion, 2018. URL `http://nuclearconnect.org/know-nuclear/science/nuclear-fusion`. 6

N Asakura, N Hosogane, K Itami, A Sakasai, S Sakurai, K Shimizu, M Shimada, H Kubo, S Higashijma, H Takenaga, H Tamai, S Konoshima, T Sugie, K Masaki, Y Koide, O Naito, H Shirai, T Takizuka, T Ishijima, S Suzuki, and A Kumagai. Role of divertor geometry on detachment and core plasma performance in jt60u. *Journal of Nuclear Materials*, 266-269:182–188, 1999a. ISSN 0022-3115. doi: https://doi.org/10.1016/S0022-3115(98)00818-6. URL `http://www.sciencedirect.com/science/article/pii/S0022311598008186`. 76, 78

N. Asakura, N. Hosogane, K. Itami, A. Sakasai, S. Sakurai, K. Shimizu, M. Shimada, H. Kubo, S. Higashijma, H. Takenaga, H. Tamai, S. Konoshima, T. Sugie, K. Masaki, Y. Koide, O. Naito, H. Shirai, T. Takizuka, T. Ishijima, S. Suzuki, and A. Kumagai. Role of divertor geometry on detachment and core plasma performance in jt60u. *Journal of Nuclear Materials*, 266-269:182–188, 1999b. ISSN 0022-3115. doi: https://doi.org/10.1016/S0022-3115(98)00818-6. URL `https://www.sciencedirect.com/science/article/pii/S0022311598008186`. 327

ASDEX Team, G. Haas, J. Gernhardt, M. Keilhacker, and E.B. Meservey. Measurements on the particle balance in diverted asdex discharges. *Journal of Nuclear Materials*, 121:151–156, 1984. ISSN 0022-3115. doi: https://doi.org/10.1016/0022-3115(84)90116-8. URL `https://www.sciencedirect.com/science/article/pii/0022311584901168`. 105

R Aymar, P Barabaschi, and Y Shimomura. The iter design. *Plasma Physics and Controlled Fusion*, 44:519–565, 4 2002. doi: 10.1088/0741-3335/44/5/304. URL `https://doi.org/10.1088%2F0741-3335%2F44%2F5%2F304`. 11

Matteo Barbarino. What is nuclear fusion, 2023. URL `https://www.iaea.org/newscenter/news/what-is-nuclear-fusion`. 6

Editors ITER Physics Basis. Chapter 4: Power and particle control. *Nuclear Fusion*, 39:2391–2469, 12 1999. doi: 10.1088/0029-5515/39/12/304. URL `https://doi.org/10.1088%2F0029-5515%2F39%2F12%2F304`. 41, 42

H.-L Berk, R H Cohen, D D Ryutov, Yu.A Tsidulko, and X Q Xu. Electron temperature gradient induced instability in tokamak scrape-off layers. *Nuclear Fusion*, 33:263–282, 2 1993. doi: 10.1088/0029-5515/33/2/i07. URL `https://doi.org/10.1088%2F0029-5515%2F33%2F2%2Fi07`. 324

M. N. A. Beurskens, T. H. Osborne, P. A. Schneider, E. Wolfrum, L. Frassinetti, R. Groebner, P. Lomas, I. Nunes, S. Saarelma, R. Scannell, P. B. Snyder,

D. Zarzoso, I. Balboa, B. Bray, M. Brix, J. Flanagan, C. Giroud, E. Giovannozzi, M. Kempenaars, A. Loarte, E. de la Luna, G. Maddison, C. F. Maggi, D. McDonald, R. Pasqualotto, G. Saibene, R. Sartori, Emilia R. Solano, M. Walsh, L. Zabeo, The DIII-D Team, The ASDEX Upgrade Team, and JET-EFDA Contributors. H-mode pedestal scaling in DIII-D, ASDEX Upgrade, and JET a). *Physics of Plasmas*, 18(5):056120, 05 2011. ISSN 1070-664X. doi: 10.1063/1.3593008. URL `https://doi.org/10.1063/1.3593008`. 173

UCS blogpost. Coal power impacts, 2019. URL `https://www.ucsusa.org/resources/coal-power-impacts`. 3

R L Boivin, J A Goetz, A E Hubbard, J W Hughes, I H Hutchinson, J H Irby, B LaBombard, E S Marmar, D Mossessian, C S Pitcher, J L Terry, B A Carreras, and L W Owen. Effects of neutral particles on edge dynamics in alcator c-mod plasmas. *Physics of Plasmas*, 7:1919–1926, 4 2000. ISSN 1070-664X. doi: 10.1063/1.874016. URL `https://doi.org/10.1063/1.874016`. doi: 10.1063/1.874016. 45

Xavier Bonnin, Wouter Dekeyser, Richard Pitts, David Coster, Serguey Voskoboynikov, and Sven Wiesen. Presentation of the new solps-iter code package for tokamak plasma edge modelling. *Plasma and Fusion Research*, 11:1403102–1403102, 2016. doi: 10.1585/pfr.11.1403102. 87, 88, 89

Allen H. Boozer. Use of nonaxisymmetric shaping in magnetic fusiona). *Physics of Plasmas*, 16(5):058102, 04 2009. ISSN 1070-664X. doi: 10.1063/1.3099330. URL `https://doi.org/10.1063/1.3099330`. 13

H-S Bosch, J C Fuchs, J Gafert, G Haas, A Herrmann, A Kallenbach, M Kaufmann, J Neuhauser, F Ryter, R Schneider, J Schweinzer, W Ullrich, U Wenzel, G C Vlases, L D Horton, G F Matthews, the ASDEX Upgrade Team, and the JET Divertor Physics Topic Group. Effect of divertor geometry on boundary and core plasma performance in asdex upgrade and jet. *Plasma Physics and Controlled Fusion*, 41: A401, 1999. URL `http://stacks.iop.org/0741-3335/41/i=3A/a=032`. 82, 126

BP. Reserves-production ratio, 2016. URL http://www.bp.com/content/dam/bp/pdf/energy-economics/statistical-review-2016/bp-statistical-review-of-world-energy-2016-full-report.pdf. 5

BJ Braams. Radiative divertor modelling for iter and tpx. *Contributions to Plasma Physics*, 36(2-3):276–281, 1996. 86

N H Brooks, R J Colchin, D T Fehling, D L Hillis, Y Mu, and E Unterberg. Filterscopes: Spectral line monitors for long-pulse plasma devices. *Review of Scientific Instruments*, 79:10F330, 2008. doi: 10.1063/1.2957777. URL https://doi.org/10.1063/1.2957777. 105

JET D Campbell. *Plasma Phys. Control. Nucl. Fusion Res*, 1:527, 1995. 327

T. N. Carlstrom, G. L. Campbell, J. C. DeBoo, R. Evanko, J. Evans, C. M. Greenfield, J. Haskovec, C. L. Hsieh, E. McKee, R. T. Snider, R. Stockdale, P. K. Trost, and M. P. Thomas. Design and operation of the multipulse thomson scattering diagnostic on diii-d (invited). *Rev. Sci. Instrum.*, 63:4901, 1992. ISSN 00346748. doi: 10.1063/1.1143545. 99

S. Carpentier, R.A. Pitts, P.C. Stangeby, J.D. Elder, A.S. Kukushkin, S. Lisgo, W. Fundamenski, and D. Moulton. Modelling of beryllium erosion–redeposition on iter first wall panels. *Journal of Nuclear Materials*, 415(1, Supplement): S165–S169, 2011. ISSN 0022-3115. doi: https://doi.org/10.1016/j.jnucmat.2010.10.081. URL https://www.sciencedirect.com/science/article/pii/S0022311510006793. Proceedings of the 19th International Conference on Plasma-Surface Interactions in Controlled Fusion. 97

D Carralero, G Birkenmeier, H W Müller, P Manz, P deMarne, S H Müller, F Reimold, U Stroth, M Wischmeier, and E Wolfrum. An experimental investigation of the high density transition of the scrape-off layer transport in {ASDEX} upgrade. *Nuclear Fusion*, 54:123005, 11 2014. doi: 10.1088/

0029-5515/54/12/123005. URL https://doi.org/10.1088%2F0029-5515%2F54%2F12%2F123005. 322

B A Carreras, L W Owen, R Maingi, P K Mioduszewski, T N Carlstrom, and R J Groebner. Effect of edge neutrals on the low-to-high confinement transition threshold in the diii-d tokamak. *Physics of Plasmas*, 5:2623–2636, 6 1998. ISSN 1070-664X. doi: 10.1063/1.872949. URL https://doi.org/10.1063/1.872949. doi: 10.1063/1.872949. 45

L. Casali, B. M. Covele, and H. Y. Guo. The effect of neutrals in the new sas divertor at diii-d as modelled by solps. *Nuclear Materials and Energy*, 19:537–543, 2019. ISSN 23521791. doi: 10.1016/j.nme.2019.03.021. 66, 125, 172, 173, 183

L Casali, D Eldon, J A Boedo, T Leonard, and B Covele. Neutral leakage, power dissipation and pedestal fueling in open vs closed divertors. *Nuclear Fusion*, 60: 76011, 6 2020. doi: 10.1088/1741-4326/ab8d06. URL https://doi.org/10.1088%2F1741-4326%2Fab8d06. xiv, 66, 68, 70, 71, 125, 183

L Casali, D Eldon, A McLean, T Osborne, A Leonard, B Grierson, and J Ren. Impurity leakage and radiative cooling in the first nitrogen and neon seeding study in the closed diii-d sas configuration. *Nuclear Fusion*, 62:26021, 1 2022. doi: 10.1088/1741-4326/ac3e84. URL https://doi.org/10.1088/1741-4326/ac3e84. 66, 125

AV Chankin, DP Coster, R Dux, Ch Fuchs, G Haas, A Herrmann, LD Horton, A Kallenbach, M Kaufmann, Ch Konz, et al. Solps modelling of asdex upgrade h-mode plasma. *Plasma physics and controlled fusion*, 48(6):839, 2006. 87

AV Chankin, DP Coster, R Dux, Ch Fuchs, G Haas, A Herrmann, LD Horton, A Kallenbach, B Kurzan, HW Müller, et al. Simulation of asdex upgrade ohmic plasmas for solps code validation. *Nuclear fusion*, 49(1):015004, 2008. 87

Christian. Plotting nuclear fusion cross sections, 2018. URL https://scipython.com/blog/plotting-nuclear-fusion-cross-sections/. 7, 8

M. Clever. Hydrogen recycling and transport in the helical divertor of textor. 2010. URL https://api.semanticscholar.org/CorpusID:93485754. 19, 20, 21

R. J. Colchin and L. W. Owen. Neutral particle fueling at the midplane of diii-d. 2003. doi: 10.1016/S0022-3115(02)01436-8. 101

R J Colchin, D L Hillis, R Maingi, C C Klepper, and N H Brooks. The filterscope. *Review of Scientific Instruments*, 74:2068–2070, 2003. doi: 10.1063/1.1537038. URL https://doi.org/10.1063/1.1537038. 105

D P Coster, A V Chankin, H.-J. Klingshirn, R Dux, E Fable, X Bonnin, A Kukushkin, and A Loarte. Solps modelling of w arising from repetitive mitigated elms in iter. *Journal of Nuclear Materials*, 463:620–623, 2015. ISSN 0022-3115. doi: https://doi.org/10.1016/j.jnucmat.2014.09.076. URL http://www.sciencedirect.com/science/article/pii/S002231151400676X. 325

DP Coster. Detachment physics in solps simulations. *Journal of nuclear materials*, 415(1):S545–S548, 2011. 87

DP Coster, X Bonnin, and M Warrier. Extensions to the solps edge plasma simulation code to include additional surface interaction posibilities. *Physica Scripta*, 2006 (T124):9, 2006. 87

Cyd Cowley, Adam Q Kuang, David Moulton, Jeremy D Lore, John M Canik, Maxim V Umansky, Michael Wigram, Sean Bozkurt Ballinger, Bruce Lipschultz, and Xavier Bonnin. Novel solps-iter simulations of x-point target and snowflake divertors. *Plasma Physics and Controlled Fusion*, 3 2023. ISSN 0741-3335. doi: 10.1088/1361-6587/ACB4BA. 23, 127

Franz Herrnegger Ewald Harmeyer Johann Kisslinger Wolf Lotz Henning Maassberg Peter Merkel Jürgen Nührenberg Fritz Rau Jörg Sapper Francesco Sardei Ruben

Scardovelli Arnulf Schlüter Craig Beidler, Günter Grieger and Horst Wobig. Physics and engineering design for wendelstein vii-x. *Fusion Technology*, 17(1): 148–168, 1990. doi: 10.13182/FST90-A29178. URL https://doi.org/10.13182/FST90-A29178. 13

Stefan Dasbach and Sven Wiesen. Towards fast surrogate models for interpolation of tokamak edge plasmas. *Nuclear Materials and Energy*, 34:101396, 2023. 86

Stephen O. Dean. *Search for the ultimate energy source*. Springer, New York, NY, 2013. ISBN 978-1-4614-6036-7. doi: https://doi.org/10.1007/978-1-4614-6037-4. URL https://link-springer-com.proxy.lib.utk.edu/book/10.1007%2F978-1-4614-6037-4#authorsandaffiliationsbook. 13

Boël Denne. The role of atomic spectroscopy in fusion research. *Physica Scripta*, T26:42–50, 1989. ISSN 0031-8949. doi: 10.1088/0031-8949/1989/t26/007. URL http://dx.doi.org/10.1088/0031-8949/1989/T26/007. 45, 46, 61, 122

R.; Dey, M.B.; Chowdhuri, J.; Ghosh, R.; Manchanda, N.; Yadava, U.C.; Nagora, P.K.; Atrey, J.V.; Raval, Y.S.; Joisa, R.L.; Tanna, and ADITYA Team. Modeling of the h emission from aditya tokamak plasmas. *Atoms*, 7, 2019. doi: https://doi.org/10.3390/atoms7040095. URL https://www.mdpi.com/2218-2004/7/4/95#cite. 43

Website DIII-D. Information about divertor langmuir probes on diii-d, 12 2023. URL https://diii-d.gat.com/diii-d/DivProbes. 103

Thomas Dolan. *PLASMA CONFINEMENT*, pages 168–216. 12 1982. ISBN 9780080255668. doi: 10.1016/B978-0-08-025566-8.50016-4. 11, 12

Thomas J Dolan. *Lecture Notes in Energy: Magnetic Fusion Technology*. Springer-Verlag London, 19 edition, 2013. ISBN 9781447155553. doi: 10.1007/978-1-4471-5556-0. URL https://www.springer.com/gp/book/9781447155553. 12, 100, 102

W. L. Dunn and J. K. Shultis. *Exploring Monte Carlo Methods, Chapter 9*. Elsevier Science Technology, 2011. ISBN 9780080930619. URL https://ebookcentral.proquest.com/lib/utk/detail.action?docID=680811. 132

M G Dunne, S Potzel, F Reimold, M Wischmeier, E Wolfrum, L Frassinetti, M Beurskens, P Bilkova, M Cavedon, R Fischer, B Kurzan, F M Laggner, R M McDermott, G Tardini, E Trier, E Viezzer, M Willensdorfer, The EUROfusion MST1 Team, and The ASDEX-Upgrade Team. The role of the density profile in the asdex-upgrade pedestal structure. *Plasma Physics and Controlled Fusion*, 59(1):014017, oct 2016. doi: 10.1088/0741-3335/59/1/014017. URL https://dx.doi.org/10.1088/0741-3335/59/1/014017. 173

R Dux, A Janzer, T Pütterich, and ASDEX Upgrade Team. Main chamber sources and edge transport of tungsten in h-mode plasmas at asdex upgrade. *Nuclear Fusion*, 51:53002, 2011. URL http://stacks.iop.org/0029-5515/51/i=5/a=053002. 326

History.com Editors. Industrial revolution, 2009. URL https://www.history.com/topics/industrial-revolution/industrial-revolution. 3

EIA. Net generation united states all sectors, 2020. URL https://www.eia.gov/electricity/data/browser/#/topic/0?agg=2. 5

U Fantz. Atomic and molecular emission spectroscopy in low temperature plasmas containing hydrogen and deuterium, 2002. URL http://inis.iaea.org/search/search.aspx?orig_q=RN:33018445. 52, 53, 54, 55, 56, 57, 58, 59, 60, 61, 62, 63

G Fishpool, John Canik, G Cunningham, J Harrison, I Katramados, A Kirk, M Kovari, H Meyer, R Scannell, et al. Mast-upgrade divertor facility and assessing performance of long-legged divertors. *Journal of Nuclear Materials*, 438:S356–S359, 2013. 66

Jeffrey P Freidberg. *Plasma Physics and Fusion Energy*. Cambridge University Press, 2007. doi: 10.1017/CBO9780511755705. 9, 14

W Fundamenski. Chapter 6: Scrape-off layer transport on jet. *Fusion Science and Technology*, 53:1023–1063, 5 2008. ISSN 1536-1055. doi: 10.13182/FST08-A1746. URL `https://doi.org/10.13182/FST08-A1746`. doi: 10.13182/FST08-A1746. 65

Wojciech Fundamenski. *Power Exhaust in Fusion Plasmas*. Cambridge University Press, 2009. doi: 10.1017/CBO9780511770609. 186, 189

F Glass, T N Carlstrom, D Du, A G McLean, D A Taussig, and R L Boivin. Upgraded divertor thomson scattering system on diii-d. *Review of Scientific Instruments*, 87: 11E508, 11 2016. ISSN 0034-6748. doi: 10.1063/1.4955281. URL `https://aip.scitation.org/doi/abs/10.1063/1.4955281`. doi: 10.1063/1.4955281. 99, 100

Vignesh Gopakumar and D Samaddar. Image mapping the temporal evolution of edge characteristics in tokamaks using neural networks. *Machine Learning: Science and Technology*, 1(1):015006, 2020. 86

M. Groth, M. E. Fenstermacher, C. J. Lasnier, R. Hernandez, J. M. Moller, and R. A. Sturz. Diagnosis of edge localized mode evolution in diii-d using fast-gated cid and infrared cameras. *Rev. Sci. Instrum.*, 74:2064, 3 2003. ISSN 00346748. doi: 10.1063/1.1537037. 70, 75, 169

World Bank Group. The world bank total population data, 2019. URL `https://data.worldbank.org/indicator/SP.POP.TOTL?end=2019&start=1960&view=chart`. 3

O. Gruber, H.-S. Bosch, S. Günter, A. Herrmann, A. Kallenbach, M. Kaufmann, K. Krieger, K. Lackner, V. Mertens, R. Neu, F. Ryter, J. Schweinzer, A. Stäbler, W. Suttrop, R. Wolf, K. Asmussen, A. Bard, G. Becker, K. Behler, K. Behringer, A. Bergmann, M. Bessenrodt-Weberpals, K. Borrass, B. Braams, M. Brambilla, R. Brandenburg, F. Braun, H. Brinkschulte, R. Brückner, B. Brüsehaber,

K. Büchl, A. Buhler, H.P. Callaghan, A. Carlson, D.P. Coster, L. Cupido, S. de Peña Hempel, C. Dorn, R. Drube, R. Dux, S. Egorov, W. Engelhardt, H.-U. Fahrbach, U. Fantz, H.-U. Feist, P. Franzen, J.C. Fuchs, G. Fussmann, J. Gafert, G. Gantenbein, O. Gehre, A. Geier, J. Gernhardt, E. Gubanka, A. Gude, G. Haas, K. Hallatschek, D. Hartmann, B. Heinemann, G. Herppich, W. Herrmann, F. Hofmeister, E. Holzhauer, D. Jacobi, M. Kakoulidis, N. Karakatsanis, O. Kardaun, A. Khutoretski, H. Kollotzek, S. Kötterl, W. Kraus, B. Kurzan, G. Kyriakakis, P.T. Lang, R.S. Lang, M. Laux, L.L. Lengyel, F. Leuterer, A. Lorenz, H. Maier, M. Manso, M. Maraschek, M. Markoulaki, K.-F. Mast, P.J. McCarthy, D. Meisel, H. Meister, R. Merkel, J.P. Meskat, H.W. Müller, M. Münich, H. Murmann, B. Napiontek, G. Neu, J. Neuhauser, M. Niethammer, J.-M. Noterdaeme, G. Pautasso, A.G. Peeters, G. Pereverzev, S. Pinches, G. Raupp, K. Reinmüller, R. Riedl, V. Rohde, H. Röhr, J. Roth, H. Salzmann, W. Sandmann, H.-B. Schilling, D. Schlögl, K. Schmidtmann, H. Schneider, R. Schneider, W. Schneider, G. Schramm, S. Schweizer, R.R. Schwörer, B.D. Scott, U. Seidel, F. Serra, S. Sesnic, C. Sihler, A. Silva, E. Speth, K.-H. Steuer, J. Stober, B. Streibl, A. Thoma, W. Treutterer, M. Troppmann, N. Tsois, W. Ullrich, M. Ulrich, P. Varela, H. Verbeek, O. Vollmer, H. Wedler, M. Weinlich, U. Wenzel, F. Wesner, R. Wunderlich, N. Xantopoulos, Q. Yu, D. Zasche, T. Zehetbauer, H.-P. Zehrfeld, H. Zohm, and M. Zouhar. Overview of asdex upgrade results. *Nuclear Fusion*, 39(9Y):1321, sep 1999. doi: 10.1088/0029-5515/39/9Y/309. URL `https://dx.doi.org/10.1088/0029-5515/39/9Y/309`. 76, 78

H Y Guo, G F Matthews, I Coffey, S K Erents, M Groth, P J Harbour, M G von Hellermann, D L Hillis, J T Hogan, L D Horton, L C Ingesson, K D Lawson, J Lingertat, C F Maggi, G M McCracken, R D Monk, P D Morgan, M F Stamp, P C Stangeby, A Taroni, and G C Vlases. Effects of divertor geometry and chemical sputtering on impurity behaviour and plasma performance in jet. *Nuclear Fusion*, 40:379–396, 2000. ISSN 0029-5515. doi: 10.1088/0029-5515/40/3/308. URL `http:`

//dx.doi.org/10.1088/0029-5515/40/3/308. 65, 126

H Y Guo, H Q Wang, J G Watkins, L Casali, B Covele, A L Moser, T Osborne, C M Samuell, M W Shafer, P C Stangeby, D M Thomas, J Boedo, R J Buttery, R Groebner, D N Hill, L Holland, A W Hyatt, A E Jaervinen, A Kellman, L L Lao, C J Lasnier, A W Leonard, C Murphy, J Ren, C F Sang, A C Sontag, T S Taylor, and the DIII-D Team. First experimental tests of a new small angle slot divertor on diii-d. *Nuclear Fusion*, 59:86054, 7 2019. doi: 10.1088/1741-4326/ab26ee. URL https://dx.doi.org/10.1088/1741-4326/ab26ee. 21, 127

HY Guo, S Zhu, and J Li. B2/eirene modeling of east divertor target power loading with enhanced wall carbon source and additional neon injection. *Journal of nuclear materials*, 363:162–166, 2007. 87

G Haas and H-S Bosch. In vessel pressure measurement in nuclear fusion experiments with asdex gauges. *Vacuum*, 51(1):39–46, 1998. ISSN 0042-207X. doi: https://doi.org/10.1016/S0042-207X(98)00131-6. URL https://www.sciencedirect.com/science/article/pii/S0042207X98001316. 106

N Den Harder, S Brezinsek, T Pütterich, N Fedorczak, G F Matthews, A Meigs, M F Stamp, M C M van de Sanden, G J Van Rooij, and J E T Contributors. Elm-resolved divertor erosion in the jet iter-like wall. *Nuclear fusion*, 56:26014, 2016. ISSN 0029-5515. 326

E Havlíčková, J Harrison, B Lipschultz, G Fishpool, A Kirk, A Thornton, M Wischmeier, S Elmore, and S Allan. Solps analysis of the mast-u divertor with the effect of heating power and pumping on the access to detachment in the super-x configuration. *Plasma Physics and Controlled Fusion*, 57(11):115001, 2015. 66

E Havlíčková, W Fundamenski, M Wischmeier, G Fishpool, and A W Morris. Investigation of conventional and super-x divertor configurations of mast upgrade using scrape-off layer plasma simulation. *Plasma Physics and Controlled Fusion*,

56:75008, 2014. ISSN 0741-3335. doi: 10.1088/0741-3335/56/7/075008. URL http://dx.doi.org/10.1088/0741-3335/56/7/075008. 126

Claire Hopley. A history of the british cotton industry, 2020. URL https://britishheritage.com/history/history-british-cotton-industry. 3

L D Horton, G C Vlases, P Andrew, V P Bhatnagar, A V Chankin, S Clement, G D Conway, S J Davies, J C M de Haas, J K Ehrenberg, G M Fishpool, E Gauthier, H Y Guo, P J Harbour, L C Ingesson, H J Jäckel, J Lingertat, A Loarte, C G Lowry, C F Maggi, G F Matthews, G M McCracken, R Mohanti, R D Monk, R Reichle, E Righi, G Saibene, R Sartori, R Simonini, M F Stamp, A Taroni, and K Thomsen. Studies in jet divertors of varied geometry. i: Non-seeded plasma operation. *Nuclear Fusion*, 39:1–17, 1 1999. doi: 10.1088/0029-5515/39/1/301. URL https://doi.org/10.1088/0029-5515/39/1/301. 66, 82, 125

A Huber, S Brezinsek, M Groth, P C de Vries, V Riccardo, G van Rooij, G Sergienko, G Arnoux, A Boboc, P Bilkova, G Calabro, M Clever, J W Coenen, M N A Beurskens, T Eich, S Jachmich, M Lehnen, E Lerche, S Marsen, G F Matthews, K McCormick, A G Meigs, Ph. Mertens, V Philipps, J Rapp, U Samm, M Stamp, M Wischmeier, and S Wiesen. Impact of the iter-like wall on divertor detachment and on the density limit in the jet tokamak. *Journal of Nuclear Materials*, 438:S139–S147, 2013. ISSN 0022-3115. doi: https://doi.org/10.1016/j.jnucmat.2013.01.022. URL http://www.sciencedirect.com/science/article/pii/S0022311513000305. 323, 324, 326

I H Hutchinson. Thermal front analysis of detached divertors and {MARFEs}. *Nuclear Fusion*, 34:1337–1348, 10 1994. doi: 10.1088/0029-5515/34/10/i04. URL https://doi.org/10.1088%2F0029-5515%2F34%2F10%2Fi04. 322

I. H. Hutchinson. *Principles of Plasma Diagnostics*. Cambridge University Press, 2 edition, 2002. 46, 47, 49, 50, 51

I H Hutchinson, B LaBombard, J A Goetz, B Lipschultz, G M McCracken, J A Snipes, and J L Terry. The effects of field reversal on the alcator c-mod divertor. *Plasma Physics and Controlled Fusion*, 37(12):1389, dec 1995. doi: 10.1088/0741-3335/37/12/004. URL https://dx.doi.org/10.1088/0741-3335/37/12/004. 328

IEA. Gas, 2018a. URL https://www.iea.org/fuels-and-technologies/gas. 3

IEA. World gross electricity production, by source, 2018b. URL https://www.iea.org/data-and-statistics/charts/world-gross-electricity-production-by-source-2018. 3

IEA. World energy consumption per capita, 2018c. URL https://www.iea.org/data-and-statistics/?country=WORLD&fuel=Energyconsumption&indicator=Electricityconsumptionpercapita. 3

IEA. Nuclear, 2018d. URL https://www.iea.org/fuels-and-technologies/nuclear. 5

IEA. World nuclear electricity generation, 2018e. URL https://www.iea.org/fuels-and-technologies/nuclear. 5

IEA. Coal, 2019a. URL https://www.iea.org/reports/coal-2019. 3

IEA. World gross electricity production by source, 1 2019b. URL https://www.iea.org/data-and-statistics/charts/world-gross-electricity-production-by-source-2019. 3, 4

IEA. Hydropower, 2019c. URL https://www.iea.org/fuels-and-technologies/hydropower. 5

IEA. World electricity final consumption by sector, 2020. URL https://www.iea.org/data-and-statistics/charts/world-electricity-final-consumption-by-sector-1974-2018. 3

ITER. What is iter?, 2023. URL https://www.iter.org/proj/inafewlines. 7

Gareth James, Daniela Witten, Trevor Hastie, and Robert Tibshirani. *An Introduction to Statistical Learning: with Applications in R*, volume 103 of *Springer texts in statistics*. Springer Nature, New York, 1 edition, 2013. ISBN 1461471389. 251, 252, 254, 255, 256, 258

E. Joffrin, P. Tamain, E. Belonohy, H. Bufferand, P. Buratti, C.D. Challis, E. Delabie, P. Drewelow, D. Dodt, L. Frassinetti, J. Garcia, C. Giroud, M. Groth, J. Hobirk, A. E. Jarvinen, H.-T. Kim, F. Koechl, U. Kruezi, B. Lipschutz, P.J. Lomas, E. de la Luna, T. Loarer, P. Maget, C. Maggi, G. Matthews, F. Maviglia, A. Meigs, I. Nunes, G. Pucella, F. Rimini, S. Saarelma, E. Solano, A.C.C. Sips, M. Tsalas, I. Voitsekhovitch, H. Weisen, and the JET Contributors. Impact of divertor geometry on h-mode confinement in the jet metallic wall. *Nuclear Fusion*, 57(8):086025, jun 2017. doi: 10.1088/1741-4326/aa6e1c. URL https://dx.doi.org/10.1088/1741-4326/aa6e1c. 172

L C Johnson and E Hinnov. Ionization, recombination, and population of excited levels in hydrogen plasmas. *Journal of Quantitative Spectroscopy and Radiative Transfer*, 13:333–358, 1973. ISSN 0022-4073. doi: https://doi.org/10.1016/0022-4073(73)90064-2. URL http://www.sciencedirect.com/science/article/pii/0022407373900642. 61, 122

T T C Jones. High performance joint european torus (jet) plasmas for deuterium–tritium operation with the mkii divertor. *Physics of Plasmas*, 4: 1725–1735, 5 1997. ISSN 1070-664X. doi: 10.1063/1.872361. URL https://doi.org/10.1063/1.872361. doi: 10.1063/1.872361. 65, 126

M B Kadomtsev, V Kotov, V S Lisitsa, V S Neverov, and V A Shurygin. Kinetics of hydrogen atom radiation emission of the sol plasma in iter. a. 126

M B Kadomtsev, V Kotov, V S Lisitsa, and V A Shurygin. Ballistic model for neutral hydrogen distribution in iter edge plasma. b. 126

A Kallenbach, R Dux, J Gafert, G Haas, L D Horton, M Jakobi, B Kurzan, H W M ller, R Neu, J Neuhauser, R Pugno, T P tterich, V Rohde, W Sandmann, S.-W Yoon, and the ASDEX Upgrade Team. Edge transport and its interconnection with main chamber recycling in asdex upgrade. *Nuclear Fusion*, 43:573–578, 2003. ISSN 0029-5515. doi: 10.1088/0029-5515/43/7/310. URL `http://dx.doi.org/10.1088/0029-5515/43/7/310`. 70, 73, 77

H. Kawashima, S. Sengoku, T. Ogawa, H. Ogawa, K. Uehara, Y. Miura, H. Kimura, and JFT-2M Group. Study of a closed divertor with strong gas puffing on jft-2m. *Nuclear Fusion*, 39(11Y):1679, nov 1999. doi: 10.1088/0029-5515/39/11Y/307. URL `https://dx.doi.org/10.1088/0029-5515/39/11Y/307`. 82

H. Kawashima, K. Shimizu, and T. Takizuka. Development of integrated sol/divertor code and simulation study of the jt-60u/jt-60sa tokamaks. *Plasma Phys. Control. Fusion*, 49:S77, 7 2007. ISSN 07413335. doi: 10.1088/0741-3335/49/7/s05. 126

S.M. Kaye, M.G. Bell, K. Bol, D. Boyd, K. Brau, D. Buchenauer, R. Budny, A. Cavallo, P. Couture, T. Crowley, D.S. Darrow, H. Eubank, R.J. Fonck, R. Goldston, B. Grek, K.P. Jaehnig, D. Johnson, R. Kaita, H. Kugel, B. Leblanc, J. Manickam, D. Manos, D. Mansfield, E. Mazzucato, R. McCann, D. McCune, K. McGuire, D. Mueller, A. Murdock, M. Okabayashi, K. Okano, D.K. Owens, D.E. Post, M. Reusch, G.L. Schmidt, S. Sesnic, R. Slusher, S. Suckewer, C. Surko, H. Takahashi, F. Tenney, H. Towner, and J. Valley. Attainment of high confinement in neutral beam heated divertor discharges in the pdx tokamak. *Journal of Nuclear Materials*, 121:115–125, 1984. ISSN 0022-3115. doi: https://doi.org/10.1016/0022-3115(84)90111-9. URL `https://www.sciencedirect.com/science/article/pii/0022311584901119`. 80

M Keilhacker. H-mode confinement in tokamaks. *Plasma Physics and Controlled Fusion*, 29:1401–1413, 10 1987. doi: 10.1088/0741-3335/29/10a/320. URL https://doi.org/10.1088%2F0741-3335%2F29%2F10a%2F320. 16

M Keilhacker, K Lackner, K Behringer, H Murmann, and H Niedermeyer. Plasma boundary layer in limiter and divertor tokamaks. *Physica Scripta*, T2B:443–453, 1 1982. doi: 10.1088/0031-8949/1982/t2b/022. URL https://doi.org/10.1088%2F0031-8949%2F1982%2Ft2b%2F022. 37

Mitsuru Kikuchi. *Frontiers in Fusion Research*. Springer-Verlag London, 1 edition, 2011. ISBN 978-1-84996-411-1. doi: 10.1007/978-1-84996-411-1. 6

J E Kinsey, G M Staebler, J Candy, R E Waltz, and R V Budny. Iter predictions using the gyro verified and experimentally validated trapped gyro-landau fluid transport model. *Nuclear Fusion*, 51:83001, 6 2011. doi: 10.1088/0029-5515/51/8/083001. URL https://doi.org/10.1088%2F0029-5515%2F51%2F8%2F083001. 16

C.C. Klepper, J.T. Hogan, D.N. Hill, R. Maingi, L.W. Owen, D.A. Buchenauer, M.A. Mahdavi, and M.J. Schaffer. Divertor neutral pressure enhancement with a baffle in diii-d. *Nuclear Fusion*, 33(4):533, apr 1993. doi: 10.1088/0029-5515/33/4/I02. URL https://dx.doi.org/10.1088/0029-5515/33/4/I02. 80, 105, 106, 108

T Klinger, A Alonso, S Bozhenkov, R Burhenn, A Dinklage, G Fuchert, J Geiger, O Grulke, A Langenberg, M Hirsch, G Kocsis, J Knauer, A Krämer-Flecken, H Laqua, S Lazerson, M Landreman, H Maaßberg, S Marsen, M Otte, N Pablant, E Pasch, K Rahbarnia, T Stange, T Szepesi, H Thomsen, P Traverso, J L Velasco, T Wauters, G Weir, T Windisch, and The Wendelstein 7-X Team. Performance and properties of the first plasmas of wendelstein 7-x. *Plasma Physics and Controlled Fusion*, 59(1):014018, oct 2016. doi: 10.1088/0741-3335/59/1/014018. URL https://dx.doi.org/10.1088/0741-3335/59/1/014018. 14

T. Klinger, T. Andreeva, S. Bozhenkov, C. Brandt, R. Burhenn, B. Buttenschön, G. Fuchert, B. Geiger, O. Grulke, H.P. Laqua, N. Pablant, K. Rahbarnia, T. Stange, A. von Stechow, N. Tamura, H. Thomsen, Y. Turkin, T. Wegner, I. Abramovic, S. Äkäslompolo, J. Alcuson, P. Aleynikov, K. Aleynikova, A. Ali, A. Alonso, G. Anda, E. Ascasibar, J.P. Bähner, S.G. Baek, M. Balden, J. Baldzuhn, M. Banduch, T. Barbui, W. Behr, C. Beidler, A. Benndorf, C. Biedermann, W. Biel, B. Blackwell, E. Blanco, M. Blatzheim, S. Ballinger, T. Bluhm, D. Böckenhoff, B. Böswirth, L.-G. Böttger, M. Borchardt, V. Borsuk, J. Boscary, H.-S. Bosch, M. Beurskens, R. Brakel, H. Brand, T. Bräuer, H. Braune, S. Brezinsek, K.-J. Brunner, R. Bussiahn, V. Bykov, J. Cai, I. Calvo, B. Cannas, A. Cappa, A. Carls, D. Carralero, L. Carraro, B. Carvalho, F. Castejon, A. Charl, N. Chaudhary, D. Chauvin, F. Chernyshev, M. Cianciosa, R. Citarella, G. Claps, J. Coenen, M. Cole, M.J. Cole, F. Cordella, G. Cseh, A. Czarnecka, K. Czerski, M. Czerwinski, G. Czymek, A. da Molin, A. da Silva, H. Damm, A. de la Pena, S. Degenkolbe, C.P. Dhard, M. Dibon, A. Dinklage, T. Dittmar, M. Drevlak, P. Drewelow, P. Drews, F. Durodie, E. Edlund, P. van Eeten, F. Effenberg, G. Ehrke, S. Elgeti, M. Endler, D. Ennis, H. Esteban, T. Estrada, J. Fellinger, Y. Feng, E. Flom, H. Fernandes, W.H. Fietz, W. Figacz, J. Fontdecaba, O. Ford, T. Fornal, H. Frerichs, A. Freund, T. Funaba, A. Galkowski, G. Gantenbein, Y. Gao, J. García Regaña, D. Gates, J. Geiger, V. Giannella, A. Gogoleva, B. Goncalves, A. Goriaev, D. Gradic, M. Grahl, J. Green, H. Greuner, A. Grosman, H. Grote, M. Gruca, C. Guerard, P. Hacker, X. Han, J.H. Harris, D. Hartmann, D. Hathiramani, B. Hein, B. Heinemann, P. Helander, S. Henneberg, M. Henkel, J. Hernandez Sanchez, C. Hidalgo, M. Hirsch, K.P. Hollfeld, U. Höfel, A. Hölting, D. Höschen, M. Houry, J. Howard, X. Huang, Z. Huang, M. Hubeny, M. Huber, H. Hunger, K. Ida, T. Ilkei, S. Illy, B. Israeli, S. Jablonski, M. Jakubowski, J. Jelonnek, H. Jenzsch, T. Jesche, M. Jia, P. Junghanns, J. Kacmarczyk, J.-P. Kallmeyer, U. Kamionka, H. Kasahara, W. Kasparek, Y.O. Kazakov, N. Kenmochi, C. Killer, A. Kirschner, R. Kleiber, J. Knauer, M. Knaup, A. Knieps, T. Kobarg,

G. Kocsis, F. Köchl, Y. Kolesnichenko, A. Könies, R. König, P. Kornejew, J.-P. Koschinsky, F. Köster, M. Krämer, R. Krampitz, A. Krämer-Flecken, N. Krawczyk, T. Kremeyer, J. Krom, M. Krychowiak, I. Ksiazek, M. Kubkowska, G. Kühner, T. Kurki-Suonio, P.A. Kurz, S. Kwak, M. Landreman, P. Lang, R. Lang, A. Langenberg, S. Langish, H. Laqua, R. Laube, S. Lazerson, C. Lechte, M. Lennartz, W. Leonhardt, C. Li, C. Li, Y. Li, Y. Liang, C. Linsmeier, S. Liu, J.-F. Lobsien, D. Loesser, J. Loizu Cisquella, J. Lore, A. Lorenz, M. Losert, A. Lücke, A. Lumsdaine, V. Lutsenko, H. Maaßberg, O. Marchuk, J.H. Matthew, S. Marsen, M. Marushchenko, S. Masuzaki, D. Maurer, M. Mayer, K. McCarthy, P. McNeely, A. Meier, D. Mellein, B. Mendelevitch, P. Mertens, D. Mikkelsen, A. Mishchenko, B. Missal, J. Mittelstaedt, T. Mizuuchi, A. Mollen, V. Moncada, T. Mönnich, T. Morisaki, D. Moseev, S. Murakami, G. Náfrádi, M. Nagel, D. Naujoks, H. Neilson, R. Neu, O. Neubauer, U. Neuner, T. Ngo, D. Nicolai, S.K. Nielsen, H. Niemann, T. Nishizawa, R. Nocentini, C. Nührenberg, J. Nührenberg, S. Obermayer, G. Offermanns, K. Ogawa, J. Ölmanns, J. Ongena, J.W. Oosterbeek, G. Orozco, M. Otte, L. Pacios Rodriguez, N. Panadero, N. Panadero Alvarez, D. Papenfuß, S. Paqay, E. Pasch, A. Pavone, E. Pawelec, T.S. Pedersen, G. Pelka, V. Perseo, B. Peterson, D. Pilopp, S. Pingel, F. Pisano, B. Plaum, G. Plunk, P. Pölöskei, M. Porkolab, J. Proll, M.-E. Puiatti, A. Puig Sitjes, F. Purps, M. Rack, S. Récsei, A. Reiman, F. Reimold, D. Reiter, F. Remppel, S. Renard, R. Riedl, J. Riemann, K. Risse, V. Rohde, H. Röhlinger, M. Romé, D. Rondeshagen, P. Rong, B. Roth, L. Rudischhauser, K. Rummel, T. Rummel, A. Runov, N. Rust, L. Ryc, S. Ryosuke, R. Sakamoto, M. Salewski, A. Samartsev, E. Sanchez, F. Sano, S. Satake, J. Schacht, G. Satheeswaran, F. Schauer, T. Scherer, J. Schilling, A. Schlaich, G. Schlisio, F. Schluck, K.-H. Schlüter, J. Schmitt, H. Schmitz, O. Schmitz, S. Schmuck, M. Schneider, W. Schneider, P. Scholz, R. Schrittwieser, M. Schröder, T. Schröder, R. Schroeder, H. Schumacher, B. Schweer, E. Scott, S. Sereda, B. Shanahan, M. Sibilia, P. Sinha, S. Sipliä, C. Slaby, M. Sleczka, H. Smith, W. Spiess, D.A. Spong, A. Spring, R. Stadler, M. Stejner, L. Stephey,

U. Stridde, C. Suzuki, J. Svensson, V. Szabó, T. Szabolics, T. Szepesi, Z. Szökefalvi-Nagy, A. Tancetti, J. Terry, J. Thomas, M. Thumm, J.M. Travere, P. Traverso, J. Tretter, H. Trimino Mora, H. Tsuchiya, T. Tsujimura, S. Tulipán, B. Unterberg, I. Vakulchyk, S. Valet, L. Vano, B. van Milligen, A.J. van Vuuren, L. Vela, J.-L. Velasco, M. Vergote, M. Vervier, N. Vianello, H. Viebke, R. Vilbrandt, A. Vorköper, S. Wadle, F. Wagner, E. Wang, N. Wang, Z. Wang, F. Warmer, T. Wauters, L. Wegener, J. Weggen, Y. Wei, G. Weir, J. Wendorf, U. Wenzel, A. Werner, A. White, B. Wiegel, F. Wilde, T. Windisch, M. Winkler, A. Winter, V. Winters, S. Wolf, R.C. Wolf, A. Wright, G. Wurden, P. Xanthopoulos, H. Yamada, I. Yamada, R. Yasuhara, M. Yokoyama, M. Zanini, M. Zarnstorff, A. Zeitler, D. Zhang, H. Zhang, J. Zhu, M. Zilker, A. Zocco, S. Zoletnik, and M. Zuin. Overview of first wendelstein 7-x high-performance operation. *Nuclear Fusion*, 59(11):112004, jun 2019. doi: 10.1088/1741-4326/ab03a7. URL `https://dx.doi.org/10.1088/1741-4326/ab03a7`. 14

E Kolemen, P J Vail, M A Makowski, S L Allen, B D Bray, M E Fenstermacher, D A Humphreys, A W Hyatt, C J Lasnier, A W Leonard, A G McLean, R Maingi, R Nazikian, T W Petrie, V A Soukhanovskii, and E A Unterberg. Initial development of the diii-d snowflake divertor control. *Nuclear Fusion*, 58: 66007, 4 2018. doi: 10.1088/1741-4326/aab0d3. URL `https://doi.org/10.1088%2F1741-4326%2Faab0d3`. 23, 127

Mike Kotschenreuther, Prashant Valanju, Brent Covele, and Swadesh Mahajan. Magnetic geometry and physics of advanced divertors: the x-divertor and the snowflake. *Phys. Plasmas*, 20:102507, 10 2013. ISSN 1070664X. doi: 10.1063/1.4824735. 23, 127

S I Krasheninnikov. Two-dimensional effects in plasma radiation fronts and radiation front jumps in tokamak divertor plasmas. *Physics of Plasmas*, 4:3741–3743, 11 1997. ISSN 1070-664X. doi: 10.1063/1.872539. URL `https://doi.org/10.1063/1.872539`. doi: 10.1063/1.872539. 322

S. I. Krasheninnikov. Divertor plasma detachemnt past and future, 2018. URL http://www.firefusionpower.org/PSI2018_Krash_Divertor_Detached_Review.pdf. 35, 38, 39, 321, 322

S I Krasheninnikov and A S Kukushkin. Physics of ultimate detachment of a tokamak divertor plasma. *Journal of Plasma Physics*, 83:155830501, 2017. doi: 10.1017/S0022377817000654. 19, 37, 38, 40, 41, 45, 321, 322, 324, 325, 326

S. I. Krasheninnikov, A. S. Kukushkin, and A. A. Pshenov. Divertor plasma detachment. *Phys. Plasmas*, 23:055602, 5 2016. ISSN 10897674. doi: 10.1063/1.4948273. 41

Predrag S Krstic and David R Schultz. Elastic scattering and charge transfer in slow collisions: isotopes of h and hcolliding with isotopes of h and with he. *Journal of Physics B: Atomic, Molecular and Optical Physics*, 32:3485–3509, 7 1999. doi: 10.1088/0953-4075/32/14/317. URL https://doi.org/10.1088%2F0953-4075%2F32%2F14%2F317. 37

A S Kukushkin and H D Pacher. Critical evaluation of the determination of the sol transport mechanism from a statistical examination of experimental data. *Contributions to Plasma Physics*, 46:545–550, 9 2006. ISSN 0863-1042. doi: 10.1002/ctpp.200610042. URL https://doi.org/10.1002/ctpp.200610042. doi: 10.1002/ctpp.200610042. 321

A. S. Kukushkin, H. D. Pacher, G. Janeschitz, A. Loarte, D. P. Coster, G. Matthews, D. Reiter, R. Schneider, and V. Zhogolev. Basic divertor operation in iter-feat. *Nuclear Fusion*, 42:187–191, 2 2002. ISSN 00295515. doi: 10.1088/0029-5515/42/2/310. 126

A.S. Kukushkin, G. Janeschitz, A. Loarte, H.D. Pacher, D. Coster, D. Reiter, and R. Schneider. Critical issues in divertor optimisation for iter–feat. *Journal of Nuclear Materials*, 290-293:887–891, 2001. ISSN 0022-3115. doi: https:

//doi.org/10.1016/S0022-3115(00)00457-8. URL https://www.sciencedirect.com/science/article/pii/S0022311500004578. 14th Int. Conf. on Plasma-Surface Interactions in Controlled Fusion D evices. 326

AS Kukushkin, HD Pacher, Vladislav Kotov, GW Pacher, and Detlev Reiter. Finalizing the iter divertor design: The key role of solps modeling. *Fusion engineering and design*, 86(12):2865–2873, 2011. 85, 87

AS Kukushkin et al. Fusion energy 1998 (proc. 17th int. conf. yokohama, 1998), 1999. 326

C Kurz, B LaBombard, B Lipschultz, G M McCracken, A Niemczewski, and J L Terry. Measurements of neutral density based on emissivity in the alcator c-mod divertor. *Plasma physics and controlled fusion*, 39:963, 1997. ISSN 0741-3335. 63, 64

B. LaBombard, J. Goetz, C. Kurz, D. Jablonski, B. Lipschultz, G. McCracken, A. Niemczewski, R. L. Boivin, F. Bombarda, C. Christensen, S. Fairfax, C. Fiore, D. Garnier, M. Graf, S. Golovato, R. Granetz, M. Greenwald, S. Horne, A. Hubbard, I. Hutchinson, J. Irby, J. Kesner, T. Luke, E. Marmar, M. May, P. O'Shea, M. Porkolab, J. Reardon, J. Rice, J. Schachter, J. Snipes, P. Stek, Y. Takase, J. Terry, G. Tinios, R. Watterson, B. Welch, and S. Wolfe. Scaling and transport analysis of divertor conditions on the Alcator C-Mod tokamak. *Physics of Plasmas*, 2(6):2242–2248, 06 1995. ISSN 1070-664X. doi: 10.1063/1.871248. URL https://doi.org/10.1063/1.871248. 327

B LaBombard, M V Umansky, R L Boivin, J A Goetz, J Hughes, B Lipschultz, D Mossessian, C S Pitcher, J L Terry, and Alcator Group. Cross-field plasma transport and main-chamber recycling in diverted plasmas on alcator c-mod. *Nuclear Fusion*, 40:2041–2060, 2000. ISSN 0029-5515. doi: 10.1088/0029-5515/40/12/308. URL http://dx.doi.org/10.1088/0029-5515/40/12/308. 72, 73, 75, 115

B. LaBombard, A.Q. Kuang, D. Brunner, I. Faust, R. Mumgaard, M.L. Reinke, J.L. Terry, J.W. Hughes, J. Walk, M. Chilenski, Y. Lin, E. Marmar, G. Wallace, D. Whyte, S. Wolfe, and S. Wukitch. High-field side scrape-off layer investigation: Plasma profiles and impurity screening behavior in near-double-null configurations. *Nuclear Materials and Energy*, 12:139–147, 2017. ISSN 2352-1791. doi: https://doi.org/10.1016/j.nme.2016.10.006. URL `https://www.sciencedirect.com/science/article/pii/S2352179116300400`. Proceedings of the 22nd International Conference on Plasma Surface Interactions 2016, 22nd PSI. 175

K Lackner, R Chodura, M Kaufmann, J Neuhauser, K G Rauh, and W Schneider. Control of particle and energy transport across the boundary of a tokamak plasma. *Plasma Physics and Controlled Fusion*, 26:105–115, 1 1984. doi: 10.1088/0741-3335/26/1a/328. URL `https://doi.org/10.1088%2F0741-3335%2F26%2F1a%2F328`. 37

Catherine Lane. Nuclear energy pros and cons, 2020. URL `https://www.solarreviews.com/blog/nuclear-energy-pros-and-cons`. 5

P.T. Lang, A. Loarte, G. Saibene, L.R. Baylor, M. Becoulet, M. Cavinato, S. Clement-Lorenzo, E. Daly, T.E. Evans, M.E. Fenstermacher, Y. Gribov, L.D. Horton, C. Lowry, Y. Martin, O. Neubauer, N. Oyama, M.J. Schaffer, D. Stork, W. Suttrop, P. Thomas, M. Tran, H.R. Wilson, A. Kavin, and O. Schmitz. Elm control strategies and tools: status and potential for iter. *Nuclear Fusion*, 53(4):043004, mar 2013. doi: 10.1088/0029-5515/53/4/043004. URL `https://dx.doi.org/10.1088/0029-5515/53/4/043004`. 16, 17

C.J. Lasnier, D.N. Hill, T.W. Petrie, A.W. Leonard, T.E. Evans, and R. Maingi. Survey of target plate heat flux in diverted diii-d tokamak discharges. *Nuclear Fusion*, 38(8):1225, aug 1998. doi: 10.1088/0029-5515/38/8/209. URL `https://dx.doi.org/10.1088/0029-5515/38/8/209`. 79

J D Lawson. Some criteria for a power producing thermonuclear reactor. *Proceedings of the Physical Society. Section B*, 70:6–10, 1 1957. doi: 10.1088/0370-1301/70/1/303. URL https://doi.org/10.1088%2F0370-1301%2F70%2F1%2F303. 9

Jarrod Leddy. Integrated modelling of tokamak core and edge plasma turbulence. January 2016. URL https://etheses.whiterose.ac.uk/13207/. 87

B Lehnert. Screening of a high-density plasma from neutral gas penetration. *Nuclear Fusion*, 8:173–181, 10 1968. doi: 10.1088/0029-5515/8/3/005. URL https://doi.org/10.1088%2F0029-5515%2F8%2F3%2F005. 37

A W Leonard, T H Osborne, M E Fenstermacher, R J Groebner, M Groth, C J Lasnier, M A Mahdavi, T W Petrie, P B Snyder, J G Watkins, and L Zeng. Transport of edge localized modes energy and particles into the scrape off layer and divertor of diii-d. *Physics of Plasmas*, 10:1765–1772, 4 2003. ISSN 1070-664X. doi: 10.1063/1.1567723. URL https://doi.org/10.1063/1.1567723. doi: 10.1063/1.1567723. 114, 126

B Lipschultz and B LaBombard. Comparison of particle transport in the scrape-off layer plasmas of alcator c-mod and diii-d. *Plasma Physics and Controlled Fusion Fusion*, pages 1559–1578, 2005. doi: 10.1088/0741-3335/47/10/001. 68, 69, 125, 169

B Lipschultz, B LaBombard, E S Marmar, M M Pickrell, J L Terry, R Watterson, and S M Wolfe. Marfe: an edge plasma phenomenon. *Nuclear Fusion*, 24:977–988, 1984. ISSN 0029-5515. doi: 10.1088/0029-5515/24/8/002. URL http://dx.doi.org/10.1088/0029-5515/24/8/002. 322

LLNL. How icf works, 2020. URL https://lasers.llnl.gov/science/icf/how-icf-works. 12

A. Loarte. Understanding the edge physics of divertor experiments by comparison of 2d edge code calculations and experimental measurements. *Journal of Nuclear*

Materials, 241-243:118–134, 1997a. ISSN 0022-3115. doi: https://doi.org/10.1016/S0022-3115(97)80035-9. URL https://www.sciencedirect.com/science/article/pii/S0022311597800359. 326, 327

A Loarte. *Controlled Fusion and Plasma Physics*, 21A:1049, 1997b. 80

A. Loarte and P.J. Harbour. Effect of the magnetic flux geometry of a poloidal divertor on the profiles and parameters at the target. *Nuclear Fusion*, 32(4):681, apr 1992. doi: 10.1088/0029-5515/32/4/I13. URL https://dx.doi.org/10.1088/0029-5515/32/4/I13. 79

A. Loarte, R. D. Monk, J. R. Martín-Solís, D. J. Campbell, A. V. Chankin, S. Clement, S. J. Davies, J. Ehrenberg, S. K. Erents, H. Y. Guo, P. J. Harbour, L. D. Horton, L. C. Ingesson, H. Jäckel, J. Lingertat, C. G. Lowry, C. F. Maggi, G. F. Matthews, K. McCormick, D. P. O'Brien, R. Reichle, G. Saibene, R. J. Smith, M. F. Stamp, D. Stork, and G. C. Vlases. Plasma detachment in jet mark i divertor experiments. *Nucl. Fusion*, 38:331, 1998. ISSN 00295515. doi: 10.1088/0029-5515/38/3/303. 41, 327

A Loarte, B Lipschultz, A S Kukushkin, G F Matthews, P C Stangeby, N Asakura, G F Counsell, G Federici, A Kallenbach, K Krieger, A Mahdavi, V Philipps, D Reiter, J Roth, J Strachan, D Whyte, R Doerner, T Eich, W Fundamenski, A Herrmann, M Fenstermacher, P Ghendrih, M Groth, A Kirschner, S Konoshima, B LaBombard, P Lang, A W Leonard, P Monier-Garbet, R Neu, H Pacher, B Pegourie, R A Pitts, S Takamura, J Terry, E Tsitrone, the ITPA Scrape-off Layer, and Divertor Physics Topical Group. Chapter 4: Power and particle control. *Nuclear Fusion*, 47:S203, 2007. 26, 84, 85

Alberto Loarte. Effects of divertor geometry on tokamak plasmas. *Plasma Physics and Controlled Fusion*, 43:R183–R224, 5 2001. doi: 10.1088/0741-3335/43/6/201. URL https://doi.org/10.1088/0741-3335/43/6/201. 66, 67, 76, 79, 80, 81, 84, 125, 126, 172, 327, 328, 329

Alberto Loarte Prieto. *Estudio de los flujos de energía y partículas en el borde del plasma del Tokamak jet*. PhD thesis, 1992. 79, 81

J. D. Lore, R. S. Wilcox, J. M. Canik, L. Wang, G. S. Xu, and R. Maingi. Optimization of pumping performance in the east upgraded divertor*. *Plasma Physics and Controlled Fusion*, 61:065001, 4 2019. ISSN 0741-3335. doi: 10.1088/1361-6587/AB110E. URL `https://iopscience.iop.org/article/10.1088/1361-6587/ab110ehttps://iopscience.iop.org/article/10.1088/1361-6587/ab110e/meta`. 126, 128, 132

D. Lumma, J. L. Terry, and B. Lipschultz. Radiative and three-body recombination in the Alcator C-Mod divertor. *Physics of Plasmas*, 4(7):2555–2566, 07 1997. ISSN 1070-664X. doi: 10.1063/1.872234. URL `https://doi.org/10.1063/1.872234`. 326

J.L. Luxon. A design retrospective of the diii-d tokamak. *Nuclear Fusion*, 42(5): 614, may 2002. doi: 10.1088/0029-5515/42/5/313. URL `https://dx.doi.org/10.1088/0029-5515/42/5/313`. 21, 22

C Maggi. *Controlled Fusion and Plasma Physics*, 23J:201, 1999. 328

M Ali Mahdavi, J C DeBoo, C L Hsieh, N Ohyabu, R D Stambaugh, and J C Wesley. Particle exhaust from plasma discharges with an expanded-boundary divertor. *Phys. Rev. Lett.*, 47:1602–1605, 11 1981. doi: 10.1103/PhysRevLett.47.1602. URL `https://link.aps.org/doi/10.1103/PhysRevLett.47.1602`. 38

R Maingi, J G Watkins, M A Mahdavi, and L W Owen. Pump plenum pressure dependence on divertor plasma parameters and magnetic geometry in the diii-d tokamak. *Nuclear Fusion*, 39:1187–1192, 1999. ISSN 0029-5515. doi: 10.1088/0029-5515/39/9/311. URL `http://dx.doi.org/10.1088/0029-5515/39/9/311`. 23, 125, 127, 128, 132

R Maingi, J G Watkins, M A Mahdavi, and R J Colchin. Neutral pressure dynamics in the upper plenums in the {DIII}-d tokamak. *Nuclear Fusion*, 44:909–916, 7 2004. doi: 10.1088/0029-5515/44/8/009. URL https://doi.org/10.1088%2F0029-5515%2F44%2F8%2F009. 125, 132, 148

G.M. McCracken, M.F. Stamp, R.D. Monk, A.G. Meigs, J. Lingertat, R. Prentice, A. Starling, R.J. Smith, and A. Tabasso. Evidence for volume recombination in jet detached divertor plasmas. *Nuclear Fusion*, 38(4):619, apr 1998. doi: 10.1088/0029-5515/38/4/311. URL https://dx.doi.org/10.1088/0029-5515/38/4/311. 326

A. G. McLean, A. W. Leonard, M. A. Makowski, M. Groth, S. L. Allen, J. A. Boedo, B. D. Bray, A. R. Briesemeister, T. N. Carlstrom, D. Eldon, M. E. Fenstermacher, D. N. Hill, C. J. Lasnier, C. Liu, T. H. Osborne, T. W. Petrie, V. A. Soukhanovskii, P. C. Stangeby, C. Tsui, E. A. Unterberg, and J. G. Watkins. Electron pressure balance in the sol through the transition to detachment. *Journal of Nuclear Materials*, 463:533–536, 2015. ISSN 00223115. doi: 10.1016/j.jnucmat.2015.01.066. URL http://dx.doi.org/10.1016/j.jnucmat.2015.01.066. 322, 323

A G McLean, T Rognlien, J Canik, S L Allen, A W Leonard, P C Stangeby, T Abrams, J A Boedo, I Bykov, and A Briesemeister. The role of drifts and radiating species in ex-d detached divertor operation at diii-d. 2016. 326

A.G. McLean, J.D. Elder, P.C. Stangeby, S.L. Allen, J.A. Boedo, N.H. Brooks, M.E. Fenstermacher, M. Groth, S. Lisgo, A. Nagy, D.L. Rudakov, W.R. Wampler, J.G. Watkins, W.P. West, and D.G. Whyte. Divimp modeling of the toroidally symmetrical injection of 13ch4 into the upper sol of diii-d. *Journal of Nuclear Materials*, 337-339:124–128, 2005. ISSN 0022-3115. doi: https://doi.org/10.1016/j.jnucmat.2004.10.130. URL https://www.sciencedirect.com/science/article/pii/S0022311504008542. PSI-16. 97

Ph Mertens, S Brezinsek, P T Greenland, J D Hey, A Pospieszczyk, D Reiter, U Samm, B Schweer, G Sergienko, and E Vietzke. Hydrogen release from plasma-facing components into fusion plasmas - recent results from a spectroscopic approach. *Plasma Physics and Controlled Fusion*, 43:A349–A373, 11 2001. doi: 10.1088/0741-3335/43/12a/327. URL https://doi.org/10.1088%2F0741-3335%2F43%2F12a%2F327. 122

C De Michelis and M Mattioli. Spectroscopy and impurity behaviour in fusion plasmas. *Reports on Progress in Physics*, 47, 1984. doi: https://doi.org/10.1088/0034-4885/47/10/001. URL https://iopscience.iop.org/article/10.1088/0034-4885/47/10/001. 52

Kenro Miyamoto. *Plasma Physics and Controlled Nuclear Fusion*. Springer-Verlag Berlin Heidelberg, 2005. ISBN 978-3-540-28097-2v. doi: 10.1007/3-540-28097-9. URL https://www.springer.com/gp/book/9783540242178. 6, 7, 9

Jan Mlynar. Focus on: Jet, 2007. 11

R Monk. *Controlled Fusion and Plasma Physics*, 21A(1):117, 1997. 329

S. Mordijck. Overview of density pedestal structure: role of fueling versus transport. *Nuclear Fusion*, 60(8):082006, jul 2020. doi: 10.1088/1741-4326/ab8d04. URL https://dx.doi.org/10.1088/1741-4326/ab8d04. 174, 175, 176

D K Morozov and J J Herrera. Slow thermal waves in impurity seeded radiative plasmas. *Physical review letters*, 76:760–763, 1 1996. ISSN 1079-7114 (Electronic). doi: 10.1103/PhysRevLett.76.760. 325

A.L. Moser, A.W. Leonard, A.G. McLean, H.Q. Wang, and J.G. Watkins. The effect of divertor closure on detachment onset in diii-d. *Nuclear Materials and Energy*, 19:67–71, 2019. ISSN 2352-1791. doi: https://doi.org/10.1016/j.nme.2019.01.017. URL https://www.sciencedirect.com/science/article/pii/S2352179118302576. 173

T Nakano, N Asakura, H Takenaga, H Kubo, Y Miura, K Shimizu, S Konoshima, K Masaki, S Higashijima, and the JT-60Team. Impact of wall saturation on particle control in long and high-power-heated discharges in {JT}-60u. *Nuclear Fusion*, 46: 626–634, 4 2006. doi: 10.1088/0029-5515/46/5/013. URL https://doi.org/10.1088%2F0029-5515%2F46%2F5%2F013. 324

R Nave. Hydrogen energies and spectrum, 2005. URL http://hyperphysics.phy-astr.gsu.edu/hbase/hyde.html. 57

A V Nedospasov. Turbulence near the wall in tokamaks. *Fizika Plazmy*, 15:1139–1142, 1989. ISSN 0367-2921. URL http://inis.iaea.org/search/search.aspx?orig_q=RN:21048084. 324

J Neuhauser, W Schneider, and R Wunderlich. Thermal instabilities and poloidal asymmetries in the tokamak edge plasma. *Nuclear Fusion*, 26:1679–1692, 12 1986. doi: 10.1088/0029-5515/26/12/009. URL https://doi.org/10.1088%2F0029-5515%2F26%2F12%2F009. 322

M Ntampaka, H Trac, J Cisewski, al, Jubee Sohn, H Jabran Zahid, Margaret J Geller, A B Kukushkin, A S Kukushkin, V S Lisitsa, V S Neverov, A A Pshenov, and V A Shurygin. Ballistic model of recycling of atomic and molecular hydrogen and its application to the iter main chamber. *Plasma Physics and Controlled Fusion*, 63:035025, 1 2021. ISSN 0741-3335. doi: 10.1088/1361-6587/ABD97F. URL https://iopscience.iop.org/article/10.1088/1361-6587/abd97fhttps://iopscience.iop.org/article/10.1088/1361-6587/abd97f/meta. 126

J. Nührenberg and R. Zille. Stable stellarators with medium and aspect ratio. *Physics Letters A*, 114(3):129–132, 1986. ISSN 0375-9601. doi: https://doi.org/10.1016/0375-9601(86)90539-6. URL https://www.sciencedirect.com/science/article/pii/0375960186905396. 13

University of Edinburgh. Hydrogen and deuterium spectroscopy, 2020. URL https://www2.ph.ed.ac.uk/~mim/spectroscopy_poster2.pdf. 57

J Ongena, R Koch, R Wolf, and H Zohm. Magnetic-confinement fusion. *Nature Physics*, 12:398–410, 2016. ISSN 1745-2481. 13

A Yu Pigarov, S I Krasheninnikov, E M Hollmann, and T D Rognlien. Modeling of small-sized elms in detached divertor plasmas. *Contributions to Plasma Physics*, 56:742–747, 2016. ISSN 0863-1042. 325

C S Pitcher and P C Stangeby. Experimental divertor physics. *Plasma Physics and Controlled Fusion*, 39:779–930, 6 1997. doi: 10.1088/0741-3335/39/6/001. URL https://doi.org/10.1088%2F0741-3335%2F39%2F6%2F001. 65, 125

C. S. Pitcher, C. J. Boswell, J. A. Goetz, B. LaBombard, B. Lipschultz, J. E. Rice, and J. L. Terry. The effect of divertor baffling on Alcator C-Mod discharges. *Physics of Plasmas*, 7(5):1894–1903, 05 2000. ISSN 1070-664X. doi: 10.1063/1.874013. URL https://doi.org/10.1063/1.874013. 76, 82, 83

C.S. Pitcher, C.J. Boswell, T. Chung, J.A. Goetz, B. LaBombard, B. Lipschultz, J.E. Rice, D.P. Stotler, and J.L. Terry. The effect of baffling on divertor leakage in alcator c-mod. *Journal of Nuclear Materials*, 290-293:812–819, 2001. ISSN 0022-3115. doi: https://doi.org/10.1016/S0022-3115(00)00537-7. URL https://www.sciencedirect.com/science/article/pii/S0022311500005377. 14th Int. Conf. on Plasma-Surface Interactions in Controlled Fusion D evices. 78, 82

R Pitts. *IAEA-CN-77/EXP4/23*, 2000. 328

RA Pitts, A Kukushkin, A Loarte, A Martin, M Merola, CE Kessel, V Komarov, and M Shimada. Status and physics basis of the iter divertor. *Physica Scripta*, 2009 (T138):014001, 2009. 85

Richard Pitts, Richard Buttery, and Simon Pinches. Fusion: the way ahead, 2006. URL https://physicsworld.com/a/fusion-the-way-ahead/. 9, 11

Richard A. Pitts. Tokamak edge physics and plasma - surface interactions. 2007. 35, 37, 41

D. M. Ponce-Marquez, B. D. Bray, T. M. Deterly, C. Liu, and D. Eldon. Thomson scattering diagnostic upgrade on DIII-Da). *Review of Scientific Instruments*, 81 (10):10D525, 10 2010. ISSN 0034-6748. doi: 10.1063/1.3495759. URL `https://doi.org/10.1063/1.3495759`. 99, 101

Richard F Post. Controlled fusion research—an application of the physics of high temperature plasmas. *Rev. Mod. Phys.*, 28:338–362, 7 1956. doi: 10.1103/RevModPhys.28.338. URL `https://link.aps.org/doi/10.1103/RevModPhys.28.338`. 13

JET Team (prepared by R.D. Monk). Recent results from divertor and scrape-off layer studies at jet. *Nuclear Fusion*, 39(11Y):1751, nov 1999. doi: 10.1088/0029-5515/39/11Y/315. URL `https://dx.doi.org/10.1088/0029-5515/39/11Y/315`. 76, 78, 80, 81, 82

R Preuss and U von Toussaint. Gaussian processes for solps data emulation. *Fusion Science and Technology*, 69(3):605–610, 2016. 86

W Andrew Pruett and Robert L Hester. The creation of surrogate models for fast estimation of complex model outcomes. *PloS one*, 11(6):e0156574, 2016. 86

J Rapp, W Fundamenski, L C Ingesson, S Jachmich, A Huber, G F Matthews, P Morgan, and M F Stamp. Septum assessment of the jet gas box divertor. *Plasma Physics and Controlled Fusion*, 50:95015, 2008. ISSN 0741-3335. doi: 10.1088/0741-3335/50/9/095015. URL `http://dx.doi.org/10.1088/0741-3335/50/9/095015`. 65, 126

D Reiter, H Kever, GH Wolf, Martine Baelmans, R Behrisch, and R Schneider. Helium removal from tokamaks. *Plasma Physics and Controlled Fusion*, 33(13):1579, 1991. 85

Detlev Reiter, Martine Baelmans, and Petra Boerner. The eirene and b2-eirene codes. *Fusion science and technology*, 47(2):172–186, 2005. 86, 90, 91, 92

H. Renner, J. Boscary, H. Greuner, H. Grote, F. W. Hoffmann, J. Kisslinger, E. Strumberger, and B. Mendelevitch. Divertor concept for the w7-x stellarator and mode of operation. *Plasma Phys. Control. Fusion*, 44:1005, 2002. ISSN 07413335. doi: 10.1088/0741-3335/44/6/325. 126

Paolo Ricci. Simulation of the scrape-off layer region of tokamak devices. *Journal of Plasma Physics*, 81(2):435810202, 2015. 84, 85

Fitzpatrick Richard. Thomson scattering, 2014. URL `https://farside.ph.utexas.edu/teaching/jk1/lectures/node107.html`. 99

TD Rognlien, PN Brown, RB Campbell, TB Kaiser, DA Knoll, PR McHugh, GD Porter, ME Rensink, and GR Smith. 2-d fluid transport simulations of gaseous/radiative divertors. *Contributions to plasma physics*, 34(2-3):362–367, 1994. 85

William Rosen. *The Most Powerful Idea in the World: A Story of Steam, Industry, and Invention*. 2010. URL `https://books.google.com/books/about/The_Most_Powerful_Idea_in_the_World.html?id=-TStyXy7F6oC&printsec=frontcover&source=kp_read_button#v=onepage&q&f=false`. 3

D. L. Rudakov, J. A. Boedo, R. A. Moyer, P. C. Stangeby, J. G. Watkins, D. G. Whyte, L. Zeng, N. H. Brooks, R. P. Doerner, T. E. Evans, M. E. Fenstermacher, M. Groth, E. M. Hollmann, S. I. Krasheninnikov, C. J. Lasnier, A. W. Leonard, M. A. Mahdavi, G. R. McKee, A. G. McLean, A. Yu Pigarov, W. R. Wampler, G. Wang, W. P. West, and C. P.C. Wong. Far sol transport and main wall plasma interaction in diii-d. *Nuclear Fusion*, 45:1589–1599, 12 2005. ISSN 00295515. doi: 10.1088/0029-5515/45/12/014. 27, 126, 322

David Neil Ruzic. *Electric Probes for Low Temperature Plasmas*. Number M-12 in AVS Monograph Series. American Vacuum Society, 1994. ISBN 9781563964206. 103, 104

D. D. Ryutov. Geometrical properties of a "snowflake" divertor. *Physics of Plasmas*, 14, 2007. ISSN 1070664X. doi: 10.1063/1.2738399. 23, 127

A Sakasai, H Takenaga, H Kubo, N Akino, S Higashijima, S Sakurai, H Tamai, K Itami, and N Asakura. Helium exhaust in divertor–closure configuration with w-shaped divertor of jt-60u. *Journal of nuclear materials*, 290:957–961, 2001. 65

Chaofeng Sang, H. Y. Guo, P. C. Stangeby, L. L. Lao, and T. S. Taylor. Solps analysis of neutral baffling for the design of a new diverter in diii-d. *Nucl. Fusion*, 57:56043, 4 2017. ISSN 17414326. doi: 10.1088/1741-4326/aa6548. 126

R Schneider, D Reiter, HP Zehrfeld, B Braams, Martine Baelmans, J Geiger, H Kastelewicz, J Neuhauser, and R Wunderlich. B2-eirene simulation of asdex and asdex-upgrade scrape-off layer plasmas. *Journal of nuclear materials*, 196: 810–815, 1992. 85

R. Schneider, H. S. Bosch, J. Neuhauser, D. Coster, K. Lackner, and M. Kaufmann. Divertor geometry optimization for asdex upgrade. *J. Nucl. Mater.*, 241:701, 2 1997. ISSN 00223115. doi: 10.1016/s0022-3115(97)80125-0. 126

R Schneider, H.-S Bosch, D Coster, J.C Fuchs, J Gafert, G Haas, A Herrmann, M Kaufmann, A Kallenbach, J Neuhauser, J Schweinzer, U Wenzel, and ASDEX Upgrade Teams. Role of divertor geometry on detachment in asdex upgrade. *Journal of Nuclear Materials*, 266-269:175–181, 1999. ISSN 0022-3115. doi: https://doi.org/10.1016/S0022-3115(98)00524-8. URL `https://www.sciencedirect.com/science/article/pii/S0022311598005248`. 327

Debashree Sen. Nuclear energy vs fossil fuel, 2019. URL `https://sciencing.com/about-6134607-nuclear-energy-vs--fossil-fuel.html`. 5

J. H. Nichols J. D. Elder J. D. Duran P. C. Stangeby D. C. Donovan D. L. Rudakov A. Wingen Shawn Zamperini, T. Abrams and C. Crowe. Separatrix-to-wall simulations of impurity transport with a fully three-dimensional wall in diii-d. *Fusion Science and Technology*, 79(1):36–45, 2023. doi: 10.1080/15361055.2022.2082791. URL https://doi.org/10.1080/15361055.2022.2082791. 97

K Shimizu, T Takizuka, S Sakurai, H Tamai, H Takenaga, H Kubo, and Y Miura. Simulation of divertor detachment characteristics in jt-60 with superconducting coils. *Journal of nuclear materials*, 313:1277–1281, 2003. 85

R Simonini, G Corrigan, G Radford, J Spence, and A Taroni. Models and numerics in the multi-fluid 2-d edge plasma code edge2d/u. *Contributions to Plasma Physics*, 34(2-3):368–373, 1994. 85

W M Solomon, P B Snyder, K H Burrell, M E Fenstermacher, A M Garofalo, B A Grierson, A Loarte, G R McKee, R Nazikian, and T H Osborne. Access to a new plasma edge state with high density and pressures using the quiescent h mode. *Phys. Rev. Lett.*, 113:135001, 9 2014. doi: 10.1103/PhysRevLett.113.135001. URL https://link.aps.org/doi/10.1103/PhysRevLett.113.135001. 16

A C Sontag, X Chen, J Canik, A Leonard, J D Lore, A L Moser, M Murakami, J M Park, and C Petty. Sol effects on the pedestal structure in diii-d discharges. *Nuclear Fusion*, 57:76025, 5 2017. doi: 10.1088/1741-4326/aa6cb6. URL https://doi.org/10.1088/1741-4326/aa6cb6. 66, 126, 173

Jr. Spitzer, Lyman. The Stellarator Concept. *The Physics of Fluids*, 1(4):253–264, 07 1958. ISSN 0031-9171. doi: 10.1063/1.1705883. URL https://doi.org/10.1063/1.1705883. 19

P. C. Stangeby. Can detached divertor plasmas be explained as self-sustained gas targets? *Nucl. Fusion*, 33:1695, 1993. ISSN 00295515. doi: 10.1088/0029-5515/33/11/i10. 319

P C Stangeby. *The Plasma Boundary of Magnetic Fusion Devices*. Taylor Francis, 2000. ISBN 9780750305594. URL https://books.google.com/books?id=qOliQgAACAAJ. 14, 19, 25, 26, 27, 28, 29, 30, 31, 32, 33, 34, 36, 38, 40, 44, 45, 64, 70, 74, 92, 93, 94, 97, 126

P C Stangeby. Modeling plasma contact with the main vessel walls of a divertor tokamak. *Physics of Plasmas*, 9:3489–3507, 7 2002. ISSN 1070-664X. doi: 10.1063/1.1493207. URL https://doi.org/10.1063/1.1493207. doi: 10.1063/1.1493207. 114, 126

P C Stangeby and C Farrell. The plasma contamination efficiency of different impurity generation mechanisms in limiter tokamaks. *Plasma Physics and Controlled Fusion*, 32(9):677, sep 1990. doi: 10.1088/0741-3335/32/9/001. URL https://dx.doi.org/10.1088/0741-3335/32/9/001. 97

P.C. Stangeby and J.D. Elder. Calculation of observable quantities using a divertor impurity interpretive code, divimp. *Journal of Nuclear Materials*, 196-198:258–263, 1992. ISSN 0022-3115. doi: https://doi.org/10.1016/S0022-3115(06)80042-5. URL https://www.sciencedirect.com/science/article/pii/S0022311506800425. Plasma-Surface Interactions in Controlled Fusion Devices. 97

P.C. Stangeby and J.D. Elder. Impurity retention by divertors. i. one dimensional models. *Nuclear Fusion*, 35(11):1391, nov 1995. doi: 10.1088/0029-5515/35/11/I06. URL https://dx.doi.org/10.1088/0029-5515/35/11/I06. 97

P.C. Stangeby, C. Farrell, S. Hoskins, and L. Wood. Monte carlo modelling of impurity ion transport for a limiter source/sink. *Nuclear Fusion*, 28(11):1945, nov 1988. doi: 10.1088/0029-5515/28/11/003. URL https://dx.doi.org/10.1088/0029-5515/28/11/003. 97

P.C. Stangeby, J.D. Elder, W. Fundamenski, A. Loarte, L.D. Horton, R. Simonini, A. Taroni, O.F. Matthews, and R.D. Monk. Code-code comparisons of divimp's 'onion-skin model' and the edge2d fluid code. *Journal of Nuclear Materials*, 241-243:358–362, 1997. ISSN 0022-3115. doi: https://doi.org/10.1016/S0022-3115(97)80064-5. URL https://www.sciencedirect.com/science/article/pii/S0022311597800645. 97

P.C. Stangeby, J.D. Elder, J.A. Boedo, B. Bray, N.H. Brooks, M.E. Fenstermacher, M. Groth, R.C. Isler, L.L. Lao, S. Lisgo, G.D. Porter, D. Reiter, D.L. Rudakov, J.G. Watkins, W.P. West, and D.G. Whyte. Interpretive modeling of simple-as-possible-plasma discharges on diii-d using the oedge code. *Journal of Nuclear Materials*, 313-316:883–887, 2003. ISSN 0022-3115. doi: https://doi.org/10.1016/S0022-3115(02)01470-8. URL https://www.sciencedirect.com/science/article/pii/S0022311502014708. Plasma-Surface Interactions in Controlled Fusion Devices 15. 97

E. Stefanikova, L. Frassinetti, S. Saarelma, A. Loarte, I. Nunes, L. Garzotti, P. Lomas, F. Rimini, P. Drewelow, U. Kruezi, B. Lomanowski, E. de la Luna, L. Meneses, M. Peterka, B. Viola, C. Giroud, C. Maggi, and JET contributors. Effect of the relative shift between the electron density and temperature pedestal position on the pedestal stability in jet-ilw and comparison with jet-c. *Nuclear Fusion*, 58(5): 056010, mar 2018. doi: 10.1088/1741-4326/aab216. URL https://dx.doi.org/10.1088/1741-4326/aab216. 173

D P Stotler, J Lang, C S Chang, R M Churchill, and S Ku. Neutral recycling effects on itg turbulence. *Nuclear Fusion*, 57:86028, 7 2017. doi: 10.1088/1741-4326/aa7807. URL https://doi.org/10.1088%2F1741-4326%2Faa7807. 43

Gang Sun and Shuyue Wang. A review of the artificial neural network surrogate modeling in aerodynamic design. *Proceedings of the Institution of Mechanical*

Engineers, Part G: Journal of Aerospace Engineering, 233(16):5863–5872, 2019. 86

H J Sun, E Wolfrum, T Eich, B Kurzan, S Potzel, and U Stroth. Study of near scrape-off layer ({SOL}) temperature and density gradient lengths with thomson scattering. *Plasma Physics and Controlled Fusion*, 57:125011, 11 2015. doi: 10.1088/0741-3335/57/12/125011. URL https://doi.org/10.1088%2F0741-3335%2F57%2F12%2F125011. 322

A Tanga, K H Behringer, A E Costley, M Brusati, B Denne, A Edwards, A Gibson, R D Gill, N Gottardi, R Granetz, P J Harbour, H Jäckel, M Keilhacker, E Lazzaro, M Malacarne, P D Morgan, P Noll, J O'Rourke, P E Stott, D R Summers, J A Tagle, and P R Thomas. Magnetic separatrix experiments in jet. *Nuclear Fusion*, 27:1877–1895, 1987. ISSN 0029-5515. doi: 10.1088/0029-5515/27/11/011. URL http://dx.doi.org/10.1088/0029-5515/27/11/011. 16

H.Y. Guo A.L. Moser M. Shafer T.H. Osborne, L. Casali. Comparison of h-mode pedestal characteristics in sas and open divertor configurations on diii-d. *46th EPS Conference on Plasma Physics*, 2019. URL http://ocs.ciemat.es/EPS2019PAP/pdf/P5.1035.pdf. 173

Christian Theiler. Basic investigation of turbulent structures and blobs of relevance for magnetic fusion plasmas. 12 2011. doi: 10.5075/epfl-thesis-5228. 14

M V Umansky, S I Krasheninnikov, B LaBombard, and J L Terry. Comments on particle and energy balance in the edge plasma of alcator c-mod. *Physics of Plasmas*, 5:3373–3376, 9 1998. ISSN 1070-664X. doi: 10.1063/1.873051. URL https://doi.org/10.1063/1.873051. doi: 10.1063/1.873051. 322

Ezekial A. Unterberg, Edward W. Garren, Kirtan M. Davda, Anton L. Neff, Holly R. Ray, and Dan T. Fehling. The filterscope: A technical guide user's manual, 2019. URL https://www.osti.gov/biblio/1615788-filterscope-technical-guide-users-manual. 104, 105, 122

Bogdan Vacaliuc, William Andrews, Dan Fehling, E A Unterberg, Dwight Clayton, and Don Hillis. A new generation filterscope for remote visualization and analysis of high temperature plasma. pages 1–5, 2005. 105

Karel Lucas van de Plassche, Jonathan Citrin, Clarisse Bourdelle, Yann Camenen, Francis J Casson, Victor I Dagnelie, Federico Felici, Aaron Ho, Simon Van Mulders, and JET Contributors. Fast modeling of turbulent transport in fusion plasmas using neural networks. *Physics of Plasmas*, 27(2), 2020. 86

G C Vlases. A review of progress towards a next step divertor. *Plasma Physics and Controlled Fusion*, 35(SB):B67, dec 1993. doi: 10.1088/0741-3335/35/SB/005. URL https://dx.doi.org/10.1088/0741-3335/35/SB/005. 327

F Wagner. *Plasma Phys. Control. Nucl. Fusion Res.*, 1:277, 1991. 80

F Wagner, G Becker, K Behringer, D Campbell, A Eberhagen, W Engelhardt, G Fussmann, O Gehre, J Gernhardt, G v. Gierke, G Haas, M Huang, F Karger, M Keilhacker, O Klüber, M Kornherr, K Lackner, G Lisitano, G G Lister, H M Mayer, D Meisel, E R Müller, H Murmann, H Niedermeyer, W Poschenrieder, H Rapp, H Röhr, F Schneider, G Siller, E Speth, A Stäbler, K H Steuer, G Venus, O Vollmer, and Z Yü. Regime of improved confinement and high beta in neutral-beam-heated divertor discharges of the asdex tokamak. *Phys. Rev. Lett.*, 49:1408–1412, 11 1982. doi: 10.1103/PhysRevLett.49.1408. URL https://link.aps.org/doi/10.1103/PhysRevLett.49.1408. 16

H.Q. Wang, H.Y. Guo, A.W. Leonard, A.L. Moser, T.H. Osborne, P.B. Snyder, E. Belli, R.J. Groebner, D.M. Thomas, J.G. Watkins, Z. Yan, and the DIII-D group.

Effects of divertor geometry on h-mode pedestal structure in attached and detached plasmas in the diii-d tokamak. *Nuclear Fusion*, 58(9):096014, jul 2018. doi: 10.1088/1741-4326/aacbde. URL https://dx.doi.org/10.1088/1741-4326/aacbde. 173

Stanislaw Weglarczyk. Kernel density estimation and its application. *ITM Web Conf.*, 23:00037, 2018. doi: 10.1051/itmconf/20182300037. URL https://doi.org/10.1051/itmconf/20182300037. 162, 163

John Wesson. *Tokamaks*. Oxford University Press, 4 edition, 2011. ISBN 9780199592234. URL https://global.oup.com/academic/product/tokamaks-9780199592234?cc=us&lang=en&#. 9

D G Whyte, B L Lipschultz, P C Stangeby, J Boedo, D L Rudakov, J G Watkins, and W P West. The magnitude of plasma flux to the main-wall in the diii-d tokamak. *Plasma Physics and Controlled Fusion*, 47:1579–1607, 9 2005. doi: 10.1088/0741-3335/47/10/002. URL https://doi.org/10.1088%2F0741-3335%2F47%2F10%2F002. 114, 115, 119, 120, 122, 125, 126, 168, 169, 171, 193

S Wiesen, W Fundamenski, M Wischmeier, M Groth, S Brezinsek, and V Naulin. Relevance of collisionality in the transport model assumptions for divertor detachment multi-fluid modelling on jet. *Journal of Nuclear Materials*, 415: S535–S539, 2011. ISSN 0022-3115. doi: https://doi.org/10.1016/j.jnucmat.2010.12.010. URL http://www.sciencedirect.com/science/article/pii/S0022311510008287. 322

Sam Wurzel. Measuring progress in fusion energy: The triple product, 2019. URL https://www.fusionenergybase.com/article/measuring-progress-in-fusion-energy-the-triple-product/#fn-3. 9

Samuel E. Wurzel and Scott C. Hsu. Progress toward fusion energy breakeven and gain as measured against the Lawson criterion. *Physics of Plasmas*, 29(6):062103,

06 2022. ISSN 1070-664X. doi: 10.1063/5.0083990. URL https://doi.org/10.1063/5.0083990. 10, 11

AP Wynn. Investigations of radial transport in the scrape-off layer of jet-ilw. 8 2017. URL https://etheses.whiterose.ac.uk/19970/13/A_Wynn_Thesis_Final.pdf. 12, 169

S.A. Zamperini, J.D. Elder, P.C. Stangeby, J.H. Nichols, D.C. Donovan, J.D. Duran, E.A. Unterberg, and D.L. Rudakov. Reproduction of collector probe deposition profiles using the far-sol impurity transport code 3dlim. *Nuclear Materials and Energy*, 25:100811, 2020. ISSN 2352-1791. doi: https://doi.org/10.1016/j.nme.2020.100811. URL https://www.sciencedirect.com/science/article/pii/S2352179120300867. 97

S.A. Zamperini, J.H. Nichols, P.C. Stangeby, D.C. Donovan, J.D. Duran, J.D. Elder, E.A. Unterberg, and D.L. Rudakov. The role of bt-dependent flows on w accumulation at the edge of the confined plasma. *Nuclear Fusion*, 62(2):026037, jan 2022. doi: 10.1088/1741-4326/ac3fe7. URL https://dx.doi.org/10.1088/1741-4326/ac3fe7. 97

Yaoyu Zhang and Lai-Sang Young. Dnn-assisted statistical analysis of a model of local cortical circuits. *Scientific reports*, 10(1):20139, 2020. 86

Ben Zhu, Menglong Zhao, Harsh Bhatia, Xue-qiao Xu, Peer-Timo Bremer, William Meyer, Nami Li, and Thomas Rognlien. Data-driven model for divertor plasma detachment prediction. *Journal of Plasma Physics*, 88(5):895880504, 2022. 86

Sizheng Zhu and Xuejun Zha. Numerical predictions for the ht-7u divertor. *Journal of nuclear materials*, 313:1020–1024, 2003. 65

S J Zweben, J A Boedo, O Grulke, C Hidalgo, B LaBombard, R J Maqueda, P Scarin, and J L Terry. Edge turbulence measurements in toroidal fusion devices. *Plasma*

Physics and Controlled Fusion, 49:S1–S23, 6 2007. doi: 10.1088/0741-3335/49/7/s01. URL https://doi.org/10.1088%2F0741-3335%2F49%2F7%2Fs01. 322

Appendix

Appendix A

Comprehensive Analysis of the Filterscope Diagnostic Tool

A.1 Hardware Overview

As mentioned before, the Filterscope is divided into three main parts: Fiber, Filter and PMT. A detailed schematic, seen in Figure A.1, shows the radiation from the plasma source that is collected by collection optics (labeled as CO – detailed schematic found in Figure A.2 (C)) and is transferred towards the narrow bandpass filter through an optical fiber (Label 1). This light is then split by Beam Splitters (BS) and filtered through a narrow bandpass filter (Label 2 and 3) to get to the PMT (Label 4). The PMT converts the incoming light to photoelectron current which is then converted into voltage signal and amplified by an op-amp (Label 5) and is acquired by Data Acquisition and Control (DAQC) (Label 6) that is then stored on the DIII-D server available to all facility users (Ezekial A. Unterberg et al. 2019).

In DIII-D, the Filterscope system has line of sights that cover the lower divertor, upper divertor, SAS and the midplane system with a total of 96 channels ready to acquire data. The Upper divertor has 8 line of sights, the lower divertor has 9 line of sights, the SAS divertor has 4 line of sights, the midplane has 8 line of sights and

one line of sight goes poloidally across the DIII-D tokamak. The line of sights for Filterscope covering upper, lower and midplane locations are seen in Figure 2.28. All these lines of sights are beam slitted and analyzed in the 96 channels Filterscope system. Midplane Filterscope light of sight (represented as 'red' dots in Figure 2.28) are more vividly depicted in Figure A.2. If a light from a calibrated light source (Figure A.2 (D)) is passed through the fiber optic cable (Figure A.2 (C)) it would get reflected and adjusted through the collimating optics mount that will let the light pass through the vacuum vessel and magnetic shielding to pass tangentially through the DIII-D vessel (Figure A.2 (A)) between 0^{o} and 90^{o} to be collected in the 'beam box' or the 'view-dump' (Figure A.2(B)). The view dump is created in a manner that would not reflect any light back and is embedded in the graphite wall tiles.

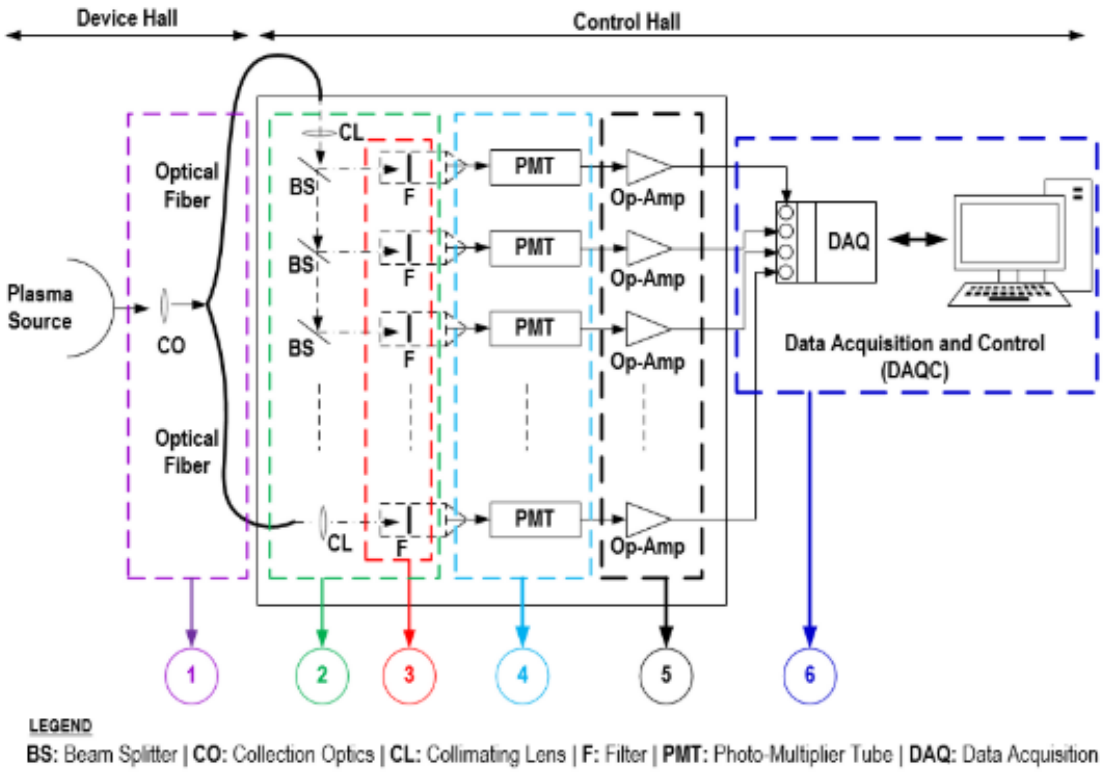


Figure A.1: A detailed schematic of the Filterscope system. Image from (Ezekial A. Unterberg et al. 2019)

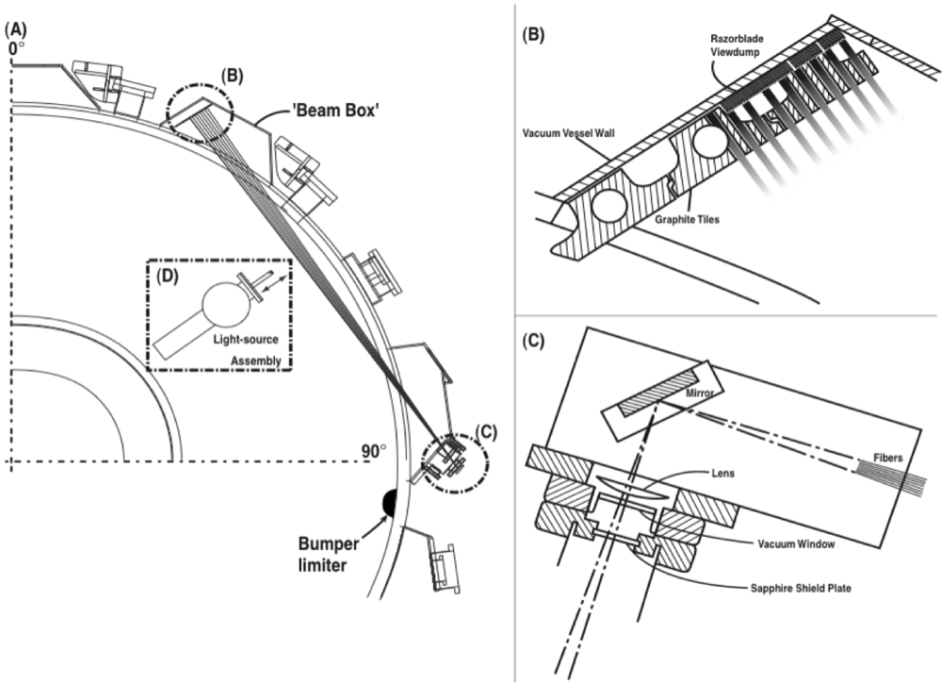


Figure A.2: (A) Schematic representation of the DIII-D tokamak from top view depicting the eight midplane Filterscope view chords poloidally across. (B) A detailed cartoon of the beam box where the line of sight terminates. The 'view dump' is embedded in the graphite tile and has a razorblade structure to avoid reflection. (C) The detailed schematic of the beam mount – the location that connects the DIII-D vessel to the diagnostic room. It consists of several lenses and mirrors that go across vacuum vessels and magnetic shielding. (D) A calibrated light source used. This portion is depicted as Label 1 in Figure A.1

A.2 Operating Principle

In order to understand the Filterscope calibration philosophy, we must understand its operating principle. Figure A.3 shows a detailed schematic of the Filterscope Electronics modules which does not include the Optic fiber and the narrow bandpass filter. The PMT module converts the incoming light from the light source (in our case DIII-D tokamak) and converts it to photoelectric current (I_k) that is produced by the photocathode due to the bombardment of photons on its surface. This current is then amplified through a series of electron multiplying dynodes to output the anode current (I_a). The ratio of the anode current to the photoelectric cathode current is termed as the PMT gain ($G_PMT = I_a/I_k$). The anode current is then passed on to the trans-impedance amplifier converting it into output voltage (V_{out}). This output voltage passed through non-inverting amplifier and other electronics also has an amplifier gain, called G_{amp}. Therefore, the total gain of the Filterscope system is termed as $G_{TOT} = G_{PMT}$ x G_{AMP}. The signal outputted from the amplifier electronics is termed as V_{PMT} (due to the fact that the voltage signal is outputted from the complete PMT module). Therefore, G_{AMP} can be defined as $G_{AMP} = V_{PMT}/V_{OUT}$ (Ezekial A. Unterberg et al. 2019; Neff et al. 2020).

As the digitizer registers voltage signals, we must relate the current from the PMT to voltages. Taking into consideration the Ampere's law, we can say, $I_a = V_{OUT}/R_f$, where R_f is the trans-impedance amplifier resistance and $I_k = V_{IN}/1_R$, where 1_R is the resistance across the first dynode and V_{IN} is the voltage generated across the first dynode resistor due to the anode current. Therefore, we can redefine $G_{PMT} = V_{OUT}/V_{IN}$ for a Filterscope channel and $G_{TOT} = V_{PMT}/V_{IN}$ where G_{AMP} is assumed to be equal to 1 (Ezekial A. Unterberg et al. 2019; Neff et al. 2020).

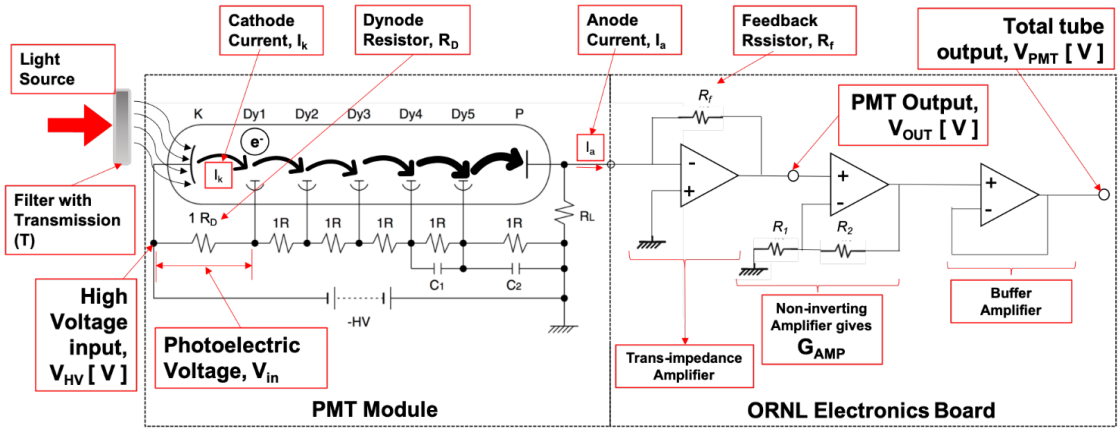


Figure A.3: Detailed schematic of the PMT module describing the operating principle of the Filterscope system. Image from (Ezekial A. Unterberg et al. 2019; Neff et al. 2020)

A.3 Determining the output of the Filterscope: Line Normalized Radiance

Filterscope, a radiometer, measures radiant power through the optical fiber cables over a particular bandpass filter range. This spectral power is different from a spectral information (that is related to a spectrometer). This spectral power, called line normalized radiance can be defined as

$$L_{A_{i\to k}} = 5.03 \times 10^{24} \lambda_{i\to k} \frac{\Delta\lambda_{i\to k}}{\Delta\lambda_{PN}} L_{PN} \left[\frac{\text{ph}}{\text{s-str-cm}^2}\right] \tag{A.1}$$

Where, $L_{A_{i\to k}}$ is the wavelength of interest, $\Delta\lambda_{i\to k}$ is the band pass of the line normalization, $\Delta\lambda_{PN}$ is the band pass of peak normalization, and 'L'_{PN} is the peak normalized radiance which can be defined as

$$L_{PN} = \left[\frac{V_{PMT}}{G_{TOT}}\right]_{\text{sig}} \frac{1}{R_{PN}(\lambda_{PN})} \tag{A.2}$$

Where, the $[V_{PMT}/G_{TOT}]_{sig}$ is the effective photo-electron current and is used to adjust sensitivity of the system. $R_{PN}\lambda_{PN}$ is the peak normalized responsivity and is defined in A.4.4.1.

A.4 Calibration Philosophy

$$R_{PN}(\lambda_{PN}) = \frac{V_{PMT-cal}}{G_{TOT-cal}} \cdot \frac{1}{L_{\text{filter-Total}}} \left[\frac{\text{Vm}^2\text{str}}{W}\right] \tag{A.3}$$

There are two types of calibrations performed on the Filterscope system: (1) Radiance response calibration and (2) Gain Calibration; in order to interpret the data from Filterscope. The radiance response calibration process takes into account the response of each PMT that is connected to an external calibrated light source with a known spectral radiance. This response can be calculated using peak normalized responsivity. It can be defined in equation A.3.

Where: R_{PN} is the peak normalized responsivity. λ_{PN} is the peak normalized wavelength of interest (for example, for D_α, $\lambda_{PN} = 656.1$nm). $V_{PMT-cal}$ is the output voltage of the channel during calibration, i.e., the output voltage of the PMT when it is attached to the calibrated light source (generally an integrating sphere). $G_{TOT-cal}$ is the total gain of the PMT during the calibration process. $L_{\text{filter-Total}}$ is the total integrated spectral radiance over λ_{PN}.

The filtered spectral radiance L_{filter} is related to the calibrated light source by its transmission fraction (which is generally provided by the manufacturer of the integrated light source). In order to determine L_{filter}, it is based on the transmission fraction of the filter and the spectral radiance of the calibrated light source over a wavelength of interest (as seen in Figure A.4(a)). Figure A.4(a) depicts the transmission curve of the filter along with the spectral radiance of the calibrated light source plotted against the wavelength. Integrating $L_{\text{filter}}(\lambda)$ over λ and pass filter would give $L_{\text{filter-Total}}$ as shown as the shaded region in Figure A.4(b).

As previously mentioned, the total gain of a PMT is given by:

$$G_{TOT} = G_{PMT} \cdot G_{AMP} \tag{A.4}$$

In general, it is assumed that G_{AMP} is linear and does not need calibrating, hence $G_{AMP} = 1$. On the other hand, G_{PMT} represents the current amplification in the PMT, i.e., it can be defined as:

$$G_{PMT} = \frac{I_a}{I_k} \propto \frac{V_{PMT}}{V_{PMT-min}} \tag{A.5}$$

Where, 'I_a' and 'I_k' are anode and cathode current, respectively, as shown in Figure A.3. Both 'I_a' and 'I_k' are non-linearly dependent on the gain setting of the Filterscope, i.e., the control voltage (V_{cont}). Each PMT is different and demonstrates different characteristics for G_{PMT}. Hence, in order to characterize it, a gain calibration step is needed to be done. Since it is complex in nature to determine 'I_a' and 'I_k', we can just compare it to the ratios of the PMT voltages as shown in

Equation A.5, where V_{PMT_min} is the output voltage at the lowest V_{cont} setting, i.e., $G_{PMT} = 1$. The gain calibration procedure, in a way, can be thought of as effectively matching the PMT and Filterscope electronics impedance.

The gain calibration process regulates all the PMTs in the Filterscope system at every gain setting (V_{cont} values) using a light source that encompasses a broad range of wavelengths. This natural log of the data is then fit with a polynomial that can be functionally written as:

$$G_{TOT} = e^{k} \tag{A.6}$$

Since $G_{AMP} = 1$, $G_{TOT} = G_{PMT}$. Where, $k = A_4 V_{cont}^4 + A_3 V_{cont}^3 + A_2 V_{cont}^2 + A_1 V_{cont} + A_0$.

This relationship can be plotted and best described as seen in Figure A.5. The natural log of V_{plot} with respect to the gain settings of the PMT is depicted with a fourth-order polynomial fit in Figure A.5(a). Here, $V_{plot} = \frac{V_{PMT}}{\text{Transmission}}$, where the transmission is defined as the amount of light transmitted onto the photocathode of the PMT from the light source. Figure A.5(b) depicts the relationship between V_{plot} vs. the gain setting of the PMT. Figure A.5(c) depicts the statistical goodness of fit using Median Percentage Error (MPE). MPE can be defined as:

$$(MPE) \approx \left| \frac{V_{\text{plot}_i} - e_i^{\ln(V_{\text{plot}})}}{V_{\text{plot}_i}} \right| \times 100\% \tag{A.7}$$

MPE is similar to MAPE (Mean Absolute Percentage Error), but instead of the mean, we use the median of the data to calculate the statistical goodness of fit. The fit with $(MPE) \leq 5\%$ is the fit that is selected for calibrating the Filterscope PMT. The fit can be a fourth-order fit or a 3rd-order fit, depending on the MPE value.

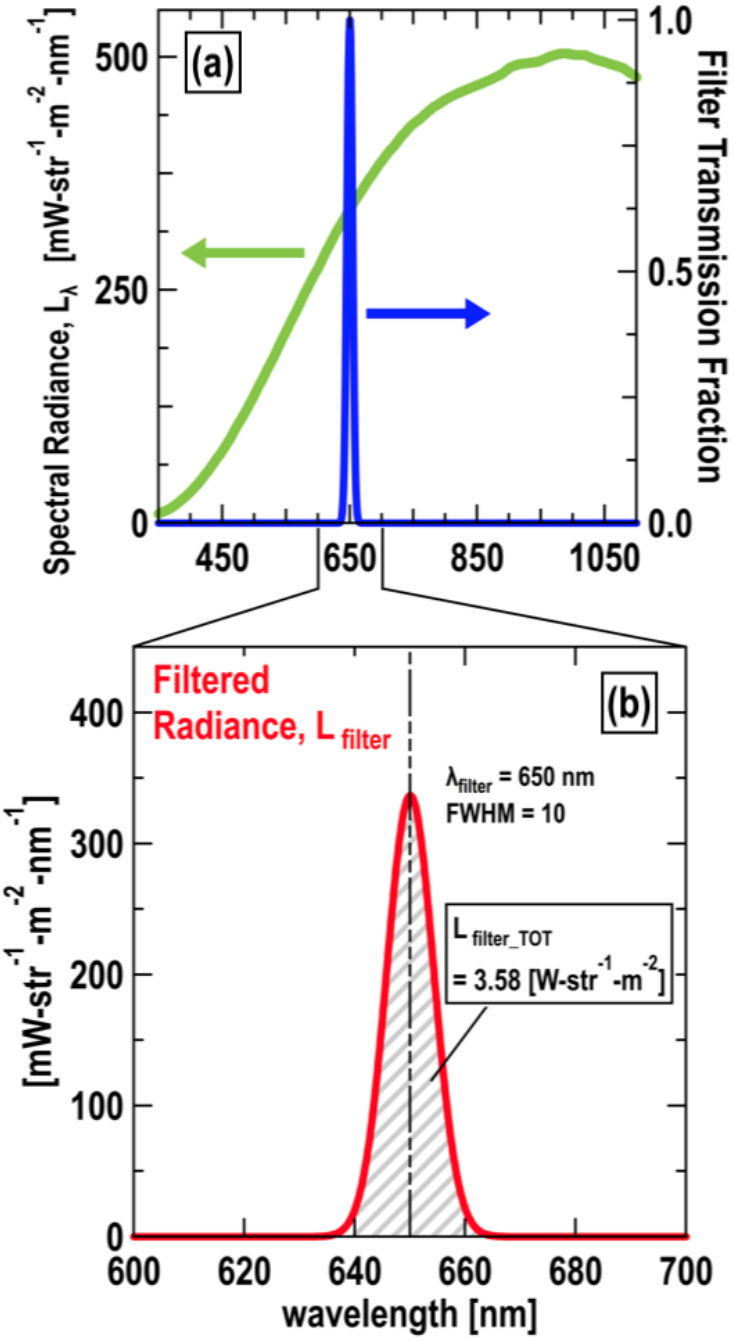


Figure A.4: (a) Filter transmission fraction along with the spectral radiance of the calibrated light source is plotted against the wavelength. (b). The area under the curve (shaded) gives the total spectral responsivity of the PMT for a wavelength of interest. Image from Manual Ezekial etc.

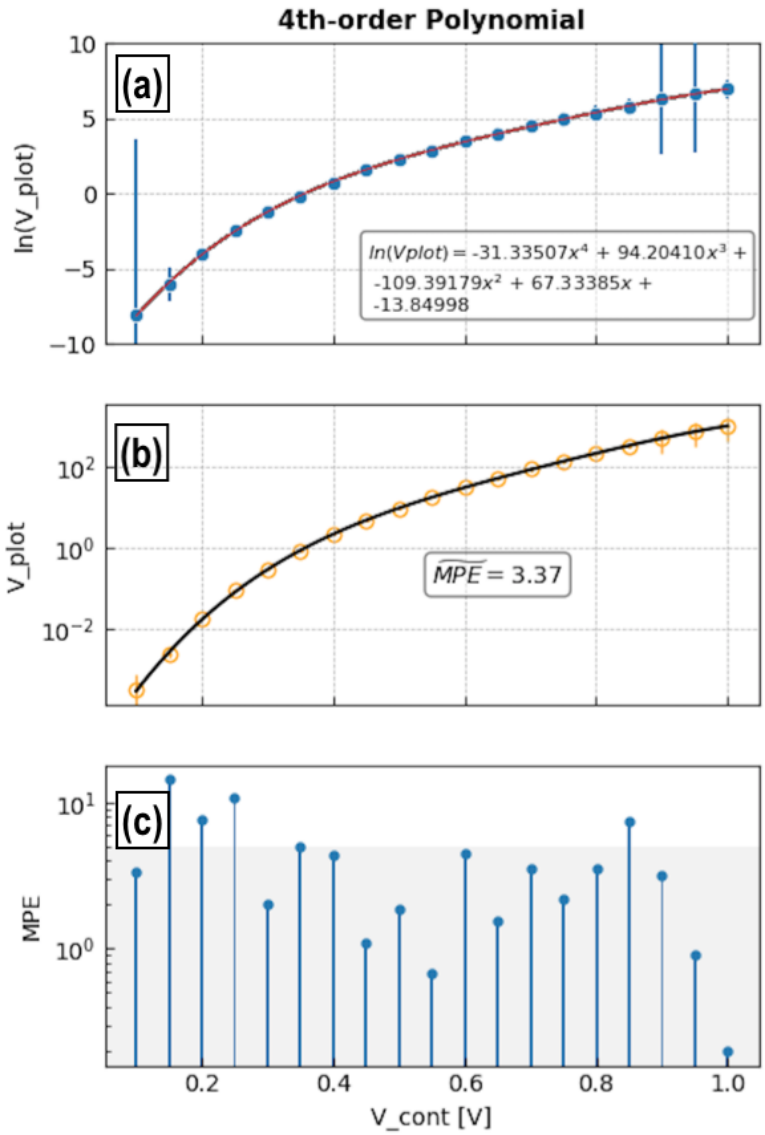


Figure A.5: Fourth order polynomial fit of G_{PMT} on a single PMT of the Filterscope system. Image from Manual Ezekial etc.

A.5 Introduction to Statistical Machine Learning for Estimating the Calibration coefficients

Statistical learning is defined as a set of approaches to estimate $f(x)$, which helps predict and infer the relationship between x and y, given as:

$$y = f(x) + \Sigma \tag{A.8}$$

Where: - x is termed as the input variable / variable / predictor / independent variable / feature. - y is termed as the output variable / response / dependent variable. - Σ is the error function, providing systematic information for x James et al. [2013].

Equation A.8 can be estimated using prediction and interference. In the prediction approach, when the value of x is given, the estimate of y is defined as $\hat{y} = \hat{f}(x)$, and the error function is zero. The error between the output variable and its estimate is given as James et al. [2013]:

$$E(Y - \hat{Y})^2 = [f(X) - \hat{f}(X)]^2 + \text{var}(\epsilon) \tag{A.9}$$

Where: - $\text{var}(\epsilon)$ is the variance of the error, also known as the irreducible error. - $f(X) - \hat{f}(X)$ is the reducible error, and the goal is to reduce the reducible error James et al. [2013].

There are two ways to find $\hat{f}(X)$, i.e., the estimate of $f(X)$: Parametric and Non-Parametric approaches. The parametric approach is a two-step process: Step 1 assumes the data fits a linear curve (for example: $k = \beta_0 + \beta_1 \ln(V_{cont})$), and Step 2 estimates parameters using the least square method. Figure A.6 shows a plot estimating the parameters using the parametric approach, where the parameters / gain calibration coefficients are $\beta_0 = 8.34$ and $\beta_1 = 7.19$. The disadvantage of this method is that the data can easily be overfitted/underfitted, and the estimate would not perfectly match the data set. Therefore, for more accurate estimation of the

parameters/gain calibration coefficients, we calculate the mean squared error (MSE). The smaller the MSE, the response is closer to a true response. MSE can be calculated by James et al. [2013]:

$$MSE = \frac{1}{n}\sum_{i=1}^{n}[y_i - \hat{f}(X_i)]^2 \tag{A.10}$$

As stated in Equation A.10 and as seen in Figure A.6, the term MPE is used in estimating the Filterscope gain calibration coefficients as it provides a more accurate estimate James et al. [2013].

Another way to estimate $f(x)$ is by linear regression. It predicts $\hat{Y}$ based on the estimation of the coefficients: $\hat{y} = (\hat{\beta}_0) + (\hat{\beta}_1)x$. In terms of the Filterscope gain calibration, the estimation can be written as: $k = (\hat{\beta}_0) + (\hat{\beta}_1)\ln(V_{cont})$. The estimation of error is also an important step, which can be done by $e_i = y_i - (\hat{y}_i)$. To find the coefficients, one must find the residual sum of squared (RSS) James et al. [2013]:

$$RSS = e_1^2 + e_2^2 + \ldots + e_n^2 \tag{A.11}$$

Where $e_i = y_i - (\hat{y}_i)$.

$$RSS = [k_1 - (\hat{\beta}_0) - (\hat{\beta}_1)\ln(V_{cont_0})]^2 + \ldots + [k_n - (\hat{\beta}_0) - (\hat{\beta}_1)\ln(V_{cont_n})]^2 \tag{A.12}$$

That gives us:

$$(\hat{\beta}_0) = \bar{k} - (\hat{\beta}_1)\ln(V_{cont}) \tag{A.13}$$

$$(\hat{\beta}_1) = \frac{\sum_{i=1}^{n}\left[(V_{cont_i} - \bar{V_{cont}})(k_i - \bar{k})\right]}{\sum_{i=1}^{n}\left(V_{cont_i} - \bar{V_{cont}}\right)^2} \tag{A.14}$$

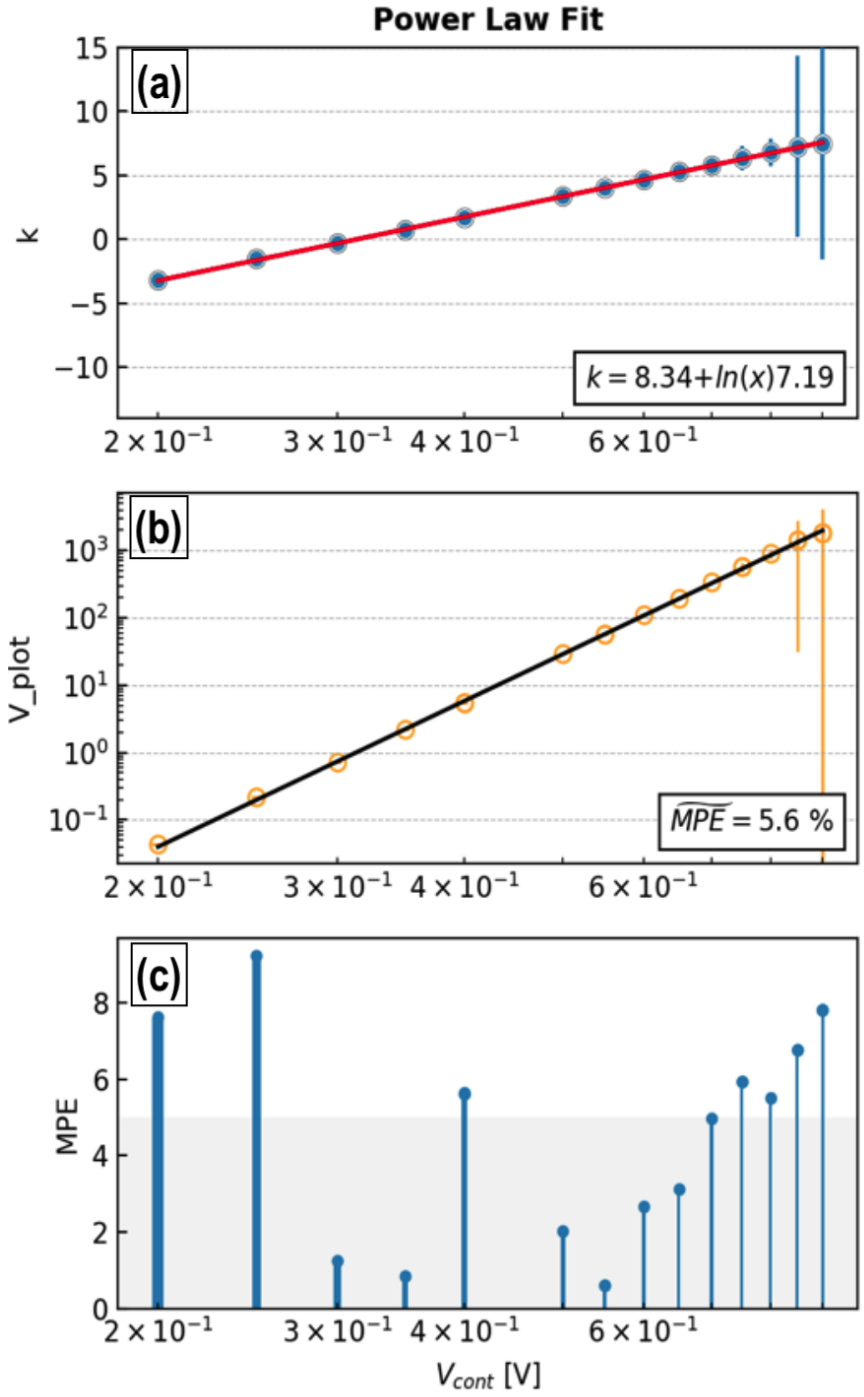


Figure A.6: Estimation of gain calibration coefficients using the parametric approach. Image from Manual Ezekial etc.

Equations A.13 and A.13 show how we estimate the gain calibration coefficients. To assess the accuracy of the estimate, we find the standard error of the mean (Equation A.15) and the coefficients (Equation A.16) James et al. [2013]:

$$\text{Var}(\mu) = \text{SE}(\mu) = \frac{\sigma^2}{n} \tag{A.15}$$

$$\text{SE}((\hat{\beta}_0)^2) = \sigma^2 \left[\frac{1}{n} + \frac{(\bar{V_{cont}})^2}{\sum_{i=1}^{n} \left(V_{cont_i} - \bar{V_{cont}}\right)^2} \right] \text{SE}((\hat{\beta}_1)^2) = \frac{\sigma^2}{\sum_{i=1}^{n} \left(V_{cont_i} - \bar{V_{cont}}\right)^2}$$

Where σ^2 is estimated using $RSE = \sqrt{RSS/(n-2)} = \sqrt{(e_1^2 + e_2^2 + \ldots + e_n^2)/(n-2)}$.

The estimation of the standard error can also be done using hypothesis testing, where two hypotheses are tested: null hypothesis (H_0) and non-null hypothesis (H_a). Recall the estimated output variable equation James et al. [2013]:

$$\hat{y} = (\hat{\beta}_0) + (\hat{\beta}_1)x \tag{A.16}$$

The hypothesis test suggests:

$H_0 : (\hat{\beta}_1) = 0$ and $H_a : (\hat{\beta}_1) \neq 0$

Where the hypothesis can be tested using a 't-test':

$$t = \frac{(\hat{\beta}_1) - 0}{\text{SE}((\hat{\beta}_1))} = \frac{(\hat{\beta}_1) - 0}{\sqrt{\sigma^2 / \sum_{i=1}^{n} (x_i - \bar{x})^2}} \tag{A.17}$$

Equation A.17 would provide an estimate using the p-value derived from the t-test and would reject the null hypothesis, meaning there is some relation between x and y. This relationship can be quantified using RSE, R^2, F-statistics. The RSE (Error of the root squared is the average amount which the y deviates from the true regression line. RSE measures the lack of fit and when RSE is small, $y_i \approx (\hat{y}_i)$. The R^2 statistics is independent of y, unlike the RSE, and measures the proportion of variability in y that can be explained using x. When R^2 approaches 1, there is large variability, and

when it approaches 0, it means that x does not explain y very well. R^2 can be defined as James et al. [2013]:

$$R^2 = \frac{\sum (y_i - \bar{y})^2 - \sum (y_i - (\hat{y}_i))^2}{\sum (y_i - \bar{y})^2} \tag{A.18}$$

Where $\sum (y_i - \bar{y})^2 = \text{TSS}$, the total sum squared that measures the variance in y.

Another way to estimate $f(x)$ is through multiple linear regression – a parametric way, which is given by:

$$\hat{y} = (\hat{\beta}_0) + (\hat{\beta}_1)x_1 + (\hat{\beta}_2)x_2 + \ldots + (\hat{\beta}_p)x_p \tag{A.19}$$

Where RSS for multiple linear regression can be defined as: $RSS = \sum (y_i - (\hat{y}_i))^2$. However, since the model we have (Equation A.16) fits perfectly with a linear regression, I will be skipping multiple linear regression notes here. Also, there are multiple factors that make multiple linear regression disadvantageous, such as non-linearity, correlation of error terms, non-constant variance of error terms, outliers, high-leverage points, and collinearity James et al. [2013].

Easy fitting and easy estimation of a few coefficients are the two strong points of linear regression with a parametric approach. However, a strong assumption is that the approach assumes the form of $f(x)$, which is not necessarily the same for all data points. This is when the non-parametric approach comes into play. One such non-parametric approach is called k-nearest neighbor (KNN) regression. KNN regression identifies 'k' training observations near a prediction point x_0 and is given as:

$$\hat{f}(x) = \frac{1}{k} \sum_{i=1}^{k} y_i \tag{A.20}$$

Where the optimal value for 'k' depends on a bias-variance tradeoff. Therefore, a lower value of 'k' leads to a more flexible fit, low bias, and high variance, while a higher value of 'k' results in a smoother fit with less variability. However, since the

form in Equation A.16 closely matches linear regression with a parametric approach, we will be neglecting the details about KNN regression here as well James et al. [2013].

As of now, linear regression with a parametric approach is shown above, which follows the least squares for the estimation of 'y'. However, for better prediction accuracy and model interpretability, we must move away from least square estimation. Table 6 shows why fitting anything other than least squares is important James et al. [2013].

There are three main alternatives to the least square estimate: (1) subset selection; (2) shrinkage; and (3) dimension reduction. Figure A.7 shows the different types of these alternatives. Out of the three, the shrinkage method is widely popular and often used. The shrinkage method comprises regression techniques such as Ridge, Lasso, and Huber. The backbone of the shrinkage method is to shrink the coefficient estimates towards 0, and as it reduces it, the variance of the estimate becomes lower. Just like the least squares, ridge regression estimates by minimizing the ridge coefficient:

$$RSS + \lambda \sum \beta^2 \tag{A.21}$$

Where λ is the tuning parameter, and the term $\sum \beta^2$ is known as the shrinkage penalty. The tuning parameter controls the relative impact of β. When $\lambda = 0$, the penalty has no effect, and ridge regression becomes the same as least squares. When λ approaches infinity, the penalty's effect increases, and β tends to move towards 0 James et al. [2013].

Ridge regression produces a different set of $\hat{\beta}^R$ for each λ, i.e., it shrinks β_1 only and does nothing to β_0. The major advantage of Ridge regression over least squares is rooted in the bias-variance trade-off. As λ increases, the flexibility of ridge regression decreases, i.e., if the variance is lower, bias becomes higher.

Table A.1: Description of model interpretability and model accuracy for using non-least squares estimates

Better Prediction Accuracy	Better Model Interpretability
- If x and y have a linear relationship; bias is low - $n \gg p$: least square fit has low variance - $n > p$: least square over fits and has high variance - $p > n$: least squares has no estimate, i.e., infinite variance and zero bias.	- Many variables in multiple linear regression are irrelevant. - But least square would not be able to do that. - We need to find an alternative way to minimize the estimate.

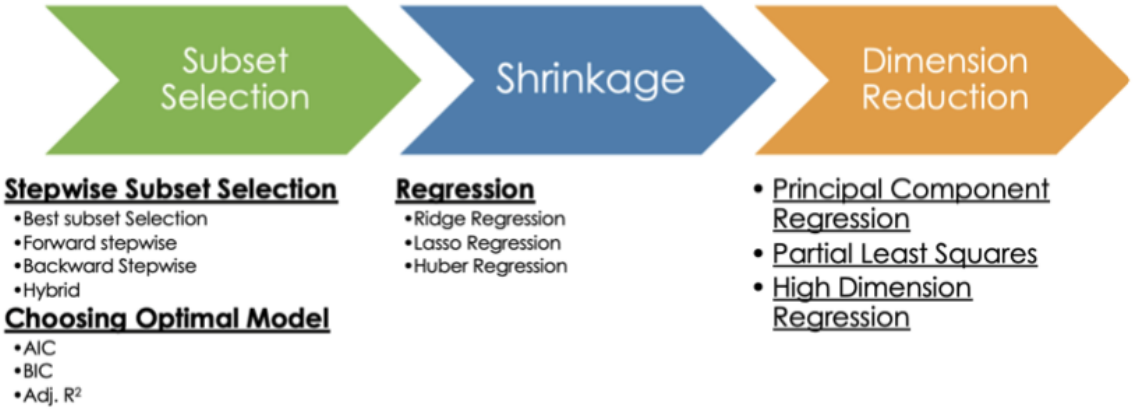


Figure A.7: Alternatives to least square Estimation

If 'x' and 'y' have a linear relationship, then fitting least squares will have low bias but might have high variance, which means that a small change in the training data would have a large change in β estimate. If $p \approx n$, the least square fit will be variable, and if $p > n$, the least square will have no unique solution. Therefore, Ridge regression is best to be done when least squares have high variance James et al. [2013].

Some disadvantages of ridge regression are: (1) The penalty shrinks all $\hat{\beta}^R$ to 0; (2) If $\lambda \neq \infty$, it will not shrink all $\hat{\beta}^R$ to 0; and (3) This is a problem for better prediction accuracy and can occur with a large 'p' - the number of variables. Hence, Lasso regression is used James et al. [2013]James et al. [2013]. Similar to Ridge regression, Lasso regression can be found by minimizing:

$$\text{RSS} + \lambda \sum_{j=1}^{p} |\beta_j| \tag{A.22}$$

Where, similar to ridge regression, 'λ' is the tuning parameter, and '$\sum_{j=1}^{p} |\beta_j|$' is the Lasso penalty. Lasso regression works by minimizing the Lasso coefficient ('$(\hat{\beta}_\lambda^L)$') to 0. Lasso will set some $(\hat{\beta}_\lambda^L)$ to 0 when λ is very high. It will perform variable selection so that the models are easily interpreted, and it will produce sparse models that will only involve a subset of variables James et al. [2013].

Appendix B

GRP Estimation Flow Chart

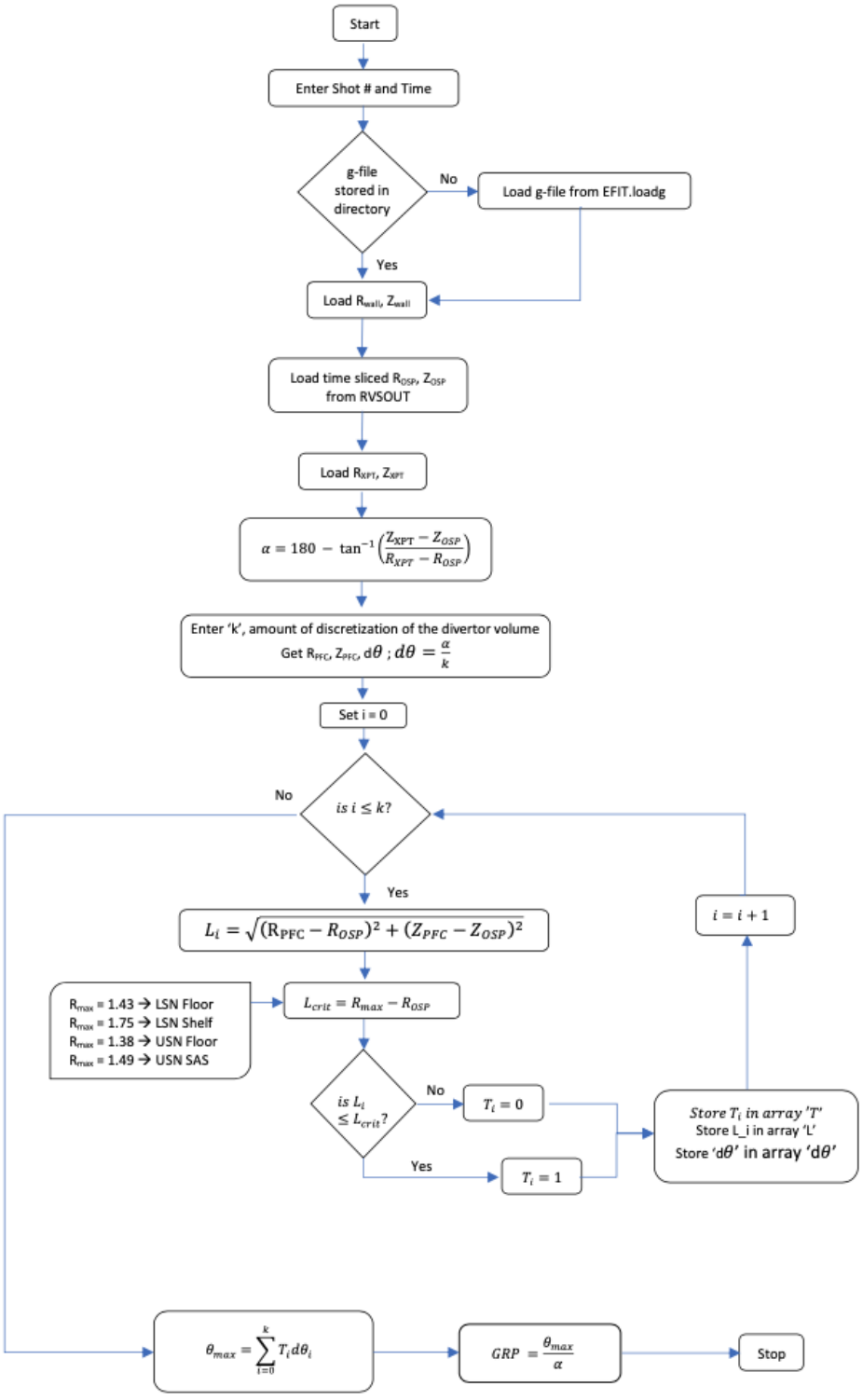


Figure B.1: A flowchart of GRP Estimation for divertor restriction

Appendix C

Details about running a successful OEDGE case

This chapter serves as a guide for readers seeking an introduction to the modeling world, particularly within the context of OEDGE. By delving into the intricacies of the IRIS framework (Section C.1), we provide a thorough exploration of the foundational steps required to establish an OEDGE workspace. This initial setup lays the groundwork for subsequent simulations and analyses, making it a crucial entry point for those venturing into the modeling domain. Building upon this foundation, we turn our attention to the creation of computational grids using the DG-Carre method, a pivotal aspect for precision in simulations (Section C.2). The subsequent sections then guide the reader through the step-by-step processes involved in extracting electron temperature (T_e) and electron density (n_e) profiles from Thomson Scattering using the OMFIT framework and Langmuir Probe measurements with Python, respectively. This comprehensive exploration aims to equip the reader with the essential knowledge and skills needed to navigate the modeling landscape, with a particular focus on leveraging OEDGE capabilities for plasma diagnostics and analysis.

C.1 Setting up OEDGE workspace in IRIS

Note: Please contact `fus@fusion.gat.com` to be added into the 'OEDGE' and 'SOLPS' working groups and to request access to ADAS database.

Step 1: Once you have been added to the working groups of 'OEDGE' and 'SOLPS', follow the steps provided below:

1. `cd /fusion/projects/codes/oedge`
2. `mkdir [iris username]`
3. `cd [iris username]`
4. `mkdir cases shots results data`
5. `cd /fusion/projects/codes/oedge/[iris username]`
6. `cp /fusion/projects/codes/oedge/zamperinis/rundiv_master.iris .`
7. `cp /fusion/projects/codes/oedge/zamperinis/rundiv.sh .`

The initial script functions as the primary shell script responsible for executing either OSM-EIRENE or DIVIMP. Given that iris employs a job scheduler for job submissions, akin to many clusters, a slurm script is required to submit tasks to the queue. This is the purpose of the second script.

Step 2: Once you have followed the steps prescribed above, you will have to change the following lines in the run scripts.

1. `geany rundiv_master.iris`
   (a) `PROGDIR=master`
   (b) `DATAROOT=/fusion/projects/codes/oedge/[iris username]`
   (c) `RUNROOT=/fusion/projects/codes/oedge/[iris username]`
   (d) `RESULTSROOT=/fusion/projects/codes/oedge/[iris username]`

2. `geany rundiv.sh`

    (a) `echo "srun ./rundiv_master.iris $1 $4 $2 $5 none $3" ≫ $1.sh`

Note: For more information, please visit the OEDGE guide website. This provides a great starting guide for OEDGE. This was created by S. Zamperini.

C.1.1 Configuration of the Bash profile

Having all the essential components for initiating a productive OEDGE run, we will systematically undertake a sequence of procedures to configure our bash profile. This configuration will enable the incorporation of shortcut commands, streamlining our workflow for increased efficiency. To access the bash profile in your workspace, utilize either '`emacs .bashrc`' or, if you favor the geany command, employ '`geany .bashrc`'.

1. `export OBJECTCODE="linux.pgf90"`
2. `export TOKAMAK="D3D"`
3. `export DGHOME="/fusion/projects/solps-results/[iris username]/dg-carre"`
4. `alias dghome='cd /fusion/projects/solps-results/[iris username]/dg-carre'`
5. `alias dg='/fusion/projects/solps-results/[iris username]/dg-carre/DivGeo/dg/linux.ifort64/dg'`
6. `alias e2d='/fusion/projects/solps-results/[iris username]/dg-carre/DG/equtrn/e2d'`
7. `alias dg2dg='/fusion/projects/solps-results/[iris username]/dg-carre/DG/equtrn/linux.pgf90/dg2dg'`

C.2 Creating a grid using DG - Carre

Meshes created from individual equilibrium files should be stored in a directory located within the $DGHOME/class directory. Launch IDL from the mesh creation folder, retrieve the g-file corresponding to a specific DIII-D shot and time slice, and subsequently exit the IDL environment. Convert the obtained g-file into a DG-compatible equilibrium file. To attain a satisfactory resolution for mesh generation, increase the resolution of the equilibrium file by doubling it three times.

Following are the steps to create a DG-Carre grid and mesh

1. `cd /fusion/projects/solps-results/[iris username]/dg-carre/class/examples/`
2. `mkdir d3d_[iris username]`
3. `cd d3d_[iris username]`
    - *Optional Note:* you can make another sub-folder with respect to divertor geometries, for example, USN, LSN Floor, SAS, etc.
4. `mkdir [shotnumber]_[time_slices]`
5. `cd [shotnumber]_[time_slices]`
6. `idl`
7. `writeg, [shotnumber], [time slice in ms]`
8. `exit`
9. `e2d [gfile] output.eq`
10. `dg2dg output.eq outputx2.eq`
11. `dg2dg outputx2.eq outputx4.eq`

12. `dg2dg outputx4.eq outputx8.eq`

13. `dg &`

Once you open the 'DG' gui, we can get to making a grid. Here are the thing you must do initially to setup your DG workspace

1. File ≫ import ≫ Template

    - The template should be stored at `fusion/projects/solps-results/[iris username]/dg-carre/DG/SAS_prototypeL1R2b_extmesh2.org`. See Figure C.1

2. Ctrl + P → to zoom into the template

3. Commands ≫ Convert ≫ Template to Elements (Make sure the surface normals are pointing outside

4. File ≫ import ≫ Equilibrium

    - This is where previously made 'outputx8.eq' comes into play. Once you have imported the equilibrium, you should see the DG GUI as seen in Figure C.2. Here LSN Shelf divertor configuration is taken for representative purposes.

5. File ≫ import ≫ Topology

    Note: Topology files are stored in the $DGHOME/DivGeo/dg/topologies directory. Select the correct topology. Keep the "Detect X Points" box checked.

    - SN = lower single null
    - SN-up = upper single null
    - CDN = connected double null
    - DDN = disconnected double null, lower primary X-point

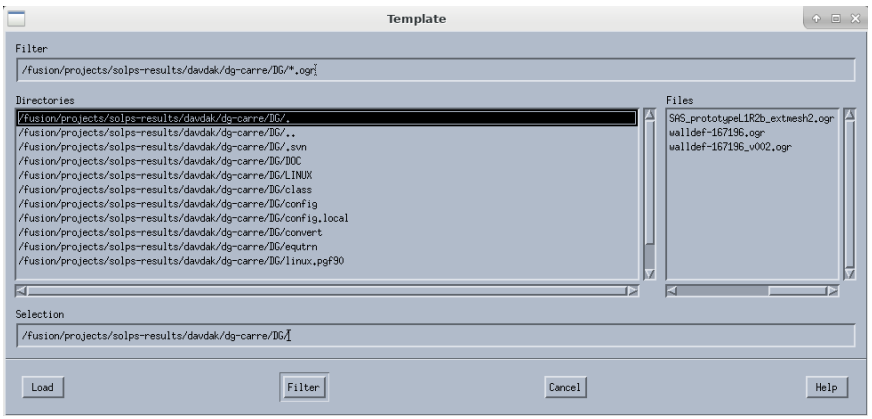


Figure C.1: Screen cap of DG system to grab Template

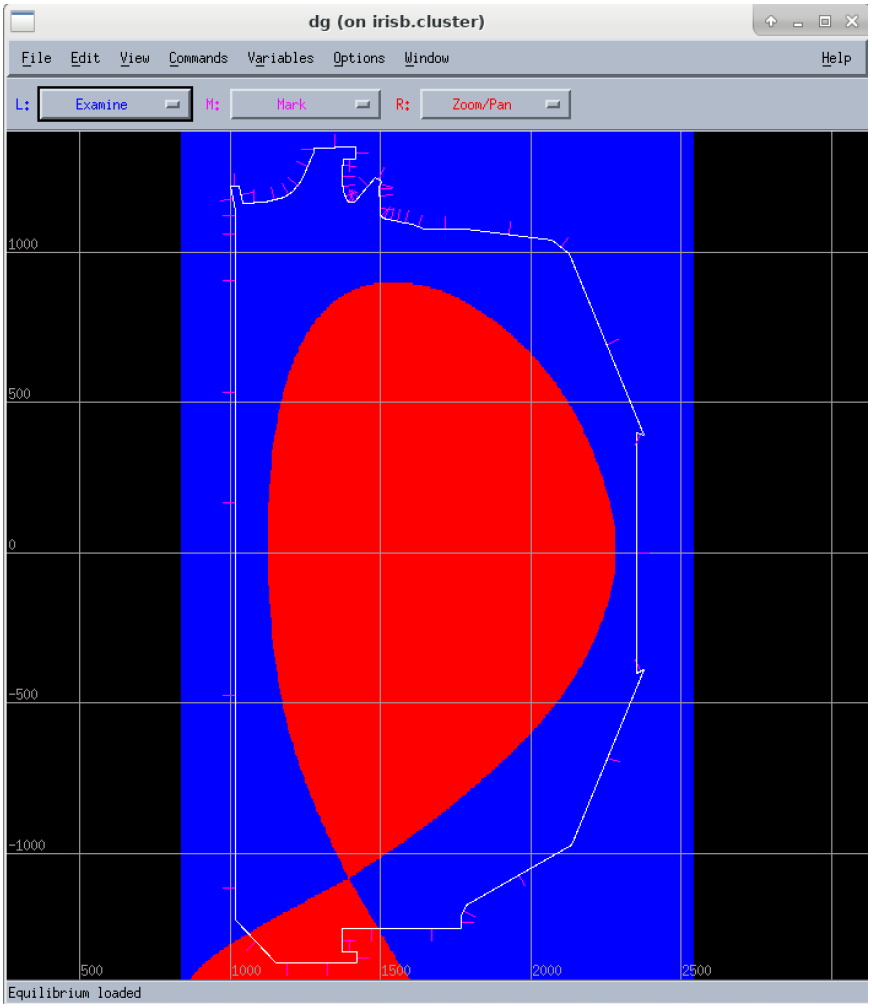


Figure C.2: Screen cap of DG system to grab equilibrium

- DDN-up = disconnected double null,upper primary X-point

6. View ≫ Display ≫ click on dashes (yellow) ≫ click on 'points' ≫ click on 'Equilibrium'

   This will make the equilibrium down to LCFS only and bring up points for every section of the wall. See Figure C.3

7. Next thing we need to consider, is to make surface around the LCFS. For this change the 'Right mouse click (R):' to 'Add Surface'. Next, right click and drag near the SOL to know where the last surface could be made in the DG system without being interrupted by another wall. As seen in Figure C.4, this is where the DG grid would be made up until. It is important to note the location at which the outer and inner SOL surface are made.

8. Zoom into the divertor region

9. File ≫ create ≫ Point

10. Make a triangle in the PFR region, and near the outer SOL region. This is something that will help you constrain the surface creation and help in mesh creation. See Figure C.5 for reference. It is to note that the triangle mad ein the SOL region can and hass been moved near the crown region to provide constraint from the upstream location. There is no specific rule of where one can put a triangle in.

11. DG-Carre system requires the divertor target to be a closed polygon, therefore create points near the divertor target in order to make the divertor a closed polygon.

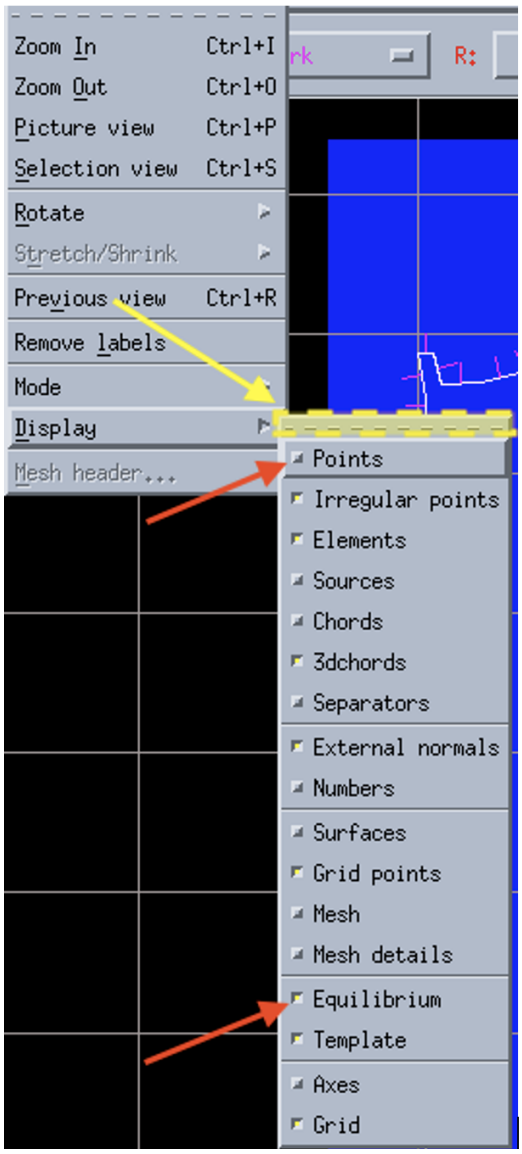


Figure C.3: Screen cap of DG system to have better display option

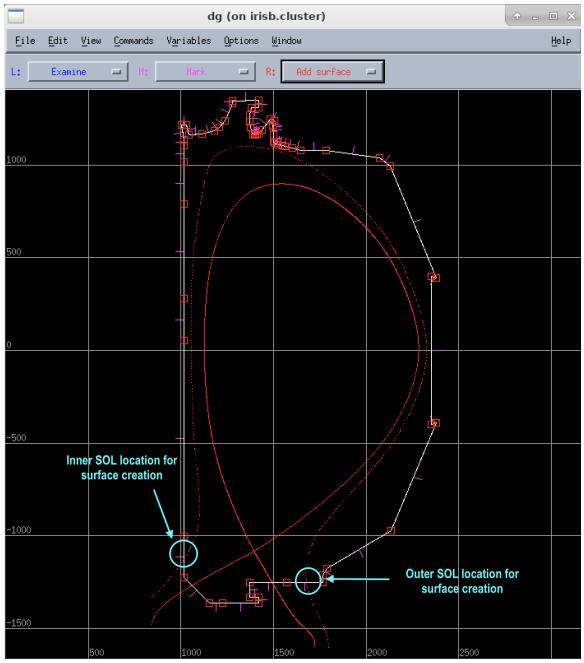


Figure C.4: Screen cap of DG system to have SOL surfaces known using the right click mouse option. Right click and drag into SOL region to know up until where the SOL surfaces can be created.

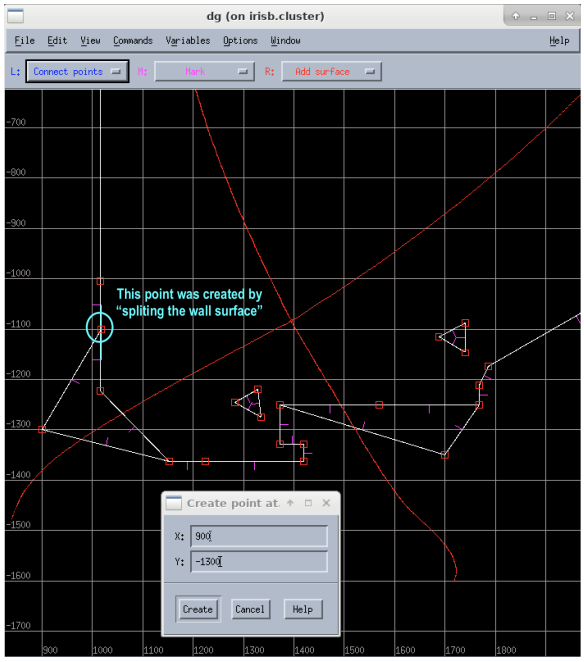


Figure C.5: Screen cap of DG system to have SOL surfaces known using the right click mouse option. Right click and drag into SOL region to know up until where the SOL surfaces can be created.

12. Variables ≫ Structure

13. Left Mouse click ≫ Mark

14. Mark Inner target and click Set (see Figure C.6 for reference).

15. Ctrl + U ≫ Mark Outer target and click Set (see Figure C.6 for reference).

16. Ctrl + U ≫ Ctrl + A, deselect surface just outside both the targets (see Figure C.7 for reference).

17. Edit ≫ Create ≫ Grid Points (See Figure C.8 for reference)

18. Start with SOL, set cells = 55, Delta1 = 0.006, Delta2 = 0.006

19. Select Outer Divertor, Set cells ≈ 20, and make the curve convex, i.e., Delta1 > Delta2.

20. Select Inner Divertor, Set cells ≈ 25, and make the curve convex, i.e., Delta1 > Delta2. As seen in Figure C.8.

21. Remember, the goal for grid point making is not to set numbers, but to make sure the distance between the 'spokes' in the grid points near the x-point are equidistant. Zoom in on the x-point region and check if the grid points from all four direction seen equidistant or not. If not, change Delta1, Delta2 for outer and inner divertor along with SOL region. Figure C.9 shows the equidistantly placed grid points for this examples case we have.

22. Left Mouse Click ≫ Add Surface

23. Click on center or near the core to create a surface

24. Edit ≫ Create ≫ Surface(s) (See Figure C.10)

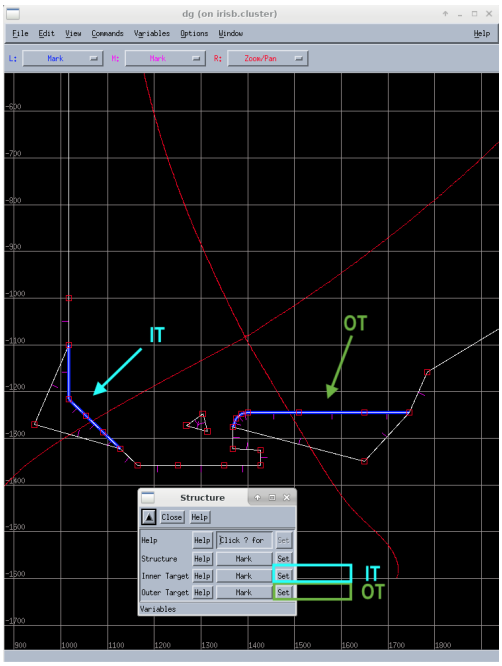


Figure C.6: Screen cap of DG system to select target surfaces. One must mark the outer target surface (OT) and then click on the Set in the Structure Gui, similarly repeat for the inner target (OT) as well.

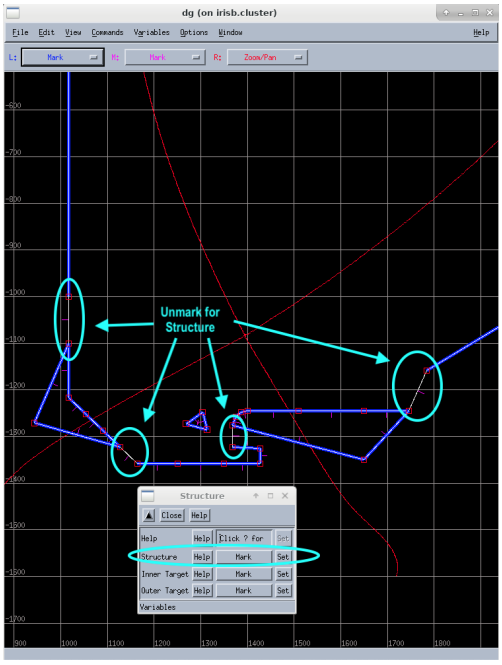


Figure C.7: Screen cap of DG system to select structure surfaces. One must mark all the elements except the ones that are unmarked just outside the target allocated in the previous step.

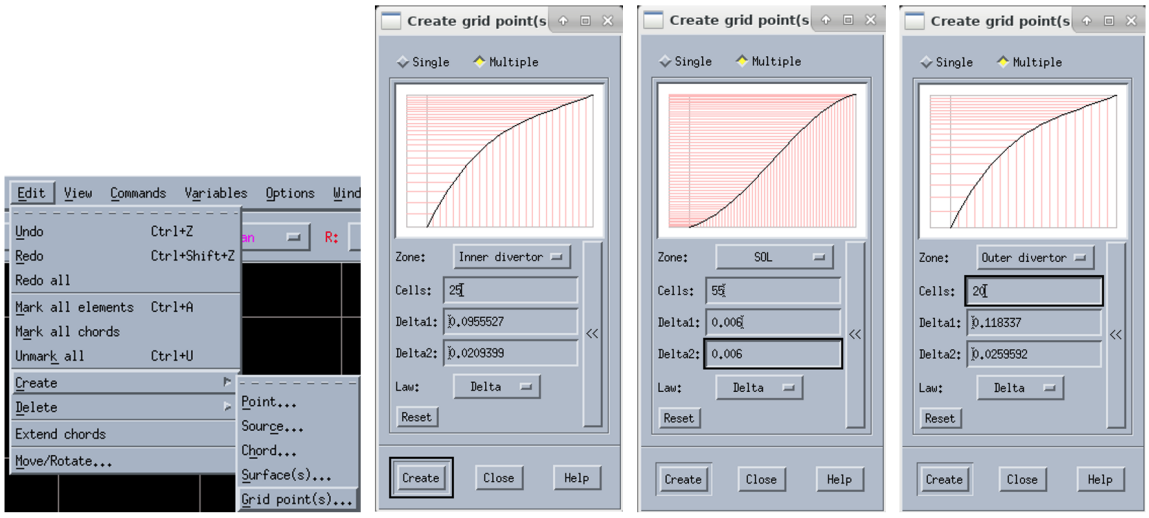


Figure C.8: Screen cap of DG system to produce grid points on the equilibrium. One must start from SOL option and make it an 'S' curve, whereas the outer and inner target needs to be a convex curve

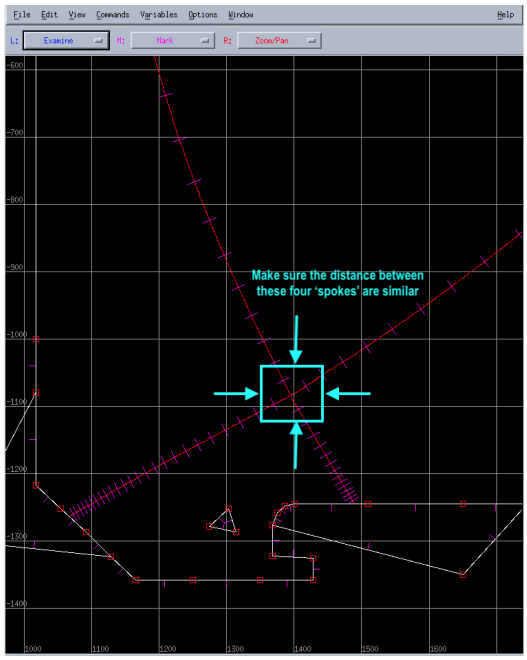


Figure C.9: Screen cap of DG system showing an example of equidistant 'spoke' or grid points present on the equilibrium

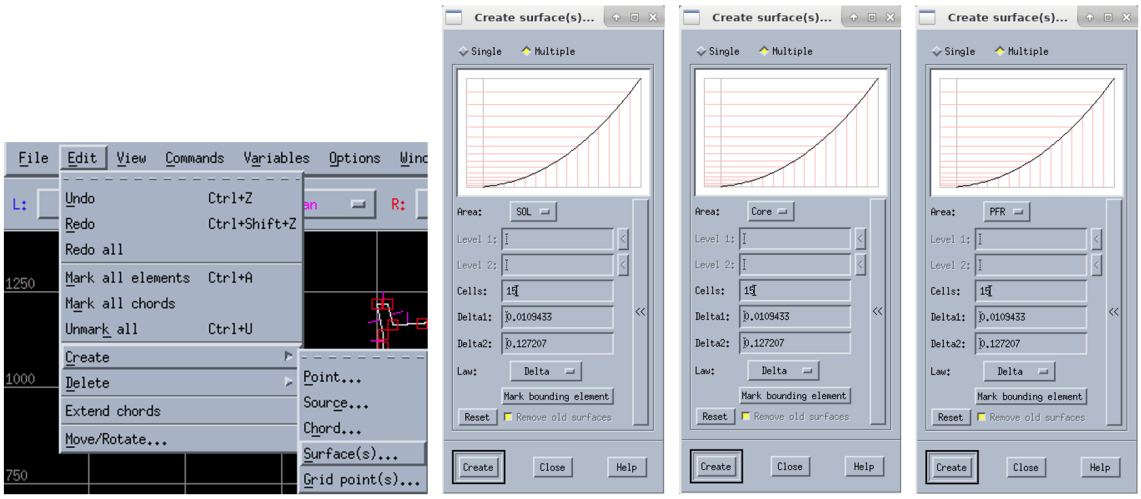


Figure C.10: Screen cap of DG system to produce grid points on the equilibrium. One must start from SOL option and make it an 'S' curve, whereas the outer and inner target needs to be a convex curve

It is to note that cells of each SOL, Core, and PFR regions are same. Here, for the example reference cases we have set cells for all three regions as 15 and all the regions are set to concave shape. Just like the grid points, the surfaces also need to be similarly equidistant near the x-point.

25. Variables ≫ target specification ≫ #1 for inner target and #2 for outer target.
    - #1: inner target (LSN), outer target (USN), lower inner target (DN)
    - #2: outer target (LSN), inner target (USN), upper inner target (DN)
    - #3: upper outer target (DN)
    - #4: lower outer target (DN)
26. Make sure to select SOL edge and PFR edge for each target, inner (#1) and outer (#2) divertor. See Figure C.11.
27. Commands ≫ Check variables → this is done to check for errors
28. Commands ≫ Rebuild Carre Objects
29. File ≫ Save ≫ write the name of the file for example, 'dg_[Shot Number]_[Time Slice].dg'
30. File ≫ output
    This will save the following into .dgo, .str, and .trg files.
31. `cd $DGHOME/class`
32. `./lns examples/d3d_[iris username]/[shot number]_[time slices]/dg_[Shot Number]_[Time Slice]`
33. `cd $DGHOME/Carre`
34. `./carre -`
35. `Type p and press enter`

36. `Type g and press enter`

37. `Type in Y and press enter`

38. `Type in Y and press enter`

39. `Type in C and press enter`

40. `Type in t and press enter`

41. `Type in q and press enter`

42. In the DG Gui, File ≫ import ≫ Mesh

43. Select the .sno file that was generated. Check for inconsistencies, if none, you are ready to use the grid for OEDGE case. See Figure C.12.

44. `/fusion/projects/codes/oedge/[iris username]/shots`

45. `cp /fusion/projects/solps-results/[iris username]/dg-carre/Carre/data/meshes/dg_[Shot Number]_[Time Slice].griddivimp .`

46. Now that we have copied the grid into the OEDGE folder. Let us now create an input file for OEDGE

47. `geany &`

48. Copy an existing .d6i file for the shot you are trying to analyze

49. `./rundiv.sh d3d-186791-1200v6-v1 dg186791_1200v6.v001.griddivimp none none none`

    - d3d-186791-1200v6-v1 is the input .d6i file
    - dg186791_1200v6.v001.griddivimp is the grid file that was created by DG Carre

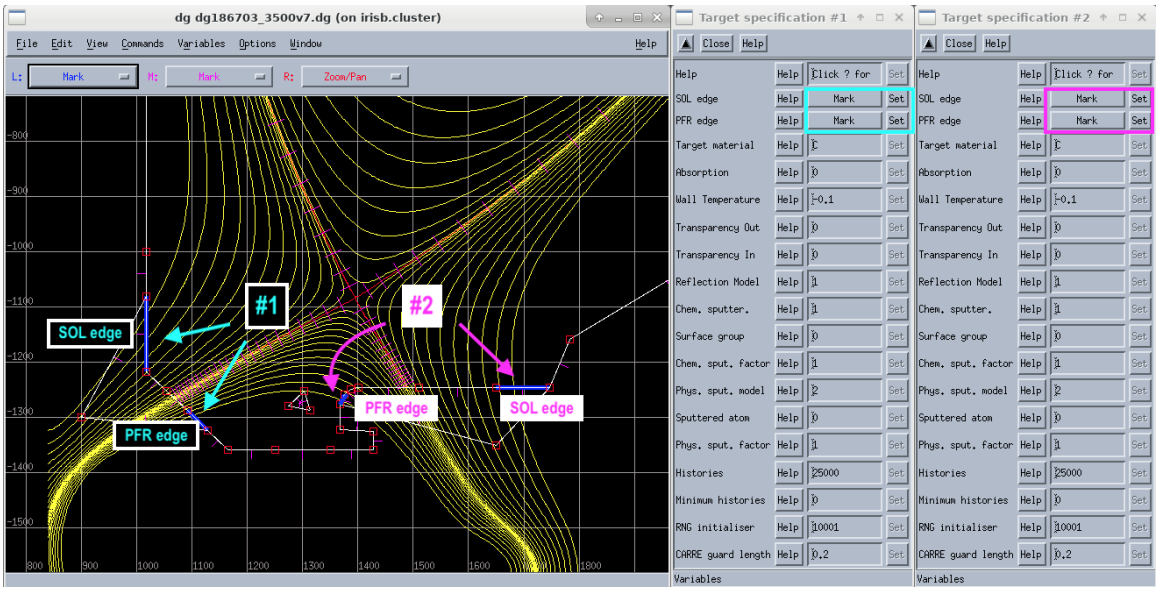


Figure C.11: Screen cap of DG system showing the SOL edge and PFR edge for inner and outer target

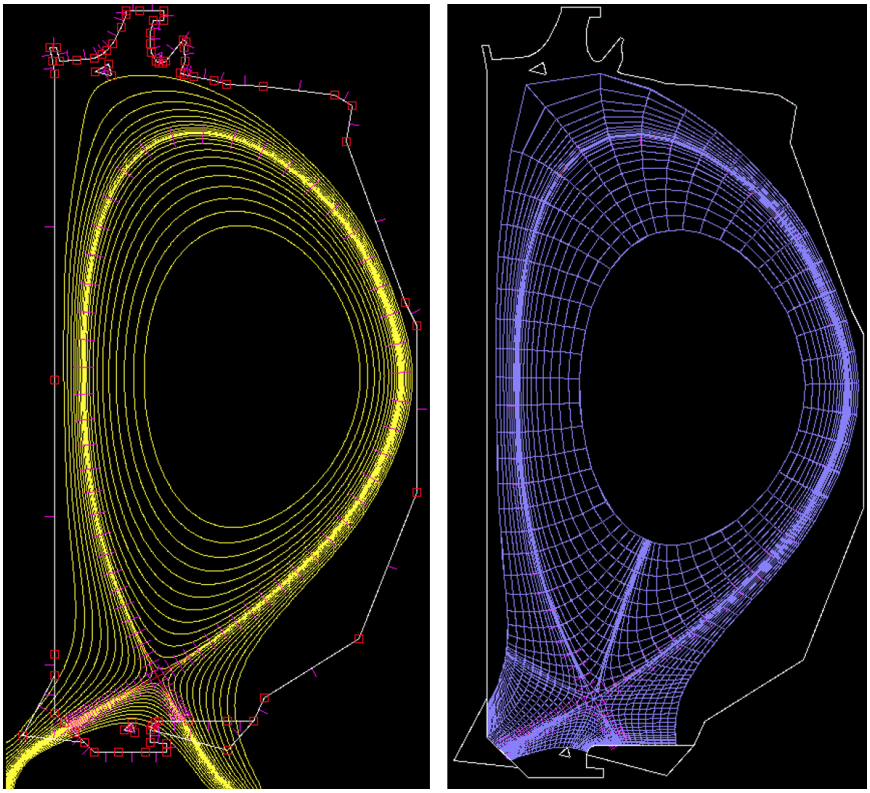


Figure C.12: Screen cap of DG system showing the surface and meshes created for the example case

50. **In case of an issue for importing equilibrium**

    - `cropequ outputx8.eq outputx8c.eq`
    - input the following
        - : 513
        - : 0.84
        - : 2.54
        - : 513
        - : -1.6
        - : 1.45

51. **Note:** For more information and debugging, please visit the OEDGE guide website. This was created by S. Zamperini.

Appendix D

Details about obtaining I_{wall} and I_{div} for all divertor configurations

The objective of this chapter is to conduct a comparative analysis between experimental and modeled data, aiming to identify and comprehend f_{wall} and $f_{wall-OEDGE}$ and any disparities that may exist between the two. The chapter is structured into five primary sections:

Section D.1 presents an overview of the types of plasma discharges used in the analysis, showcasing global parameters based on the L and H mode as well as the $B \times \nabla B$ drift direction.

Following that, Section D.2 delves into the Edge measurements of n_e and T_e, along with Filterscope measurements of D_α emissivity and neutral density for the analyzed shots.

Subsequently, Section 3.2 elucidates the details of the GRP formula. With these foundational details in place, Section 5.3.1 describes the determination of I_{wall} and I_{div} through modified window frame experiments in various divertor configurations. Parallelly, Section D.3 outlines a similar analysis using OEDGE modeling.

D.1 Global parameters compared between plasma discharges used for closure interoperability

All plasma discharges or shots documented in this thesis exhibit diverted, single-null magnetic equilibrium with $B \times \nabla B$ ion drift directed both towards (Reverse) and away (Forward) from the X-point. The primary focus of this thesis is on conventional divertor geometries to estimate f_{wall}: LSN Shelf, LSN Floor, and USN Floor.

Figure D.1 shows the basic global parameters for plasma discharges that are compared. Global Parameters of Plasma discharges in Rev B_t configuration are depicted here. (a1-a4) shows Line averaged density, (b1-b4) shows pedestal temperature, (c1-c4) shows injected power, (d1-d4) shows the outer gap of plasma to the main chamber wall, and (e1-e4) shows the location of the outer strike point. The divertor configuration of LSN Floor is depicted in black, USN Floor is depicted in red and LSN Shelf if depicted in blue thoughout the comparison.

Figure D.1 (a1, b1, c1, d1, e1) showcase density, pedestal temperature, injected power, outer strike point location and outer gap. In the case of the LSN Floor discharge (shot #167234), the analysis focused on the time slice spanning 2000 to 4000 ms, with a magnetic field strength (B_t) of 2 T, an electric current (I_p) of 1.19 MA, an injected power of 1 kW, and an electron density of 3e19 m^{-3}. Similarly, the LSN Shelf discharge (shot #163210) involved a time slice from 3000 to 4000 ms, a B_t of 2 T, I_p of 1 MA, injected power of 1.1 kW, and an electron density of 3e19 m^{-3}. The USN Floor discharge (shot #184533), conducted over the time range 2000 to 4000 ms with a reversed magnetic field ($-2T$ B_t), featured an I_p of 1 MA, injected power of 4 kW, and an electron density of 4e19 m^{-3}. Finally, the SAS discharge (shot #184549) encompassed the time interval 1800 to 2000 ms, with a $-2T$ B_t, I_p of 1 MA, injected power of 2.2 kW, and an electron density of 4e19 m^{-3}.

Figure D.1 (a2, b2, c2, d2, e2) showcase density, pedestal temperature, injected power, outer strike point location and outer gap. In the case of the LSN Floor discharge (shot #167245), the analysis focused on the time slice spanning 3000 to

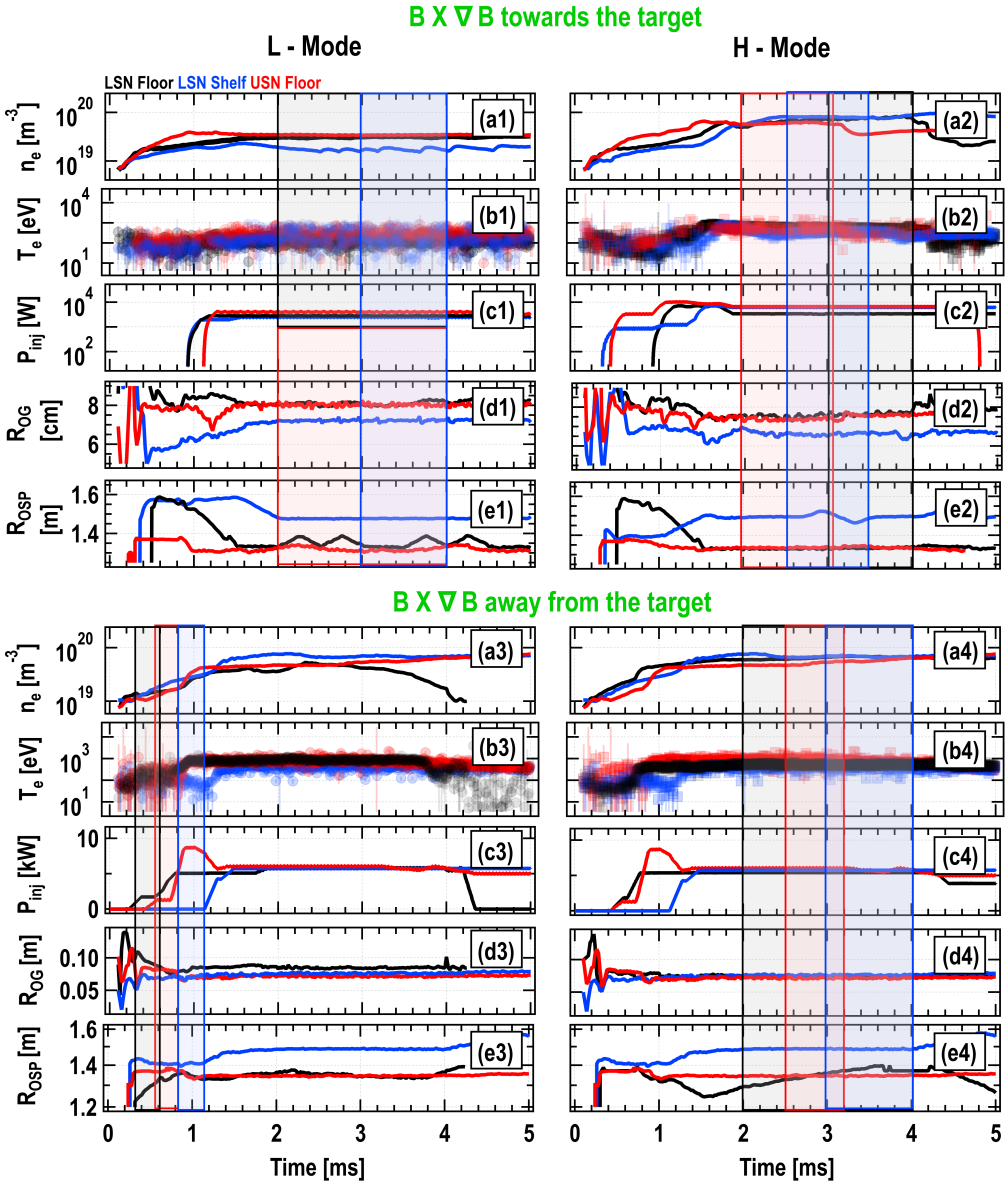


Figure D.1: Global Parameters of Plasma discharges in Rev B_t configuration are depicted here. (a1-a4) shows Line averaged density, (b1-b4) shows pedestal temperature, (c1-c4) shows injected power, (d1-d4) shows the outer gap of plasma to the main chamber wall, and (e1-e4) shows the location of the outer strike point

4000 ms, with a magnetic field strength (B_t) of 2 T, an electric current (I_p) of 1.19 MA, an injected power of 4 kW, and an electron density of 6e19 m^{-3}. Similarly, the LSN Shelf discharge (shot #186703) involved a time slice from 3000 to 3500 ms, a B_t of 2 T, I_p of 1.3 MA, injected power of 6 kW, and an electron density of 8e19 m^{-3}. The USN Floor discharge (shot #179974), conducted over the time range 2000 to 3100 ms with a reversed magnetic field ($-2T$ B_t), featured an I_p of 1.3 MA, injected power of 6.5 kW, and an electron density of 6e19 m^{-3}. Finally, the SAS discharge (shot #185857) encompassed the time interval 3000 to 4500 ms, with a $-2T$ B_t, I_p of 1.3 MA, injected power of 8 kW, and an electron density of 7e19 m^{-3}.

Figure D.1 (a3, b3, c3, d3, e3) showcase density, pedestal temperature, injected power, outer strike point location and outer gap. In the case of the LSN Floor discharge (shot #174803), the analysis focused on the time slice spanning 450 to 600 ms, with a magnetic field strength (B_t) of $-2T$, an electric current (I_p) of 0.9 MA, an injected power of 1.7 kW, and an electron density of 1.4e19 m^{-3}. Similarly, the LSN Shelf discharge (shot #186791) involved a time slice from 900 to 1100 ms, a B_t of $-2T$, I_p of 1 MA, with only ohmic power, and an electron density of 2.8e19 m^{-3}. The USN Floor discharge (shot #179760), conducted over the time range 600 to 750 ms with a reversed magnetic field (2T B_t), featured an I_p of 1 MA, injected power of 1.32 kW, and an electron density of 1.45e19 m^{-3}. Finally, the SAS discharge (shot #169048) encompassed the time interval 3300 to 4900 ms, with a $2T$ B_t, I_p of 1 MA, injected power of 1kW, and an electron density of 2.16e19 m^{-3}.

Figure D.1 (a4, b4, c4, d4, e4) showcase density, pedestal temperature, injected power, outer strike point location and outer gap. In the case of the LSN Floor discharge (shot #175937), the analysis focused on the time slice spanning 2000 to 4000 ms, with a magnetic field strength (B_t) of $-2T$, an electric current (I_p) of 1.3 MA, an injected power of 5.1 kW, and an electron density of 6.2e19 m^{-3}. Similarly, the LSN Shelf discharge (shot #186791) involved a time slice from 3000 to 4000 ms, a B_t of $-2T$, I_p of 1.3 MA, with 5.7kW of injected power, and an electron density of 6.8e19 m^{-3}. The USN Floor discharge (shot #179760), conducted over the time

range 2500 to 3200 ms with a reversed magnetic field (2T B_t), featured an I_p of 1.3 MA, injected power of 6.15 kW, and an electron density of 4.8e19 m^{-3}. Finally, the SAS discharge (shot #174910) encompassed the time interval 3000 to 5000 ms, with a 2T B_t, I_p of 1.3 MA, injected power of 4kW, and an electron density of 9e19 m^{-3}.

It is noteworthy that, in all these diverse configurations, global parameters at the selected time slices are deliberately maintained to exhibit similarity among values. This approach facilitates a more meaningful comparison of results, particularly in cases where the underlying physics appears ostensibly similar, with the divergence primarily attributed to variations in divertor geometry.

D.2 Diagnostic measurements in DIII-D tokamak

As seen in Chapter 2.5, there are three main diagnostics useful in understanding and calculation of f_{wall}, namely, Thomson Scattering to inform n_e and T_e data inside the separatrix which is useful to understand the SXB values and the Filterscope data that is useful in Equation 3.11. Langmuir probe measurements to inform the n_e and T_e data at the divertor target which is useful for Equation 3.13.

D.2.1 Electron Density and Temperature Measurements

n_e from Thomson Scattering - $B_T \times \nabla B \downarrow$

The electron density profiles obtained from Thomson Scattering data are depicted in Figure D.2. In Figure D.2(a, b), the electron density profiles for the LSN Floor (black) configuration in l-mode and H-moode configurations. Configuration D.2(c, d) showcase LSN Shelf divertor electron density profiles and subfigure (e and f) show USN Floor floor electron density profiles in $B_T \times \nabla B \downarrow$ conditions. It is important to note that the presented electron density data corresponds to a $B_T \times \nabla B \downarrow$ and both L mode and H mode configuration. Subfigure (b, d, f) showcases the discernible presence of a pedestal, signifying the occurrence of H mode in the shots. Furthermore,

H-mode shots demonstrates electron density values that are at least two times higher compared to those observed in L-mode.

T_e from Thomson Scattering - $B_T \times \nabla B \downarrow$

The electron temperature profiles obtained from Thomson Scattering data are depicted in Figure D.3. In Figure D.3(a, b), the electron density profiles for the LSN Floor (black) configuration in L-mode and H-mode configurations. Configuration D.3(c, d) showcase LSN Shelf divertor electron density profiles and subfigure (e and f) show USN Floor floor electron density profiles in $B_T \times \nabla B \downarrow$ conditions. It is important to note that the presented electron density data corresponds to a $B_T \times \nabla B \downarrow$ and both L mode and H mode configuration. Subfigure (b, d, f) showcases the discernible presence of a pedestal, signifying the occurrence of H mode in the shots. Furthermore, H-mode shots demonstrates electron density values that are at least two times higher compared to those observed in L-mode.

n_e and T_e from Thomson Scattering - $B_T \times \nabla B \uparrow$

The electron density and temperature profiles, derived from Thomson Scattering data, offer insights into the plasma behavior across various divertor configurations for $B_T \times \nabla B \uparrow$ in L mode and H mode configurations as seen in Figures D.4, and D.5.

Figures D.4, and D.5 collectively present profiles of electron density and temperature for various L mode scenarios. For L-mode D.4, and D.5 subfigure (a), the electron density and temperature profiles are displayed for the LSN Floor configuration in Shot 174803, covering the time range of 450 to 600 ms. Meanwhile, Subfigure (c) showcases similar profiles for the LSN Shelf configuration in Shot 186791, focusing on the time interval between 900 and 1100 ms. Additionally, Subfigure (e) provides electron density and temperature data for the USN Floor in Shot 179760, spanning the period from 600 to 750 ms. It is essential to note that the presented data corresponds to a forward B_T and L mode configuration.

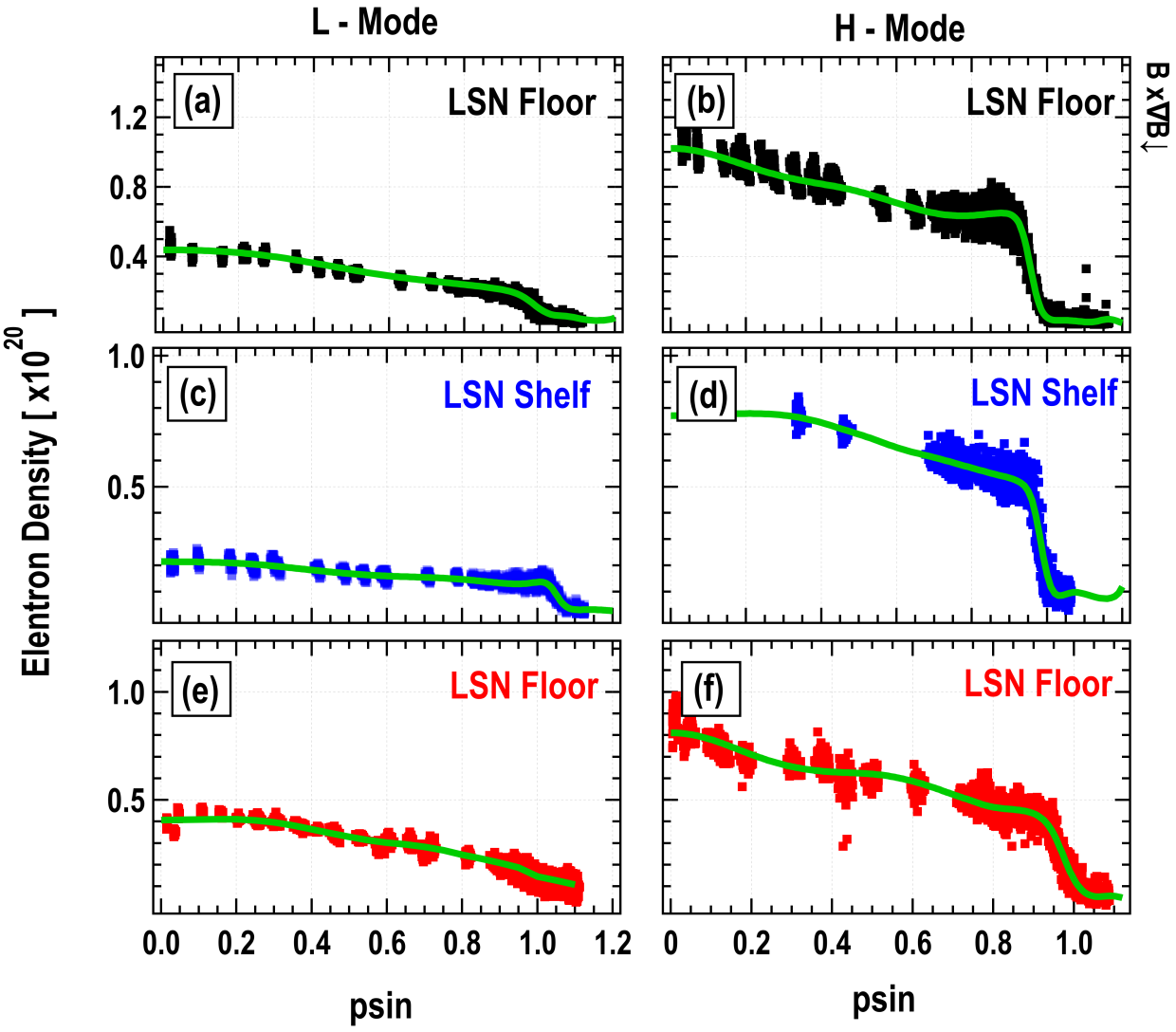


Figure D.2: n_e from Thomson Scattering - $B_T \times \nabla B \downarrow$ in L mode and H mode configuration depicting all the data, along with time sliced average data fit. This data is derived from OMFITprofiles module on OMFIT

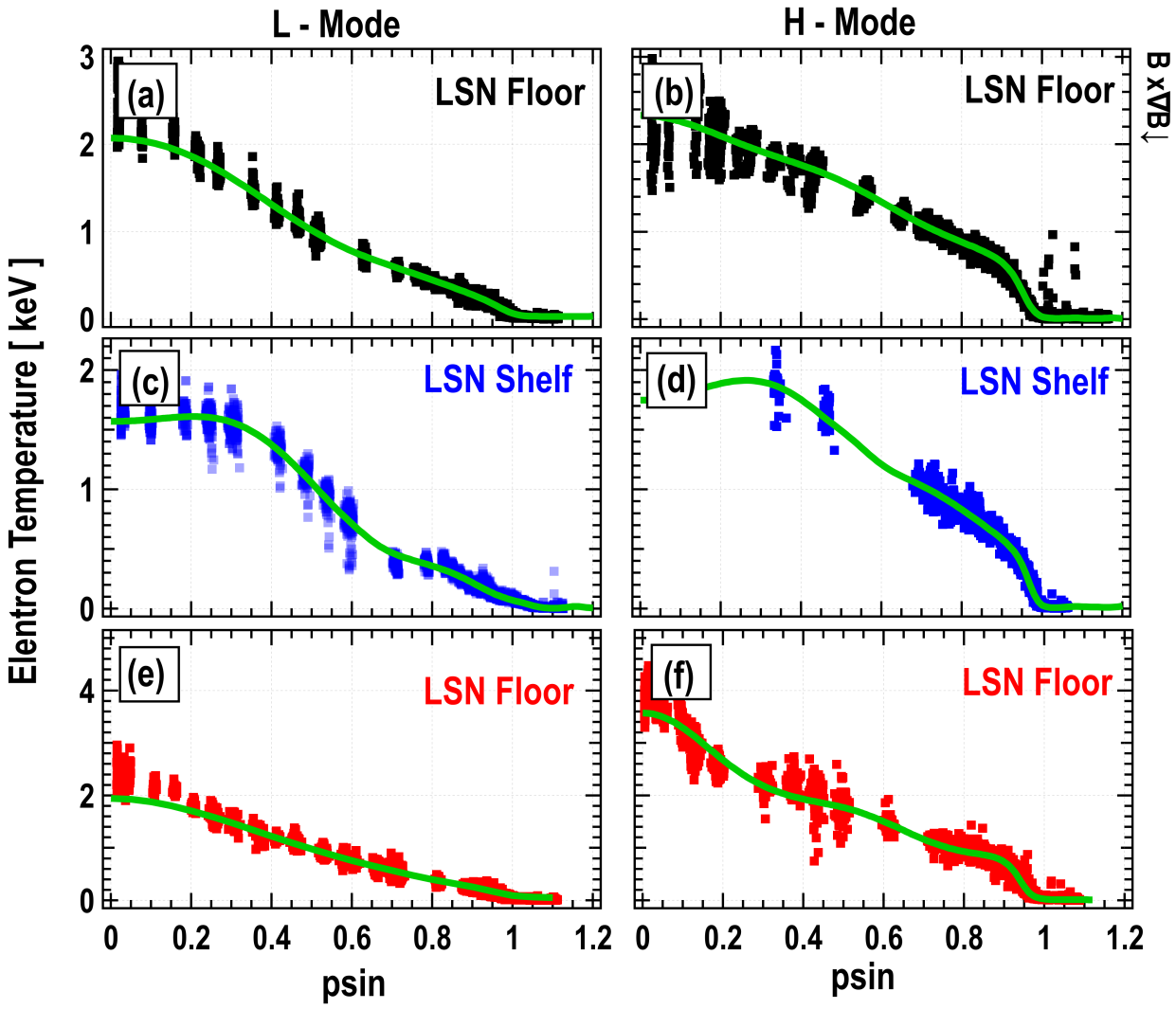


Figure D.3: T_e from Thomson Scattering - $B_T \times \nabla B \downarrow$ in L mode and H mode configuration depicting all the data, along with time sliced average data fit. This data is derived from OMFITprofiles module on OMFIT

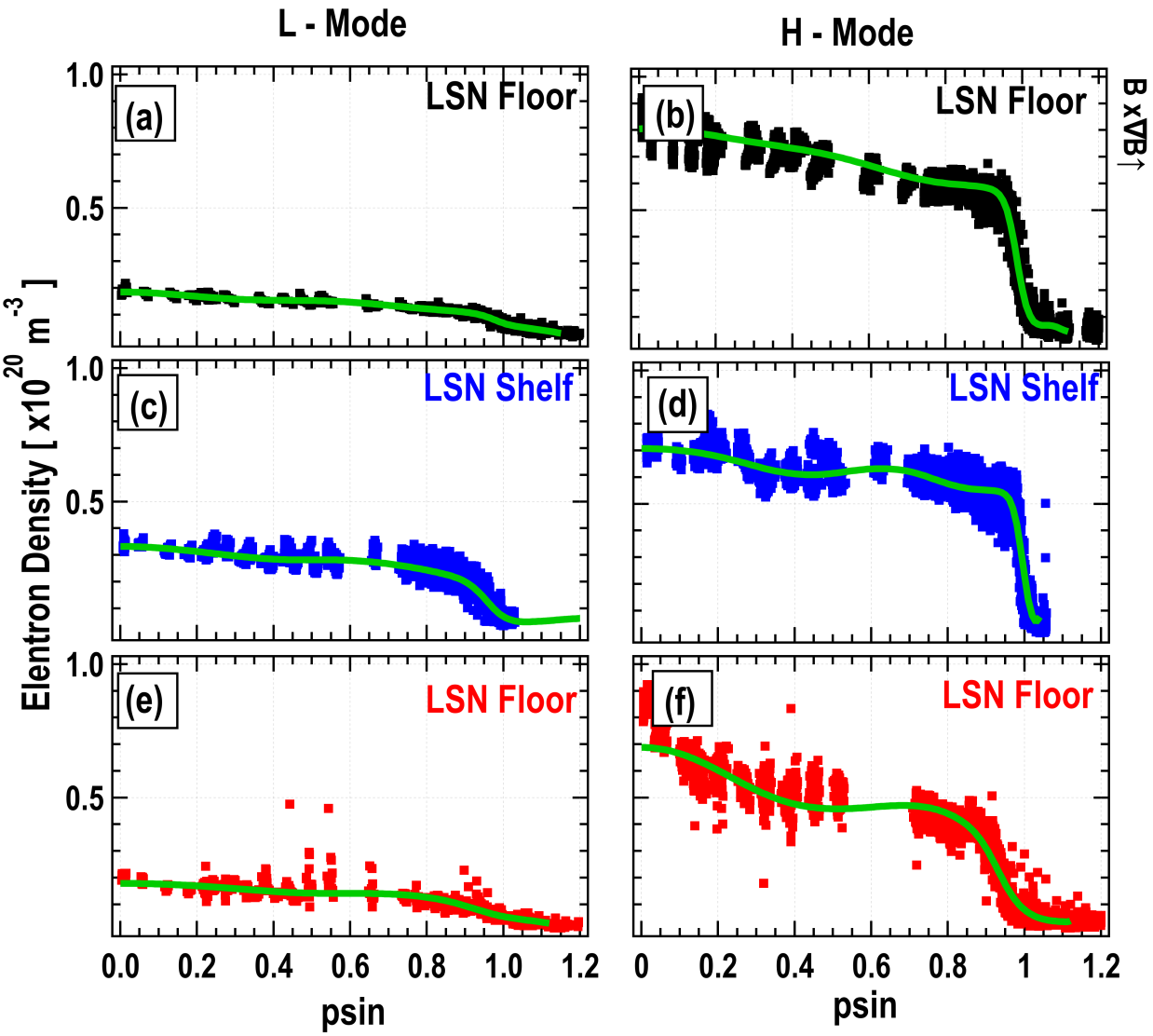


Figure D.4: T_e from Thomson Scattering - $B_T \times \nabla B \uparrow$ in L mode and H mode configuration depicting all the data, along with time sliced average data fit. This data is derived from OMFITprofiles module on OMFIT

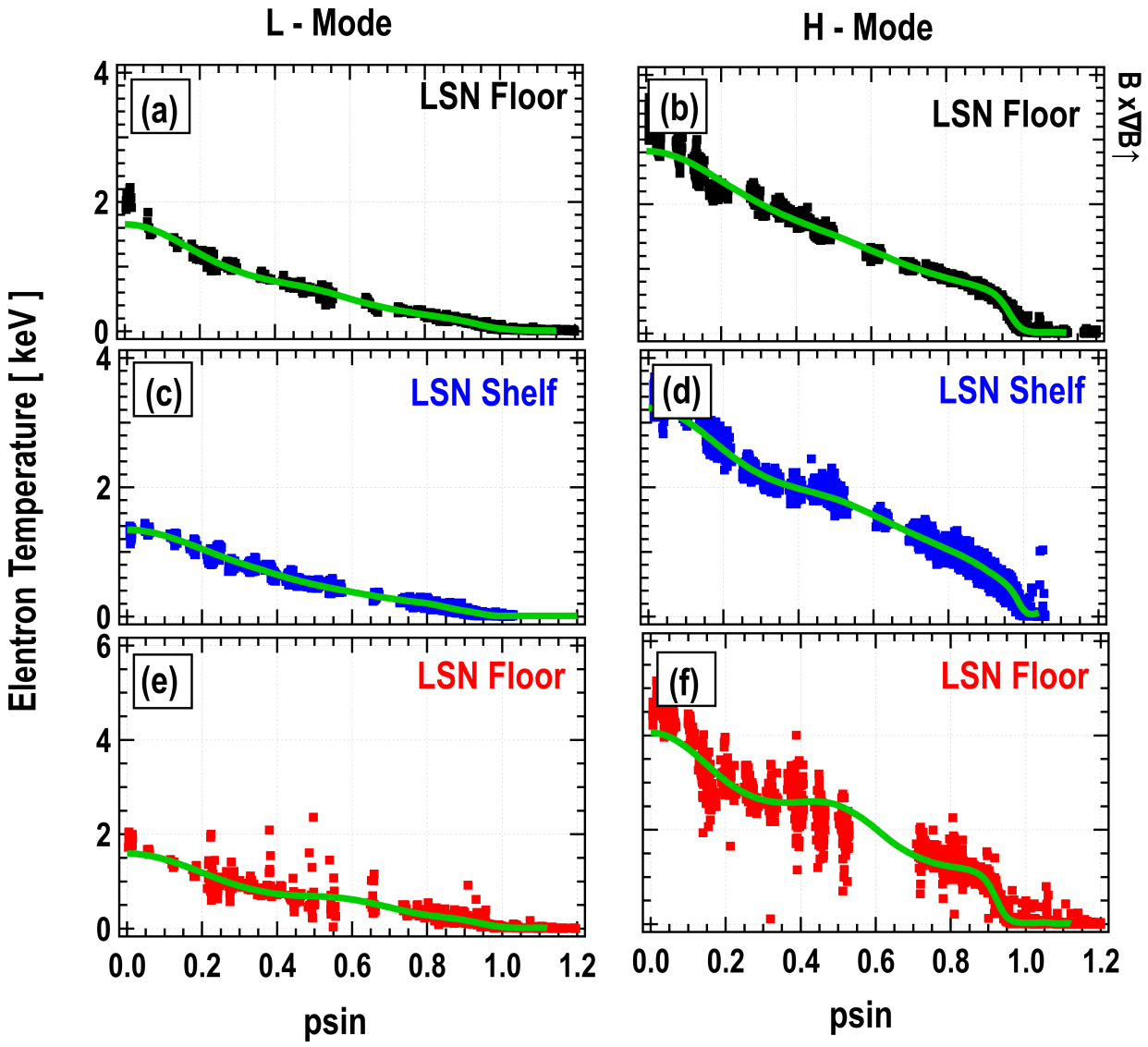


Figure D.5: T_e from Thomson Scattering - $B_T \times \nabla B$ ↑in L mode and H mode configuration depicting all the data, along with time sliced average data fit. This data is derived from OMFITprofiles module on OMFIT

Corresponding H mode profiles are depicted in D.4, and D.5, revealing distinctive features such as the presence of a pedestal and significantly higher electron temperature values characteristic of the H mode regime. Moreover, the H mode data corresponds to different plasma discharges. Subfigure (b) illustrates the LSN Floor configuration of Shot 175937 from 2000 to 4000 ms. Subfigure (d) showcases the LSN Shelf configuration for Shot 186791, the same as the L mode shot but at a different time slice between 3000 and 4000 ms. Finally, Subfigure (f) also displays the same shot as the L mode configuration but at a different time slice, similar to that of the LSN Shelf configuration, from 2500 to 3200 ms.

The data presented in the figures exhibit a goodness-of-fit (χ^2) value ranging from 1.1 to 4.8. All the aforementioned results were obtained through the OMFIT profiles module, accessible to all users on the IRIS server at OMFIT.

Langmuir Probe Measurements in Reverse B_T and Forward B_T

Figures D.6 and D.7 depict measurements of electron density, temperature, and current density in the LSN Floor, LSN Shelf, and USN divertor configurations under forward B_T conditions during L mode and H mode, respectively. A notable observation across all divertor configurations is the noticeable increase in electron density and current density at the divertor as the system transitions from L mode to H mode conditions. The figures include a goodness-of-fit measure associated with each measurement, providing an indication of the fitting accuracy. It is essential to acknowledge that the χ^2 value may be elevated due to variations in the available data.

The same for reverse B_T is depicted in Figures D.8 and D.9. It is to note that the J_{sat} profile seen in the subfigures here is used to calculate I_{div} from Equation 3.12.

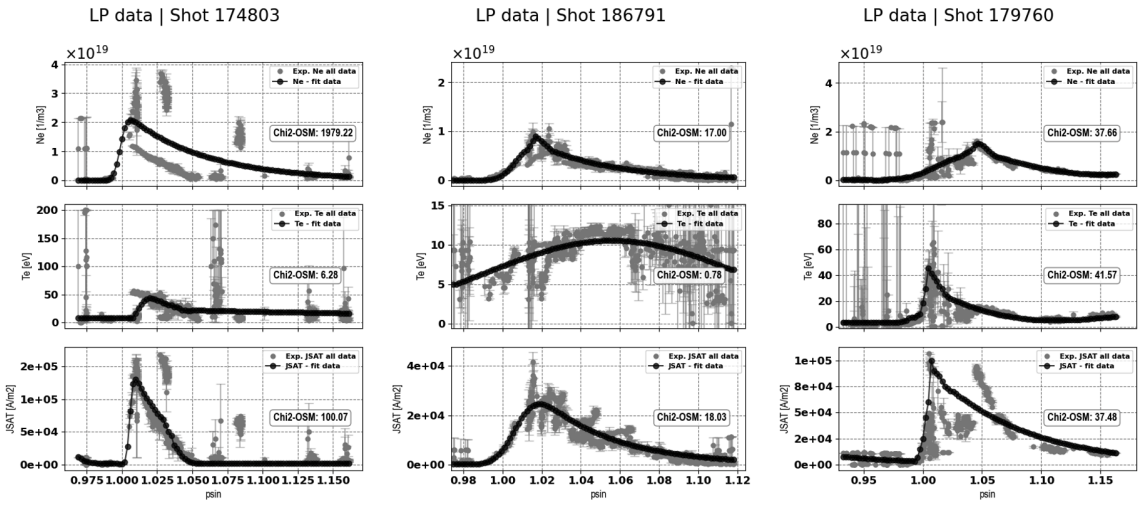


Figure D.6: n_e, T_e and J_{sat} as measured by embedded Langmuir probes on the divertor targets LSN Floor (left plot), LSN Shelf (middle plot), USN Floor (right plot). The data shows measurements from L mode plasma discharge in forward B_T configuration

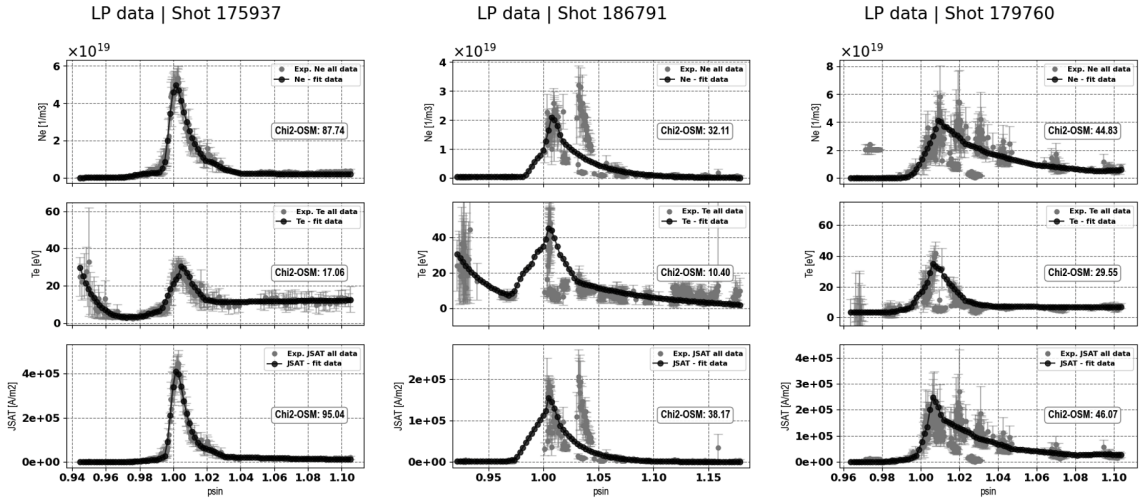


Figure D.7: n_e, T_e and J_{sat} as measured by embedded Langmuir probes on the divertor targets LSN Floor (left plot), LSN Shelf (middle plot), USN Floor (right plot). The data shows measurements from H mode plasma discharge in forward B_T configuration

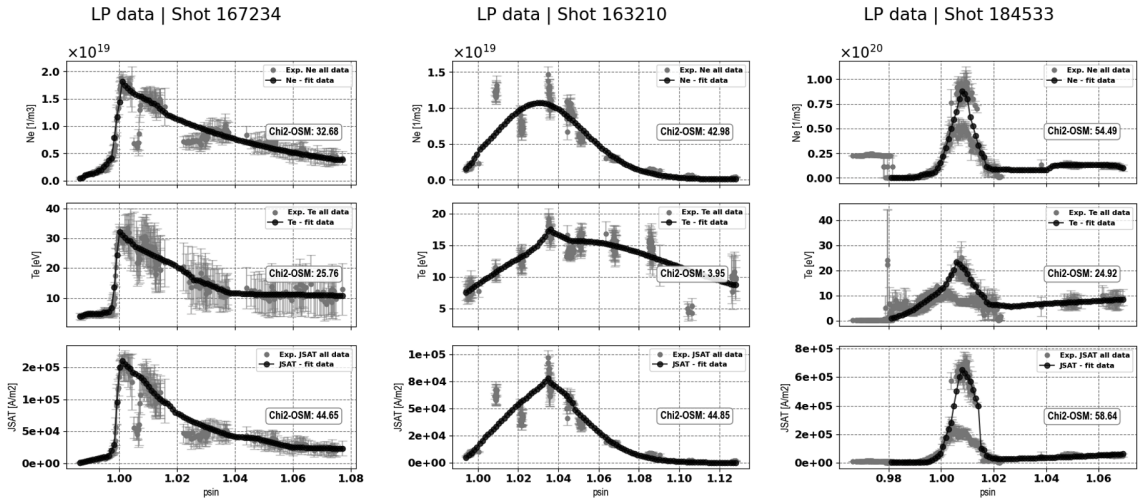


Figure D.8: n_e, T_e and J_{sat} as measured by embedded Langmuir probes on the divertor targets LSN Floor (left plot), LSN Shelf (middle plot), USN Floor (right plot). The data shows measurements from L mode plasma discharge in forward B_T configuration

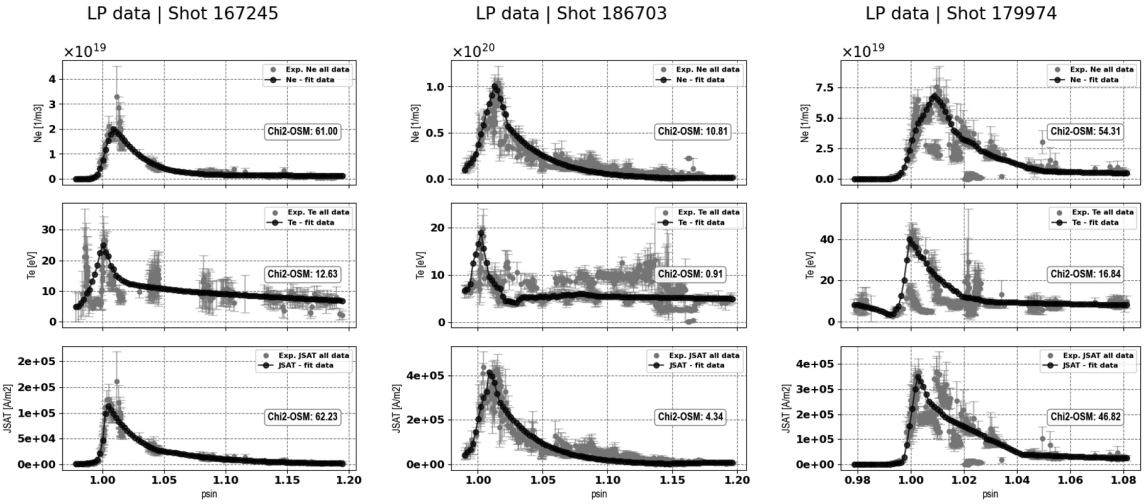


Figure D.9: n_e, T_e and J_{sat} as measured by embedded Langmuir probes on the divertor targets LSN Floor (left plot), LSN Shelf (middle plot), USN Floor (right plot). The data shows measurements from H mode plasma discharge in forward B_T configuration

D.2.2 Filterscope Measurements

As previously mentioned, the Filterscope system is employed for measuring the emissivity and radiance associated with D_α. Figure D.10 illustrates radiance and emissivity in both L mode and H mode, considering both forward and reverse B_T directions in the LSN Floor divertor configuration. Similar representations are provided for the LSN Shelf in Figure D.11 and the USN Floor in Figure D.12. A noteworthy observation is that in H mode, the emissivity is approximately three times higher on average in reverse B_T. Additionally, regardless of the B_T direction, the radiance exhibits a radial decrease towards the main chamber wall. The emissivity, influenced by recycling, tends to increase near the Last Closed Flux Surface (LCFS) and then gradually decreases.

D.3 Divertor Plasma Solution using OEDGE

As outlined in the preceding Section 5.3.1, we examined the experimental values of f_{wall} in relation to the GRP. The objective in this section remains analogous, involving the plotting of $f_{wall-oedge}$ and the corresponding DLP_{OEDGE} against GRP values. Our focus here is to explore divertor plasma solutions derived using OEDGE for specific divertor configurations under both Forward B_T and Reverse B_T setups. The subsequent subsections are organized based on divertor geometry and individual plasma discharges associated with that geometry in both L mode and H mode scenarios.

D.3.1 LSN Shelf Configuration

Lower Single Null (LSN) Shelf as seen in Figure 4.13(b) is a divertor geometry represented with a flat plate without any baffle conditions. This divertor geometry is considered the most open geometry as it does not have the features to contain particles and is reflected with a lower GRP value.

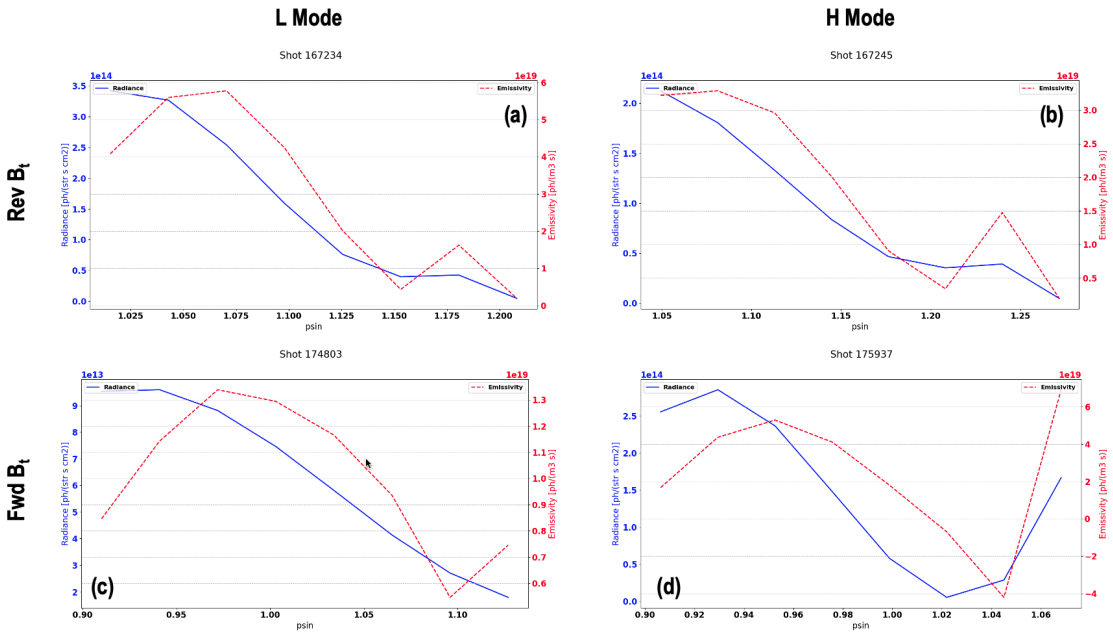


Figure D.10: D_α radiance and emissivity as measured by midplane Filterscope system for LSN Shelf configuration. The figure shows both L mode and H mode measurements in both forward and reverse B_T configuration

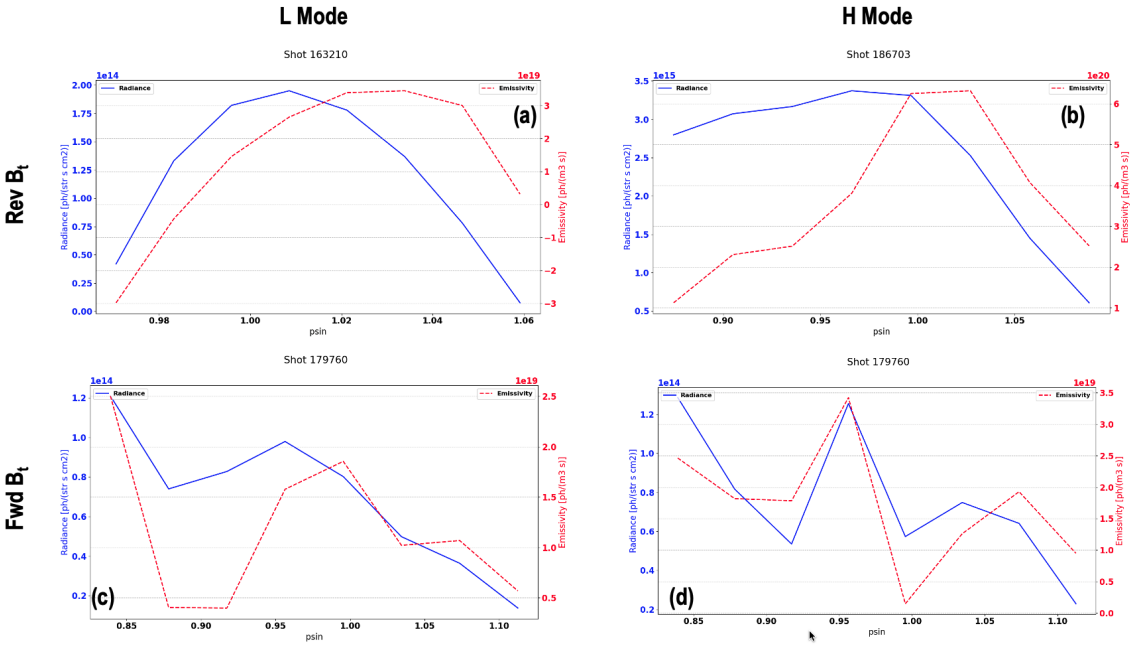


Figure D.11: D_α radiance and emissivity as measured by midplane Filterscope system for LSN Shelf configuration. The figure shows both L mode and H mode measurements in both forward and reverse B_T configuration

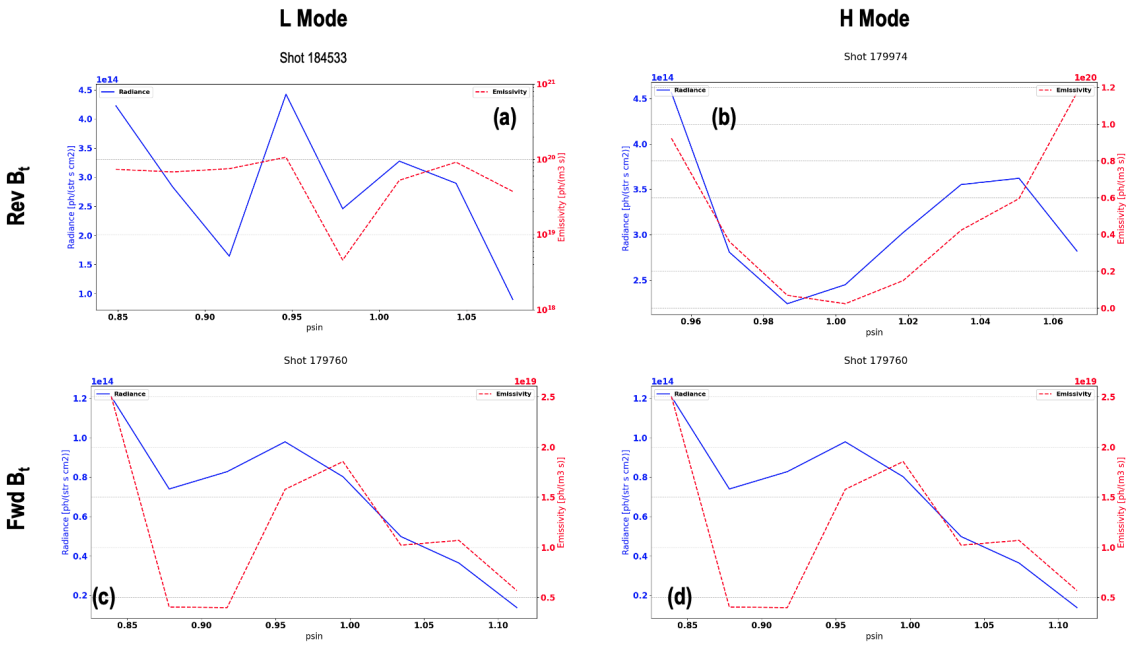


Figure D.12: D_α radiance and emissivity as measured by midplane Filterscope system for USN Floor configuration. The figure shows both L mode and H mode measurements in both forward and reverse B_T configuration

In the name of completeness, there are four LSN Shelf shots in L mode and H mode configurations and in forward B_T and Reverse B_T that will be discussed here.

L mode Plasma Discharges

In Section D.1, our examination centers on Shot # 186791 and Shot # 163210, which correspond to LSN Shelf plasma shots under forward and reverse B_T configurations, respectively. Section D.1 provides exhaustive details on these shots and their associated global parameters. Figures D.13 and D.14 showcase the distribution of electron density (n_e), plasma velocity (v), and particle flux (Γ) across all regions, with the separatrix and windowpane visibly marked. The figures reveal that, in the forward B_T plasma discharge, the overall density is lower, but there is a higher velocity in the same regions, resulting in a similar flux presence in those regions. It's noteworthy that the measured flux at the windowpane region for the forward B_T discharge is lower compared to the flux in the other plasma discharge.

Additionally, Figures D.15 and D.16 present 2D plots for Shot # 163210 and Shot # 186791, respectively. These plots illustrate the distribution of electron density (n_e), electron temperature (T_e), plasma velocity (v), and particle flux (Γ) throughout the tokamak, as simulated by OEDGE. Importantly, the negative values observed in the flux, as shown in Figures D.15 and D.16, stem from the negative plasma velocity values, indicating a reversal in the flow of particles within the SOL.

H mode Plasma Discharges

Here, we focus on Shot # 186791 and Shot # 186703, which correspond to LSN Shelf plasma shots under forward and reverse B_T configurations in H mode conditions, respectively. Section D.1 provides exhaustive details on these shots and their associated global parameters. Figures D.17 and D.18 showcase the distribution of electron density (n_e), plasma velocity (v), and particle flux (Γ) across all regions, with the separatrix and windowpane visibly marked.

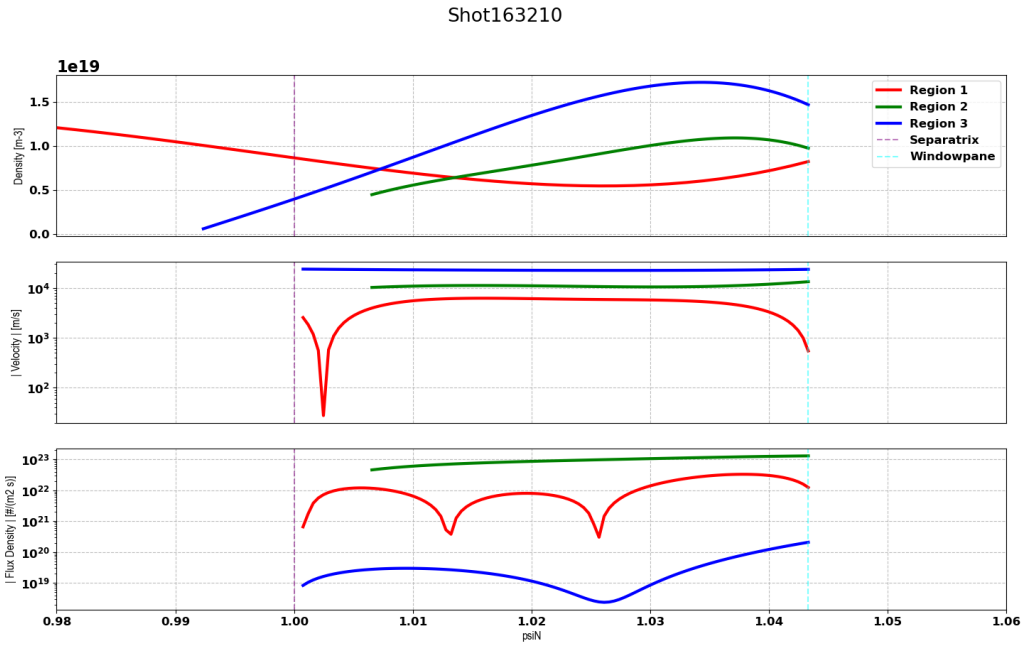


Figure D.13: Electron density, velocity, and Flux density estimation at regions 1, 2 and 3

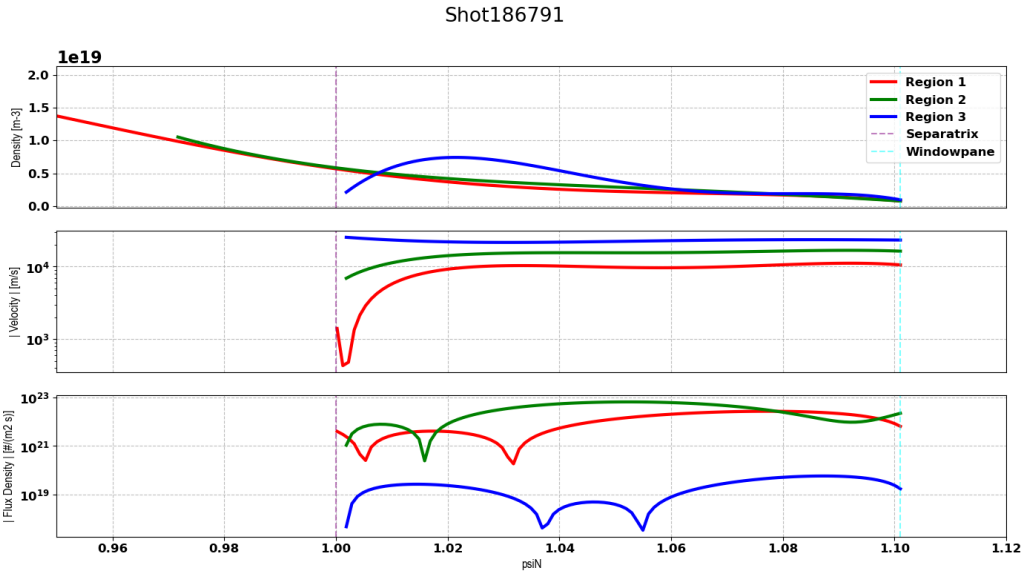


Figure D.14: Electron density, velocity, and Flux density estimation at regions 1, 2 and 3

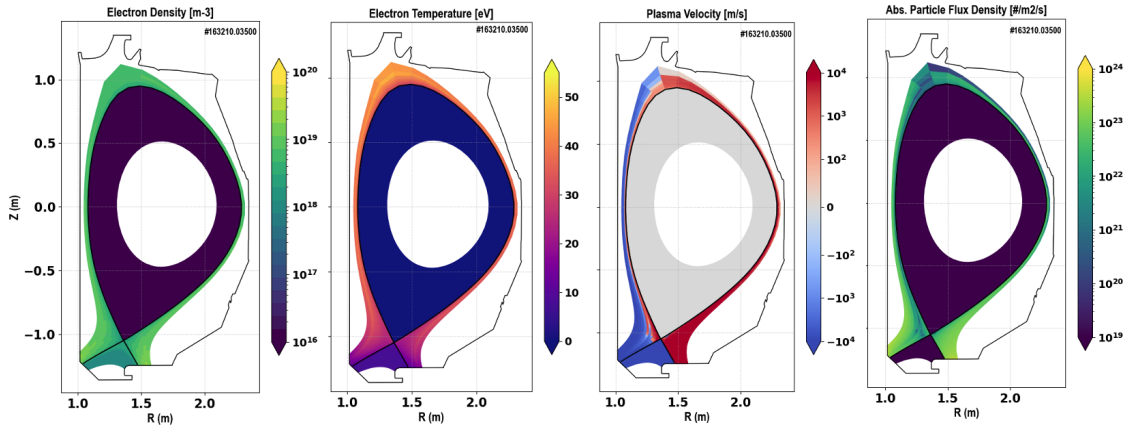


Figure D.15: 2D measurements of Density, Velocity, temperature and flux of Shot 163210

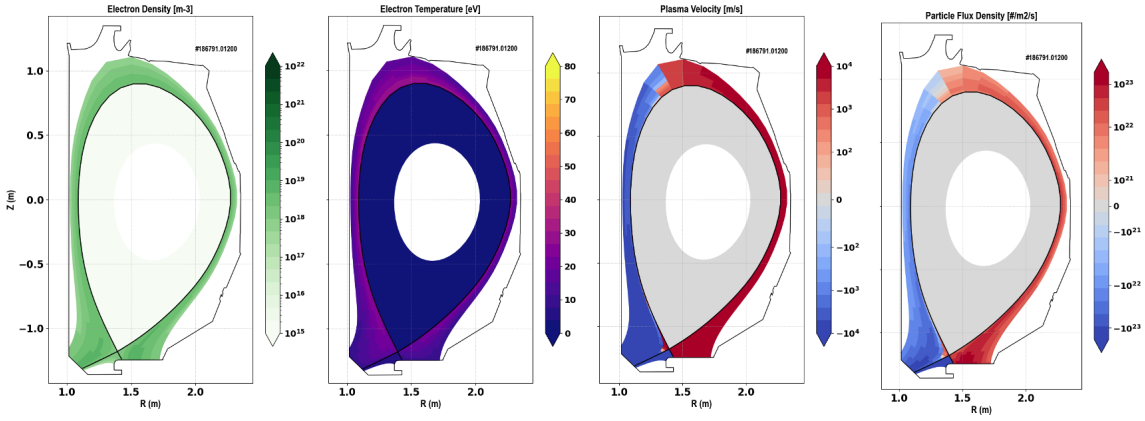


Figure D.16: 2D measurements of Density, Velocity, temperature and flux of Shot 186791

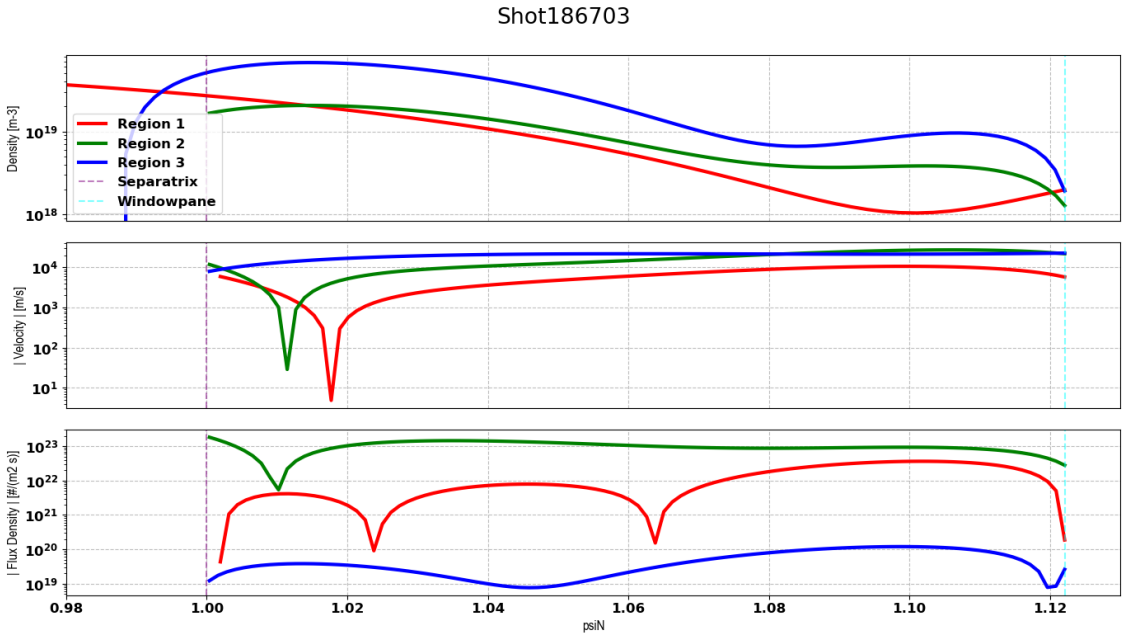


Figure D.17: Flux density estimation at regions 1, 2 and 3

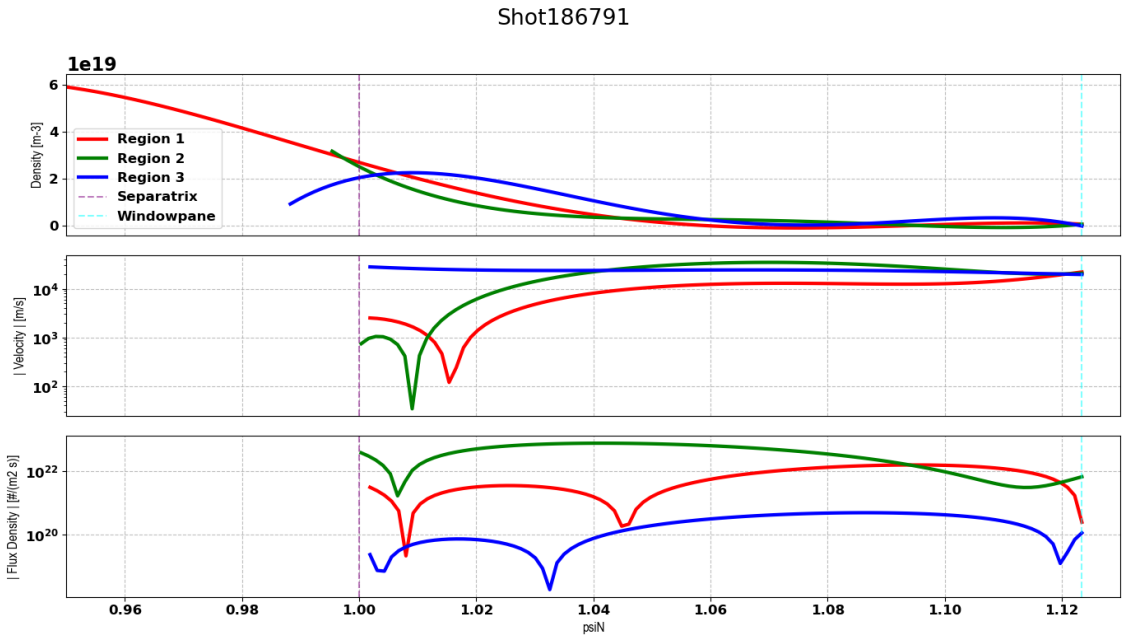


Figure D.18: Electron density, velocity, and Flux density estimation at regions 1, 2 and 3

The figures reveal that, in the forward B_T plasma discharge, the overall density is lower, but there is a higher velocity in the same regions, resulting in a similar flux presence in those regions. It's noteworthy that the measured flux at the windowpane region for the forward B_T discharge is lower compared to the flux in the other plasma discharge. Additionally, Figures D.20 and D.19 present 2D plots for Shot # 186791 and Shot # 186703, respectively. These plots illustrate the distribution of electron density (n_e), electron temperature (T_e), plasma velocity (v), and particle flux (Γ) throughout the tokamak, as simulated by OEDGE. Importantly, the negative values observed in the flux, as shown in Figures D.20 and D.19, stem from the negative plasma velocity values, indicating a reversal in the flow of particles within the SOL.

D.3.2 LSN Floor Configuration

Lower Single Null (LSN) Floor as seen in Figure 4.13(c) is a divertor geometry represented with a flat plate with a baffle present near the target. This divertor geometry is considered the when contain particles need to be exhausted using pumps and is reflected with a lower GRP value. In the name of completeness, there are four LSN Floor shots in L mode and H mode configurations and in forward B_T and Reverse B_T that will be discussed here.

L mode Plasma Discharges

Here, our examination centers on Shot # 174803 and Shot # 167234, which correspond to LSN Floor plasma shots under forward and reverse B_T configurations in Lmode, respectively. Section D.1 provides exhaustive details on these shots and their associated global parameters. Figures D.21 and D.22 showcase the distribution of electron density (n_e), plasma velocity (v), and particle flux (Γ) across all regions, with the separatrix and windowpane visibly marked. The figures reveal that, in the forward B_T plasma discharge Shot #174803, the overall density is lower in all regions, whereas in the other shot the density is higher in Region 3, that is at the divertor,

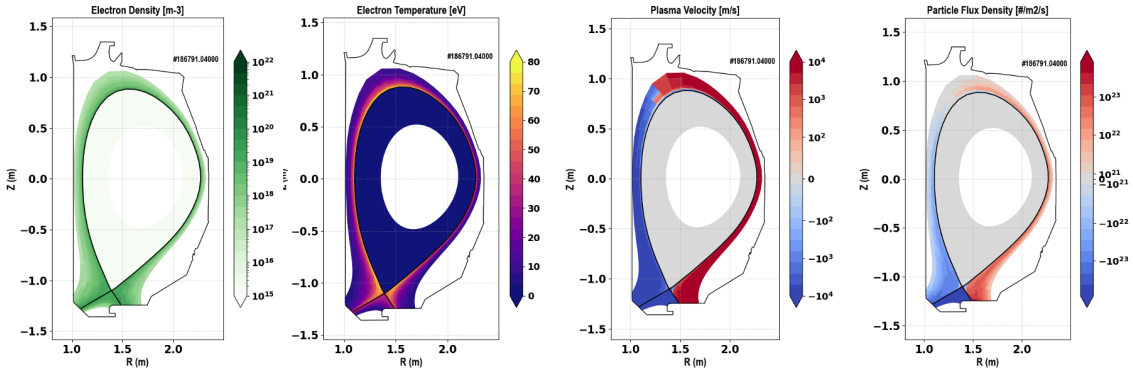


Figure D.19: 2D measurements of Density, Velocity, temperature and flux

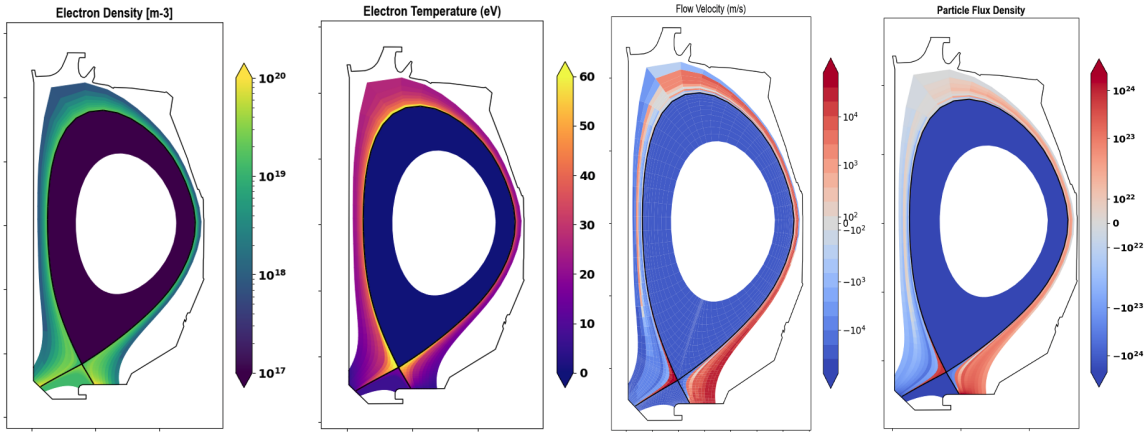


Figure D.20: 2D measurements of Density, Velocity, temperature and flux



Figure D.21: Electron density, velocity, and Flux density estimation at regions 1, 2 and 3

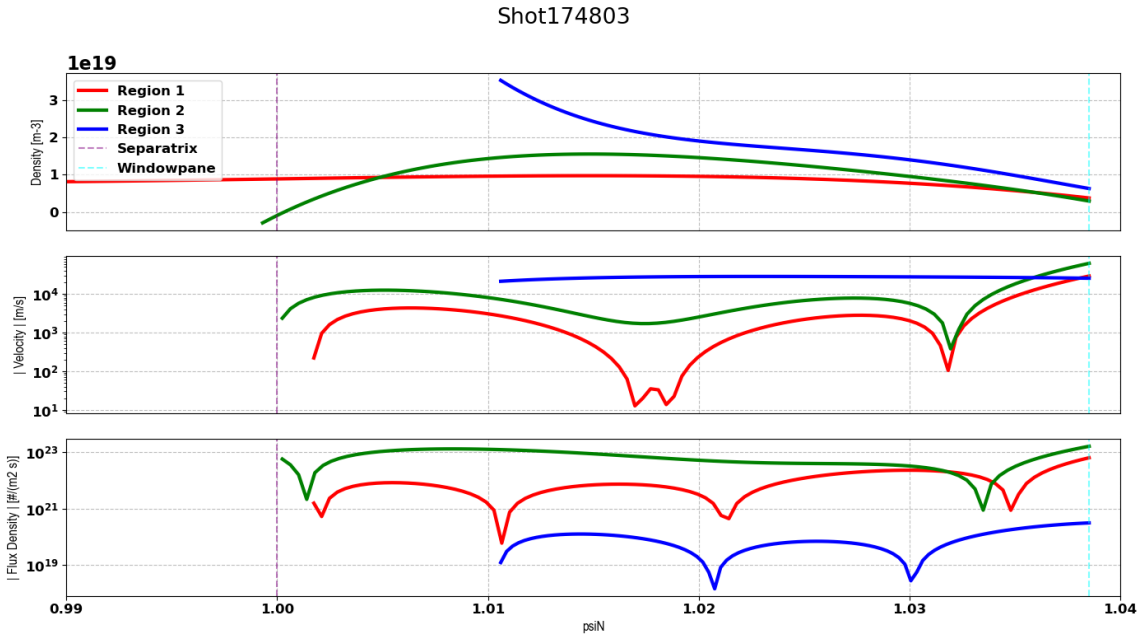


Figure D.22: Electron density, velocity, and Flux density estimation at regions 1, 2 and 3

but there is a higher velocity in the same regions, resulting in a similar flux presence in those regions. It's noteworthy that the measured flux at the windowpane region for the forward B_T discharge is lower compared to the flux in the other plasma discharge. Additionally, Figures D.23 and D.24 present 2D plots for Shot # 167234 and Shot # 174803, respectively. These plots illustrate the distribution of electron density (n_e), electron temperature (T_e), plasma velocity (v), and particle flux (Γ) throughout the tokamak, as simulated by OEDGE. Importantly, the negative values observed in the flux, as shown in Figures D.23 and D.24, stem from the negative plasma velocity values, indicating a reversal in the flow of particles within the SOL.

H mode Plasma Discharges

Here, our examination centers on Shot # 175937 and Shot # 167245, which correspond to LSN Floor plasma shots under forward and reverse B_T configurations in H-mode, respectively. Section D.1 provides exhaustive details on these shots and their associated global parameters. Figures D.26 and D.25 showcase the distribution of electron density (n_e), plasma velocity (v), and particle flux (Γ) across all regions, with the separatrix and windowpane visibly marked.

The figures reveal that, in the forward B_T plasma discharge Shot #175937, the overall density is lower in all regions, however a higher velocity in the same regions, results in a similar flux presence in those regions. It's noteworthy that the measured flux at the windowpane region for the forward B_T discharge is lower compared to the flux in the other plasma discharge.

Additionally, Figures D.27 and D.28 present 2D plots for Shot # 167245 and Shot # 175937, respectively. These plots illustrate the distribution of electron density (n_e), electron temperature (T_e), plasma velocity (v), and particle flux (Γ) throughout the tokamak, as simulated by OEDGE. Importantly, the negative values observed in the flux, as shown in Figures D.27 and D.28, stem from the negative plasma velocity values, indicating a reversal in the flow of particles within the SOL.

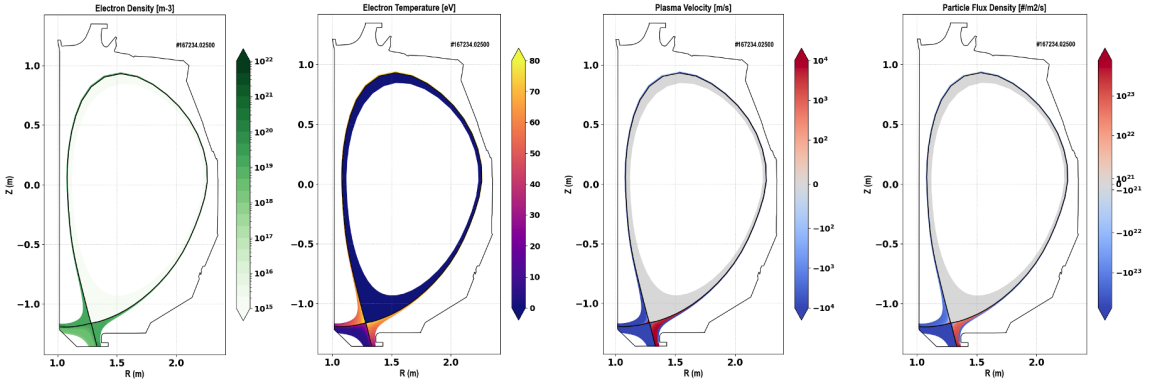


Figure D.23: 2D measurements of Density, Velocity, temperature and flux

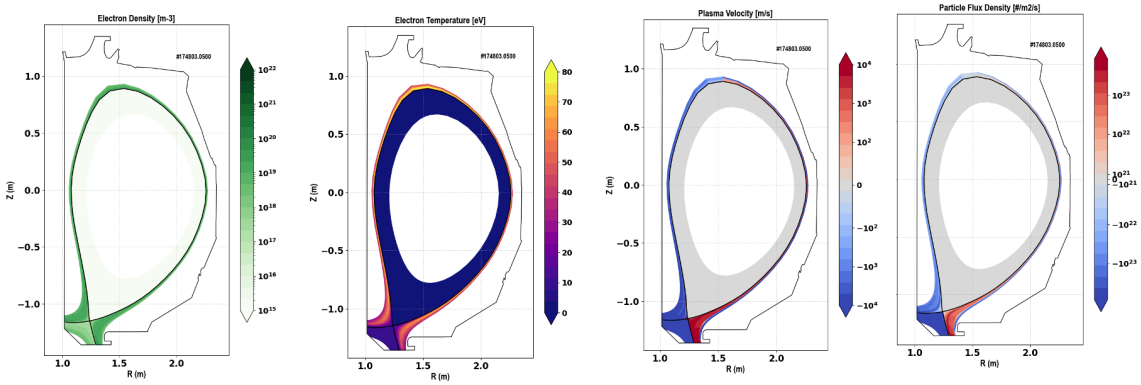


Figure D.24: 2D measurements of Density, Velocity, temperature and flux

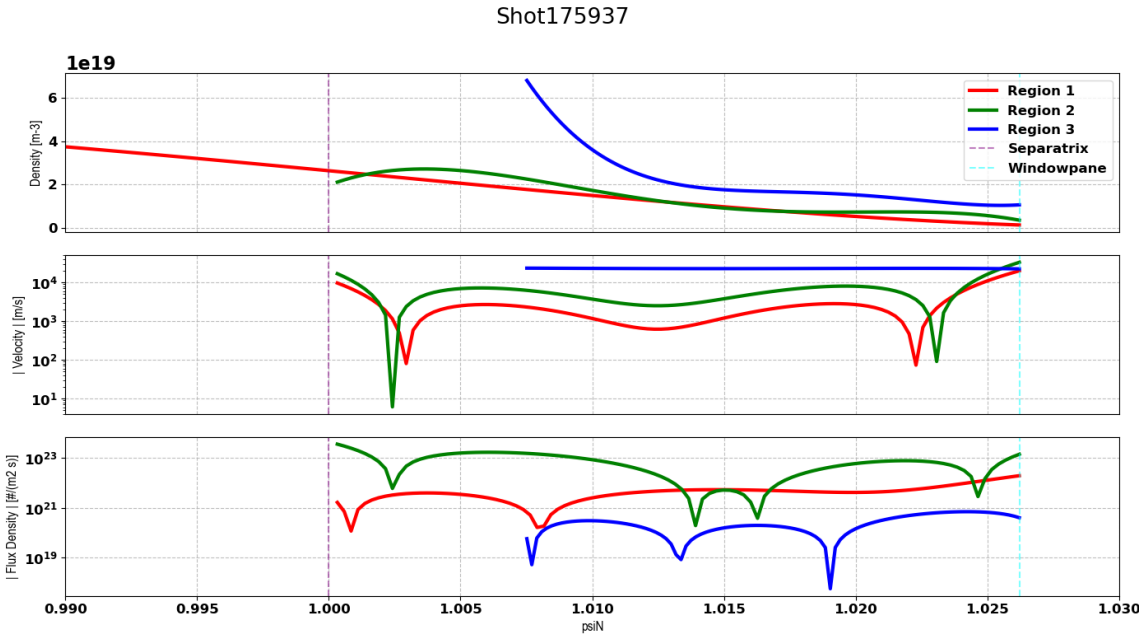


Figure D.25: Electron density, velocity, and Flux density estimation at regions 1, 2 and 3

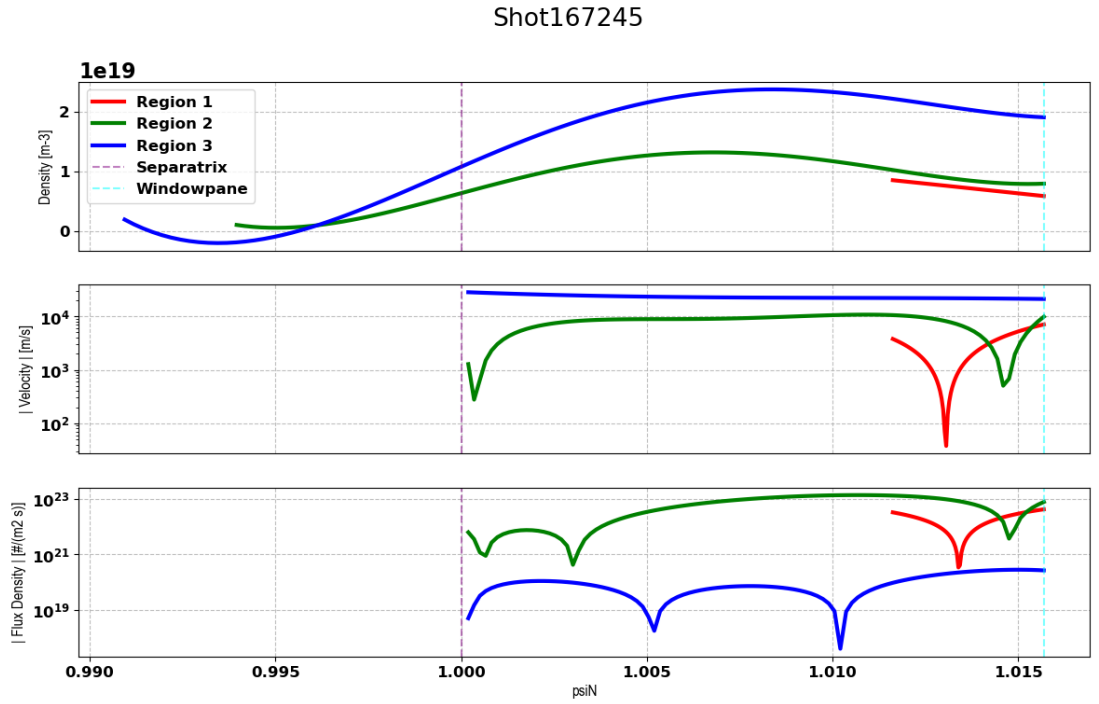
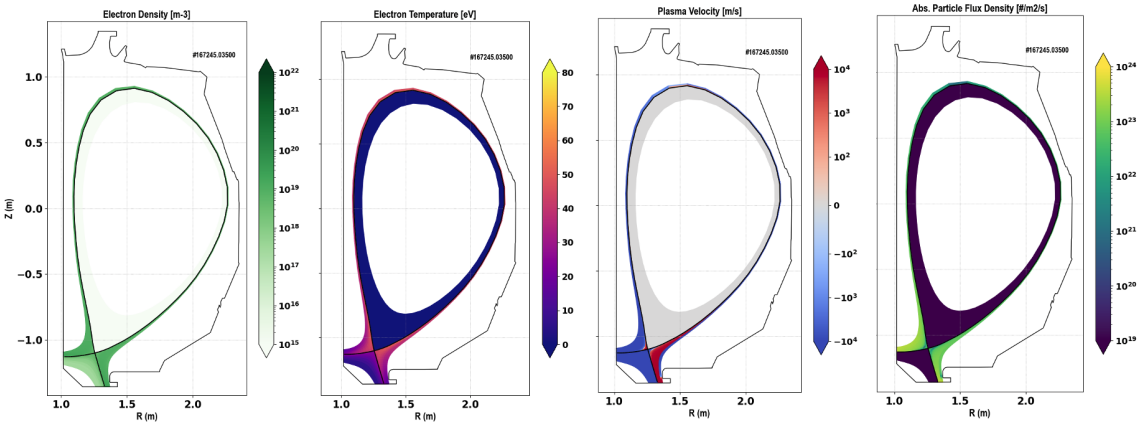
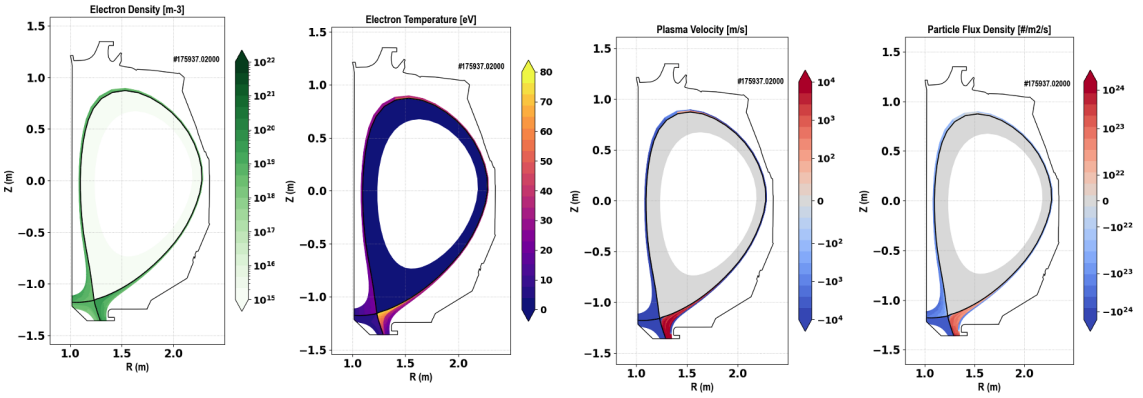


Figure D.26: Electron density, velocity, and Flux density estimation at regions 1, 2 and 3



22

Figure D.27: 2D measurements of Density, Velocity, temperature and flux



22

Figure D.28: 2D measurements of Density, Velocity, temperature and flux

A notation concerning the varied lengths of the measurements depicted in the figure is attributed to the grid dimensions established through the DG-Carre system. The absence of a uniform mesh structure gives rise to distinct array sizes for measurements in each region.

D.3.3 USN Floor Configuration

Upper Single Null (USN) Floor as seen in Figure 4.13(d) is a divertor geometry represented with a flat plate with a bottle-neck baffle structure near the target. This divertor geometry is considered the when contain particles need to be exhausted using pumps and is reflected with a lower GRP value. In the name of completeness, there are four USN Floor shots in L mode and H mode configurations and in forward B_T and Reverse B_T that will be discussed here.

L mode Plasma Discharges

Here, our examination centers on Shot # 179760 and Shot # 184533, which correspond to USN Floor plasma shots under forward and reverse B_T configurations in L-mode, respectively. Section D.1 provides exhaustive details on these shots and their associated global parameters. Figures D.29 and D.30 showcase the distribution of electron density (n_e), plasma velocity (v), and particle flux (Γ) across all regions, with the separatrix and windowpane visibly marked.

The figures reveal that, in the forward B_T plasma discharge Shot #179760, the overall density is higher in all regions, however a higher velocity in the same regions, results in a similar flux presence in those regions. It's noteworthy that the measured flux at the windowpane region for the forward B_T discharge is lower compared to the flux in the other plasma discharge. Additionally, Figures D.31 and D.32 present 2D plots for Shot # 179760 and Shot # 184533, respectively. These plots illustrate the distribution of electron density (n_e), electron temperature (T_e), plasma velocity (v), and particle flux (Γ) throughout the tokamak, as simulated by OEDGE. Importantly,

the negative values observed in the flux, as shown in Figures D.31 and D.32, stem from the negative plasma velocity values, indicating a reversal in the flow of particles within the SOL.

H mode Plasma Discharges

Here, our examination centers on Shot # 179760 and Shot # 179974, which correspond to USN Floor plasma shots under forward and reverse B_T configurations in L-mode, respectively. Section D.1 provides exhaustive details on these shots and their associated global parameters. Figures D.34 and D.33 showcase the distribution of electron density (n_e), plasma velocity (v), and particle flux (Γ) across all regions, with the separatrix and windowpane visibly marked.

The figures reveal that, in both the forward B_T and reverse B_T plasma discharges, the overall density, velocity is similar in all regions, resulting in a similar flux presence in those regions. It's noteworthy that the measured flux at the windowpane region for the forward B_T discharge is lower compared to the flux in the other plasma discharge. Additionally, Figures D.36 and D.35 present 2D plots for Shot # 179760 and Shot # 179974, respectively. These plots illustrate the distribution of electron density (n_e), electron temperature (T_e), plasma velocity (v), and particle flux (Γ) throughout the tokamak, as simulated by OEDGE. Importantly, the negative values observed in the flux, as shown in Figures D.36 and D.35, stem from the negative plasma velocity values, indicating a reversal in the flow of particles within the scrape-off layer (SOL).

A notation concerning the varied lengths of the measurements depicted in the figure is attributed to the grid dimensions established through the DG-Carre system. The absence of a uniform mesh structure gives rise to distinct array sizes for measurements in each region.

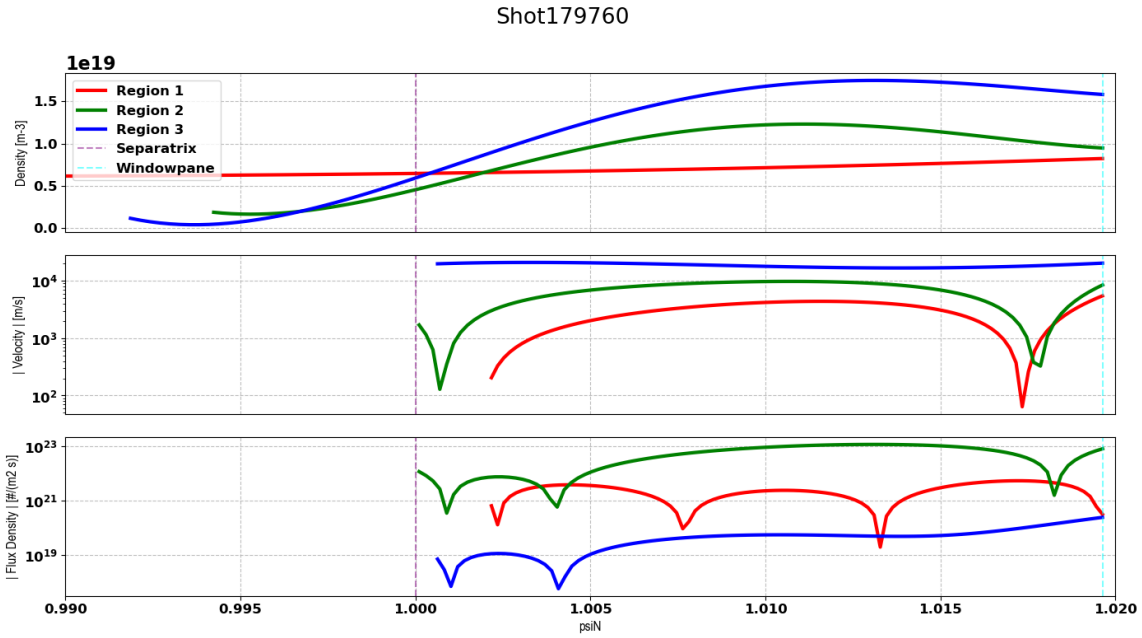


Figure D.29: Electron density, velocity, and Flux density estimation at regions 1, 2 and 3

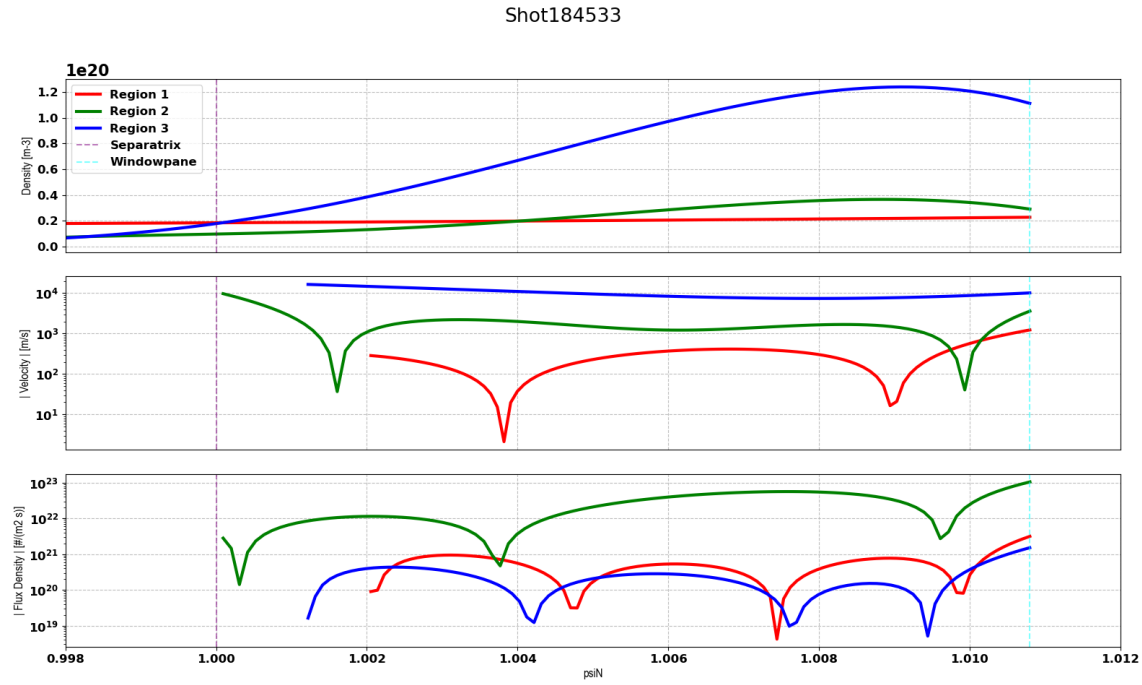
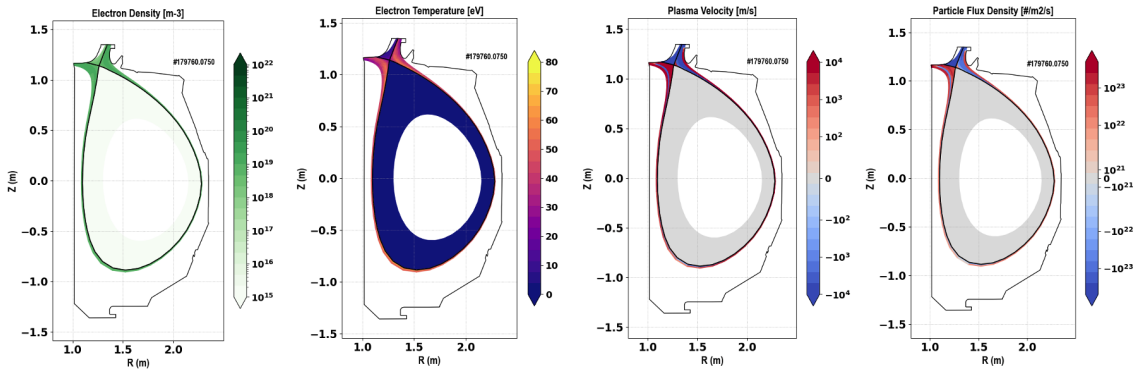
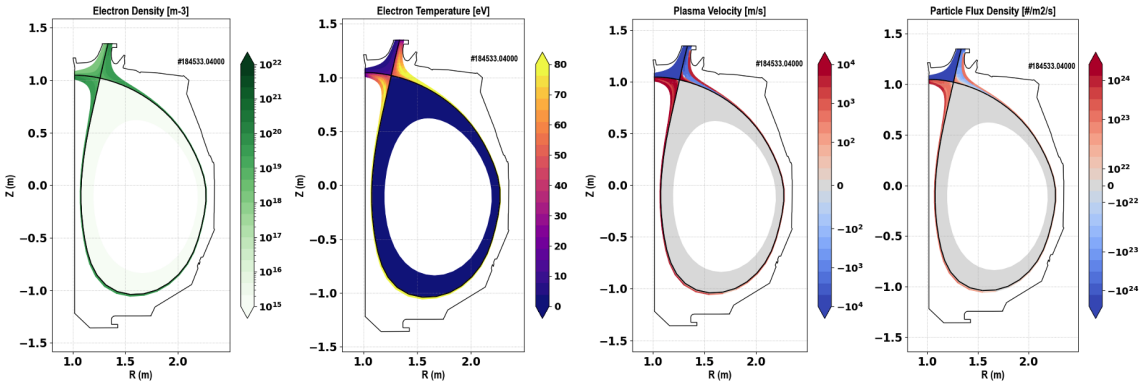


Figure D.30: Electron density, velocity, and Flux density estimation at regions 1, 2 and 3



22

Figure D.31: 2D measurements of Density, Velocity, temperature and flux



22

Figure D.32: 2D measurements of Density, Velocity, temperature and flux

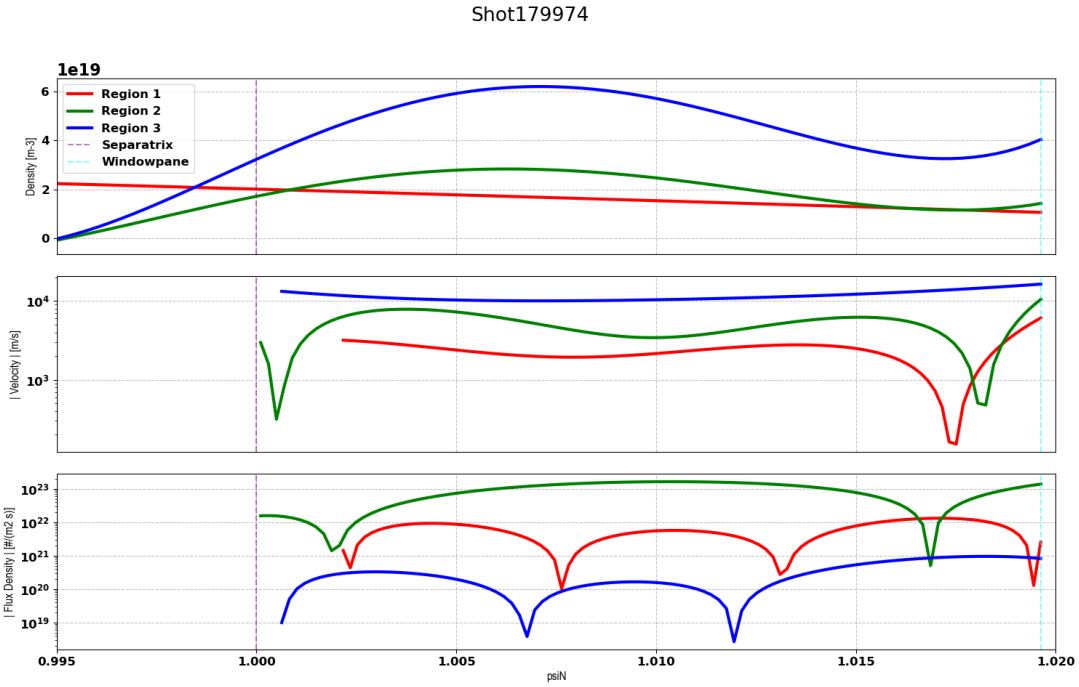


Figure D.33: Electron density, velocity, and Flux density estimation at regions 1, 2 and 3

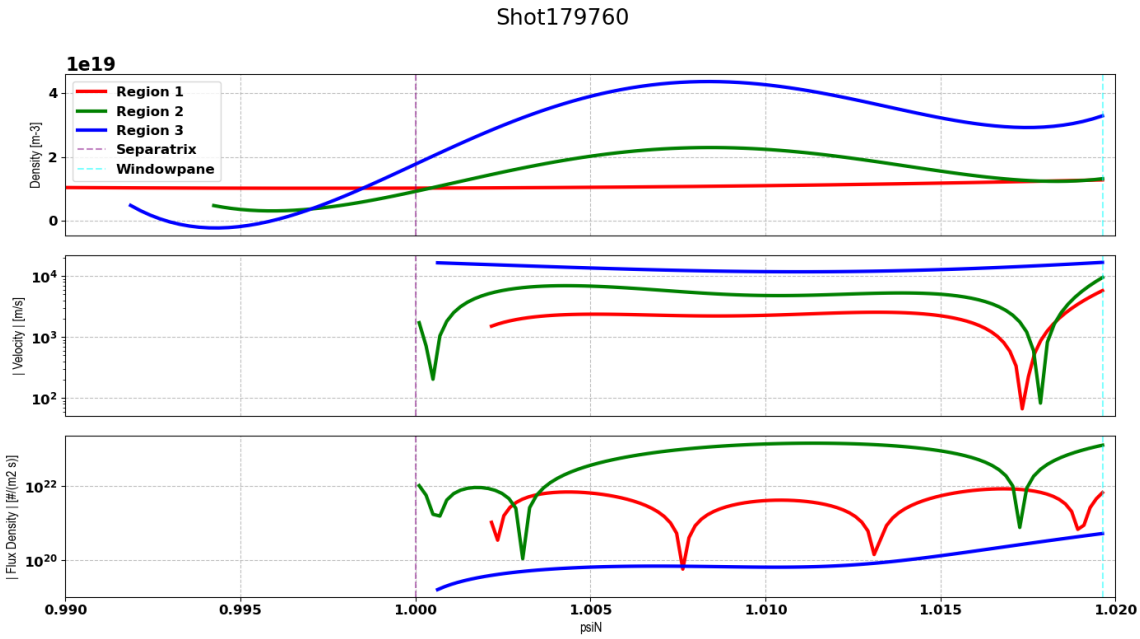
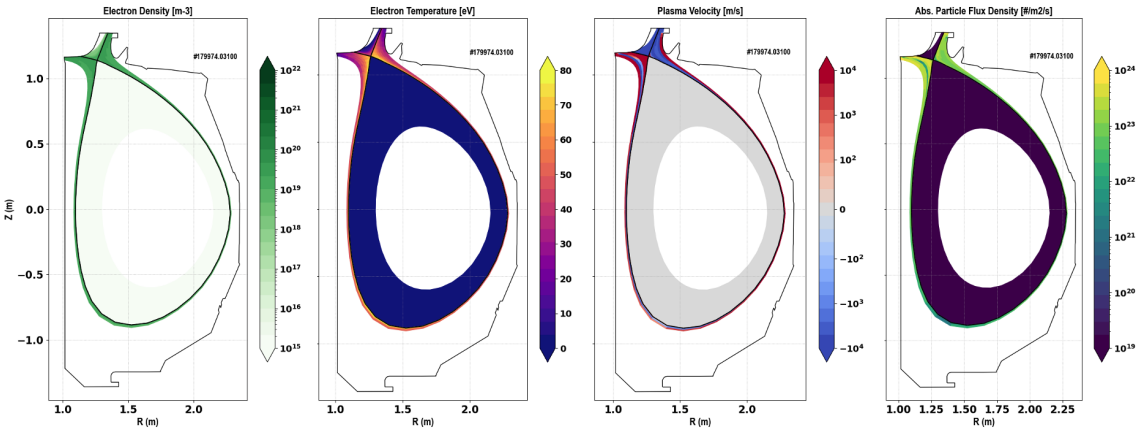
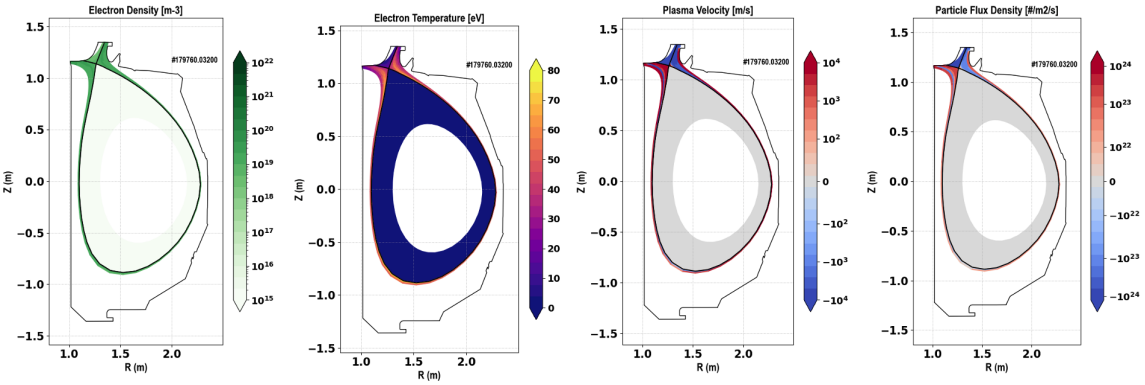


Figure D.34: Electron density, velocity, and Flux density estimation at regions 1, 2 and 3



22

Figure D.35: 2D measurements of Density, Velocity, temperature and flux



22

Figure D.36: 2D measurements of Density, Velocity, temperature and flux

Appendix E

DIII-D Mini proposal for an experiment

Title: Impact of divertor geometry on divertor and main chamber recycling **Collaborator(s):** K.Davda, E. Unterberg, P. Stangeby, M. Shafer, L. Casali, J. Nichols, A. Leonard, J. Watkins, D. Rudakov, F. Laggner, and F. Scotti

E.1 Purpose of the Experiment

- Assess effect of magnetic and physical closure on neutral leakage & main chamber in L mode and H mode
- Determine the impact of outer gap & x-point height variation on mid-plane and divertor neutral pressure
- Estimate the role of leaked neutrals in inducing main chamber recycling

E.2 Background

Next step fusion devices need to have an optimized divertor that is capable of handling increased heat and particle flux to mitigate surface damage on the divertor

target [1]. A way to optimize the divertor is by increasing divertor closure, which depends on physical baffling and magnetic parameters [2]. As the closure increases, the neutral compression (Pdivertor/Pmain-chamber) increases [2] along with an increase in neutral density in the divertor region that aids in neutral recirculation [3], energy dissipation [4] and in detachment onset [4-7]. However, divertor closure does not effectively trap neutrals as they tend to leak/escape from the divertor towards the main chamber through the SOL [2]. Increased neutral leakage could potentially increase localized fueling, plasma facing component (PFC) sputtering [2] and main chamber recycling (MCR) [8,9]; all of which has the potential to deteriorate plasma confinement. Recently, neutral leakage was quantified using a divertor leakage parameter (DLP) between two divertor types – open (LSN floor) and closed (USN floor) in DIII-D. This measurement found that DLP decreases as divertor undergoes closure and the rate of change of neutral leakage in the more closed divertor configuration is less compared to the open configuration [7].

In this work, we will systematically vary outer gap and x-point height in four different divertor configuration on DIII-D with different degree of closure, i.e., LSN floor, LSN shelf, USN floor, closed vertical target (USN edge). Firstly, the variation of outer gap would help achieve an understanding of the impact of plasma edge to the PFC near the main chamber that could potentially induce MCR and impact the neutral leakage. Secondly, the x-point plays an important role in power dissipation at the target though magnetic flux expansion. Varying the x-point height could potentially change the rate at which neutrals are formed, recycled, and leaked from the divertor region. Lastly, the goal of neutral leakage estimation in these variations will be achieved using a modified version of the Window Frame Analysis (WFA) [10] that will measure neutral flux in the main chamber and in the divertor using a slew of diagnostics present at DIII-D, viz., neutral pressure gauge at the midplane, LLAMA, RCP, Filterscope, Thomson Scattering, and Langmuir probes. In this work, we estimate neutral leakage by taking the ratio of the neutral flux at the main chamber to the neutral flux at the divertor.

This experiment will provide data that will help validate neutral modelling. It will also inform the role of magnetic geometry with respect to the divertor baffles for neutral leakage. This will also help inform the role of leaked neutrals in inducing MCR.

1. Stangeby & Leonard, Nucl. Fusion 51 (2011) 063001
2. Loarte, Plasma Phys. Control. Fusion 43 (2001) R183-R224
3. Kukushkin & Pacher Nucl. Fusion 56 (2016) 126012
4. Sang et. al, Plasma Phys. Control. Fusion 59 (2017) 025009
5. Casali et. al., Contributions to Plasma Physics 58 (2018) 725– 731
6. Moser et.al., Nuclear Materials and Energy 19 (2019) 67–71
7. Casali et. al., Nucl. Fusion 60 (2020) 076011
8. Niemczewski et. al., Nucl. Fusion 37 (1997) 151
9. LaBombard et. al., Nucl. Fusion 40 (2000) 2041
10. Whyte et. al., Plasma Phys. Control. Fusion 47 (2005) 1579

E.3 Experimental Approach

The aim for this experiment is to quantify neutral leakage and main chamber recycling (MCR) due to divertor closure along with variation in outer gap and x-point height in both L mode and H mode. This will be analyzed using the window frame analysis (WFA) which estimates neutral leakage by taking the ratio of neutral particle flux in the main chamber, I_{wall}, to neutral particle flux at the divertor target, I_{div}, for each outer gap and density variation.

The experiment is to be carried in the Upper single null (USN) configuration. This will help assess the impact of physical geometrical divertor baffles on neutral leakage along with the magnetic closure applied via outer gap and x-point height variation.

Establish plasma USN discharge with similar parameters as seen in Shot 186198. We will have 2 strike point throughout the half day. The first strike point will be on the horizontal divertor target surface of the USN and the other will on the outer edge of the USN divertor near the bottle neck area. For each strike point we will keep same separatrix density $\approx 5 \times 10^{19} m^{-3}$. The variable in the experiment will be outer gap and x-point height with fixed strike point. We will investigate the neutral particle flux in the main chamber and in the divertor region while the variables of the experiment are varied.

E.4 Resources

- +/− 2.05T, 1.3MA
- 6MW neutral beams
- Gas: GAS C – D2, GAS D – N2 / GAS E – N2
- Cryopumps: Off
- IC – coil requirements: Standard EFC

E.4.1 Diagnostic Requirements

Essential:

- Filterscope (divertor, mid-plane)
- ASDEX Gauges
- REciprocating LP at the midplane

- Floor Langmuir Probes
- Thomson Scattering (extended core, tangential, divertor)
- MDS Spectrometer
- CER

Important:

- Tangetial TV
- Bolometers

E.4.2 Analysis Requirements

Provide list of roles for executing the experiment on the day, and who will do them.

- MP author: Davda
- Session Leader: Davda / Unterberg
- Diagnostic Coordinator: Nichols
- Inter-Shot Analysis: Davda
- Physics operator: Shafer
- Reciprocating Probe Guru: Boedo
- Beam Operator: Wilcox
- Spectroscopy Setup: Wilcox, McLean, Scotti
- Filterscope: Herfindal
- Pressure Gauges: Shafer

Provide list of analysis tasks to be pursued after experiment completed, and who will do them (please also review analysis needs with your physics area meeting once experiment has been run).

- MDS Analysis: Davda, Unterberg
- LP Analysis: Davda
- TS and FSCOPE analysis: Davda, Herfindal
- CERFIT: Chrystal
- ASDEX analysis: Davda

E.5 Experimental Plan

Run in L mode initially: One shot will fulfill 3 conditions: So total shots: 6

Redo in H mode: One Shot will fulfill 2 conditions: So total shots: 12

Total 1/2 day shots: 18. See Figure E.1 and Table E.1

E.6 Analysis plan and Deliverables

1. Assess the role of outer gap and x-point height variation on neutral leakage
2. Assess main chamber particle flux & compare it with divertor particle flux using window frame analysis
3. Compute Decay length incorporating RCP & TS Te
4. Effect of neutral leakage on main chamber recycling
5. Interpretive analysis using OEDGE modeling

E.7 Radiation Awareness

A site boundary limit of 600 μrem is requested

Table E.1: Shot plan during the experiment day

	Outer Gap [m] →	2.22	2.25	2.28
	X-point Height [m] ↓			
USN Floor				
	0.1	Condition #1	Condition #2	Condition #3
	0.2	Condition #4	Condition #5	Condition #6
	0.3	Condition #7	Condition #8	Condition #9
USN Edge				
	0.1	Condition #10	Condition #11	Condition #12
	0.2	Condition #13	Condition #14	Condition #15
	0.3	Condition #16	Condition #17	Condition #18

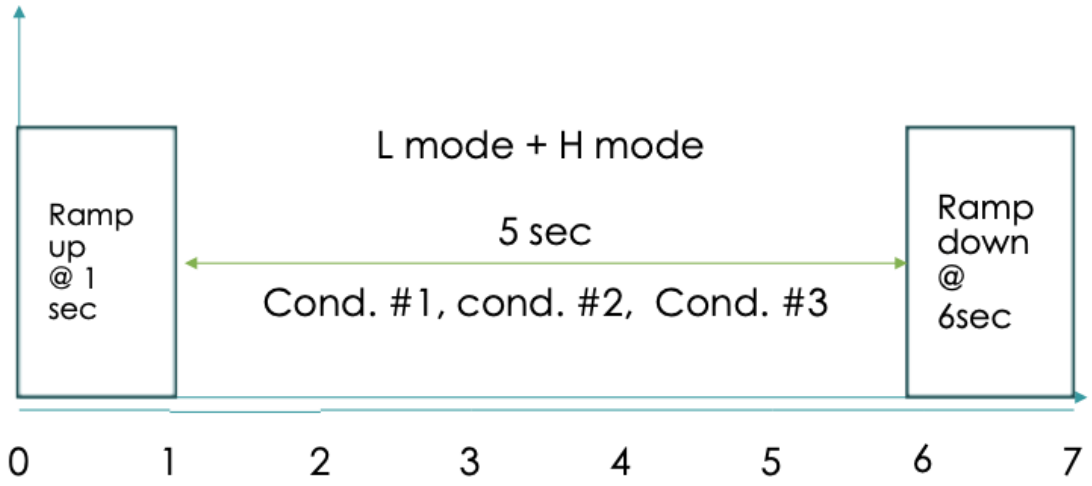


Figure E.1: Shot plan review and the conditions being met during one plasma discharge

Appendix F

Divertor Detachment

This appendix goes into details about physics of detachment. This optimization of divertor using detachment is planned to be used for future reactor level situations. This sections digs into the details of detachment.

Underlying Mechanism of the Detached Regime

An explanation of the rollover of the plasma flux on the divertor target was proposed by Stangeby in 1993 that postulated the use of large pressure drop between the main chamber (upstream) and the divertor region by ion-neutral collisions to reduce the particle flux impinging on the target Stangeby [1993]. The neutral ionization source Γ_{ion} equalizes the plasma flux to the wall Γ_t and the volumetric recombination Γ_{rec} which is given by Equation F.1 below. When the Γ_{rec} is absent, the only way to decrease the plasma flux to the wall Γ_t is by reducing the ionization source Γ_{ion}. The plasma recycling process is primarily fueled by the power from the core that flows to the target through ionization and recombination processes can be analyzed through a global power balance in the edge, as shown in equation F.2.

$$\Gamma_{ion} = \Gamma_t + \Gamma_{rec} \tag{F.1}$$

$$Q_{SOL} = Q_{imp} + Q_H + Q_{cx} + \gamma\, T_t\, \Gamma_t \tag{F.2}$$

$$Q_{ion} = E_{ion}\, \Gamma_{ion} \tag{F.3}$$

$$Q_{cx} = E_{cx}\, \Gamma_{ion} \tag{F.4}$$

In Equation F.2, Q_{SOL} is the power flux coming in the SOL from the core through the separatrix, Q_{imp} is the impurity radiation loss, Q_H is the power loss due to hydrogen ionization, Q_{cx} is the power delivered to the wall through neutrals – ion charge exchange, and $\gamma\, T_t\, \Gamma_t$ represents the kinetic energy of the plasma transferred onto the wall with effective plasma temperature T_t, and effective sheath transmission factor γ.

Q_H is related to Γ_{ion} through Equation F.3, also Q_{cx} is related to Γ_{ion} through Equation F.4. In equation F.4, E_{cx} is the effective energy delivered through the charge exchange process per ionization process. The particle and heat diffusivities are comparable in a dense divertor plasma where the neutral related transport in particle and energy are equivalent. Hence in the dense divertor, E_{cx} is estimated to be present at a temperature of around 3-5 eV in the ionization region. From Equations F.2 and F.3, we get the following equation:

$$\Gamma_t = \frac{Q_{SOL} - Q_{imp} - (E_{ion} + E_{cx})\, \Gamma_{rec}}{(E_{ion} + E_{cx}) + \gamma\, T_t} \tag{F.5}$$

With $E_{ion} \approx 30eV > E_{cx} \approx 3 - 5eV$, and $T_t \approx 1eV$ for a detached regime, the plasma flux on the wall is given by:

$$\Gamma_t = \frac{Q_{SOL} - Q_{imp}}{E_{ion} - \Gamma_{rec}} \tag{F.6}$$

From Equation F.6, we can conclude that the plasma flux on the target can only be reduced by either increasing the volumetric recombination, Γ_{rec}, and/or by increasing the impurity radiation loss, Q_{imp}, in a detached divertor regime.

Onset to Detachment

As seen in Equation F.6, the key to divertor detachment is the start of plasma recombination and the impurity radiation loss in a divertor. However, plasma recombination results in a significantly lower Γ_{ion} if the Γ_{ion} is below the minimum level, i.e., Γ_{ion}^{min}. While the plasma pressure at the separatrix remain the same, the power going to the inner and outer divertor (same as 'inside' and 'outside' divertor seen in Figure 2.3) varies due to the edge plasma transport. As a result, at the onset of detachment, the inner divertor is detached first followed by the outer divertor. Once the inner divertor is detached, the neutrals flow from the inner towards the outer divertor through the private flux region below the X – point in the divertor Kukushkin and Pacher [2006]. With additional neutrals in the outer divertor, plasma back flows from the divertor to the SOL resulting in lowered recycled heat flux at the outer divertor. Also, when the inner divertor is completely detached, MARFE-like structures are developed near the X point that stop the power radiating from the SOL towards the outer divertor, thus reducing the recycled heat flux at the outer divertor and resulting an onset to complete divertor detachment Krasheninnikov and Kukushkin [2017].

For a given magnetic flux tube, an onset to detachment is determined by Krasheninnikov [2018]:

$$\frac{P_{up}}{q_{recycl}} \gtrsim \left.\frac{P_{up}}{q_{recycl}}\right|_{\text{crit}} \tag{F.7}$$

where, P_{up} is the upstream plasma pressure and q_{recycl} is the heat flux entering the recycling region. Equation F.7 states that detachment onset occurs if the ratio of

upstream plasma pressure to the heat flux entering the recycling region is greater to or equal to its critical value Krasheninnikov [2018].

Transition to Detachment

Transition to detachment depends primarily on the energy flux Umansky et al. [1998] entering the recycling region (q_{recycl}) which depends on the width of the SOL. So, it can be stated that the transition to detachment depends on the width of the SOL (Δ_{SOL}), i.e., on the cross-field plasma transport upstream and its impurity radiation loss in the Δ_{SOL}. In both L mode Rudakov et al. [2005], Umansky et al. [1998], Wiesen et al. [2011] and H mode plasma Carralero et al. [2014], Sun et al. [2015] with high energy density, the Δ_{SOL} increases when approaching detachment due to intermittent impurity radiation in the form of blobby plasma transport Zweben et al. [2007]. In conclusion, as Δ_{SOL} increases, the chances of divertor becoming detached increases, which further increases Δ_{SOL} and hence bifurcation-like transition occurs in divertor detachment Krasheninnikov and Kukushkin [2017].

There are two ways the divertor transitions to detached regime: bifurcation-like increment (Figure F.1); and gradually increment of plasma flux (Figure F.2). Figure F.1 shows the bifurcation like alteration of electron temperature at the outer strike point in DIII-D with increments in plasma density where there is a sudden drop in temperature – seen as the yellow band in the image McLean et al. [2015]. Bifurcation-like transition to detachment (as seen in Figure F.1) is due to impurity radiation Krasheninnikov [1997], Hutchinson [1994] that is produced by strong radiating structures (such a MARFE Lipschultz et al. [1984]) that are formed near the X point (Neuhauser et al. [1986]). 2D modelling suggest that an increase in neon impurity results in smooth reduction of plasma flux on the divertor target and promotes divertor detachment by preventive developments of thermal instabilities at the divertor Krasheninnikov and Kukushkin [2017].

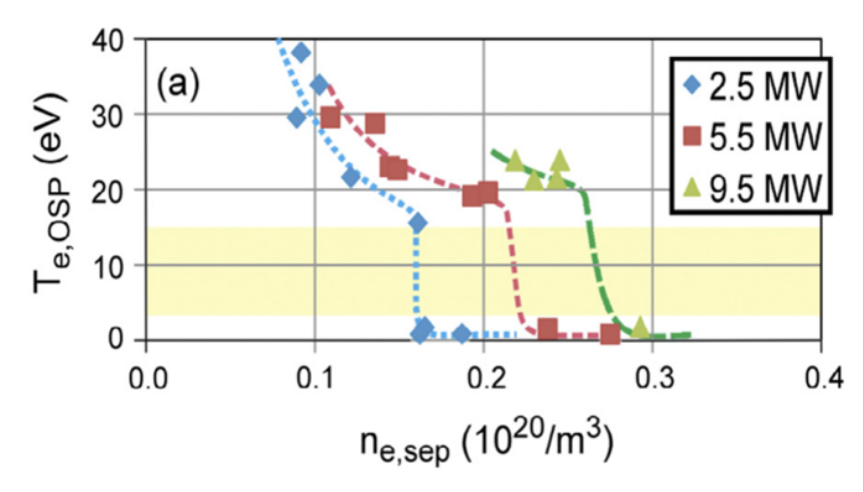


Figure F.1: Transition to detachment through bifurcation like process with increasing plasma density at DIII-D. Image from McLean et al. [2015]

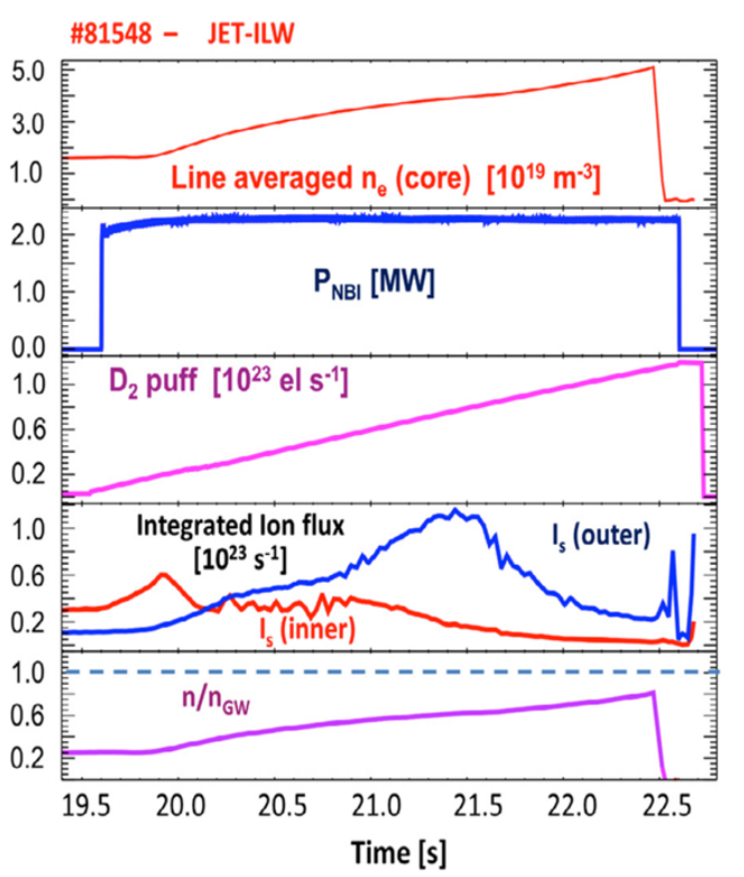


Figure F.2: Gradual transition to detachment in JET-ILW with time. Image from Huber et al. [2013]

Another reason, apart from impurity radiation loss, for bifurcation like transition to detachment is the breakdown of quasi-equilibrium processes between the absorption and ionization on the PFC. With the fuel (hydrogen) being trapped in the PFC, with processes like desorption, there may be, large release in gas that may cause bifurcation like jump to detachment Nakano et al. [2006], Krasheninnikov and Kukushkin [2017].

Figure F.2 shows the gradual increase in plasma flux on both the inner and outer divertor geometry in JET-ILW, also with increments in plasma density Huber et al. [2013]. It shows a L mode discharge in JET-ILW. With constant input power and gas fueling into the inner divertor leg, the plasma density was raised consistently. The ion flux measured in the outer divertor is seen to be decreasing while the inner divertor leg seems to have a constant ion flux, seemingly pointing to the fact that the inner divertor leg is partially detached while the outer divertor is not. As the density increases, while the neutral pressure continues to rise, the ion neutral flux to the inner divertor falls. Once that happens, the outer divertor ion flux saturates around 21.5 seconds, signaling the gradual transition to detachment Krasheninnikov and Kukushkin [2017].

Transients and Effects of Drifts During Divertor Detachment

Transient effects produced in detached divertor are not necessarily seen in attached divertor conditions. There are three main types of transient effects noticed in the detached divertor regime: (1) Self Sustained Oscillations (SSO); (2) the current-convective 'rippling' instability; and (3) Edge Localized Modes (ELMs) Berk et al. [1993], Nedospasov [1989].

One of the prominent phenomena observed in simulated ITER-like scenarios is the occurrence of Self-Sustained Oscillations (SSO) involving impurity ions at the parameters of the edge plasma. SSO exhibits a relatively slow frequency of 100Hz. As impurity ions undergo radiation and condensation, the thermal force generated propels the impurity ions toward regions of elevated temperature, transitioning the radiation-condensation instabilities into a transient non-linear phase known as SSO,

as outlined by Morozov in 1996 Morozov and Herrera [1996]. Remarkably, the SSO mechanism remains consistent for both low Z impurity (Nitrogen) and hydrogen fuel species, as demonstrated by Krasheninnikov and Kukushkin in 2017 Krasheninnikov and Kukushkin [2017]. In this process, low Z neutrals undergo ionization within a highly dense plasma region, subsequently flowing along open magnetic lines. This flow of ionized neutrals across flux tubes results in radiation and emission, causing a reduction in temperature and an increase in ionization rate within the flux tube. This phenomenon, characterized by the emission and radiation of ionized neutrals in the flux tube, is referred to as SSO Krasheninnikov and Kukushkin [2017].

The subsequent transient observed in the detached divertor is known as the current-convective instability, commonly referred to as the rippling effect. This phenomenon arises from the asynchronous detachment of the inner and outer divertors, generating an electrostatic potential between the attached and detached divertor regions. The combined current in the divertor results in an instability due to current-convective fluctuations, driven by radiation loss between the two divertor sides. The frequency of this instability is measured at 10 kHz, and in a tokamak, stabilization of the rippling effect is achieved upon the detachment of the outer divertor Krasheninnikov and Kukushkin [2017].

The final transient occurring during the detachment process is associated with Edge Localized Modes (ELMs), capable of delivering substantial heat and particle flux to the Plasma-Facing Components (PFC), posing a significant risk of material damage. ELMs are anticipated to expel approximately 1 MJ of energy per ELM from the core plasma onto the PFC, potentially penetrating the detached divertor regime Coster et al. [2015]. In this regime, impurity ions in the cold, non-radiating region predominantly occupy the divertor legs, maintaining detachment during inter-ELM transitions. However, during intra-ELM transitions, the presence of ELMs and the injection of 1 MJ of energy transform the once cold, non-radiative region into a hot and radiating state, leading to detachment failure Pigarov et al. [2016]. Consequently, it is anticipated that physical sputtering and erosion of high Z material will be significant

during the intra-ELM cycle, as supported by studies such as Dux et al. [2011], Harder et al. [2016], Krasheninnikov and Kukushkin [2017].

The impact of drifts on the detachment is due to the influence on the poloidal symmetry of the plasma parameters. The suitable choice for the toroidal field decides the equilibria between the inner and outer divertor. In an experiment done on DIII-D McLean et al. [2016], the evolution of electron temperature was measured with respect to the forward toroidal magnetic field and it was found that the inner divertor detaches before the outer one in the forward B_T direction whereas both inner and outer divertor detaches almost at the same time in reverse B_T configuration Huber et al. [2013].

Effect of Vertical and horizontal divertor target on detachment

To ensure an acceptable peak power load on the divertor in future tokamaks that would operate as operational reactor, it is essential for a significant portion of the power entering the plasma edge (usually around 60 %) to be dissipated in the divertor through volumetric mechanisms, such as hydrogen and impurity radiation, before reaching the divertor target. These desired losses can only be realized in a divertor characterized by low temperature and high density, situated close to plasma detachment Loarte [1997a], Kukushkin et al. [1999, 2001]. A detached divertor has lower power flux, lower ion flux on the target ad reduced material erosion Lumma et al. [1997], McCracken et al. [1998].

The primary distinction in a detached divertor lies in the impact of physical geometry. As previously mentioned, in the vertical divertor, recycling neutrals are emitted towards the separatrix, where ionization occurs at lower temperatures and higher densities. This facilitates the onset of detachment at lower main plasma densities, accompanied by higher volumetric energy losses. This phenomenon was observed in Alcator C-Mod, the first diverted tokamak to employ a vertical target geometry. Figure F.3 illustrates the differences in density and temperature for both horizontal and vertical target geometries. The electron temperature at the divertor

strike point is compared for similar discharges in Alcator C-mod, conducted on both the horizontal (flat-plate) and vertical (vertical-plate) sections of the divertor. Open symbols represent attached divertor plasmas, while full symbols correspond to partially detached divertor plasmas. The measured temperature at the main SOL separatrix is also presented for reference, indicating that no discernible impact of the divertor configuration on the SOL temperature is observed. Discharges with a vertical target achieve divertor detachment at 40 % lower density compared to those with a horizontal target Loarte et al. [1998], Loarte [1997a, 2001].

For vertical targets, density profiles exhibit peaks near the separatrix, while temperature profiles generally show lower values near the separatrix without pronounced peaks. This observation was initially documented in JET (refer to Vlases [1993], Campbell [1995] and has been substantiated by subsequent studies in other vertically diverted tokamaks (see LaBombard et al. [1995], Schneider et al. [1999], Asakura et al. [1999b]. In contrast, an outward-inclined horizontal target produces the opposite effect compared to a vertical divertor. Here, the recycling neutrals are directed away from the separatrix.

In the case of a horizontal target, the ionization of recycled neutrals takes place away from the separatrix, marking the initiation of detachment. Detachment is typically characterized by the Degree of Detachment (D.O.D), a normalized measure indicating an elevated ion flux with increasing upstream plasma density, while maintaining a constant power flux into the edge plasma, compared to the high recycling scaling. The introduction of D.O.D at JET was prompted by the lack of routinely available upstream density and temperature profile data resolved with plasma recombination.

The measured D.O.D is illustrated in Figure F.4, depicting the behavior of two comparable density scans for vertical and horizontal targets. In the case of the vertical target, detachment (D.O.D >1) initiates at the separatrix and progresses across the SOL with an increase in density, exhibiting all phases of detachment – onset detachment, partial detachment, and ultimately full detachment Loarte et al. [1998].

Conversely, the horizontal divertor target demonstrates plasma detachment occurring away from the separatrix, while the plasma at the separatrix remains attached until the formation of the divertor MARFE Loarte [2001].

The occurrence of asymmetric inner and outer divertor plasma results from divertor detachment. This asymmetry is not primarily attributed to the physical shape of the divertor but rather to plasma drifts. In the case of Fwd B_t, the power flux to the outer target is maximized, leading to the detachment of the inner divertor at lower densities compared to the outer divertor Hutchinson et al. [1995]. Despite this inherent asymmetry, the physical structure of the divertor does influence the onset of detachment. Introducing a dome structure or another physical barrier between the inner and outer divertor could potentially mitigate the asymmetry in the onset of detachment Maggi [1999], Pitts [2000].

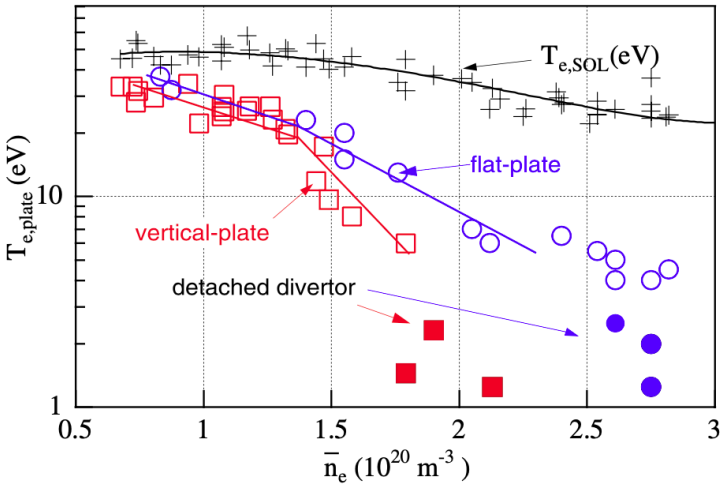


Figure F.3: Attached vs Detached divertor with vertical and horizontal target configuration shown at Alcator C-Mod Loarte [2001]

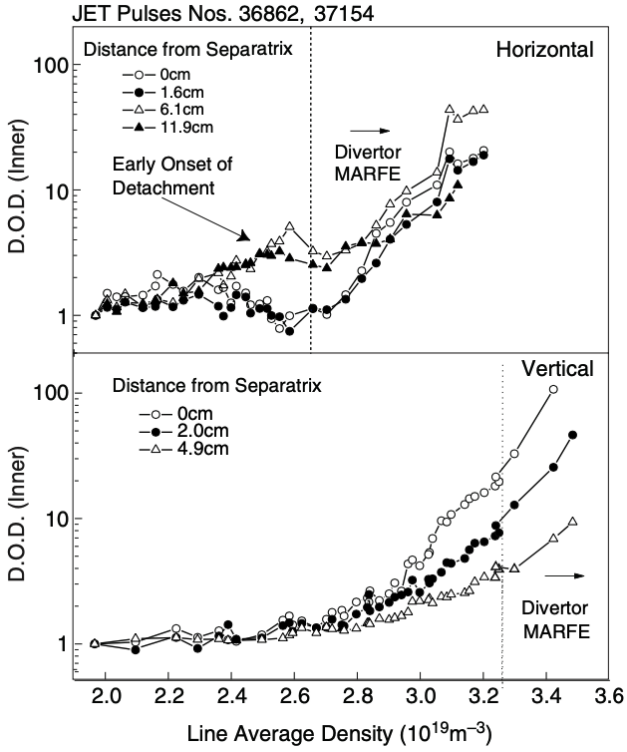


Figure F.4: Degree of Detachment (D.O.D) depicted over density scan for inner JET target in L-mode density scans. The upper figure shows early onset to detachment for horizontal divertor and lower figure shows detachment progressing from the separatrix to the SOL in a vertical divertor Monk [1997]

Vita

Kirtan Davda, born in India, grew up in the Middle East - Qatar, Bahrain, and the UAE. Later, he obtained a B.Tech in Electrical Engineering with a focus on high-voltage plasma. Subsequently, he graduated with an M.S. in Applied Energy and Electromechanical Systems from UNC-Charlotte. From 2017 onwards, he joined the Ph.D. program at the Bredesen Center at UTK and ORNL. His Ph.D. focused on Divertor Physics and neutral dynamics. After completing his Ph.D., he will be joining the NCSU FPAC lab as a postdoc, working with Dr. Florian Laggner. Kirtan Davda has volunteered at the local BAPS Hindu temple as an AV and Photography lead. With an interdisciplinary background and experience in policy-making and teaching, Kirtan Davda aims to focus on research and empower graduate students to pursue fusion.